

DESIGN OF INITIAL SHOTCRETE LINING FOR A MINE SHAFT USING TWO-DIMENSIONAL FINITE AND HYBRID FINITE-DISCRETE ELEMENT METHODS

by

Saeed Naseri

Submitted in partial fulfilment of the requirements
for the degree of Master of Applied Science

at

Dalhousie University
Halifax, Nova Scotia
March 2020

TABLE OF CONTENTS

TABLE OF CONTENTS	II
LIST OF TABLES	VII
LIST OF FIGURES	X
ABSTRACT	XXII
LIST OF SYMBOLS	XXIII
LIST OF ABBREVIATIONS	XXVII
ACKNOWLEDGEMENTS.....	XXIX
CHAPTER 1 INTRODUCTION.....	1
1.1. Overview	1
1.2. Motivation for Research.....	3
1.3. Objectives.....	4
1.4. Assumptions	5
1.5. Thesis Outline	6
CHAPTER 2 LITERATURE REVIEW	8
2.1. Introduction	8
2.2. Stresses and Displacements Around Circular Excavations	9
2.2.1. Kirsch Equations.....	9
2.2.2. Salencon Equations.....	12
2.3. Strength of Intact Rocks and Jointed Rock Masses	17
2.3.1. Mohr-Coulomb (<i>MC</i>) Failure Criterion.....	17
2.3.2. Hoek-Brown (<i>HB</i>) Failure Criterion	19

2.4.	Convergence Confinement Method (CCM)	22
2.4.1.	Ground Reaction Curve (GRC).....	24
2.4.1.1.	Analytical methods.....	24
2.4.1.2.	Numerical methods.....	32
2.4.2.	Longitudinal Displacement Profile (LDP)	41
2.4.3.	Support Characteristic Curve (SCC).....	49
2.5.	Support Factor of Safety	51
2.6.	Support Capacity Diagrams	57
2.7.	Time-dependent Properties of Shotcrete	59
2.7.1.	Young's Modulus	63
2.7.2.	Compressive Strength.....	65
2.7.3.	Poisson's Ratio	66
2.7.4.	Tensile Strength	67
2.8.	Summary	68

CHAPTER 3 STABILITY ASSESSMENT OF INITIAL SHOTCRETE LINING SIMULATED AS A STRUCTURAL ELEMENT USING 2D FINITE ELEMENT METHOD 70

3.1.	Introduction	70
3.2.	Case History	70
3.3.	Numerical Analysis	74
3.4.	Model Calibration	76
3.5.	Shotcrete Properties	79
3.6.	Stability Analysis of Initial Shotcrete Lining	80
3.6.1	Load Factor of Safety	80
3.6.2	Support Capacity Diagram	82
3.4.	Summary	84

CHAPTER 4 STABILITY ASSESSMENT OF INITIAL SHOTCRETE LINING SIMULATED AS A MATERIAL MODEL USING 2D FINITE ELEMENT METHOD 86

4.1.	Introduction	86
-------------	---------------------------	-----------

4.2.	RS2 Model Specifications	87
4.2.1.	Model Geometry.....	88
4.2.2.	Results of New Model.....	90
4.2.2.1.	Plastic zone.....	91
4.2.2.2.	Ground reaction curve	92
4.2.2.3.	Extensometer measurements	93
4.3.	Simulation of Initial Shotcrete Lining Using Material Model	94
4.4.	Stability Analysis of Initial Shotcrete Lining.....	98
4.4.1.	Shotcrete as an Elastic Material	98
4.4.2.	Shotcrete as an Elasto-plastic Material	100
4.4.2.1.	Progressive yielding of initial shotcrete liner	100
4.4.2.2.	Strain factor of safety for initial shotcrete liner	103
4.5.	Stability Analysis of Final Concrete Lining	109
4.6.	Summary	113

CHAPTER 5 STABILITY ASSESSMENT OF INITIAL SHOTCRETE LINING USING HYBRID FINITE-DISCRETE ELEMENT METHOD..... 115

5.1.	Introduction	115
5.2.	Finite-Discrete Element Method (FDEM).....	116
5.3.	Laboratory Tests on Fiber Reinforced Shotcrete by Saw et al. (2009)	122
5.3.1.	Mix Design and Curing Time for Shotcrete Specimens.....	123
5.3.2.	Methods of Axial Strain Measurements	123
5.3.3.	Uniaxial Compressive Test	124
5.3.4.	Brazilian Tensile Test.....	127
5.4.	Calibration of Laboratory-scale Model of Shotcrete	127
5.4.1.	Calibration Procedure	128
5.4.2.	Simulation of UCS Test Using FDEM Model with Fine Mesh	130
5.4.3.	Influence of Platen-Specimen Contact Friction and Gravity.....	133
5.4.4.	Simulation of Brazilian Test Using FDEM Model with Fine Mesh.....	139
5.5.	Sensitivity Analysis.....	141
5.5.1.	Model Sensitivity to Cohesion and Tensile Strength of Crack Elements	141

5.5.2.	Model Sensitivity to Friction Angle of Crack Elements.....	143
5.5.3.	Model Sensitivity to Fracture Energy Parameters of Crack Elements.....	144
5.5.4.	Model Sensitivity to Penalty Parameters of Crack Elements.....	146
5.6.	Simulation of UCS Test Using FDEM Model with Coarse Mesh	148
5.6.1.	Shotcrete Model Calibration.....	148
5.6.2.	Concrete Model Calibration.....	153
5.7.	Simulation of 3D Shaft Advance Using 2D FDEM Model.....	156
5.7.1.	Model Geometry.....	157
5.7.2.	Model Calibration	159
5.7.2.1.	Convergence confinement method.....	163
5.8.	Stability Analysis of Initial Shotcrete Liner	169
5.8.1.	Analysis of Scenario A.....	170
5.8.2.	Analysis of Scenario B	173
5.9.	Summary	175
CHAPTER 6	INFLUENCE OF EXCAVATION ADVANCE RATE ON STABILITY OF INITIAL SHOTCRETE LINING.....	177
6.1.	Introduction	177
6.2.	Advance Rates in Drill and Blast and Mechanized Tunnels.....	177
6.2.1.	Drill and Blast (D&B) Excavation.....	177
6.2.2.	Mechanized (Mech) Excavation.....	179
6.3.	Advance Rates in Drill and Blast and Mechanized Shafts	179
6.4.	Stability Analysis of Shotcrete Lining in D&B and Mech Excavations	181
6.4.1.	Load Factor of Safety in CCM.....	182
6.4.2.	Thrust-Moment Diagram	184
6.4.3.	Strength Factor	186
6.4.4.	Strain Factor of Safety	188
6.5.	Summary	192
CHAPTER 7	SUMMARY, CONCLUSIONS, AND RECOMMENDATIONS	194

7.1. Summary	194
7.2. Conclusions	195
7.3. Recommendations for Future Work.....	197
REFERENCES	200

LIST OF TABLES

Table 2-1 Rock properties used for calculating stresses and displacements around a circular excavation using Kirsch and Salencon equations	15
Table 2-2 Input parameters for constructing <i>GRC</i> using analytical and numerical methods	30
Table 2-3 <i>GRC</i> parameters for different analytical methods.....	32
Table 2-4 Face closure equations (from Oke et al., 2018).....	42
Table 3-1 The in-situ stress field at the formation (after Rafiei Renani et al., 2016)	71
Table 3-2 Mechanical properties of the intact rock determined from lab tests (after Rafiei Renani et al., 2016)	71
Table 3-3 Calibrated rock mass properties by Rafiei Renani et al. (2016).....	73
Table 3-4 Properties of 12-hour shotcrete lining used in the numerical model	80
Table 4-1 Overloaded sections of shotcrete liner with $FS < 1$	98
Table 4-2 RS2 stages and corresponding internal pressures.....	110
Table 4-3 Properties of final concrete liner used in the numerical model (Shütz, 2010)	112
Table 5-1 Mix design of the fiber reinforced shotcrete sample used in laboratory tests by Saw et al. (2009)	123
Table 5-2 Properties of 12-hr shotcrete used to calibrate the shotcrete model in Irazu	129

Table 5-3 Micro-properties of the shotcrete model meshed with fine elements and calibrated to the laboratory properties of 12-hr shotcrete	133
Table 5-4 Comparison between macro-properties of calibrated shotcrete model meshed with fine elements and target values	133
Table 5-5 Micro-properties of the shotcrete model meshed with coarse elements and calibrated to the properties of 12-hr shotcrete	150
Table 5-6 Comparison between properties of shotcrete models constructed with coarse and fine mesh elements and target 12-hr shotcrete.....	152
Table 5-7 Properties of 28-day concrete	153
Table 5-8 Micro-properties of the concrete model calibrated to the laboratory properties of 28-day concrete under unconfined condition.....	154
Table 5-9 Comparison between macro-properties of calibrated concrete model and laboratory properties of 28-day concrete	156
Table 5-10 Micro-properties of the rock mass in the shaft model calibrated to extensometer data.....	163
Table 5-11 Comparison between the results of calibrated RS2 and Irazu models.....	165
Table 6-1 Advance rates of <i>TBM</i> in different rock qualities (Bruland, 1998)	179
Table 6-2 Properties of shotcrete used for numerical simulations of shaft advance with different advance rates.....	182
Table 6-3 Comparison between percentage of overloaded sections of shotcrete liner simulated using material model and structural element in different excavation methods	188

Table 6-4 Calculated factors of safety for initial shotcrete lining in D&B and Mech excavations 193

LIST OF FIGURES

Figure 2-1 Geometry, coordinate system and parameters for calculating stresses and displacement around a circular excavation in a biaxial stress field using the method by Kirsch (1898) 10

Figure 2-2 Stresses and displacements near a circular excavation with a radius of 5 m in an isotropic stress field ($P_1 = P_2 = 26$ MPa) for $\theta = 0^\circ$ based on Kirsch equations: a) radial and tangential stresses; and b) radial and tangential displacements 11

Figure 2-3 Schematic view of a circular excavation under isotropic stress field of P_0 showing a plastic zone that is developed around the excavation boundary and the corresponding plastic radial displacement (u_r^{pl})..... 12

Figure 2-4 Stresses and displacements around a circular excavation calculated using Salencon equations for elasto-plastic medium and Kirsch equations for elastic medium: a) radial and tangential stresses; and b) radial displacement (rock properties are provided in Table 2-1) 15

Figure 2-5 Shear failure on plane ab (after Brady and Brown, 2005)..... 17

Figure 2-6 The MC strength envelope in terms of shear and normal stresses and its parameters..... 18

Figure 2-7 GSI chart (after Hoek and Marinos, 2000)..... 21

Figure 2-8 a) Longitudinal section of an advancing circular excavation showing the radial displacement profile and the internal pressures at three sections along the excavation; b) Ground Reaction Curve (GRC) and the Support Characteristic Curve (SCC); and c) Longitudinal Displacement Profile (LDP) 23

Figure 2-9 Schematic *GRC* and its parameters in elastic and elasto-plastic rocks proposed by: a) Panet (1993); and b) Hoek et al. (1995)..... 26

Figure 2-10 a) Comparison between *GRCs* obtained using methods proposed by Panet (1993), Hoek et al. (1995) and Carranza-Torres and Fairhurst (2000) for a circular excavation with a radius of 5 m under a 50 MPa isotropic stress field with rock properties given in Table 2-1; and b) zoomed-in view of the boxed area in Figure 2-10a 31

Figure 2-11 Methods to capture 3D excavation advance in a 2D model using: a) Internal Pressure Reduction ($P_i = 5$ MPa); b) Concentric Ring Excavation; c) Core Softening (core has a smaller Young's modulus than surrounding rock mass); and d) combined *CRE* and *CS* methods (centre of core has a smaller Young's modulus than surrounding rock mass and the outer rings) 33

Figure 2-12 a) Comparison between *GRCs* constructed using Panet (1993), Hoek et al. (1995), Carranza-Torres and Fairhurst (2000) and the *CS* and the *IPR* methods; b) zoomed-in view of the boxed area in Figure 2-12a 35

Figure 2-13 Geometries of; a) circular; b) cart; c) horse-shoe tunnels (after Gonza'lez-Nicieza et al., 2008)..... 36

Figure 2-14 Comparison between the convergence of three tunnel geometries at a depth of 250 m (after Gonza'lez-Nicieza et al., 2008) 37

Figure 2-15 *GRCs* constructed for different tunnel geometries and their comparison with the *GRC* obtained from Panet's method (after Gonza'lez-Nicieza et al., 2008)..... 37

Figure 2-16 a) Various post-peak behaviours for rock masses with different *GSI* values; b) definition of drop modulus in a strain-softening rock mass (modified from Alejano et al., 2009) 38

Figure 2-17 Different <i>GRCs</i> for elasto-plastic, elastic-brittle and strain-softening rock mass behaviors obtained using the method proposed by Alonso et al. (2003) for: a) weak rocks ($GSI < 35$); b) hard rocks ($65 < GSI < 75$); and c) average quality rocks ($40 < GSI < 60$) (modified from Alejano et al., 2009)	40
Figure 2-18 Schematic geometry of yielding zone around an advancing tunnel when: a) plastic zone is smaller than tunnel diameter; and b) plastic zone is larger than tunnel diameter (after Vlachopoulos and Diederichs, 2009).....	45
Figure 2-19 Representation of excavation sequences with supported and unsupported spans, using <i>TBM</i> , mechanical, and drill and blast excavation methods in axisymmetric numerical models (after Oke et al., 2018)	48
Figure 2-20 Comparison between <i>LDPs</i> obtained using empirical and semi-empirical approaches for a circular excavation with a radius of 5 m under a 26 MPa isotropic stress field with input parameters listed in Table 2-2	49
Figure 2-21 Schematic of the <i>GRC</i> and the <i>SCC</i> (after Oreste, 2003a)	50
Figure 2-22 Definition of FS_{load} for: a) $FS_{load} > 1$; and b) $FS_{load} < 1$	53
Figure 2-23 The CCM for conditions when the equilibrium pressure is reached: a) in the elastic portion of the <i>SCC</i> ($u_{eq} \geq u_{el}$); and b) in the plastic portion of the <i>SCC</i> ($u_{eq} < u_{el}$) .	54
Figure 2-24 The <i>GRC</i> with the <i>SCCs</i> for 10 cm and 25 cm shotcrete liner (after Alejano et al., 2017)	55
Figure 2-25 The <i>GRC</i> and the <i>SCC</i> for an excavation supported with rock bolts (after Li, 2017)	56
Figure 2-26 Support capacity diagrams for a tunnel: a) thrust-moment diagram; b) thrust-shear force diagram (after Carranza-Torres and Diederichs, 2009)	58

Figure 2-27 Influence of advance rate on capacity of shotcrete liners with and without yielding elements (after Gscwandtner and Galler, 2012).....	60
Figure 2-28 The SCC for a shotcrete liner in Kielder Experimental Tunnel (after Oreste, 2003b) (P_{eq} and U_{eq} are the pressure and displacement at equilibrium when the liner and ground interact)	62
Figure 2-29 Comparison between empirical equations for estimating Young's modulus of shotcrete with time with $s_{sh}= 0.2$, $a_{sh} = 1.132$, and $c_{sh} = -0.915$ (after Schutz, 2010)	64
Figure 2-30 Comparison between different empirical equations for estimating the compressive strength of shotcrete as a function of age	66
Figure 2-31 Poisson's ratio of shotcrete as a function of age (Aydan et al., 1992)	67
Figure 2-32 Change in the tensile strength of shotcrete with time (Byfors, 1980).....	68
Figure 3-1 Extensometers and support installation during shaft advance (after Rafiei Renani et al., 2016)	72
Figure 3-2 Measured displacements along: a) Ext. 1; b) Ext. 2; c) Ext. 3; and d) Ext. 4 (after Rafiei Renani et al. 2016)	73
Figure 3-3 a) RS2 model geometry; and b) mesh type and geometry near the simulated shaft	75
Figure 3-4 a) GRC obtained from RS2 model; and b) yielded zone predicted using calibrated RS2 model	77
Figure 3-5 Comparison of measured and simulated displacements along: a) Ext. 2; b) Ext. 3; and c) Ext. 4.....	78
Figure 3-6 Load factor of safety (FS_{load}) calculated for 50 mm initial shotcrete lining.....	81

Figure 3-7 FS_{load} distribution around the shaft boundary for shotcrete thicknesses of 50 mm, 75 mm, and 100 mm.....	81
Figure 3-8 Thrust-moment diagrams and overloaded sections of initial shotcrete lining (red segments) with thicknesses of: a and b) 50 mm; c and d) 75 mm; e and f) 100 mm	83
Figure 4-1 Error message in RS2 regarding the use of radial mesh with additional material model	87
Figure 4-2 Comparison between geometries of RS2 models constructed using: a) radial mesh; and b) uniform mesh.....	89
Figure 4-3 Comparison between RS2 models constructed using: a) uniform (left images) and radial (right images) mesh elements; b) zoomed-in view of the two models.....	90
Figure 4-4 Comparison between the extent of plastic zone near the shaft using: a) radial mesh; and b) uniform mesh.....	91
Figure 4-5 a) Comparison between the <i>GRCs</i> constructed for the unsupported shaft based on the models with radial and uniform mesh; and b) zoomed-in view of the boxed area in Figure 4-5a	92
Figure 4-6 Comparison between simulated radial displacements in models constructed using radial and uniform mesh elements along: a) Ext. 2; b) Ext. 3; and c) Ext. 4	93
Figure 4-7 Comparison between RS2 models with shotcrete liner simulated as a material model (left) and a structural element (right).....	94
Figure 4-8 Shotcrete liner simulated as a material model with thicknesses of: a) 50 mm; b) 75 mm; and c) 100 mm.....	95
Figure 4-9 Installation of shotcrete simulated as a material model: a) initial stage; b) shotcrete installation stage; and c) final stage with zero internal pressure	96

Figure 4-10 Comparison between *GRCs* in supported and unsupported models with: a) shotcrete liner simulated as a structural element in a model with the radial mesh; b) zoomed-in view of the boxed area in Figure 4-10a; and c) shotcrete liner simulated as a material model in a model with the uniform mesh; d) zoomed-in view of the boxed area in Figure 4-10c..... 97

Figure 4-11 Comparison between overloaded sections of initial shotcrete lining (highlighted in red) simulated as structural elements (left images) and material models (right images) with thicknesses of: a and b) 50 mm; c and d) 75 mm; and e and f) 100 mm 99

Figure 4-12 Yielding of the rock mass and 100 mm initial shotcrete liner 100

Figure 4-13 Closer views of the boxed area A in Figure 4-12 showing the progressive yielding of shotcrete liner: a) shotcrete installation stage; b) partial yielding of shotcrete; and c) complete yielding of shotcrete in the last excavation stage 101

Figure 4-14 Closer views of the boxed area B in Figure 4-12 showing the progressive yielding of shotcrete: a) shotcrete installation stage; b) partial yielding of shotcrete; and c) complete yielding of shotcrete in the last excavation stage 102

Figure 4-15 Schematic radial deformation of the shotcrete liner due to shaft wall convergence..... 103

Figure 4-16 a) Stress-strain curves from UCS tests on 50 mm shotcrete specimens of different curing times (after Saw et al., 2009); and b) Best fit curve relating lateral strain to shotcrete age 105

Figure 4-17 Radial displacements for shotcrete surface (d_b) and shaft wall (d_i) 106

Figure 4-18 a) FS_{strain} distribution around the shaft boundary for 50 mm shotcrete liner; b) zoomed-in view of the centre of Figure 4-18a 107

Figure 4-19 FS_{strain} distribution around the shaft boundary for: a) 75 mm shotcrete liner; b) zoomed-in view of the centre of Figure 4-19a; c) 100 mm shotcrete liner; and d) zoomed-in view of the centre of Figure 4-19c.....	108
Figure 4-20 GRC showing the radial displacements corresponding to the excavation face, blasts, extensometer and liner installation stages	109
Figure 4-21 RS2 model showing the 100 mm initial shotcrete liner simulated using a material model and the final concrete liner simulated using a structural element.....	111
Figure 4-22 Thrust-moment diagram for the final 200 mm concrete liner attached to the initial shotcrete liner with a thickness of 100 mm	112
Figure 5-1 View of four-noded crack elements located along edges of all adjoining triangular finite elements (after Lisjak and Grasselli, 2014; Lisjak, 2013).....	118
Figure 5-2 a) Conceptual model of a tensile crack in a heterogeneous brittle rock and the fracture process zone (FPZ); and b) theoretical FPZ model in FDEM (after Lisjak, 2013)	118
Figure 5-3 FDEM simulation process in Irazu (after Irazu 2D theory manual, 2019)	120
Figure 5-4 Constitutive behaviour for crack elements in Irazu described in terms of normal and tangential bonding stresses, σ and τ , versus relative displacements, opening (o) and sliding (s) (after Lisjak et al., 2014)	121
Figure 5-5 Stress-strain curves of shotcrete specimens under different confining pressures. Dashed lines represent the results obtained from the strain gauges and solid lines are those obtained from the displacement of the top and bottom platens (after Saw et al., 2009)	124

Figure 5-6 a) Shotcrete specimen before (left) and after (right) the *UCS* test (after Saw et al., 2009); b) failure mode of another shotcrete specimen under unconfined compression (after Saw et al., 2009)..... 125

Figure 5-7 a) Stress-strain curves for shotcrete specimens with curing periods of 1, 3, 7, and 28 days (after Saw et al., 2009); b) empirical equation derived from the relationship between the axial strain and shotcrete age 126

Figure 5-8 Shotcrete specimen after Brazilian test (after Saw et al., 2009)..... 127

Figure 5-9 Irazu model constructed with fine mesh elements (i.e. edge length of 2 mm) and used to simulate *UCS* test on 12-hr shotcrete..... 130

Figure 5-10 Stress-strain curve of the shotcrete model and its comparison with the target stress-strain curve. The lower images correspond to three stages of loading and show the progressive fracturing of shotcrete at peak and two stages in the post-peak region ... 132

Figure 5-11 Stress-strain curve of an Irazu model calibrated to the strength and elastic modulus of Lac du Bonnet granite under unconfined condition (after Vazaios et al., 2019) 134

Figure 5-12 Stress-strain curve of a PFC model calibrated to the strength and elastic modulus of Lac du Bonnet granite under unconfined condition (after Cho et al., 2007) 135

Figure 5-13 a) Stress-strain curves of the simulated shotcrete specimen with and without friction at the contact between the platens and the specimen and their comparisons with the target stress-strain curve. Failure modes of shotcrete models with platen-shotcrete friction coefficients of: b) 0.0; and c) 0.1..... 136

Figure 5-14 a) Stress-strain curves of the shotcrete model with and without the effect of gravity and their comparisons with the target stress-strain curve. The lower images show

the failure modes of: b) numerical specimen without the effect of gravity; c) numerical specimen with the effect of gravity; and d) laboratory specimen (after Saw et al., 2009)	138
Figure 5-15 Brazilian disk and the elastic platens built in Irazu.....	139
Figure 5-16 Force-displacement curve of the Brazilian test simulated on shotcrete in Irazu. The lower images correspond to three stages of loading showing progressive fracturing of shotcrete at peak (A) and two stages in the post-peak region (B and C).....	140
Figure 5-17 Comparison between the failure mode of Brazilian test on shotcrete: a) numerical simulation in Irazu; b) laboratory test by Saw et al. (2009)	141
Figure 5-18 Influence of crack element cohesion on the stress-strain response of shotcrete model under unconfined compression.....	142
Figure 5-19 Influence of crack element tensile strength on the stress-strain response of shotcrete model under unconfined compression	143
Figure 5-20 Influence of crack element friction angle on the stress-strain curve of shotcrete model under unconfined compression	144
Figure 5-21 Influence of: a) Mode I fracture energy (G_{Ic}); and b) Mode II fracture energy (G_{IIc}) on the stress-strain response of the shotcrete model	145
Figure 5-22 Influence of: a) normal penalty; b) tangential penalty; and c) fracture penalty on the stress-strain response of shotcrete model.....	147
Figure 5-23 Irazu model constructed using coarse mesh elements for the simulation of: a) UCS test; and b) Brazilian test.....	149
Figure 5-24 a) Stress-strain and c) force-displacement curves of shotcrete models meshed with fine and coarse elements. The lower images correspond to three stages of shotcrete	

loading during: b) UCS; and d) Brazilian test and show the progressive fracturing of shotcrete at peak (A and D) and two stages in the post-peak region (B, C, E, and F). Zoomed-in views of the boxed areas show cracks initiated at stages A and D..... 151

Figure 5-25 Comparison between the failure modes of shotcrete specimens: a) numerical simulation in Irazu; b) laboratory test by Saw et al. (2009) 152

Figure 5-26 a) Stress-strain and b) force-displacement curves of the concrete model with coarse mesh. The lower images correspond to three stages of loading of concrete sample during: b) UCS; and d) Brazilian test and show progressive fracturing of concrete model at peak (A and D) and two stages in the post-peak region (B, C, E, and F) 155

Figure 5-27 Comparison between the geometry and size of mesh elements in: a) shotcrete liner attached to the shaft wall; and b) shotcrete *UCS* specimen used for model calibration 157

Figure 5-28 a) Geometry of the shaft model showing the mesh size in three sub-domains as well as the shotcrete and concrete liners; b) geometry of the model of the *URL* test tunnel showing the mesh size in four sub-domains (after Vazaios et al., 2019)..... 158

Figure 5-29 Calibration procedure to determine the input parameters for the Irazu model of *URL* test tunnel (after Vazaios et al., 2019)..... 161

Figure 5-30 Comparison between *GRCs* obtained from right wall, crown notch, and bottom notch of the *URL* test tunnel in the *FDEM* model and the *GRC* obtained from the *FEM* model (after Vazaios et al., 2019)..... 162

Figure 5-31 a) Irazu model of the mine shaft showing the extent of fractured zone. Comparison between the *GRCs* obtained from calibrated Irazu and RS2 models for two points on the shaft boundary: b) *GRCs* for point A; c) *GRCs* for point B 164

Figure 5-32 Procedure to use the <i>FDEM</i> model results (e.g. radius of plastic zone and the radial displacement) to determine displacements corresponding to any given distance from the shaft face (modified from Vazaios et al., 2019).....	166
Figure 5-33 Comparison of measured and simulated displacements along: a) Ext. 2; b) Ext. 3; and c) Ext. 4.....	168
Figure 5-34 Geometry of the mine shaft supported with the initial shotcrete liner simulated in Irazu using different sub-domains with different mesh element sizes for the rock mass, the core and the liner	170
Figure 5-35 a) Extent of rock mass fracturing near the mine shaft supported with initial 12-hr shotcrete liner as the only support element; b) zoomed-in view of the boxed area in Figure 5-35a, showing bending of the shotcrete liner due to axial thrust and rock mass bulking; c) zoomed-in view of the boxed area in Figure 5-35b, indicating the failure of shotcrete liner.....	172
Figure 5-36 a) Extent of rock mass fracturing near the mine shaft supported with 12-hr shotcrete liner and 28-day concrete liner; b) zoomed-in view of the boxed area in Figure 5-36a, showing the fractured zone in the rock mass near the liner (dashed lines show concrete-shotcrete and shotcrete-rock mass contacts); and c) zoomed-in view of the boxed area in Figure 5-36b, indicating minor cracking of the shotcrete liner	174
Figure 6-1 FS_{load} distribution around the shaft boundary for shotcrete thicknesses of 50 mm and 100 mm using: a) Mech method with an excavation advance rate of 6 m/day; and b) D&B method with an excavation advance rate of 1.5 m/day	183
Figure 6-2 Thrust-moment diagrams and overloaded sections of 6-hr shotcrete lining (red segments) with thicknesses of: a) 50 mm and b) 100 mm for Mech excavation with an advance rate of 6 m/day.....	185

Figure 6-3 Thrust-moment diagrams and overloaded sections of 18-hr shotcrete lining (red segments) with thicknesses of: a) 50 mm and b) 100 mm for D&B excavation with an advance rate of 1.5 m/day 186

Figure 6-4 Comparison between overloaded sections of initial shotcrete lining (strength factor < 1 highlighted in red) simulated as material model: a) 50 mm shotcrete with advance rate of 6 m/day (i.e. fast Mech excavation); b) 50 mm shotcrete with advance rate of 1.5 m/day (i.e. slow D&B excavation); c) 100 mm shotcrete with advance rate of 6 m/day; and d) 100 mm shotcrete with advance rate of 1.5 m/day 187

Figure 6-5 a) FS_{strain} distribution around the shaft boundary for 50 mm shotcrete liner with advance rate of 6 m/day; b) zoomed-in view of the centre of Figure 6-5a; c) FS_{strain} distribution around the shaft boundary for 50 mm shotcrete liner with advance rate of 1.5 m/day; and d) zoomed-in view of the centre of Figure 6-5c..... 189

Figure 6-6 a) FS_{strain} distribution around the shaft boundary for 100 mm shotcrete liner with advance rate of 6 m/day; b) zoomed-in view of the centre of Figure 6-6a; c) FS_{strain} distribution around the shaft boundary for 100 mm shotcrete liner with advance rate of 1.5 m/day; and d) zoomed-in view of the centre of Figure 6-6c..... 191

ABSTRACT

Shotcrete is widely used as a temporary support element in the construction of underground mines and tunnels. It is sprayed on the excavation walls close to the face to provide a safe working condition for mine personnel and equipment until the permanent support elements are installed. Therefore, the ability of the shotcrete lining to resist falls of ground is of paramount importance. The mechanical properties of shotcrete, including strength and stiffness, change with time as the excavation advances. Shotcrete may also be subject to plastic deformation, if it is loaded beyond its maximum capacity, especially in fast advancing excavations. Conventional methods for the design of shotcrete lining, based on analytical and empirical approaches, do not consider the influence of advance rate on the time-dependent properties and deformation behavior of shotcrete.

In this research, two-dimensional finite and hybrid finite-discrete element methods are utilized to develop new methodologies for the design of initial shotcrete lining for a mine shaft by considering the excavation advance rate. These methods are also used to gain further insight into the damage evolution leading to the failure of shotcrete liner during the excavation advance. Through the analyses of the load and strain factors of safety calculated for the shotcrete liner based on the results of finite element models, the minimum shotcrete thickness is suggested for the mine shaft. From the results of the hybrid finite-discrete element model, it is concluded that the shotcrete liner cannot be used as a sole support element for the mine shaft as it fails during the excavation advance due to the shaft convergence. However, it can be used as a temporary support, although it may be damaged until the final, permanent concrete liner is installed.

LIST OF SYMBOLS

σ_{rr}	Radial stress (MPa)
$\sigma_{\theta\theta}$	Tangential stress (MPa)
$\sigma_{r\theta}$	Shear stress (MPa)
u_{rr}	Radial displacement (m)
$u_{\theta\theta}$	Tangential displacement (m)
R	Radius of circular excavation (m)
R_p	Plastic zone radius around a circular excavation(m)
r	Distance from the center of a circular tunnel (m)
P_0	In situ stress (far field) (MPa)
P_1	Maximum far field stress
P_2	Minimum far field stress
θ	Angle form horizontal axis in a circular excavation counted counter-clockwise (°)
P_i	Internal pressure (MPa)
K	$\frac{P_2}{P_0}$
K_{ps}	Dilation coefficient
K_s	Support stiffness
q_m, χ	Variable-dependent constant in Salencon's method
σ_{ri}	Radial stress at interface between the elastic and the plastic zone (MPa)
c	Cohesion (MPa)
φ	Friction angle (°)
ψ	Dilation angle (°)
E	Young's modulus (GPa)
E_{rm}	Young's modulus of rock mass (GPa)
G	Shear modulus (GPa)
G_{rm}	Shear modulus of rock mass (GPa)
v	Poisson's ratio

σ_{rp}	Radial stress in the plastic zone (MPa)
$\sigma_{\theta p}$	Tangential stress in the plastic zone (MPa)
σ_{re}	Radial stress in the elastic zone (MPa)
$\sigma_{\theta e}$	Tangential stress in the elastic zone (MPa)
u_{re}	Radial displacement in the elastic zone (m)
u_{rp}	Radial displacement in the plastic zone (m)
σ_n	Normal stress
λ	Confinement loss
λ_d	Confinement loss for a distance of d from the face of a circular excavation in an elastic condition
$\lambda(d)$	Confinement loss for a distance of \underline{d} from the face of a circular excavation in a plastic condition
n, m, ξ	Specific parameters (Panet, 1995)
P_I	Scaled internal pressure
S_0	Scaled in situ stress
σ_{ci}	Uniaxial compressive strength of the intact rock (MPa)
m_i, m_b, s, a	Hoek-Brown parameters
P_i^{cr}	Critical internal pressure
u_r^{el}	Radial deformation of circular excavation boundary in an elastic condition
u_r^{pl}	Radial deformation of circular excavation boundary in a plastic condition
σ_{cm}	Compressive strength of rock mass (MPa)
R^*	Plastic zone radius normalized to the tunnel radius
d^*	Distance from the excavation face normalized to the tunnel radius
u_{max}	Maximum radial displacement of excavation boundary
$u_{max\ sup}$	Maximum radial displacement of excavation boundary in a supported excavation
u_0	Radial displacement of excavation face
$u_{0\ sup}$	Radial displacement of excavation face in a supported excavation
u_r	Radial displacement of excavation boundary

u^*	Radial displacement of excavation boundary normalized to the maximum displacement of excavation boundary
u_0^*	Radial displacement of excavation face normalized to the maximum displacement of excavation face
u_a^*	Radial displacement ahead of the face normalized to the maximum radial displacement
u_b^*	Radial displacement behind the face normalized to the maximum radial displacement
A_a, A_b, B_a, B_b	Statistical constants for ahead (a) and behind (b) the face of an excavation
ϵ_a	Axial strain
ϵ_l	Lateral strain
d_b	Rock mass deformation
d_l	Liner deformation
d	Liner thickness
T_{sh}	Shotcrete age
t_{sh}	Shotcrete thickness
f_s	Shear strength
f_c	Equivalent crack nodal force in FDEM
f_r	Residual friction strength
f_t, σ_t	Tensile strength
G_{Ic}	Fracture energy mode I (tension)
G_{IIc}	Fracture energy mode II (shear)
o	Crack opening
s	Crack sliding
h	Element size in FDEM theory
p_n	Normal penalty parameter
p_t	Tangential penalty parameter
p_f	Fracture penalty parameter
p_s^{max}	Maximum support capacity
P_{eq}	Equilibrium pressure

u_{eq}	Equilibrium deformation
u_{el}	The point on the SCC where the plastic deformation of the support begins
u_{sh}	Deformation of an excavation before spraying shotcrete
u_c	Critical displacement (beyond this displacement the rock will collapse)
σ_{max}	Maximum applied pressure
f_{cp}	Compressive strength of shotcrete
$f_{cp,28}$	Compressive strength of 28-day shotcrete
$f_{cp,1}$	Compressive strength of 1-day shotcrete
σ_1	Maximum principal stress
σ_2	Intermediate principal stress
σ_3	Minimum principal stress
FS_{load}	Load factor of safety
FS_{Disp}	Displacement factor of safety
FS_{Energy}	Energy factor of safety
FS_{Strain}	Strain factor of safety
E_{sh}	Young's modulus of shotcrete
E_{28}	Young's modulus of 28-day shotcrete
f_{tp}	Tensile strength of shotcrete
ν_{sh}	Poisson's ratio of shotcrete
k_{sh}	Ratio between the compressive strength of 1-day shotcrete and 28-day shotcrete
K_s	Support stiffness
a_c, b_c, a_{sh}, s_{sh}	Material constant depending on the shotcrete mixture

LIST OF ABBREVIATIONS

2D/3D	Two/three Dimensional
CCM	Convergence Confinement Method
CRE	Concentric Ring Excavation
CS	Core Softening
D&B	Drill and Blast
DEM	Discrete Element Method
Ext.	Extensometer
FDEM	Finite Discrete Element Method
FDM	Finite Difference Method
FEM	Finite Element Method
FPZ	Fracture Process Zone
FS	Factor of Safety
GRC	Ground Reaction Curve
GSI	Geological Strength Index
HB	Hoek-Brown
IPR	Internal Pressure Reduction
LDP	Longitudinal Displacement Profile
MC	Mohr-Coulomb
Mech	Mechanized
Q (system)	Tunneling Quality Index
RMR	Rock Mass Rating
SBC	Shaft Boring Cutterhead
SBE	Shaft Boring Enlarger
SBM	Shaft Boring Machine
SBR	Shaft Boring Roadheader
SCC	Support Characteristic Curve
TBM	Tunnel Boring Machine

UCS Uniaxial Compressive Strength
URL Underground Research Laboratory

ACKNOWLEDGEMENTS

I cannot use words to express my gratitude to my supervisor and friend, Dr. Navid Bahrani. He let me choose and follow my own path and was always there to kindly steer me to the right direction during this journey. Having weekly meetings even if to just listen to my modeling difficulties has been greatly appreciated through this process.

I would like to acknowledge Dr. Andrew Corkum for his advice and help regarding the results of this thesis. I am gratefully indebted to his valuable comments on this research.

I want to address a warm thanks to all members of the Geomechanica team for providing the Irazu software used in this research. Special thanks to Dr. Omid Mahabadi and Dr. Andrea Lisjak for the complimentary training course and technical support on Irazu modeling.

Finally, I must express my very profound gratitude to my parents and to my sister for providing me with unfailing support and continuous encouragement throughout this journey. I could not have completed this thesis without their continuous encouragement, support and motivation.

Chapter 1 Introduction

1.1. Overview

The safe and economic construction of underground excavations requires effective and reliable means of ground support that can be installed in such a way that the projects can proceed without unnecessary delays. A robust design of ground support requires a deep knowledge of in situ and induced stresses and anticipated rock mass behaviours.

The most common approaches for the design of ground support in underground excavations are based on analytical, empirical and numerical methods. Analytical solutions have been developed for simple excavation geometries based on several assumptions for the in situ stress and rock mass behavior. For example, the ground reaction curve (Hoek et al., 1995) is an analytical approach that can be used to anticipate the deformation on the boundary of a circular opening during the excavation advance in a homogeneous rock mass under a hydrostatic in situ stress condition.

Empirical approaches based on rock mass classification systems are primarily used for preliminary support design, when very little detailed information on the rock mass and its stress and hydrogeologic characteristics is available. As discussed by Hoek et al. (1995), rock mass classification systems are most appropriate when used within the bounds of the case histories from which they were developed. Therefore, care must be taken when applying these classification schemes to other rock engineering problems.

Numerical modeling methods are used to determine the distribution of stresses and deformation at and near excavation boundaries and to design ground support. The advantage of numerical methods over analytical solutions and empirical approaches is that they can also be used to obtain the induced stresses, anticipated rock mass deformation and failure mode around excavations with complex geometries under non-hydrostatic stress conditions. 3D numerical models provide a more realistic

representation of stress redistribution around the excavations than 2D models. However, they are not as efficient as 2D models especially when extensive model calibration is required. For this reason, 2D models are often used as an alternative approach to simulate the progressive excavation advance, estimate the ground deformation and design the support system.

In the last few decades, all three methods described above have been used to design ground support for circular excavations such as tunnels and shafts. In recent years, with advances in numerical modeling methods, software tools and computation power, structural design has been integrated with numerical modeling to improve the design of ground support in underground excavations.

Shotcrete is widely used as a support element in the construction of mine excavations, tunnels and shafts. The initial shotcrete is sprayed close to the excavation face to provide a supported environment which permits equipment and subsequently workers to safely return to the workspace. According to Rispin et al. (2017), the functions of initial shotcrete lining in underground mine developments are:

- to hold rock pieces in place in the early stages of excavation while supporting its own weight, and
- to accommodate inward radial displacements prior to the installation of final, permanent support measures such as rock bolts and/or concrete lining, depending on the type of excavation.

Therefore, the stability of initial shotcrete lining is of paramount importance for the safe and economic construction of underground excavations. The stability analysis and design of initial shotcrete lining in circular excavations (e.g. mine shafts) is the focus of this thesis.

1.2. Motivation for Research

Conventional drill-and-blast excavation is still the norm in modern-day lateral (drifts) and vertical (shafts) developments in underground mines, although there is a tendency towards mechanized excavation techniques to increase the advance rates. One of the methods to increase the advance rate in both excavation techniques is the use of shotcrete as a temporary support measure, instead of rock bolts. Shotcrete can be sprayed by a remote operator, therefore brings safety benefits by removing people from the face of the excavation, while speeding up the development process. This, however, means that the young-age shotcrete lining is the only support element that must provide a safe environment for the personnel to continue the development until the permanent support measures are installed (Mohajerani et al. 2015).

According to Iwaki et al. (2001), a shotcrete liner with an unconfined compressive strength of 0.5 - 1 MPa should provide adequate support to resist falls of ground, although the safe re-entry time should be determined on a project base (Mohajerani et al. 2015). For this reason, the design of initial shotcrete lining should be based on the mechanical properties of early-age shotcrete.

Today, the industry norm for re-entry into a freshly shotcreted heading is the assurance of reaching 1 MPa compressive strength (Rispin et al., 2017). The re-entry time for standard shotcreted headings in many mines to reach this threshold is 8 hours (Rispin et al., 2017; personal communication with ground control engineers in Sudbury mines). However, based on the results of laboratory tests on shotcrete samples a compressive strength of 1 MPa is reached within 30 - 120 minutes (Rispin et al., 2017). This suggests a potential for increasing the advance rates by reducing the re-entry time to 2 hours or less. This, however, requires further research using laboratory tests, field experiments and monitoring and numerical modeling.

The strength and deformation properties of early-age shotcrete change progressively with time as the excavation face advances. Therefore, time-dependent behavior and properties of shotcrete need to be considered for realistic anticipation of ground-support interactions. Moreover, the initial shotcrete lining may yield and experience plastic deformation if it is sprayed close to the face, especially in fast advancing excavations. In such conditions, it is important to ensure that the initial shotcrete lining can sustain the ground deformation by the time other support elements are installed.

Different analytical, empirical and numerical approaches are being used for the design of surface support (i.e. shotcrete and concrete lining) in underground excavations. However, there is no standard methodology for the design of initial (early-age) shotcrete lining as a temporary support element in mine developments. This thesis aims at introducing new methodologies for stability analysis and design of initial shotcrete lining in circular excavations using two-dimensional (2D) continuum and discontinuum numerical methods.

1.3. Objectives

The central objective of this thesis is to improve existing approaches and develop new methodologies for the design of initial shotcrete lining in mine shafts by considering the excavation advance rate. For this purpose, 2D continuum and discontinuum numerical methods are used to simulate progressive excavation advance and assess the stability of initial shotcrete linings of various thicknesses. The numerical simulations are conducted with reference to a case history of a mine shaft described by Rafiei Renani et al. (2016). Detailed objectives of this research include:

- Investigating the stability of initial shotcrete lining based on the conventional load factor of safety;
- Investigating the stability of initial shotcrete lining simulated as a structural element using a 2D finite element program;

- Developing a methodology to simulate the initial shotcrete lining as a martial model and calculate its strain factor of safety using a 2D finite element program;
- Capturing the progressive yielding of initial shotcrete lining during excavation advance using a 2D finite element program;
- Assessing the stability of the full support system consisting of initial shotcrete and final concrete linings in a single finite element model;
- Capturing the progressive fracturing processes of the initial shotcrete lining during excavation advance using a 2D hybrid finite-discrete element program;
- Investigating the stability of the full support system including initial shotcrete and final concrete linings using a 2D hybrid finite-discrete element program; and
- Investigating the influence of excavation advance rate on the stability of initial shotcrete lining using a 2D finite element program.

The numerical simulations are conducted using the 2D finite element program RS2 (by Rocscience) and the 2D hybrid finite-discrete element program Irazu (by Geomechanica).

1.4. Assumptions

The following describes some of the main assumptions made when conducting this research:

- It is assumed in the numerical simulations that the shaft is completely circular, and the excavation boundary is smooth;
- Although the shaft was excavated using the drill-and-blast technique, the blast damage around the excavation boundary was not considered in the simulations;
- It is assumed that shotcrete properties do not change with the excavation advance (i.e. during shaft sinking). Therefore, the liner was assigned constant properties of early-age (12-hour) shotcrete in the numerical models. This assumption results in a conservative design for the liner, as in reality the shotcrete liner becomes stiffer and harder with time as the excavation advances.

1.5. Thesis Outline

The research is described, and the results are presented in seven chapters:

This introductory chapter provided an overview of the research, its objectives and assumptions.

Chapter 2 contains a comprehensive literature review on the design of ground support in circular excavations. Included in this chapter is a detailed review of the three main components of the convergence confinement method for the design of ground support including the ground reaction curve, the longitudinal displacement profile and the support characteristic curve. In the last part of this chapter, existing empirical relationships used to estimate the time-dependent mechanical properties of shotcrete are reviewed.

Chapter 3 presents the results of the numerical simulation of a mine shaft conducted using RS2. In this chapter, the initial shotcrete lining is assumed to be an elastic material and simulated using a structural element. The stability of the shotcrete liner is investigated using the load factor of safety in the convergence confinement method and the support capacity diagrams.

In Chapter 4, a material model with elastic-perfectly-plastic properties is used to simulate the shotcrete liner in RS2. This allows for better understanding the progressive yielding processes of the initial shotcrete lining during the excavation advance. In this chapter, a methodology for analyzing the stability of initial shotcrete lining by calculating its strain factor of safety is introduced. This is followed by introducing a methodology for simulating the full support system, consisting of the initial shotcrete liner simulated as a material model and the final concrete liner simulated as a structural element in a single RS2 model by considering their installation distances from the excavation face.

In Chapter 5, Irazu, which is a 2D numerical program based on the hybrid finite-discrete element method is used to simulate both the initial shotcrete and the final concrete linings using a material model. The objective of this chapter is to gain further insight into the progressive fracturing and failure processes of the initial shotcrete lining during the excavation advance, and its effectiveness as a temporary support element in stabilizing the excavation walls.

Chapter 6 presents the results of an investigation on the influence of excavation advance rate on the stability of initial shotcrete lining. For this purpose, the initial shotcrete lining is simulated using both structural element and material model in RS2 and its stability is assessed for two excavation advance rates; one representing a relatively slow drill-and-blast excavation and the other one representing a rapid mechanized excavation.

Chapter 7 provides a summary of this research including its major findings and recommendations for future work.

Chapter 2 Literature Review

2.1. Introduction

Underground excavations are susceptible to excessive deformation and failure when the induced stresses exceed the rock mass strength. Therefore, the in situ state of stress, the rock mass strength and its behavior should be considered when designing underground excavations. One of the most important factors making the design process challenging is the lack of reliable geotechnical data including the stress field and the strength and deformation properties of the rock mass. Other factors such as the interaction between the support system and the rock mass and the time-dependent behavior of the rock mass and the support elements should also be considered in the design process (González-Nicieza et al., 2008).

Through the last decades, researchers have developed several empirical and analytical methods for determining the induced stresses and deformation around underground openings. Rock mass classification systems such as the Rock Mass Rating (RMR) (Bieniawski, 1974) and the Tunneling Quality Index (Q) (Barton et al., 1974) have been used for support designs. These empirical methods provide recommendations for support selection based on rock mass quality. Analytical methods are based on several assumptions (e.g. isotropic stress field, circular excavation, etc.) that limit their applicability. Therefore, researchers have used numerical modeling methods to overcome some of the limitations of empirical and analytical approaches. It is generally suggested to use all the three methods (i.e. analytical, empirical and numerical) in order to arrive at a more reliable excavation design.

In this chapter, some of the most common analytical, empirical and numerical methods for the design of circular excavations are described and their limitations are addressed. First, analytical methods proposed by Kirsch (1898) and Salencon (1969) are briefly reviewed. Then, two commonly used failure criteria for intact rocks and jointed rock

masses are described. Next, the convergence confinement method and its components used for the design of ground support in circular excavations are reviewed in detail. In the last sections of this chapter, various methods used for stability analysis of surface support (i.e. shotcrete and concrete liners) as well as time-dependent properties of shotcrete are discussed in depth.

2.2. Stresses and Displacements Around Circular Excavations

Two primary parameters for the design of underground excavations are the in situ state of stress and the rock mass strength. The method by Kirsch (1898), known as “Kirsch equations”, provides a solution for calculating elastic stresses and displacements around an infinite circular excavation. The method proposed by Salencon (1969), referred to as “Salencon equations” in this document, is also used for infinite circular excavations but the medium is assumed to be elasto-plastic.

2.2.1. Kirsch Equations

Figure 2-1 presents a circular excavation with a radius of R subjected to a biaxial stress field, where P_1 and P_2 are the maximum and minimum far field stresses, respectively (i.e. $P_1 = P_0$, $P_2 = KP_0$, $K \leq 1$). According to Kirsch (1898), the induced stresses including radial (σ_{rr}), tangential ($\sigma_{\theta\theta}$) and shear ($\sigma_{r\theta}$) stresses and the displacements including radial (u_r) and tangential (u_θ) displacements found at any point in the rock mass with a distance of r from the centre of the excavation can be calculated using the following equations:

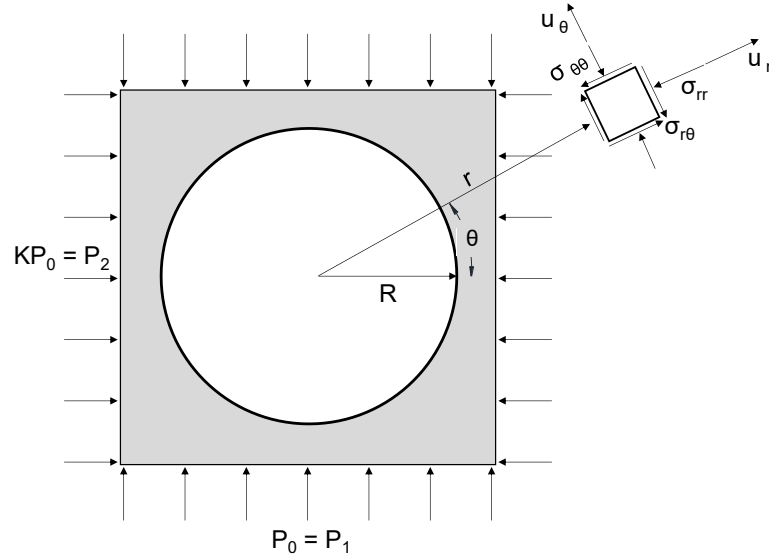


Figure 2-1 Geometry, coordinate system and parameters for calculating stresses and displacement around a circular excavation in a biaxial stress field using the method by Kirsch (1898)

$$\sigma_{rr} = \left(\frac{P_1+P_2}{2}\right)\left(1 - \frac{R^2}{r^2}\right) + \left(\frac{P_2-P_1}{2}\right)\left(1 - 4\frac{R^2}{r^2} + 3\frac{R^4}{r^4}\right)\cos 2\theta \quad \text{Equation 2-1}$$

$$\sigma_{\theta\theta} = \left(\frac{P_1+P_2}{2}\right)\left(1 + \frac{R^2}{r^2}\right) - \left(\frac{P_2-P_1}{2}\right)\left(1 + 3\frac{R^4}{r^4}\right)\cos 2\theta \quad \text{Equation 2-2}$$

$$\sigma_{r\theta} = \left(\frac{P_1-P_2}{2}\right)\left(1 + 2\frac{R^2}{r^2} - 3\frac{R^4}{r^4}\right)\sin 2\theta \quad \text{Equation 2-3}$$

$$u_{rr} = \left(\frac{P_1+P_2}{4G}\right)\left(\frac{R^2}{r}\right)\left(\frac{P_2-P_1}{4G}\right)\left(\frac{R^2}{r}\right)\left(4(1-\nu) - \frac{R^2}{r^2}\right)\cos 2\theta \quad \text{Equation 2-4}$$

$$u_{\theta\theta} = -\left(\frac{P_2-P_1}{4G}\right)\left(\frac{R^2}{r}\right) + \left(2(1-2\nu) + \frac{R^2}{r^2}\right)\sin 2\theta \quad \text{Equation 2-5}$$

In these equations, G is the shear modulus (MPa) and ν is the Poisson's ratio. Note that the angle θ is measured counter-clockwise from the horizontal position. On the

excavation boundary (i.e. $r = R$), the radial and shear stresses are zero and the magnitude of tangential stress is calculated using the following equation:

$$\sigma_{\theta\theta} = (3P_1 - P_2) \cos 2\theta \quad \text{Equation 2-6}$$

Figure 2-2 illustrates the distribution of stresses and displacements as a function of distance from the excavation boundary along the horizontal axis (i.e. $\theta = 0^\circ$). This calculation is for an excavation with a radius of 5 m in a rock with a Young's modulus of 27 GPa and a Poisson's ratio of 0.25 under an isotropic stress field ($P_0 = P_1 = P_2 = 26 \text{ MPa}$). Using Equation 2-6, the maximum tangential stress ($\sigma_{\theta\theta}$), on the excavation boundary is calculated to be 52 MPa (i.e. $\sigma_{\theta\theta} = 3P_1 - P_2 = (3 \times 26) - (26) = 52 \text{ MPa}$). Figure 2-2a shows that the tangential stress decreases from its maximum value and the radial stress increases from zero with increasing the distance from the excavation boundary. Both stresses reach the far field stress at about $r = 8R$.

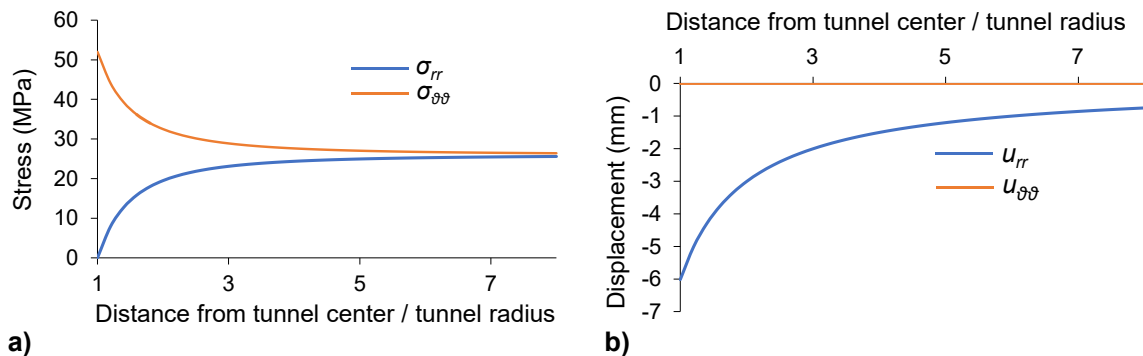


Figure 2-2 Stresses and displacements near a circular excavation with a radius of 5 m in an isotropic stress field ($P_1 = P_2 = 26 \text{ MPa}$) for $\theta = 0^\circ$ based on Kirsch equations: a) radial and tangential stresses; and b) radial and tangential displacements

Figure 2-2b shows the change in radial and tangential displacements with increasing distance from the excavation boundary for $\theta = 0^\circ$. As can be seen in this figure, the tangential displacement is zero on the excavation boundary, while the radial displacement is about 6 mm. Note that negative displacement (convergence) indicates inward displacement. The magnitude of radial displacement decreases with increasing

distance from the excavation boundary and reaches about zero far from the excavation, at $r > 8R$.

2.2.2. Salencon Equations

When the excavation-induced stresses exceed the rock strength, the rock yields and a plastic zone is developed near the excavation boundary. The analytical solution developed by Salencon (1969) for determining the stresses and displacements around a circular excavation considers the rock as an elasto-plastic medium with a plastic zone of a radius of R_p developed near the excavation boundary, as depicted in Figure 2-3.

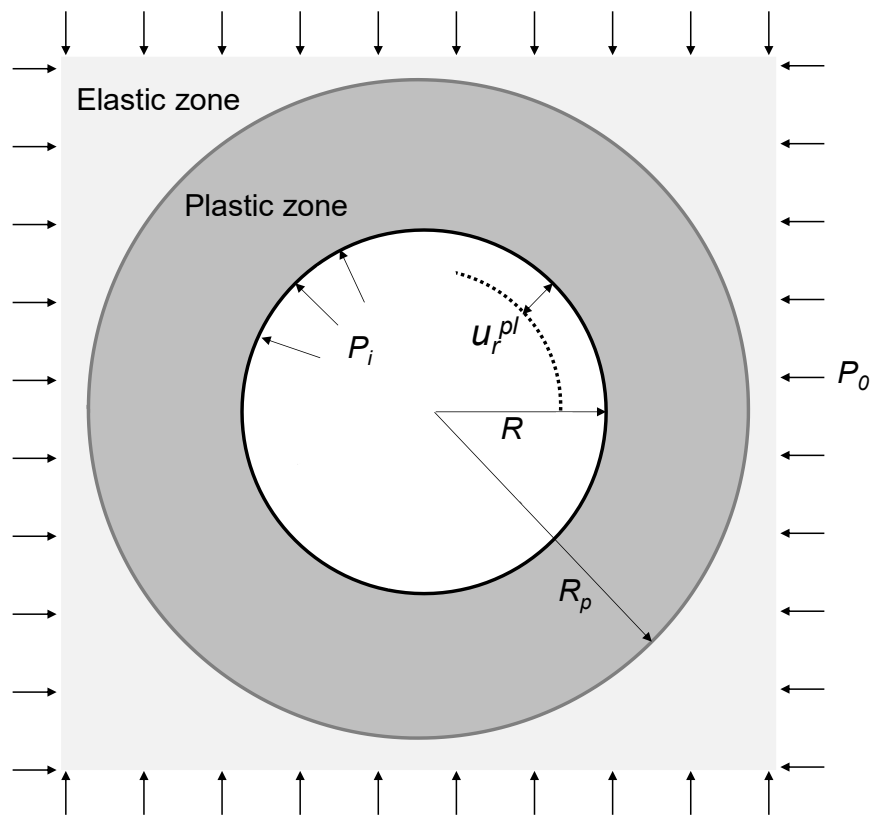


Figure 2-3 Schematic view of a circular excavation under isotropic stress field of P_0 showing a plastic zone that is developed around the excavation boundary and the corresponding plastic radial displacement (u_r^{pl})

The radius of the plastic zone and the magnitude of radial stress at the interface between the elastic and the plastic zones (σ_{ri}) can be obtained using the following equations:

$$R_p = R \left(\frac{2}{k+1} \cdot \frac{P_0 + \frac{q_m}{k-1}}{P_i + \frac{q_m}{k-1}} \right)^{\frac{1}{k-1}} \quad \text{Equation 2-7}$$

$$\sigma_{ri} = \left(\frac{1}{k-1} \right) \cdot (2P_0 - q_m) \quad \text{Equation 2-8}$$

$$q_m = 2c \tan(45 + \varphi/2) \quad \text{Equation 2-9}$$

$$k = \frac{1 + \sin(\varphi)}{1 - \sin(\varphi)} \quad \text{Equation 2-10}$$

where R_p is the radius of the plastic zone (m), P_i is the internal pressure (MPa), c is the rock cohesion (MPa), φ is the rock friction angle ($^\circ$), and k and q_m are variable-dependent constants. For a distance of r from the excavation center, the radial and tangential stresses in the plastic and elastic zones can be calculated using the following equations:

$$\sigma_{rp} = -\frac{q_m}{k-1} + \left(P_i + \frac{q_m}{k-1} \right) \cdot \left(\frac{r}{R} \right)^{k-1} \quad \text{Equation 2-11}$$

$$\sigma_{\theta p} = -\frac{q_m}{k-1} + k \left(P_i + \frac{q_m}{k-1} \right) \cdot \left(\frac{r}{R} \right)^{k-1} \quad \text{Equation 2-12}$$

$$\sigma_{re} = P_0 - (P_0 - \sigma_{ri}) \left(\frac{R_p}{r} \right)^2 \quad \text{Equation 2-13}$$

$$\sigma_{\theta e} = P_0 + (P_0 - \sigma_{ri}) \left(\frac{R_p}{r} \right)^2 \quad \text{Equation 2-14}$$

where σ_{rp} is the tangential stress in the plastic zone (MPa), $\sigma_{\theta p}$ is the radial stress in the plastic zone (MPa), σ_{re} is the tangential stress in the elastic zone (MPa), and $\sigma_{\theta e}$ is the radial stress in the elastic zone (MPa). The radial displacement in elastic (u_r^{el}) and plastic (u_r^{pl}) zones (shown in Figure 2-3) can be determined using the following equations:

$$u_r^{el} = \left(P_0 - \left(\frac{2P_0 - q_m}{k+1} \right) \right) \left(\frac{R_p^2}{2G} \right) \left(\frac{1}{r} \right) \quad \text{Equation 2-15}$$

$$u_r^{pl} = \frac{r}{2G} \chi \quad \text{Equation 2-16}$$

In Equation 2-16, χ is a variable-dependent constant and calculated using the following equation:

$$\chi = (2\nu - 1) \left(P_0 + \frac{q_m}{k-1} \right) + \left(\frac{(1-\nu)(k^2-1)}{k+K_{ps}} \right) \left(P_i + \frac{q_m}{k-1} \right) \left(\frac{R_p}{R} \right)^{(k-1)} + \left(\frac{R_p}{r} \right)^{(K_{ps}+1)} + \left((1-\nu) \frac{(kK_{ps}+1)}{(k+K_{ps})} - \nu \right) \left(P_i + \frac{q_m}{k-1} \right) \left(\frac{r}{R} \right)^{(k-1)} \quad \text{Equation 2-17}$$

The constant K_{ps} in the above equation is calculated according to the following equation:

$$K_{ps} = \frac{1+\sin(\psi)}{1-\sin(\psi)} \quad \text{Equation 2-18}$$

where ψ is the rock dilation angle ($^\circ$).

Figure 2-4 shows the stresses and displacements calculated using Salencon and Kirsch equations for a circular excavation with a radius of 5 m subjected to 26 MPa isotropic stress field. The rock properties used for this analysis are given in Table 2-1. Figure 2-4a

illustrates the influence of plastic zone on the magnitude of tangential stresses close to the excavation boundary. As can be seen in this figure, the tangential stress in the plastic zone near the excavation boundary calculated using the Salencon equations is less than P_0 and the elastic stress calculated using the Kirsch equations. With increasing distance from the excavation boundary, the magnitude of tangential stress gradually increases up to the interface between plastic and elastic zones. For $r > R_p$ (i.e. elastic zone), the tangential stress gradually decreases and eventually reaches the far field stress following the trend obtained using the Kirsch equations. The radial stresses obtained from the two methods are comparable.

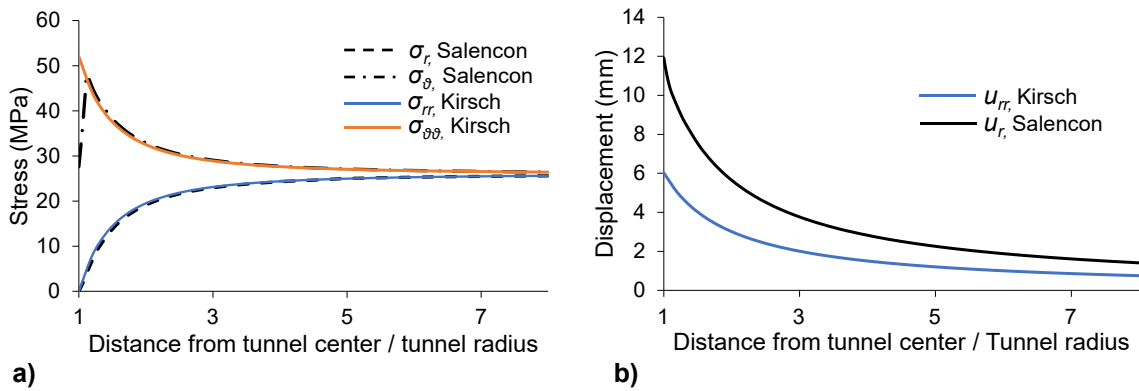


Figure 2-4 Stresses and displacements around a circular excavation calculated using Salencon equations for elasto-plastic medium and Kirsch equations for elastic medium: a) radial and tangential stresses; and b) radial displacement (rock properties are provided in Table 2-1)

Table 2-1 Rock properties used for calculating stresses and displacements around a circular excavation using Kirsch and Salencon equations

Method	E (GPa)	ν	ψ (°)	φ (°)	c (MPa)
Kirsch (1898)	27	0.25	-	-	-
Salencon (1969)	27	0.25	13	43	6

Figure 2-4b shows that the radial displacements calculated using both methods decrease with increasing distance from the excavation boundary. Near the excavation boundary, the radial displacement calculated using the Salencon equations is consistently higher than that of the Kirsch equations but gradually approaches the Kirsch's results with increasing distance from the excavation.

The two analytical methods reviewed in this section (i.e. Salencon, 1969 and Kirsch, 1898) are used to calculate the induced stresses and displacements on the excavation boundary and the surrounding rock mass in two dimensions (i.e. infinite circular excavation with no strain in the out-of-plane direction). Therefore, these methods are not applicable for determining the stresses and displacements near the face of an advancing excavation. It is known that the excavation face acts as a natural support. Therefore, a support design using two-dimensional (2D) analytical methods, in which the influence of the excavation face on the induced stresses and displacements near the face are not considered, is conservative. A proper support design should be carried out using three-dimensional (3D) numerical methods that consider the influence of the excavation face on the 3D stress changes and displacements near an advancing excavation. 2D semi-empirical approaches such as the Convergence Confinement Method (*CCM*) provide alternative solutions for support design in circular excavations.

One of the differences between the Kirsch and Salencon equations on how the stresses and displacements are calculated is the internal pressure, P_i , which is applied in the opposite direction to the excavation boundary, introduced by Salencon (1969). This parameter allows for a gradual increase in the stresses and the displacements on and near the excavation boundary, simulating a progressive excavation advance in a 2D plane strain condition. This concept forms the basis in the *CCM*, which will be discussed in detail in Section 2.4.

2.3. Strength of Intact Rocks and Jointed Rock Masses

In order to design an underground excavation, the rock strength should be obtained by performing laboratory tests (e.g. unconfined and confined compressive tests, and Brazilian and/or direct tensile tests). A failure envelope is then fitted to the rock strength values obtained from laboratory tests. In this thesis, two of the most common rock failure criteria including the Mohr-Coulomb (*MC*) (Coulomb, 1776) and the Hoek-Brown (*HB*) (Hoek and Brown, 1980; Hoek and Brown, 1997; Hoek et al., 2002) failure criteria will be used. In this regard, a brief description of these failure criteria is provided in the following sections.

2.3.1. Mohr-Coulomb (*MC*) Failure Criterion

The *MC* failure criterion represents a linear envelope that is obtained by plotting the shear stress (τ) versus the normal stress (σ_n) acting on a failure plane that has an angle of β from the horizontal axis (Figure 2-5).

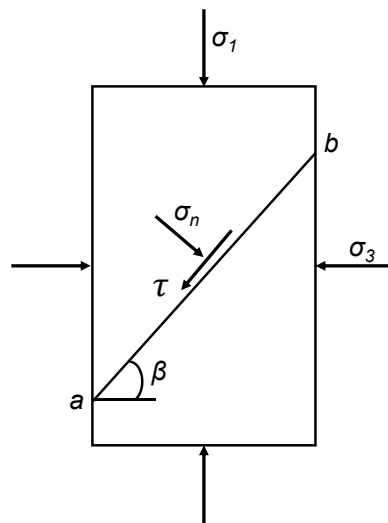


Figure 2-5 Shear failure on plane *ab* (after Brady and Brown, 2005)

The *MC* criterion can be considered as a contribution from Mohr and Coulomb. Mohr's condition is based on the assumption that failure depends on maximum and minimum

principle stresses, and Coulomb's condition is based on a linear failure envelope to determine the critical shear and normal stresses that will cause failure on a plane (Labuz and Zang, 2012). According to Coulomb (1776), the shear strength is made up of two components, a constant cohesion, c , and a normal stress dependent frictional component, φ . In this regard, Coulomb (1776) proposed the following equation:

$$\tau = \sigma_n \tan \varphi + c \quad \text{Equation 2-19}$$

Figure 2-6 shows the *MC* parameters including the cohesion and friction angle on the shear stress versus normal stress space. σ_t represents the tensile strength and can be calculated using Equation 2-20. However, the tensile strength of rock-type materials determined from laboratory tests are usually lower than what Equation 2-20 predicts. Therefore, a tensile cut-off, T_0 , is introduced to represent the actual tensile strength of rocks (Figure 2-6).

$$\sigma_t = \frac{2c \cos \varphi}{1 + \sin \varphi} \quad \text{Equation 2-20}$$

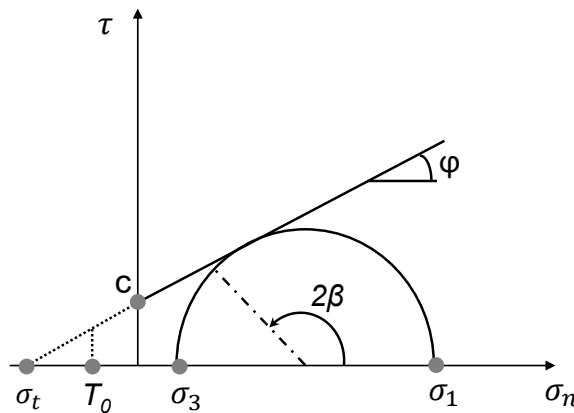


Figure 2-6 The *MC* strength envelope in terms of shear and normal stresses and its parameters

2.3.2. Hoek-Brown (*HB*) Failure Criterion

The *HB* failure criterion is a pure empirical criterion, originally proposed by Hoek and Brown (1980) and later updated by Hoek and Brown (1997) and Hoek et al. (2002). It is used for the design of underground and surface excavations in jointed rock masses. It predicts an envelope that agrees well with the strength values obtained from laboratory triaxial tests on intact rocks and from observed failures in jointed rock masses. The *HB* failure criterion for intact rocks is expressed as:

$$\sigma'_1 = \sigma'_3 + \sigma_{ci} \left(m_i \frac{\sigma'_3}{\sigma_{ci}} + 1 \right)^{0.5} \quad \text{Equation 2-21}$$

where σ'_1 and σ'_3 are the major (axial) and minor (confining) effective principal stresses at failure (MPa), σ_{ci} is the uniaxial compressive strength of the intact rock (MPa), and m_i is a material constant for the intact rock. The applicability of the *HB* criterion was expanded to jointed rock masses by defining constants m_b , s and a by Hoek and Brown (1997), called the *HB* strength parameters. The generalized *HB* failure criterion is expressed as:

$$\sigma'_1 = \sigma'_3 + \sigma_{ci} \left(m_b \frac{\sigma'_3}{\sigma_{ci}} + s \right)^a \quad \text{Equation 2-22}$$

The *HB* strength parameters are calculated using the following equations (Hoek et al., 2002; Hoek and Brown, 2019):

$$m_b = m_i e^{\left[\frac{(GSI-100)}{28-14D} \right]} \quad \text{Equation 2-23}$$

$$s = e^{\left[\frac{(GSI-100)}{9-3D} \right]} \quad \text{Equation 2-24}$$

$$a = 0.5 + \frac{e^{-GSI/15} - e^{-20/3}}{6}$$

Equation 2-25

The *HB* strength parameters m_b , s and a are functions of the Geological Strength Index (*GSI*). The *GSI* is a rock mass characterization system that is used to describe the quality of jointed rock masses. According to Hoek and Brown (1997), the *GSI* value of a rock mass can be determined based on the surface condition of the joints and the degree of interlock between the constituent rock blocks. The value of the *GSI* is determined using the *GSI* chart (Figure 2-7), originally proposed by Hoek (1994) and later updated by Hoek et al. (1995) and Hoek and Brown (1997). This index was subsequently extended for weak rock masses by Hoek and Marinos (2000).







<p>GEOLOGICAL STRENGTH INDEX FOR JOINTED ROCKS</p> <p>From the lithology, structure and surface conditions of the discontinuities, estimate the average value of GSI. Do not try to be too precise. Quoting a range from 33 to 37 is more realistic than stating that GSI = 35. Note that the table does not apply to structurally controlled failures. Where weak planar structural planes are present in an unfavourable orientation with respect to the excavation face, these will dominate the rock mass behaviour. The shear strength of surfaces in rocks that are prone to deterioration as a result of changes in moisture content will be reduced if water is present. When working with rocks in the fair to very poor categories, a shift to the right may be made for wet conditions. Water pressure is dealt with by effective stress analysis</p>		<p>SURFACE CONDITIONS</p> <p>VERY GOOD Very rough, fresh, unweathered surfaces</p> <p>GOOD Rough, slightly weathered, iron stained surfaces</p> <p>FAIR Smooth, moderately weathered and altered surfaces</p> <p>POOR Slickensided, highly weathered surfaces with compact coating or fillings of angular fragments</p> <p>VERY POOR Slickensided, highly weathered surfaces with soft clay coatings or fillings</p>				
<p>STRUCTURE</p>		<p>DECREASING SURFACE QUALITY →</p>				
 <p>INTACT OR MASSIVE- Intact rock specimens or massive in-situ rock with few widely spaced discontinuities</p>		90			N/A	N/A
 <p>BLOCKY - Well interlocked undisturbed rock mass consisting of cubical blocks formed by three intersecting discontinuity sets</p>	<p>DECREASING INTERLOCKING OF ROCK PIECES</p> <p>↓</p>	80	70			
 <p>VERY BLOCKY - Interlocked, partially disturbed mass with multi-faceted angular blocks formed by 4 or more joint sets</p>		60	50			
 <p>BLOCKY/DISTURBED/SEAMY - Folded with angular blocks formed by many intersecting discontinuity sets. Persistence of bedding planes or schistosity</p>		40	30			
 <p>DISINTEGRATED - Poorly interlocked, heavily broken rock mass with mixture of angular and rounded rock pieces</p>		20				
 <p>LAMINATED/SHEARED - Lack of blockiness due to close spacing of the weak schistosity or shear planes</p>		N/A	N/A		10	

Figure 2-7 GSI chart (after Hoek and Marinos, 2000)

The *HB* strength parameters m_b and s are also a function of the disturbance factor (D). The parameter D introduced by Hoek et al. (2002) is used to account for blast damage and stress relaxation effects near an excavation. Its value ranges from 0 for smooth blasting

to 1 for uncontrolled blasting. In the next section, the convergence confinement method used for support design in circular excavations is presented.

2.4. Convergence Confinement Method (*CCM*)

The Convergence Confinement Method (*CCM*) is a tool for anticipating the deformation characteristics of the ground along the boundary of an advancing circular excavation (e.g. tunnel or shaft) and support design. It uses a simple 2D approach to capture 3D excavation effects. During the excavation advance, the face acts as a natural support that carries a portion of the load (called “face effect”). This allows for the excavation boundary behind the face to accommodate the rest of the load. As the excavation advances, the face effect gradually diminishes causing the excavation boundary well away behind the face to carry the entire load. At this stage, the maximum inward displacement of the excavation boundary happens.

By considering a support element that is installed at a distance behind the excavation face, it is possible to calculate the support factor of safety simply by knowing the support capacity and the ground pressure. Figure 2-8a shows the longitudinal section of an advancing circular excavation and the radial displacement profile along the excavation boundary.

The conventional *CCM* is applicable to cases where the in situ stress is uniform (i.e. hydrostatic condition), the rock mass is homogeneous and the excavation is circular. The *CCM* consists of three components: The Ground Reaction Curve (*GRC*), the Longitudinal Displacement Profile (*LDP*) and the Support Characteristic Curve (*SCC*). The following sections provide a brief description of each component.

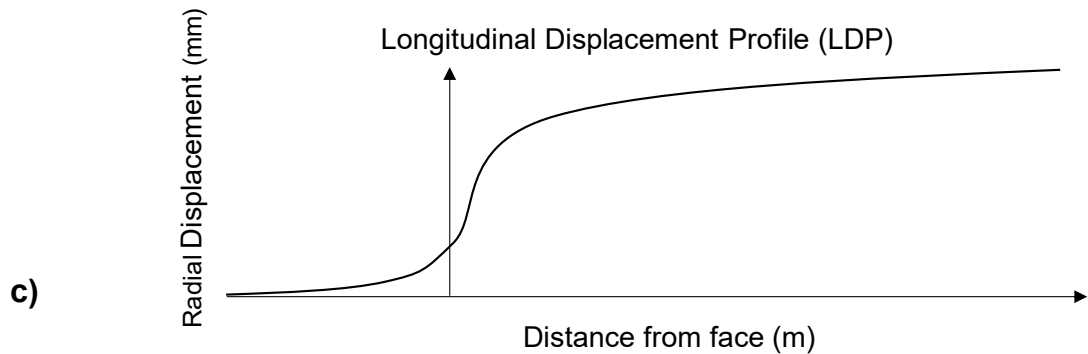
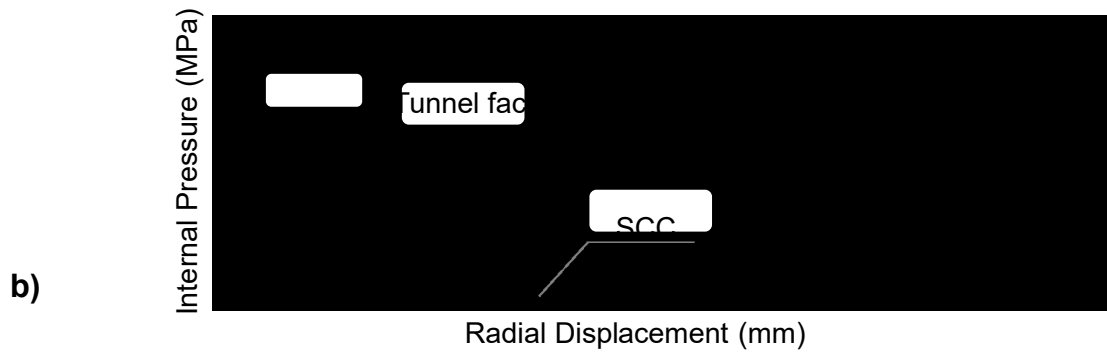
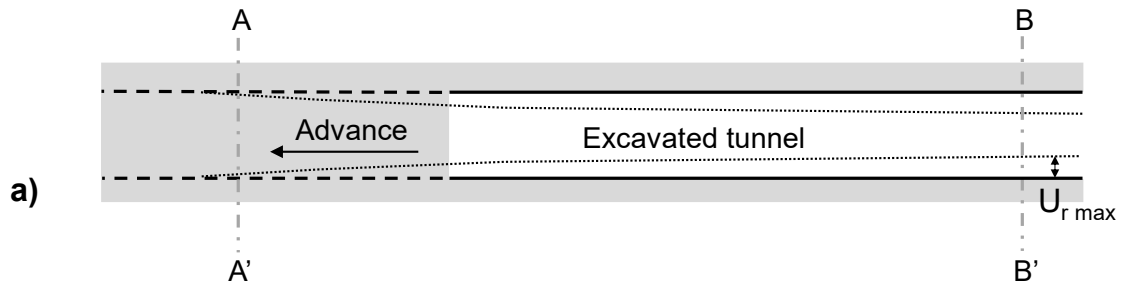


Figure 2-8 a) Longitudinal section of an advancing circular excavation showing the radial displacement profile and the internal pressures at three sections along the excavation; b) Ground Reaction Curve (GRC) and the Support Characteristic Curve (SCC); and c) Longitudinal Displacement Profile (LDP)

2.4.1. Ground Reaction Curve (GRC)

The *GRC* represents the progressive advance of a circular excavation. It provides a relationship between the internal pressure and the radial displacement of the excavation boundary (Figure 2-8b). In this approach, it is assumed that an internal pressure (P_i) equal to the magnitude of far field stress (P_0) is applied in the direction opposite to the excavation boundary ($P_i = P_0$) at a distance well ahead of the excavation face (section A-A' in Figure 2-8a). As the excavation advances (to the left in Figure 2-8b), the radial displacement gradually increases due to the progressive reduction of the internal pressure. At the excavation face, some of the ground pressure is carried by the face ($P_i < P_0$ in Figure 2-8a) and the rest is transferred to the excavation boundary behind the face. At a distance well behind the face (section B-B' in Figure 2-8a) where there is no face effect, the internal pressure is zero and the excavation boundary converges to its final radial displacement (maximum closure). Note that although the changes in the internal pressure do not represent the actual stress redistribution, it allows for a gradual increase of inward radial displacement and the development of plastic radius at and near the excavation boundary as the excavation face advances.

The *GRC* can be obtained using closed-form solutions (e.g. Panet, 1995; Hoek et al., 1995; Carranza-Torres and Fairhurst, 2000) or two-dimensional continuum models (e.g. Vlachopoulos and Diederichs, 2014), which will be reviewed in the following sections.

2.4.1.1. Analytical methods

There are several approaches that can be used to obtain the *GRC* for different rock behavior models (i.e. elastic, elasto-plastic, strain softening and elastic-brittle). In this chapter, the solutions to construct the *GRC* for an elasto-plastic rock are reviewed. In all these methods, an internal pressure P_i equal to the in situ stress is applied to the excavation boundary and is gradually reduced to simulate a progressive excavation advance.

One of the earliest analytical solutions for determining the *GRC* was proposed by Panet and Guenot (1982) and Panet (1993). According to them, the *GRC* for an elasto-plastic rock can be represented by an initial linear curve followed by a non-linear curve, representing elastic and plastic rock mass behavior during an excavation, respectively. Panet (1993) proposed a parameter called the confinement loss (λ), which varies from 0 to 1 and simulates the effect of excavation advance. The confinement loss can be determined by the magnitude of internal pressure (P_i) and the in situ stress (P_0) using the following equation:

$$\lambda = 1 - \frac{P_i}{P_0} \quad \text{Equation 2-26}$$

The critical confinement loss (λ_e) determines the transition from elastic to plastic behavior. When λ_e is smaller than λ , the rock mass behaves plastically. The equation for the critical confinement loss is expressed as:

$$\lambda_e = \frac{1}{4N^*} [(m^2 + 8mN^* + 16s)^{0.5} - m] \quad \text{Equation 2-27}$$

where m and s are the *HB* strength parameters, and N^* is determined using the following equation:

$$N^* = \frac{2P_0}{\sigma_{ci}} \quad \text{Equation 2-28}$$

The radius of plastic zone (R_p) is a function of the excavation radius (R), λ , and λ_e , according to the following equation:

$$\frac{R_p}{R} = \left[\frac{2\lambda_e}{(k+1)\lambda_e - (k-1)\lambda} \right] \quad \text{Equation 2-29}$$

Based on the value of λ_e , the displacement on the boundary of the excavation can be calculated for:

- Elastic condition ($\lambda < \lambda_e$):

$$u_r^{el} = \frac{\lambda P_0 R}{2G} \quad \text{Equation 2-30}$$

where u_r^{el} is the radial displacement when the rock behaves in an elastic manner, and

- Elasto-plastic condition ($0 < \lambda_e \leq \lambda$):

$$u_r^{pl} = \frac{\lambda_e P_0 R}{2G} \left\{ \left(\frac{R_p}{R} \right)^{K_{ps}+1} + \frac{k+1}{k-1} \times (1-2\nu) \left[\left(\frac{R_p}{R} \right)^{K_{ps}+1} - 1 \right] \right\} - \frac{1+K_{ps}k-\nu(K_{ps}+1)(k+1)}{k+K_{ps}} \left(\frac{k+1}{k-1} \lambda_e - \lambda \right) \left[\left(\frac{R_p}{R} \right)^{K_{ps}+k} - 1 \right] \quad \text{Equation 2-31}$$

where u_r^{pl} is the radial displacement when the rock mass behaves in a plastic manner.

Figure 2-9a presents a comparison between the *GRCs* constructed for elastic and elasto-plastic rocks using the method proposed by Panet (1993). This figure demonstrates how the *GRC* deviates from linearity due to rock mass yielding.

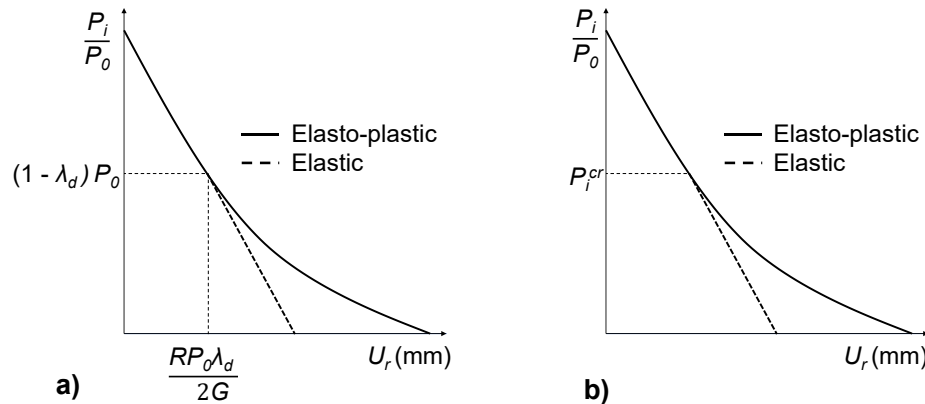


Figure 2-9 Schematic *GRC* and its parameters in elastic and elasto-plastic rocks proposed by: a) Panet (1993); and b) Hoek et al. (1995)

Hoek et al. (1995) proposed a similar method for constructing the *GRC* for elasto-plastic rocks based on the *MC* failure criterion. A schematic representation of the *GRC* and its parameters as proposed by Hoek et al. (1995) are shown in Figure 2-9b. This figure shows a critical internal pressure (P_i^{cr}), which defines the transition from elastic to plastic behavior in the rock mass. When P_i is greater than P_i^{cr} , the rock behaves elastically. When the internal pressure (P_i) is smaller than its critical value, the rock behaves plastically and a plastic zone is developed around the excavation, as illustrated in Figure 2-3. Hoek et al. (1995) proposed the following equations to calculate the critical internal pressure and the plastic radius:

$$P_i^{cr} = \frac{2P_0 - \sigma_{cm}}{1+k} \quad \text{Equation 2-32}$$

$$R_p = R \left[\frac{2[(P_0 \times (k-1)) + \sigma_{cm}]}{(1+k)[(k-1)P_i + \sigma_{cm}]} \right]^{\frac{1}{k-1}} \quad \text{Equation 2-33}$$

where σ_{cm} is the rock mass compressive strength (MPa), which is a function of rock mass cohesion (c) and friction angle (φ) according to the following equation:

$$\sigma_{cm} = \frac{2c \times \cos \varphi}{1 - \sin \varphi} \quad \text{Equation 2-34}$$

Hoek et al. (1995) proposed Equation 2-35 and Equation 2-36 for determining the radial displacement on the excavation boundary. Equation 2-35 is used to calculate the displacement when $P_i^{cr} \leq P_i$ (i.e. elastic condition) and Equation 2-36 is used to obtain the convergence when $P_i^{cr} > P_i$ (i.e. plastic condition).

$$u_r^{el} = \frac{R \times (1+\nu) \times (P_0 - P_i)}{E} \quad \text{Equation 2-35}$$

$$u_r^{pl} = \left(\frac{R \times (1 + \nu)}{E} \right) \left[\left(2(1 - \nu) \times (P_0 - P_i^{cr}) \times \left(\frac{R_p}{R} \right)^2 \right) - \left((1 - 2\nu) \times (P_0 - P_i) \right) \right] \quad \text{Equation 2-36}$$

Carranza-Torres and Fairhurst (2000) developed an analytical solution for obtaining the *GRC* based on the generalized *HB* failure criterion (Hoek et al., 2002). According to Hoek (2007), the method by Hoek et al. (1995) is applicable for obtaining the *GRC*, however the method by Carranza-Torres and Fairhurst (2000) is a more complex form of the analysis that is based on the *HB* failure criterion. Similar to the *GRC* proposed by Panet (1993) and Hoek et al. (1995), the method developed by Carranza-Torres and Fairhurst (2000) is for a circular excavation with a radius of R under an isotropic stress field P_0 .

Carranza-Torres and Fairhurst (2000) introduced two constants based on the *HB* strength parameters (m_b and s) called the scaled internal pressure (P_I) and the scaled in situ stress (S_0), which can be obtained using the following equations:

$$P_I = \frac{P_i}{m_b \sigma_{ci}} + \frac{s}{m_b^2} \quad \text{Equation 2-37}$$

$$S_0 = \frac{P_0}{m_b \sigma_{ci}} + \frac{s}{m_b^2} \quad \text{Equation 2-38}$$

The following equations are used to calculate critical internal pressure P_i^{cr} :

$$P_I^{cr} = \frac{1}{16} + \left(1 - \sqrt{1 + 16 S_0} \right)^2 \quad \text{Equation 2-39}$$

$$P_i^{cr} = \left(P_I^{cr} - \frac{s}{m_b^2} \right) m_b \sigma_{ci} \quad \text{Equation 2-40}$$

For $P_i^{cr} \leq P_i$, the rock mass behaves in an elastic manner and the following equation is used to calculate the radial elastic displacement:

$$u_r^{el} = \frac{P_o - P_i}{2G_{rm}} R \quad \text{Equation 2-41}$$

where G_{rm} is the shear modulus for the rock mass (GPa), which is a function of rock mass elastic modulus (E_{rm}) and Poisson's ratio (ν):

$$G_{rm} = \frac{E_{rm}}{2(1+\nu)} \quad \text{Equation 2-42}$$

For $P_i^{cr} > P_i$, a plastic zone is developed around the excavation and its maximum radius (R_p) is determined using Equation 2-43. The plastic radial displacement (u_r^{pl}) that occurs in this zone can be obtained by re-arranging Equation 2-44.

$$R_p = R \exp \left[2 \left(\sqrt{P_i^{cr}} - \sqrt{P_i} \right) \right] \quad \text{Equation 2-43}$$

$$\begin{aligned} \frac{u_r^{pl}}{R} \frac{2G_{rm}}{P_o - P_i^{cr}} &= \frac{K_{ps} - 1}{K_{ps} + 1} + \frac{2}{K_{ps} + 1} \left(\frac{R_p}{R} \right)^{K_{ps} + 1} + \frac{1 - 2\nu}{4(S_0 - P_i^{cr})} \left[\ln \left(\frac{R_p}{R} \right) \right]^2 \\ &- \left[\frac{1 - 2\nu}{K_{ps} + 1} \frac{\sqrt{P_i^{cr}}}{S_0 - P_i^{cr}} + \frac{1 - \nu}{2} \frac{K_{ps} - 1}{(K_{ps} + 1)^2} \frac{1}{S_0 - P_i^{cr}} \right] \\ &\times \left[(K_{ps} + 1) \ln \left(\frac{R_p}{R} \right) - \left(\frac{R_p}{R} \right)^{K_{ps} + 1} + 1 \right] \end{aligned} \quad \text{Equation 2-44}$$

Figure 2-10 provides a comparison between the *GRCs* obtained using the methods developed by Panet (1993), Hoek et al. (1995) and Carranza-Torres and Fairhurst (2000) for a circular excavation under 26 MPa isotropic stress field with rock properties listed in Table 2-2. Other parameters calculated for the *GRCs* presented in Figure 2-10 are

provided in Table 2-3. The rock properties used for this example are based on a case study that will be described in detail in Chapter 3. Note that the stress field in this case study is not isotropic (i.e. maximum and minimum principal stresses are 26 MPa and 16 MPa, respectively). However, in this chapter, the maximum principal stress (i.e. 26 MPa) is used and an isotropic condition is assumed for comparing the *GRCs*.

The comparison between the *GRCs* provided in Figure 2-10 illustrates that the *GRC* using the method proposed by Carranza-Torres and Fairhurst (2000) results in a larger radial displacement compared to that of the other two methods, and the *GRC* based on the method by Hoek et al. (1995) anticipates a larger convergence compared to that proposed by Panet (1993). It can be seen that the *GRCs* constructed using the methods by Hoek et al. (1995) and Carranza-Torres and Fairhurst (2000) are comparable. Yet, as shown in Figure 2-10b, the difference between the two *GRCs* increases for P_i/P_0 ratios less than 0.03, which corresponds to a P_i of 0.78 MPa.

Table 2-2 Input parameters for constructing *GRC* using analytical and numerical methods

Parameters	Symbols/Abbreviations	Values
Excavation radius (m)	R	5
In situ stress (MPa)	P_0	26
Intact rock elastic modulus (GPa)	E_i	27
Poisson's ratio	ν	0.25
Geological strength index	GSI	62
Disturbance factor	D	0
HB parameter	m_i	30
Intact rock compressive strength (MPa)	σ_{ci}	104
Dilation angle (°)	ψ	13

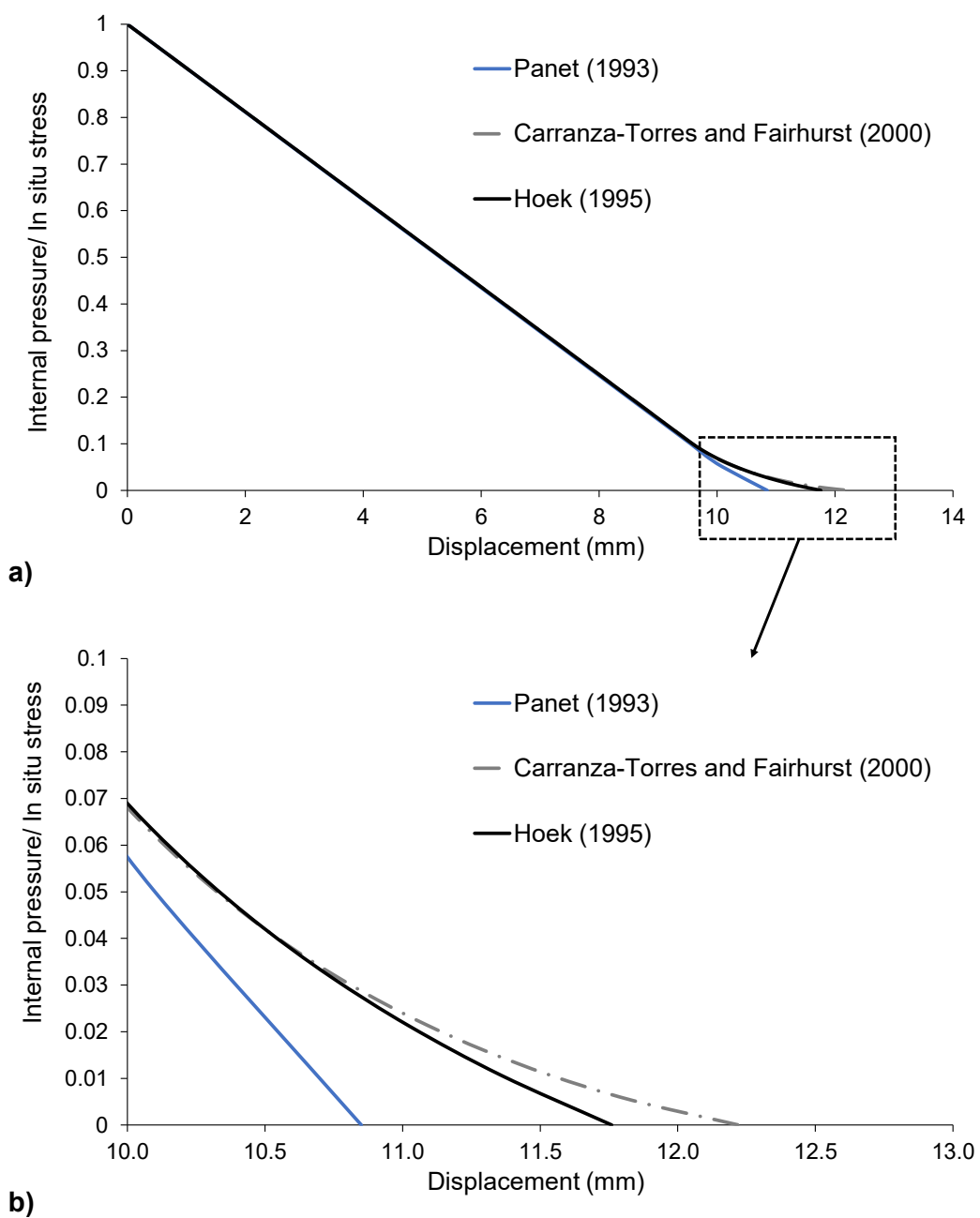


Figure 2-10 a) Comparison between *GRCs* obtained using methods proposed by Panet (1993), Hoek et al. (1995) and Carranza-Torres and Fairhurst (2000) for a circular excavation with a radius of 5 m under a 50 MPa isotropic stress field with rock properties given in Table 2-1; and **b)** zoomed-in view of the boxed area in Figure 2-10a

Table 2-3 GRC parameters for different analytical methods

Parameters		Panet (1993)	Hoek et al. (1995)	Carranza-Torres and Fairhurst (2000)
Critical pressure (MPa)	P_i^{cr}	-	2.76	2.6
Critical confinement loss	λ_e	0.89	-	-
Plastic radius (m)	R_p	5.35	5.47	5.47
Radial displacement (for $P_i=0$) (mm)	U_r	10.92	11.76	12.22
Rock mass elastic modulus (GPa)	E_{rm}	15.6	15.6	15.6
Dilatancy factor	K_{ps}	1.58	-	1.58
Scaled in situ stress	S_0	-	-	0.03
Scaled internal pressure	P_I^{cr}	-	-	0.003
Rock mass shear modulus (GPa)	G_{rm}	-	-	6.1
N constant	N	0.5	-	-
<i>HB</i> strength parameter	m_b	7.72	-	7.72
<i>HB</i> strength parameter	s	0.01	-	0.01
Slope of σ_1 vs σ_3	k	6.44	6.44	-
Rock mass strength (MPa)	σ_{cm}	-	30.7	-
Equivalent cohesion (MPa)	c	-	6	-
Equivalent friction angle (°)	φ	47	47	-

2.4.1.2. Numerical methods

Explicit simulation of the excavation advance requires a 3D numerical analysis. 2D plane strain models can also be used to simulate the excavation advance. There are three methods that can be used to mimic the 3D excavation advance in a 2D plane strain model: Internal Pressure Reduction (*IPR*), Concentric Ring Excavation (*CRE*), and Core Softening (*CS*).

In the *IPR* approach, an internal pressure equal to the in situ stress is applied to the inner boundary of the excavation in the direction opposite to the field stress vector (Figure

2-11a). The internal pressure is then gradually reduced to zero. Through this process, the displacement at the excavation boundary corresponding to the internal pressure and the depth of the plastic zone can be progressively captured. The *GRC* can then be plotted as the magnitude of internal pressure versus the inward displacement of a point on the excavation boundary.

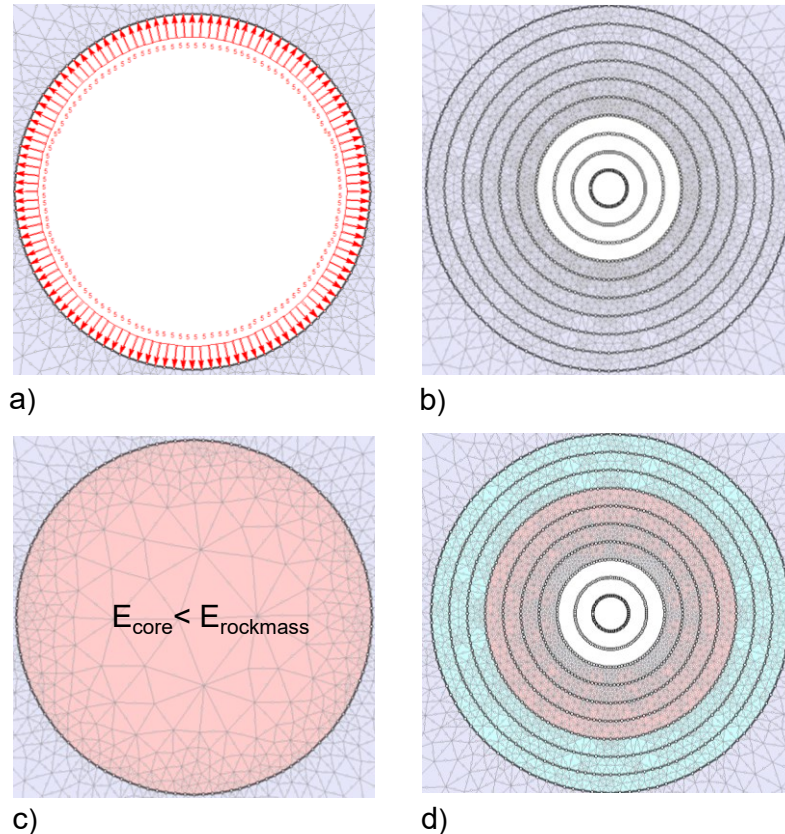


Figure 2-11 Methods to capture 3D excavation advance in a 2D model using: a) Internal Pressure Reduction ($P_i = 5 \text{ MPa}$); b) Concentric Ring Excavation; c) Core Softening (core has a smaller Young's modulus than surrounding rock mass); and d) combined *CRE* and *CS* methods (centre of core has a smaller Young's modulus than surrounding rock mass and the outer rings)

In the *CRE* method, the opening is excavated concentrically in a number of stages from the centre of the excavation towards the final excavation boundary. Figure 2-11b shows the first three discs excavated via this method out of a total of nine. This process represents the progressive weakening of the rock mass inside the excavation until it is fully excavated.

In the *CS* method, the Young's modulus of the core (i.e. tunnel) is gradually reduced from its actual value to zero in order to represent a progressive excavation advance (Figure 2-11c). As with the other methods, the weakening of the core of the excavation is used to capture the progressive deformation of the excavation boundary. This method is also known as the "core replacement method" in the literature. According to Vlachopoulos and Diederichs (2014), the *CS* and the *CRE* methods can be combined in a single model to better capture the gradual deformation of the excavation boundary (Figure 2-11d).

Figure 2-12 provides a comparison between the *GRCs* constructed for the 5 m radius circular excavation with rock properties given in Table 2-2 using the analytical methods proposed by Panet (1993), Hoek et al. (1995) and Carranza-Torres and Fairhurst (2000) in addition to the numerical methods including the *CS* and the *IPR* approaches using the 2D finite element program RS2 (version 10; Rocscience, 2019).

A closer view of the *GRCs* in Figure 2-12b indicates that the method by Panet (1993) anticipates a smaller closure than all other methods. On the other hand, the method by Carranza-Torres and Fairhurst (2000) determines the largest displacement for the excavation. Note that the vertical axis in Figure 2-12 represents the ratio between the internal pressure to the in situ stress (i.e. P_i/P_0) in the analytical and the *IPR* methods whereas it instead represents the ratio between the Young's modulus of the core and the Young's modulus of the rock mass in the *CS* method. By comparing the *GRCs* from analytical and numerical methods it is concluded that they essentially provide similar results.

According to Vlachopoulos and Diederichs (2014), the *IPR* and the *CS* methods provide similar *GRCs* for simple geometries (e.g. circular tunnel). However, the advantage of the *IPR* method over the *CS* method is that it is less sensitive to the mesh type and excavation geometry. For this reason, the *IPR* method will be used to construct the *GRC* using RS2 in Chapters 3 and 4. The *CS* method will be used in Chapter 5 using Irazu (version 4;

Geomechanica, 2019), which is a program based on the hybrid finite-discrete element method.

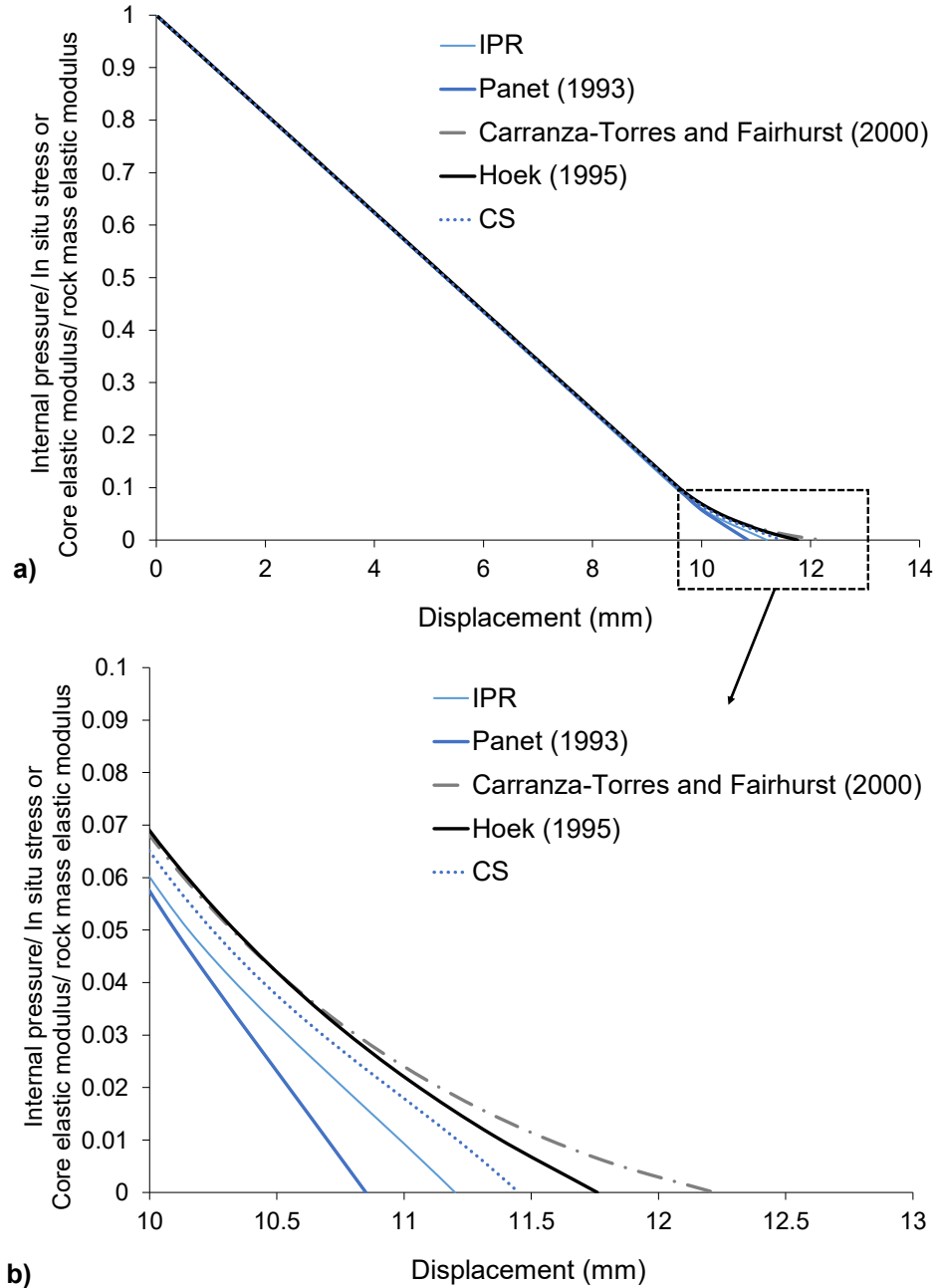


Figure 2-12 a) Comparison between GRCs constructed using Panet (1993), Hoek et al. (1995), Carranza-Torres and Fairhurst (2000) and the CS and the IPR methods; b) zoomed-in view of the boxed area in Figure 2-12a

González-Nicieza et al. (2008) investigated the influence of the shape of excavation on the *GRC*. They used 3D continuum numerical program FLAC3D (Itasca, 2014) to calculate the displacements along the tunnel boundary with circular (type I), cart (type II), and horse-shoe (type III) excavation geometries (Figure 2-13).

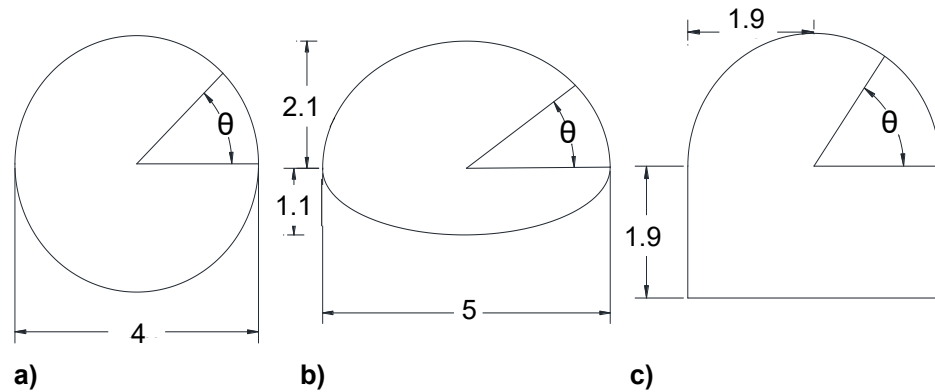


Figure 2-13 Geometries of; a) circular; b) cart; c) horse-shoe tunnels (after González-Nicieza et al., 2008)

González-Nicieza et al. (2008) proposed a method to determine the radial displacement for excavation shapes depicted in Figure 2-13 as a function of the excavation depth h , the angle θ measured counter-clockwise from the horizontal position and the distance from the excavation face d . Figure 2-14 presents the convergence of the three tunnel geometries at a depth of 250 m. It can be seen in Figure 2-14 that tunnel type II (i.e. cart) has the largest closure on the crown whereas the horse-shoe tunnel results in the smallest radial displacement on the crown. González-Nicieza et al. (2008) compared the *GRCs* obtained using the method by Panet (1993) and those for different tunnel geometries, as illustrated in Figure 2-15. This figure demonstrates how the shape of the tunnel impacts the *GRC* as well as the maximum radial displacement.

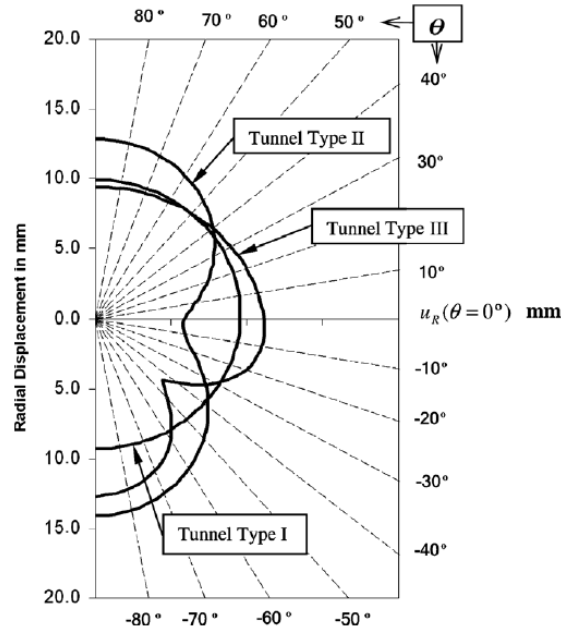


Figure 2-14 Comparison between the convergence of three tunnel geometries at a depth of 250 m (after González-Nicieza et al., 2008)

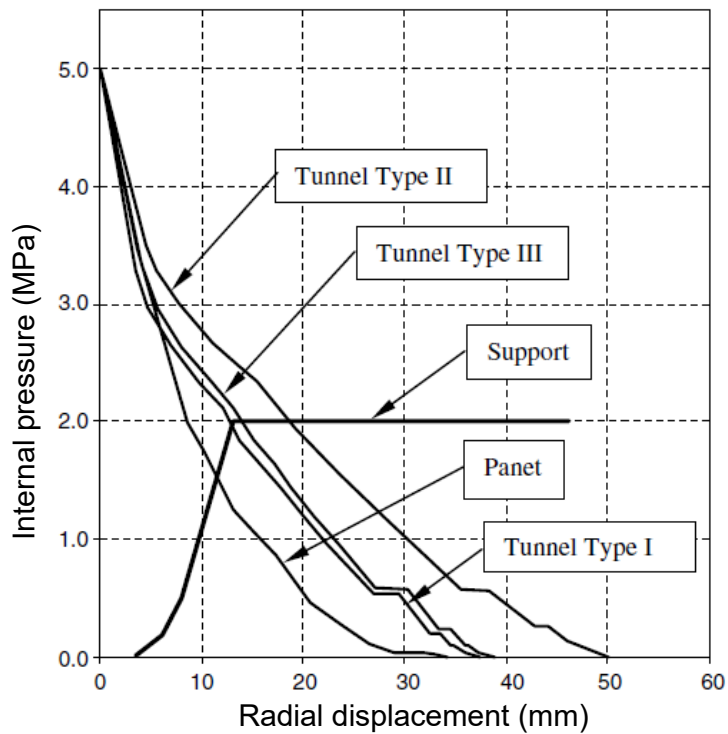


Figure 2-15 GRCs constructed for different tunnel geometries and their comparison with the GRC obtained from Panet's method (after González-Nicieza et al., 2008)

The approaches reviewed in this chapter for obtaining the *GRC* (i.e. Panet, 1993; Hoek et al., 1995; Carranza-Torres and Fairhurst, 2000; González-Nicieza et al., 2008) assume that the rock mass is an elasto-plastic material. According to Alejano et al. (2009), these approaches are suitable for elasto-plastic rock masses with *GSI* values of less than 35, while the strain-softening behavior is suitable for rock masses with *GSI* values between 40 and 60. Rock masses with *GSI* values greater than 65 are expected to behave in a brittle manner. Figure 2-16a shows the post-peak behavior of rock masses as a function of their *GSI* value. In strain-softening materials, a parameter called the drop modulus defines the slope of the stress-strain curve in the post-peak region (Figure 2-16b).

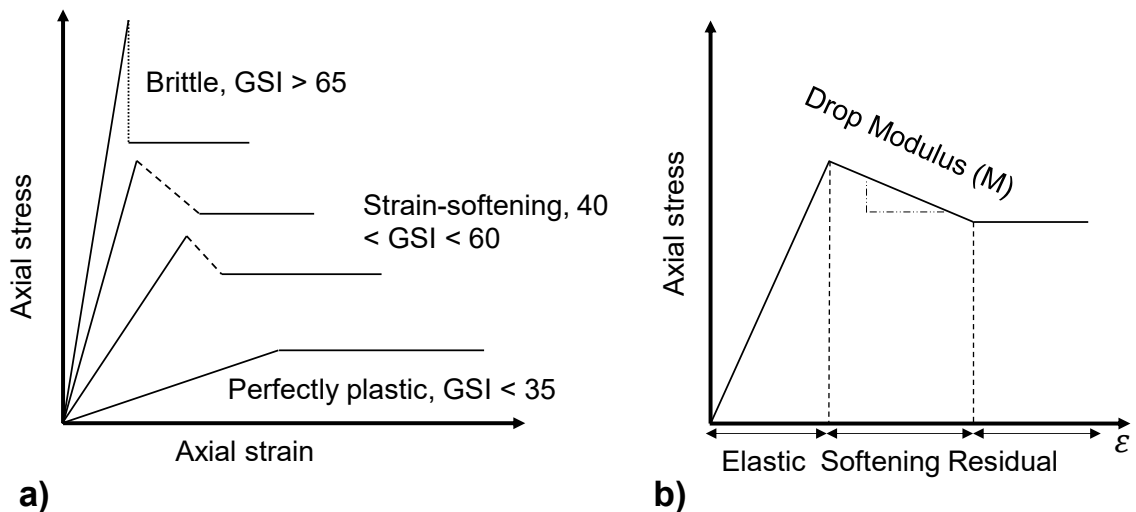


Figure 2-16 a) Various post-peak behaviours for rock masses with different *GSI* values; b) definition of drop modulus in a strain-softening rock mass (modified from Alejano et al., 2009)

Alonso et al. (2003) proposed a numerical approach to obtain the *GRC* for circular excavations in rock masses with strain-softening behaviour. This approach is based on solving a system of ordinary differential equations by defining a fictitious “time” variable using a numerical method in MATLAB. Alonso et al. (2003) found that the *GRC* constructed using this method is comparable to those obtained from analytical solutions and continuum numerical methods. According to Alonso et al. (2003), the advantage of their proposed method over 2D continuum numerical methods lies in solving the problems in a timely and efficient manner.

Alejano et al. (2009) used the method proposed by Alonso et al. (2003) and compared the *GRCs* for different rock masses of various *GSI* values. Alejano et al. (2009) suggested that, for rock masses with *GSI* values of less than 35 (i.e. weak rock masses), the error when using analytical equations for elasto-plastic rock masses is negligible. For rock masses with *GSI* values greater than 65 (i.e. hard brittle rock masses), the method by Carranza-Torres (1998) provides reasonable estimates for the displacements in circular excavations when used in tandem with the approach proposed by Cai et al. (2007) for determining the residual rock mass properties using the *GSI* system. However, for rock masses with *GSI* values between 40 and 60, the results of analytical methods (i.e. Panet, 1995; Carranza-Torres, 1998) are unacceptable and other approaches (i.e. continuum models; Alonso et al., 2003) should be used instead.

Figure 2-17 provides a comparison between the *GRCs* obtained from using the method proposed by Alonso et al. (2003) for the following post-peak responses: 1. elasto-plastic, 2. elastic-brittle, and 3. strain-softening. Figure 2-17a shows that for a weak rock mass (i.e. $GSI < 35$), the *GRCs* constructed using elasto-plastic and strain-softening models anticipate comparable radial displacements. Therefore, the elasto-plastic model can be used to construct the *GRC* for weak rock masses.

Figure 2-17b illustrates that the *GRCs* for hard rock masses with elastic-brittle and strain-softening behaviors are comparable. Therefore, the elastic-brittle model can be used to obtain the *GRC* for hard rock masses ($65 < GSI < 75$). However, as presented in Figure 2-17c, the *GRC* for an average quality rock mass ($40 < GSI < 60$) with elastic-brittle, elasto-plastic and strain-softening behaviors are significantly different. Thus, it is suggested not to use elastic-brittle or elasto-plastic models to obtain the *GRC* in an average quality rock mass. Alejano et al. (2009) recommend the use of other methods (i.e. continuum models; Alonso et al., 2003) to obtain the *GRC* in such rock masses.

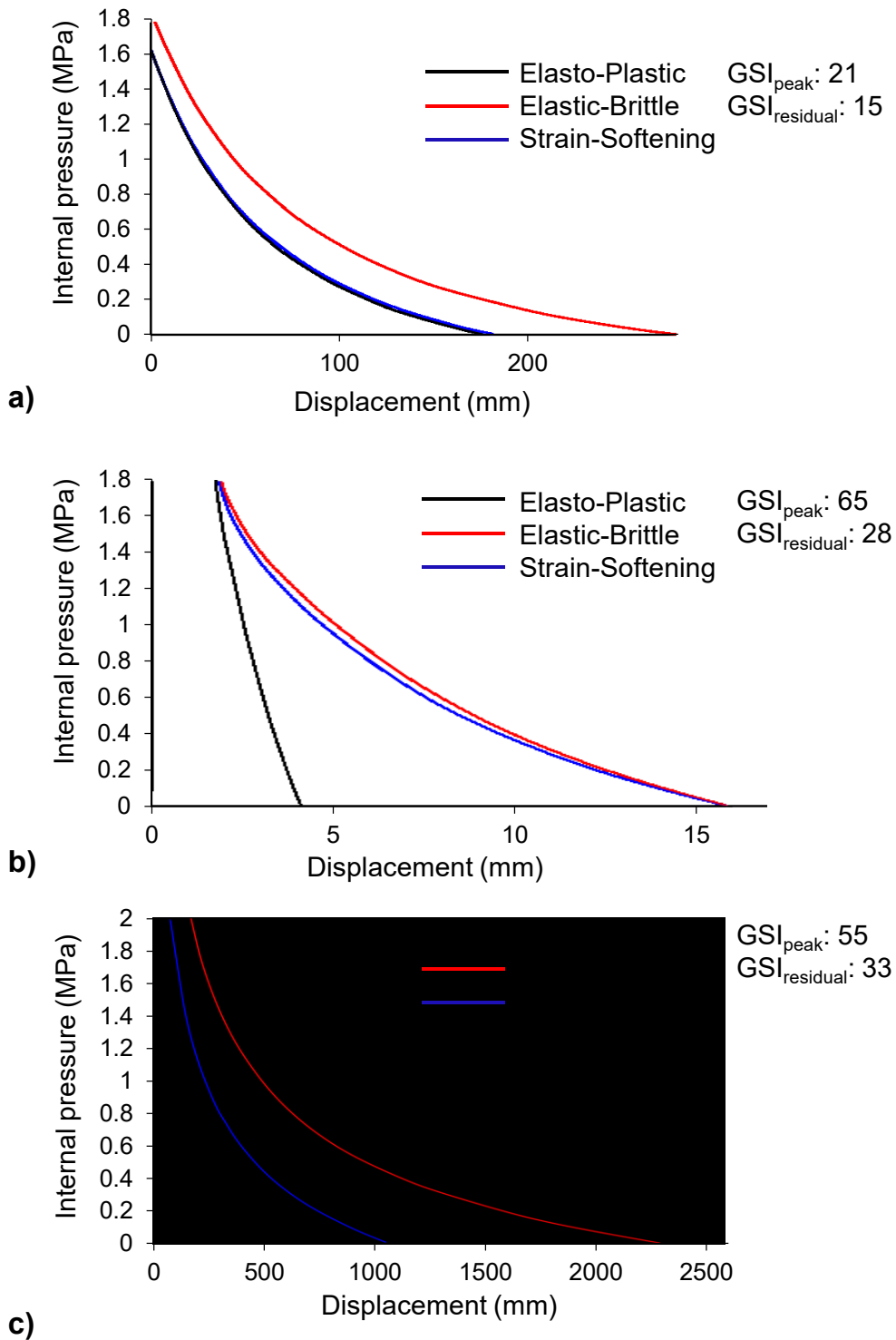


Figure 2-17 Different *GRCs* for elasto-plastic, elastic-brittle and strain-softening rock mass behaviors obtained using the method proposed by Alonso et al. (2003) for: a) weak rocks ($GSI < 35$); b) hard rocks ($65 < GSI < 75$); and c) average quality rocks ($40 < GSI < 60$) (modified from Alejano et al., 2009)

In this section, commonly used analytical, semi-empirical, and numerical methods for constructing the *GRC* were reviewed. From the review of different approaches to obtain the *GRCs* and the comparison between analytical and numerical methods presented in Figure 2-12, it is concluded that analytical approaches can be used as the first step to approximate the *GRC*. As more reliable geotechnical data such as rock and rock mass properties and in situ stresses become available from laboratory tests, field observation and monitoring, numerical modeling can be used to obtain a more representative *GRC* for the excavation. Another advantage of numerical methods over analytical methods is that numerical methods can be used to obtain the *GRC* for cases where the in situ stress field is not hydrostatic. In the following section, the *LDP* – another component of the *CCM* – will be discussed in detail.

2.4.2. Longitudinal Displacement Profile (*LDP*)

The *LDP* represents the radial displacement of the excavation boundary as a function of distance from the face inside the excavation (behind the face) and in the rock mass (ahead of the face) (Figure 2-8c). During the advance of a circular excavation, the rock starts to deform radially ahead of the excavation face due to the redistribution of the stresses. As the excavation face further advances, the inward displacement gradually increases and eventually reaches its maximum value at a distance well behind the face. It is known that the radial displacement at the excavation face is about 30% of its maximum value at a distance well behind the face where there is no face effect. By combining the *GRC* and the *LDP*, it is possible to identify the radial displacement on the *GRC* corresponding to the excavation face (see tunnel face on the *GRC* in Figure 2-8b). The *LDP* can then be used to determine the radial displacement corresponding to a distance behind the face where the ground support is installed (Figure 2-8b).

Extensive research has been carried out over the past four decades on the *LDP*. Table 2-4 presents the equations for calculating the radial displacement at the face of an excavation

(u_0) normalized to the maximum closure of the excavation boundary ($u_{r\ max}$). Most of these equations were derived from 2D axisymmetric finite element analyses. Axisymmetric modeling allows for analyzing a 3D excavation that is rotationally symmetric about an axis. While it is a 2D model, the analysis results apply to the 3D problem. Numerical simulations using 2D axisymmetric models are faster than 3D models but can only be used for symmetrical excavation geometries under an isotropic stress field.

Table 2-4 Face closure equations (from Oke et al., 2018)

$\frac{u_0}{u_{max}}$	Numerical Method	Reference	Equation #
0.265	Axisymmetric	Panet & Guenot (1982)	Equation 2-45
0.25 - 0.3	3D/2D elasto-plastic analysis	AFTES (1983)	Equation 2-46
0.29	Axisymmetric	Corbetta et al. (1991)	Equation 2-47
0.28	Axisymmetric	Panet (1993)	Equation 2-48
$0.4\nu + 0.095$	Axisymmetric	Guilloux et al. (1996)	Equation 2-49
0.29	3D elastic and elasto-plastic	Bernard & Rousset (1996)	Equation 2-50
$0.22\nu + 0.19$	3D continuum	Unlu & Gercek (2003)	Equation 2-51
$\frac{1}{3}e^{-0.15R^*}$	3D and 2D continuum	Vlachopoulos & Diederichs (2009)	Equation 2-52

R^* is the ratio between the plastic radius (R_p) and the excavation radius (R).

Corbetta et al. (1991) and Panet (1993) used elastic axisymmetric models to derive equations for the radial displacement behind the excavation face with respect to the distance from the face, d . The following equations were proposed by Corbetta et al. (1991) (Equation 2-53), and Panet (1993) (Equation 2-54) for calculating u_b^* , which is the ratio between the radial displacement behind the face, u_r , and the maximum radial displacement, u_{max} .

$$u_b^* = \frac{u_r}{u_{max}} = 0.29 + 0.71 \left[1 - \exp \left[-1.5 \left(\frac{d}{R} \right)^{0.7} \right] \right] \quad \text{Equation 2-53}$$

$$u_b^* = 0.28 + 0.72 \left[1 - \left(\frac{0.84}{0.84 + d} \right)^2 \right] \quad \text{Equation 2-54}$$

The above equations were developed for calculating the radial displacement behind the face. Guilloux et al. (1996) used axisymmetric models to determine the radial displacement at the face of an excavation as a function of Poisson's ratios ranging from 0.2 to 0.48:

$$u_0^* = \frac{u_0}{u_{rmax}} = 0.4\nu + 0.095 \quad \text{Equation 2-55}$$

In this equation, u_0^* is the radial displacement at the excavation face u_0 normalized to the maximum radial displacement u_{rmax} .

Unlu and Gercek (2003) used FLAC3D (Itasca, 1997) to simulate a tunnel and derived a set of equations to obtain the *LDP* for distances ahead and behind the excavation face. They investigated the influence of Poisson's ratio on the plastic zone around the tunnel and the corresponding displacements. The following equation proposed by Unlu and Gercek (2003) can be used to determine the radial displacement at the tunnel face for Poisson's ratios ranging from 0.05 to 0.45.

$$u_0^* = 0.22\nu + 0.19 \quad \text{Equation 2-56}$$

Unlu and Gercek (2003) proposed Equation 2-57 and Equation 2-58 to determine the radial displacement for distances ahead and behind the face, respectively. Note that the

subscripts “a” and “b” in the following equations refer to distances ahead (in the rock mass) and behind (inside the excavation) the face, respectively.

$$u_a^* = u_0^* + A_a[1 - \exp(-B_a d)] \quad \text{Equation 2-57}$$

$$u_b^* = u_0^* + A_b \left[1 - \left(\frac{B_b}{B_b + d} \right)^2 \right] \quad \text{Equation 2-58}$$

$$A_a = -0.22v - 0.19 \quad \text{Equation 2-59}$$

$$B_a = 0.73v + 0.81 \quad \text{Equation 2-60}$$

$$A_b = -0.22v + 0.81 \quad \text{Equation 2-61}$$

$$B_b = 0.39v + 0.65 \quad \text{Equation 2-62}$$

Here A_a , B_a , A_b and B_b are constants, u_a^* is the radial displacement ahead of the face normalized to the maximum radial displacement u_{max} and u_b^* is the radial displacement behind the face normalized to the maximum radial displacement u_{max} .

Vlachopoulos and Diederichs (2009) used axisymmetric finite element models and found that the equations proposed by Unlu and Gercek (2003) and Panet (1993) are unable to properly determine the radial closure around an excavation when the plastic zone exceeds two times the tunnel radius or when the plastic zone ahead of the face interacts with the yielding zone near the tunnel wall.

Figure 2-18a shows a plastic zone around an advancing tunnel for a case where there is no interaction between the plastic zone near the tunnel wall and that ahead of the tunnel face. Figure 2-18b demonstrates a condition where, according to Vlachopoulos and

Diederichs (2009), the methods by Panet (1995) and Unlu and Gercek (2003) would not reflect the influence of large plastic zones on the *LDP*.

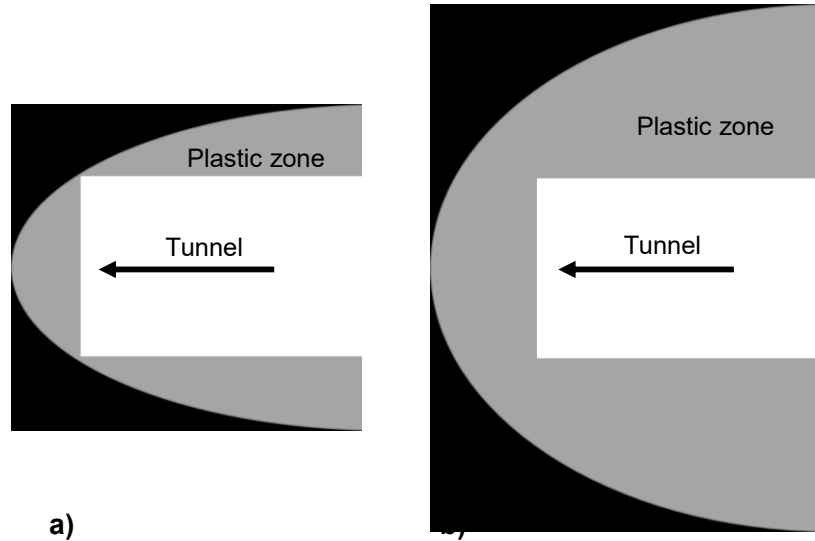


Figure 2-18 Schematic geometry of yielding zone around an advancing tunnel when: a) plastic zone is smaller than tunnel diameter; and b) plastic zone is larger than tunnel diameter (after Vlachopoulos and Diederichs, 2009)

Vlachopoulos and Diederichs (2009) suggest that the influence of Poisson's ratio on the plastic zone is negligible. In this regard, they proposed a method for calculating the *LDP* with no limitation regarding the depth of the plastic zone. The radial displacement at the excavation face can be calculated using Equation 2-63.

$$u_0^* = \frac{1}{3} e^{-0.15R^*} \quad \text{Equation 2-63}$$

Vlachopoulos and Diederichs (2009) also proposed Equation 2-64 and Equation 2-65 for calculating the radial displacements as a function of the distance d ahead and behind the face, respectively.

$$u_a^* = u_0^* e^{d^*} \quad \text{Equation 2-64}$$

$$u_b^* = 1 - (1 - u_0^*)e^{\frac{-3d^*}{2R^*}} \quad \text{Equation 2-65}$$

$$d^* = \frac{d}{R} \quad \text{Equation 2-66}$$

The support system has a direct influence on the radial displacement and the corresponding *LDP*. However, the methods reviewed above do not consider the effect of the support system on the *LDP*. Bernaud and Rousset (1996) and Nguyen-Minh and Guo (1996) were among the first researchers who proposed methods for obtaining the *LDP* for supported circular excavations using 3D and axisymmetric models. Lunardi (2000) noted that axisymmetric analysis does not capture the influence of rigid support and unsupported spans on the convergence of the rock mass ahead of the tunnel face. In this regard, Cantieni and Anagnostou (2009) proposed a method for obtaining the *LDP* applicable to tunnels supported with a rigid support. In their approach, the support system should be installed within 2 to 6 radii from the face.

Oke et al. (2013) proposed a series of equations based on the results of axisymmetric analysis in Phase2 (Rocscience Inc., 2004) to determine the maximum radial displacement in a supported tunnel. Vlachopoulos and Diederichs (2014) compared the results of FLAC3D (Itasca, 2005) and Phase2 (Rocscience Inc., 2004) and suggested the following recommendations for numerical simulations of circular tunnels:

- Use a circular geometry for the boundary of the model. The external boundary should be at least 12 radii from each side of the tunnel boundary or at least 3 plastic radii away from the plastic zone.
- For sequenced excavations (e.g. head and bench excavation), the *LDP* obtained by a 2D plane strain model has errors. However, if the bench is excavated at a long distance after excavating the heading, the *LDP* has less or no error.

- When a stiff support is installed closer than 2 radii from the tunnel face, 3D analysis is required for constructing the *LDP*.
- When support is installed close to the tunnel face (i.e. within 3 radii from the face), Equation 2-67 should be used to determine the radial displacement inside the tunnel.

$$u^* = \frac{1}{1 + e^{0.6\left(1 - 0.1\frac{d_s}{R}\right)\left(\frac{d_s}{R} - 5\frac{d}{R} - 1\right)}} \quad \text{Equation 2-67}$$

Here d_s is the distance between the tunnel face and the support system (m).

Oke et al. (2018) suggested that the *CCM* has limitations in squeezing grounds as the *LDP* is constructed based on an unsupported excavation and the overloading of the support is not included in the *CCM*. In this regard, Oke et al. (2018) used FLAC3D (Itasca, 2009) and extended the applicability of the *CCM* to a supported circular excavation where the support system is installed close to the face. According to Oke et al. (2018), the proposed equation for the *LDP* by Vlachopoulos and Diederichs (2014) (Equation 2-67) is not useful when the support is installed closer than 3 tunnel radii from the face of the excavation. Also, if the unsupported span changes during the excavation – which is inevitable when the tunnel is being excavated using the mechanical excavation method – then Equation 2-67 is inaccurate. Moreover, the *LDP* proposed by Vlachopoulos and Diederichs (2014) is limited to support stiffnesses above 1 GPa/m.

Oke et al. (2018) also investigated the accuracy of the *CCM* for different excavation methods including Tunnel Boring Machine (*TBM*), mechanical excavation (i.e. Roadheader) and drilling and blast method in both supported and unsupported conditions. A schematic view of different excavation methods is provided in Figure 2-19. In the mechanized excavation method (i.e. *TBM*), the supported span, the support segment length and the excavation step size remain constant throughout the excavation. In the mechanical excavation method, the excavation step size is smaller than the support

segment length (i.e. segment length is 4 times the excavation step size) therefore the support is installed at every four rounds of excavation. In the drill and blast excavation method, the support segments are installed at every excavation step. In this regard, the support segments are always installed up to the face before the next round of excavation initiates.

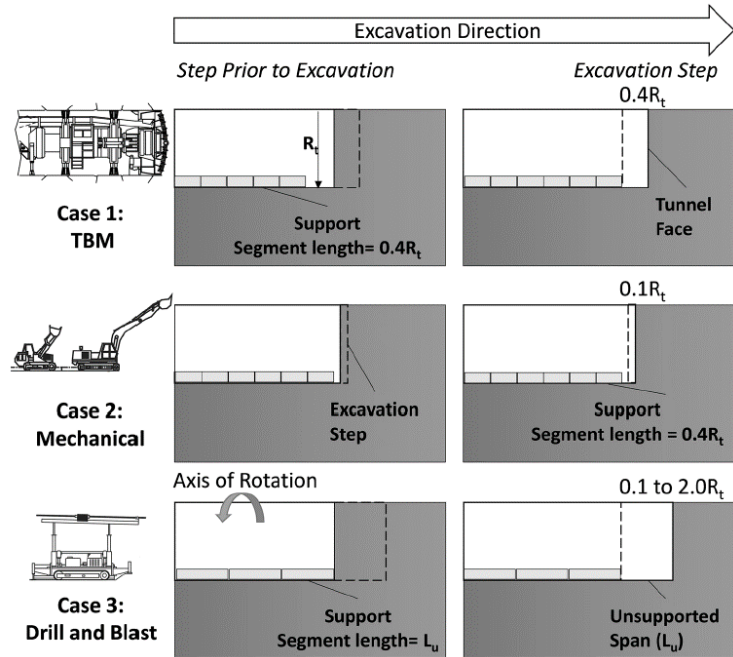


Figure 2-19 Representation of excavation sequences with supported and unsupported spans, using TBM, mechanical, and drill and blast excavation methods in axisymmetric numerical models (after Oke et al., 2018)

By analyzing three different cases in Figure 2-19, Oke et al. (2018) proposed an approach to determine the radial displacement at the face of unsupported and supported circular excavations considering different excavation methods.

The methods for obtaining the *LDP* reviewed above were based on semi-empirical approaches developed from the results of continuum numerical models. Carranza-Torres and Fairhurst (2000) proposed the following empirical equation by obtaining the best-fit curve to the convergence data reported by Chern et al. (1998) based on convergence monitoring of tunnels in the Mingtam Power Cavern project, Taiwan:

$$u_a^* = u_b^* = \left[1 + \exp\left(\frac{-d/R}{1.1}\right)^{-1.7} \right]$$

Equation 2-68

A comparison between the *LDPs* from semi-empirical and empirical approaches reviewed in this section is provided in Figure 2-20. The input parameters used for this comparison are given in Table 2-2. Note that the in situ stress is assumed to be 26 MPa.

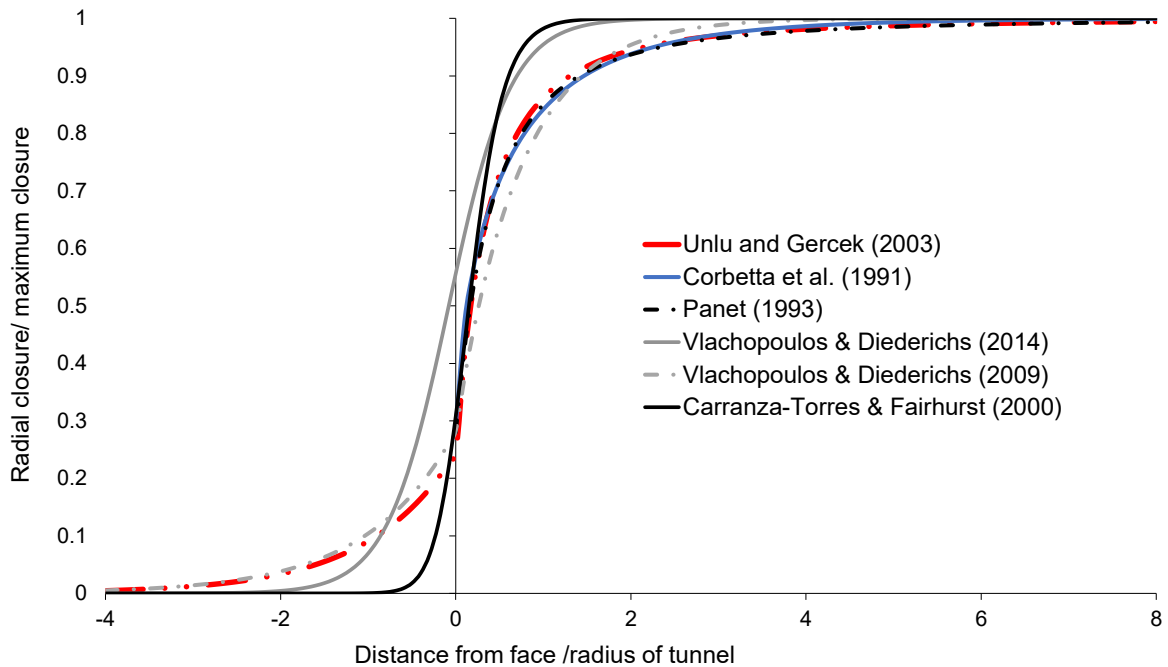


Figure 2-20 Comparison between *LDPs* obtained using empirical and semi-empirical approaches for a circular excavation with a radius of 5 m under a 26 MPa isotropic stress field with input parameters listed in Table 2-2

2.4.3. Support Characteristic Curve (SCC)

The *SCC* represents the stress-strain behavior of an elasto-plastic support in response to the excavation advance. It provides a relationship between the pressure increment on the support and the increment of the wall radial displacement. As shown in Figure 2-21, the *SCC* consists of two sections. The initial section corresponds to the elastic response of the

support element and its maximum capacity. The second section represents the plastic deformation (or strain) of the support element (i.e. post-peak response).

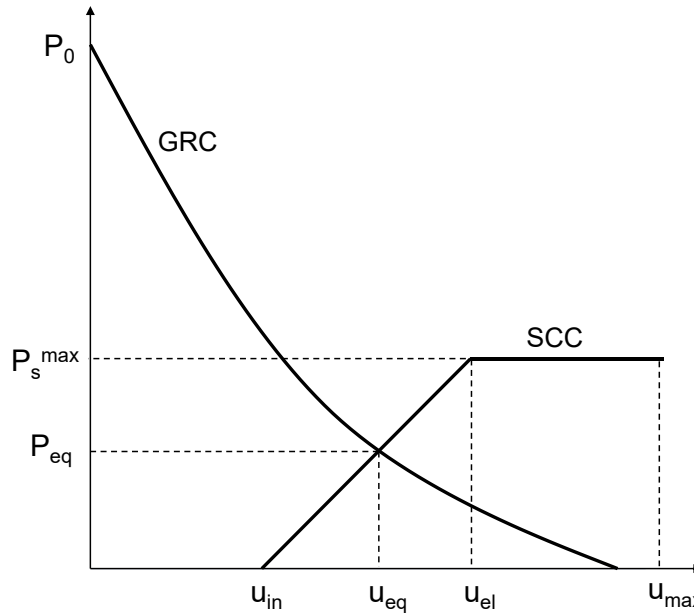


Figure 2-21 Schematic of the GRC and the SCC (after Oreste, 2003a)

The mechanical properties of support elements are required for the SCC. Equation 2-69 can be used to determine the support pressure (P_s) based on the stiffness of the support element (K_s) and the radial displacement of the excavation wall (u_r) at any distance from the excavation face (Carranza-Torres and Fairhurst, 2000).

$$P_s = K_s u_r \tag{Equation 2-69}$$

The support capacity (P_s^{max}) and the support stiffness (K_s) for shotcrete and concrete liners can be calculated using the following equations:

$$P_s^{max} = \frac{\sigma_{cc}}{2} \left[1 - \frac{(R-t_c)^2}{R^2} \right] \tag{Equation 2-70}$$

$$K_s = \frac{E_c}{(1-\nu_c)R} \frac{R^2 - (R-t_c)^2}{(1-\nu_c)R^2 + (R-t_c)^2} \quad \text{Equation 2-71}$$

Here, σ_{cc} is the unconfined compressive strength of shotcrete/concrete (MPa), E_c is the Young's modulus of shotcrete/concrete (MPa), ν_c is the Poisson's ratio of shotcrete/concrete, t_c is the thickness of shotcrete/concrete liners (m) and R is the excavation radius (m). The radial displacement of the wall related to the shotcrete ring failure can be obtained using the following equation (Oreste, 2003a):

$$u_{max} = u_{el} + \varepsilon_{br}(R - t_c) - \frac{2(1-\nu_c)R(R-t_c)}{(R-t_c)^2 + (1-2\nu_c)R^2} \frac{p_s^{max}}{K_s} \quad \text{Equation 2-72}$$

In the above equation, u_{el} is the excavation wall displacement when the plastic deformation of the support system initiates and ε_{br} is the failure strain of the support material. Further information on how to determine the SCC for other types of support elements such as rock bolts and steel sets can be found in Carranza-Torres and Fairhurst (2000) and Oreste (2003a).

2.5. Support Factor of Safety

The classical approach used to design engineering structures is to determine the Factor of Safety (FS) of the structure from the ratio between the capacity (strength or resisting force) of the element and the demand (stress or disturbing force) (Hoek et al., 1995). Failure is assumed to occur when the factor of safety is less than 1. According to Kaiser (2014; 2019), in rock engineering, different factors of safety based on the load, displacement and energy capacities of the support can be used to assess the proximity to failure. Depending on the excavation behavior and the failure mode, one or more of the following factors of safety must be assessed (Kaiser, 2014; 2019):

$$FS_{Load} = \frac{\text{Support Load Capacity}}{\text{Load Demand}} \quad \text{Equation 2-73}$$

$$FS_{Disp} = \frac{\text{Support Displacement Capacity}}{\text{Displacement Demand}} \quad \text{Equation 2-74}$$

$$FS_{Energy} = \frac{\text{Support Energy Capacity}}{\text{Energy Demand}} \quad \text{Equation 2-75}$$

For example, in structurally controlled failures under static conditions, the load factor of safety (FS_{load}) is typically used. The displacement factor of safety (FS_{disp}) becomes relevant in squeezing grounds and when the failure involves stress fracturing leading to rock mass bulking. The energy factor of safety (FS_{energy}) is applicable when the excavation and the support are dynamically loaded due to a seismic event.

One of the outcomes of the *CCM* is the determination of the *FS* for the support element. By combining the *SCC* and the *GRC*, the load factor of safety of the support element can be calculated. FS_{load} is simply the ratio of the maximum support pressure (P_s^{max}) to the pressure at the intersection point of the *GRC* and the *SCC*, called the equilibrium pressure (P_{eq}). The definitions of $FS_{load} > 1$ and $FS_{load} < 1$ are schematically shown in Figure 2-22a and Figure 2-22b, respectively.

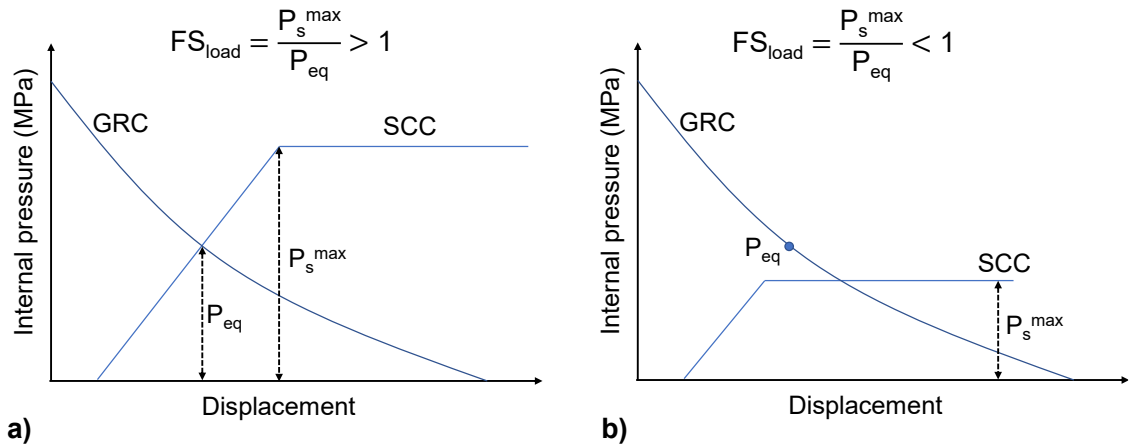


Figure 2-22 Definition of FS_{load} for: a) $FS_{load} > 1$; and b) $FS_{load} < 1$

According to Oreste (2003a), the support system remains stable when two conditions are met. First, the load factor of safety for the support system should be more than the minimum allowable factor of safety (usually 1.2 in mine excavations). Second, the convergence of the excavation wall should be within an expected design range. Based on these conditions, Oreste (2003a) introduced the concept of displacement factor of safety for evaluating the stability of support systems in tunnels using the *CCM* from the analysis of the *GRC* and the *SCC*. The FS_{disp} (or FS_{strain}) is defined as the ratio between the failure displacement (or failure strain) of the support system and the maximum displacement (or maximum strain) induced in the support system:

$$FS_{disp} = \frac{\text{Support system failure displacement}}{\text{Maximum displacement induced in the support system}} \quad \text{Equation 2-76}$$

$$FS_{strain} = \frac{\text{Support system failure strain}}{\text{Maximum strain induced in the support system}} \quad \text{Equation 2-77}$$

Oreste (2003a) developed analytical equations to determine the FS_{disp} for different support elements (e.g. shotcrete liner, steel set, etc.). The equations for calculating the FS_{disp} for the shotcrete liner are provided for the two conditions illustrated in Figure 2-23.

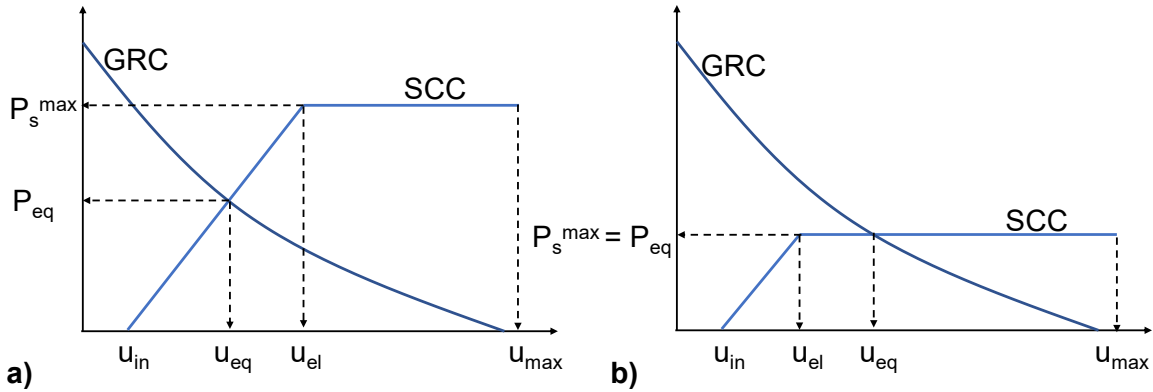


Figure 2-23 The CCM for conditions when the equilibrium pressure is reached: a) in the elastic portion of the SCC ($u_{eq} \geq u_{el}$); and b) in the plastic portion of the SCC ($u_{eq} < u_{el}$)

For $u_{eq} \geq u_{el}$ (Figure 2-23a):

$$FS_{disp} = \frac{\varepsilon_{br}(R-t)}{u_{eq}-u_{el} + \frac{2(1-\nu)R(R-t)}{(R-t)^2+(1-2\nu)R^2} \times \frac{P_s^{max}}{k}} \quad \text{Equation 2-78}$$

For $u_{eq} < u_{el}$ (Figure 2-23b):

$$FS_{disp} = \frac{\varepsilon_{br}[(R-t)^2+(1-2\nu)R^2]}{2(u_{eq}-u_{sh})R(1-\nu)} \quad \text{Equation 2-79}$$

In above equations, u_{eq} is the wall displacement at equilibrium, u_{sh} is the radial deformation occurred before the installation of the liner, u_{el} is the point on the SCC where the plastic deformation of the support begins, and P_s^{max} is the maximum pressure (capacity) of the support system. Alejano et al. (2017) used the displacement factor of safety equations developed by Oreste (2003a) to assess the stability of 10 cm and 25 cm shotcrete linings in a tunnel (Figure 2-24).

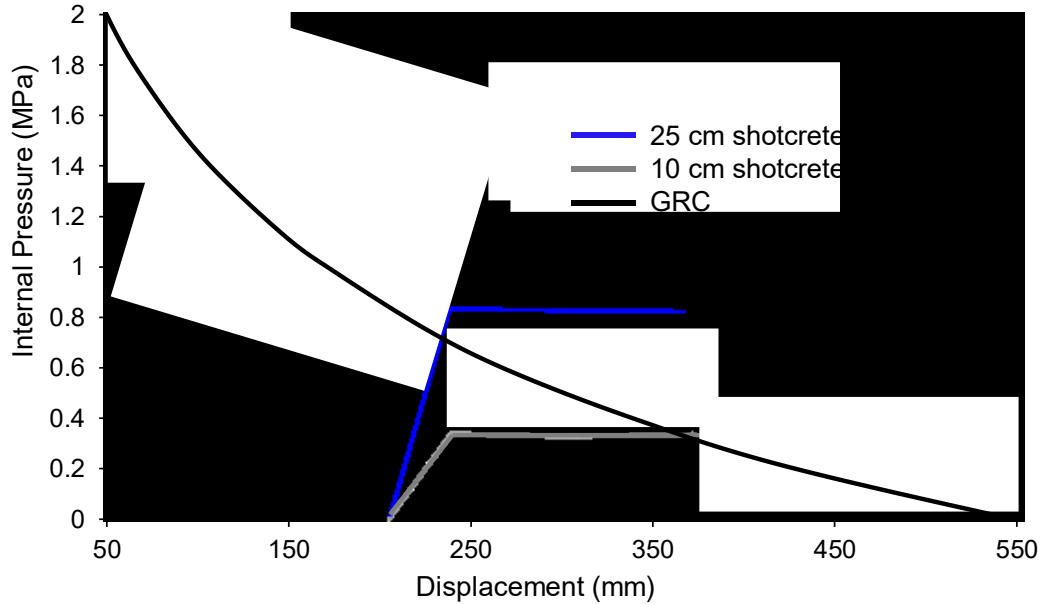


Figure 2-24 The GRC with the SCCs for 10 cm and 25 cm shotcrete liner (after Alejano et al., 2017)

As can be seen in Figure 2-24, the 10 cm shotcrete liner results in a load factor of safety of less than 1 and a displacement factor of safety of nearly 1. By increasing the shotcrete lining thickness to 25 cm, the load and displacement factors of safety increase to 1.3 and 4, respectively. From the analyses of a combination of load and displacement factors of safety, Alejano et al. (2017) recommended to use a shotcrete thickness of 25 cm for the tunnel.

The concept of displacement factor of safety was also used by Li (2017) for the stability analysis of rock bolts under different loading and ground conditions. He noted that in shallow tunnels, the function of rock bolts is to prevent rock blocks from falling. Therefore, the use of a load factor of safety is appropriate for support design. However, in high in situ stress conditions, where large deformation in soft and weak rocks and rockburst in hard and brittle rocks are anticipated, the function of the rock support is not to equilibrate the deadweight of loosened rocks but to accommodate the excessive deformation. In this regard, Li (2017) defined different types of displacement factors of safety for rock bolts based on the concept of the CCM (Figure 2-25).

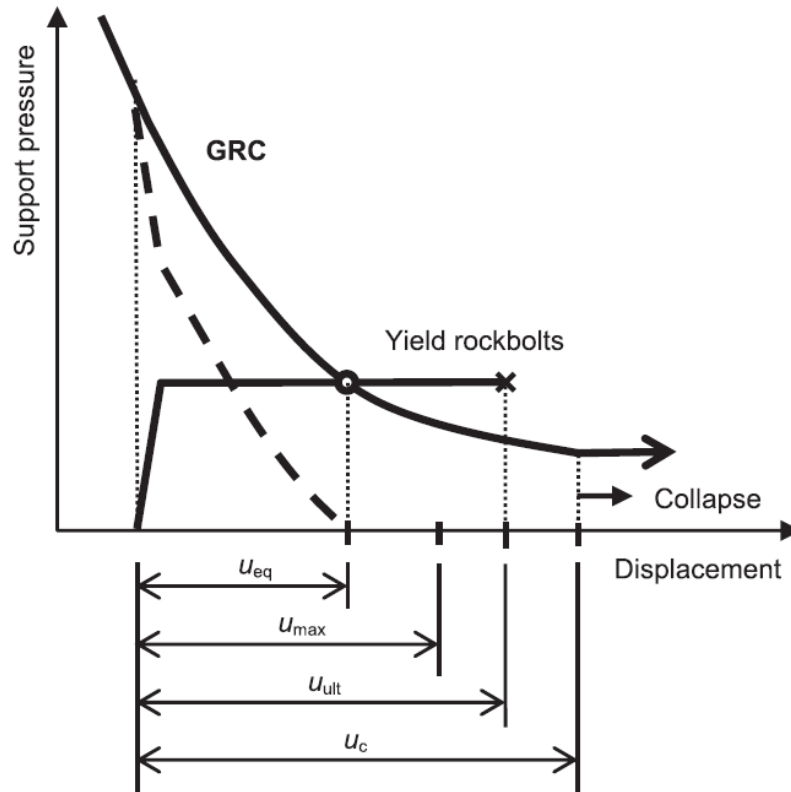


Figure 2-25 The GRC and the SCC for an excavation supported with rock bolts (after Li, 2017)

According to Li (2017), in squeezing grounds, it is suggested to use yielding rock bolts instead of stiff ones. In such conditions, the deformation capacity of the rock bolt should be considered for the design. From the stability point of view, Li (2017) suggests that the displacement of the tunnel wall at equilibrium (u_{eq}) must be smaller than the critical displacement (u_c) beyond which uncontrollable rock collapse occurs.

From the operational point of view, Li (2017) notes that there exists a maximum allowable displacement for the excavation. For example, the radial displacement of a Tunnel Boring Machine (TBM) tunnel is usually not allowed to be larger than 150 mm, in order to avoid jamming of the TBM head. In this regard, he introduced an operational factor of safety, FS_{op} , which is defined as the ratio between the maximum allowable displacement of the rock bolt (u_{max}) and the ground displacement at the equilibrium point (u_{eq}).

$$FS_{op} = \frac{u_{max}}{u_{eq}}$$

Equation 2-80

From the literature review presented in this section, it is concluded that depending on the ground condition and the function of the ground support, one or both of the load and displacement (or strain) factors of safety should be used for support design.

In this document, the conventional load factor of safety presented in Figure 2-22 is used in Chapter 3 to assess the stability of initial shotcrete liners of various thicknesses. Moreover, a new methodology to calculate the strain factor of safety for the shotcrete lining based on the results of continuum numerical modeling is introduced in Chapter 4.

2.6. Support Capacity Diagrams

Support capacity diagrams provide graphical representations of the capacity of the liner. “Beam elements” are commonly used in numerical models to simulate shotcrete/concrete liners. These elements are attached to the excavation boundaries, interact with the surrounding rock mass and limit the convergence of the excavation. In order to better understand the contribution of the liner to the stability of the excavation and to optimize the design in terms of its thickness and installation timing, the loads imposed on the liners are obtained from numerical analyses. Axial thrust, bending moment and shear force are subsequently calculated. Plots of thrust-bending moment and thrust-shear force known as support capacity diagrams are then constructed to determine whether the ground loads exceed the liner capacity or not.

Kaiser and Barlow (1986) were one of the first researchers who used the support capacity diagrams for tunnel lining design. They illustrated the load path for the concrete liner, demonstrating how a zero moment is approached quickly after the yield point is reached without a significant increase in thrust (Kaiser and Barlow, 1986).

Figure 2-26 shows typical thrust-bending moment (diamond shape) and thrust-shear force (oval shape) envelopes for different factors of safety. Factors of safety are calculated from the major and minor principal stresses induced by the axial thrust, shear force and bending moments on the liner elements.

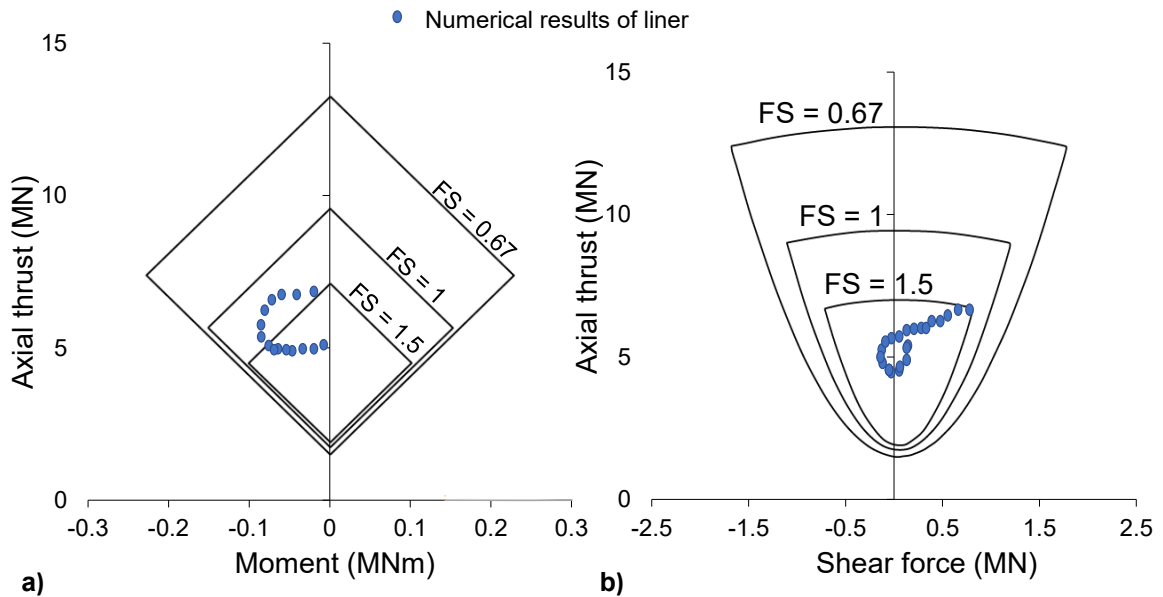


Figure 2-26 Support capacity diagrams for a tunnel: a) thrust-moment diagram; b) thrust-shear force diagram (after Carranza-Torres and Diederichs, 2009)

If the points corresponding to the liner are located inside the capacity diagrams, the factor of safety is greater than what is indicated on the curves. If the points are located outside the capacity curves, it implies that the safety factor is less than what is indicated on the diagram. An example of how to determine the *FS* is provided in Figure 2-26. In Figure 2-26a, the overall *FS* is less than 1.5 due to some data points being located outside the *FS* = 1.5 envelope. In Figure 2-26b, the overall *FS* is greater than 1.5 as all the data points are inside the capacity envelope corresponding to *FS* = 1.5.

Hoek et al. (2008) and Hoek and Guevara (2009) illustrated the application of integrating geotechnical and structural design methods for the design of tunnel liners. In this regard, they used 2D finite element models to design liners for two tunnels in weak rock masses;

a shallow tunnel excavated near a slope using the drill and blast excavation method and a water supply tunnel in Venezuela.

The support capacity diagram will be used in Chapter 3 to analyze the stability of initial shotcrete liners of various thicknesses for a mine shaft.

2.7. Time-dependent Properties of Shotcrete

Shotcrete (also known as sprayed concrete) is a mixture of cement, sand and water. According to Fowler (2009), for each unit weight of cement, four units of sand are required. If the water is added at the nozzle, the resulting shotcrete will be a dry mixture. However, if the water is premixed with sand and cement, the shotcrete will be a wet mixture. The aggregate size of shotcrete is between 4 mm and 16 mm (ASCCT, 2004).

Shotcrete liner is usually used as an initial support element in underground excavations. It provides instant support and smoothens the face for the excavation prior to the installation of the main, final lining. In this regard, the shotcrete liner must remain stable prior to installing the final support.

Shotcrete becomes stiffer and harder progressively with time as the excavation face advances. In this regard, Oreste and Pelia (1997) and Oreste (2003b) developed a methodology for determining the characteristic curve of shotcrete lining as a function of the excavation advance rate by considering the changes in the shotcrete stiffness with time. Hoek et al. (2008) described the design process for a shallow tunnel in which the liner consisted of shotcrete and lattice girders. They considered the time-dependent properties of shotcrete for tunneling lining designs.

Gschwandtner and Galler (2012) demonstrated the influence of the excavation advance rate on the time-dependent properties of shotcrete (i.e. strength and stiffness) and its factor of safety. They used two different advance rates (i.e. 2 m/day and 5 m/day) and constructed the corresponding *SCCs* and *LDPs* along with a *GRC* for a tunnel supported

with shotcrete liner and yielding elements (Figure 2-27). Figure 2-27 demonstrates how the factor of safety of the liner with yielding elements decreases as the excavation advance rate increases from 2 m/day to 5 m/day. This is because the shotcrete liner has more time to become stiffer and harder from one round to the next in the excavation with an advance rate of 2 m/day than it does with a rate of 5 m/day.

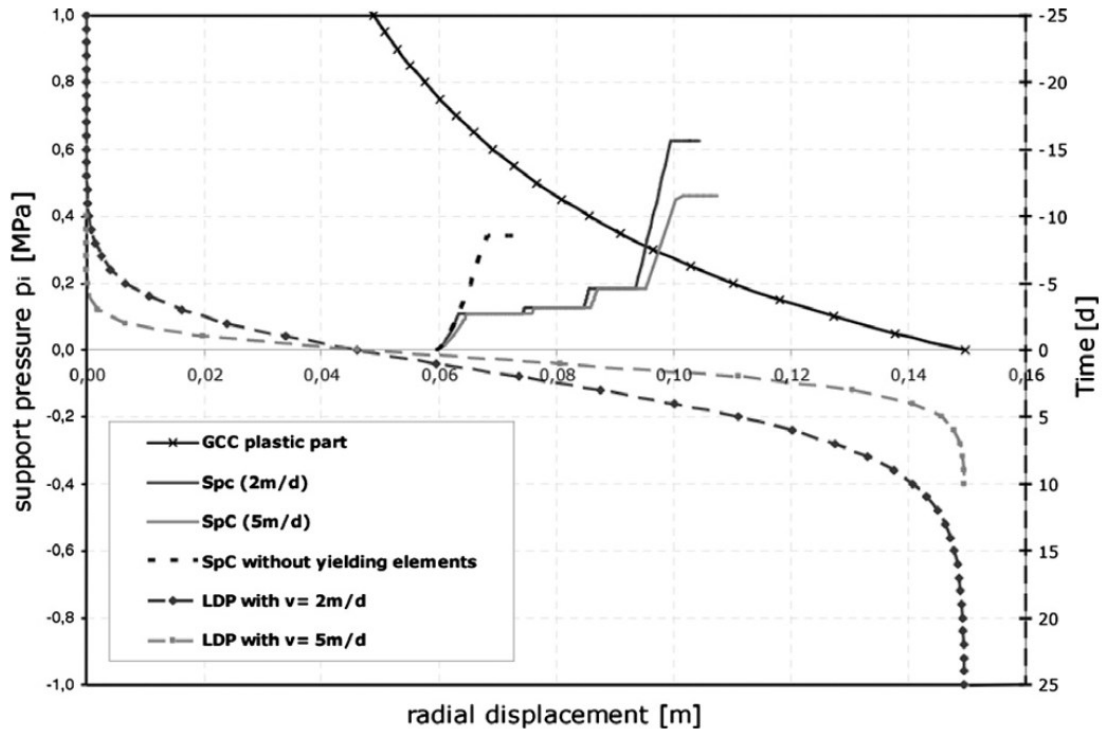


Figure 2-27 Influence of advance rate on capacity of shotcrete liners with and without yielding elements (after Gscwandtner and Galler, 2012)

Shotcrete is often sprayed close to the face of an excavation where the face effect exists. The face effect is the support pressure naturally provided by a combination of the excavation face and the walls near the face. When a wet mixture of shotcrete is sprayed on the excavation walls, its mechanical properties (i.e. strength and stiffness) gradually change over time. Shotcrete hardening takes place during the excavation advance as the face effect gradually disappears and the ground load on the shotcrete increases. The definition of constant stiffness and strength values for early-age shotcrete lining does not allow for the evaluation of the true stress state in the shotcrete layer (Oreste, 2003b).

Therefore, it is suggested to account for the change in the mechanical properties of shotcrete lining when designing a support system, especially in fast advancing excavations.

Following the application of shotcrete to the excavation boundary, not only does the shotcrete gain strength and stiffness, it may also be subject to plastic deformation if it is loaded beyond its maximum capacity (John and Mattle, 2003). This means that early-age shotcrete linings can sustain the ground load while undergoing plastic deformation before failure occurs. This aspect should also be considered when designing the initial shotcrete lining, particularly in fast advancing excavations.

According to Oreste (2003b), in order to design a shotcrete liner by using analytical methods, a mean value for the stiffness is determined and the *SCC* is plotted accordingly, which unfortunately does not account for its time-dependent behavior. Oreste (2003b) proposed a method to construct the effective *SCC* in which shotcrete becomes stiffer with time and calculated the factor of safety by considering the distance from the face or time (shotcrete age). An example of the *SCC* using this method is presented in Figure 2-28. Although this method captures the change in shotcrete stiffness with time, it only considers this hardening effect for the elastic portion of the shotcrete stress-strain behavior but not the change in the post-peak region.

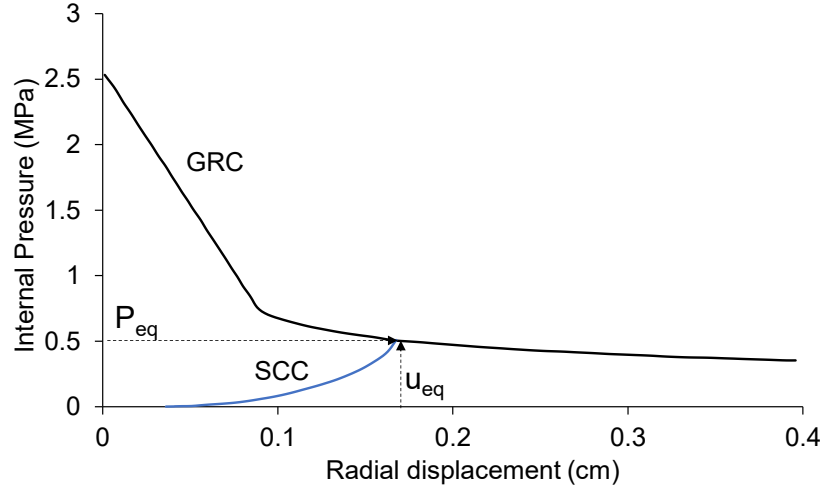


Figure 2-28 The SCC for a shotcrete liner in Kielder Experimental Tunnel (after Oreste, 2003b) (P_{eq} and U_{eq} are the pressure and displacement at equilibrium when the liner and ground interact)

By considering the change in the Young's modulus of early-age shotcrete, Oreste (1995) proposed Equation 2-81 to calculate the maximum applied pressure (σ_{max}) on shotcrete due to the excavation-induced stresses and the corresponding deformation. This stress is the maximum stress that shotcrete can tolerate. Accordingly, the shotcrete factor of safety (FS) can be determined using Equation 2-82.

$$\sigma_{max} = \frac{2R}{(1+\nu_{sh}) \times [(R-t_{sh})^2 + (1-2\nu_{sh}) \times R^2]} \int_{u_{sh}}^{u_{eq}} E_{sh}(u) du \quad \text{Equation 2-81}$$

$$FS = \frac{f_{cp}}{\sigma_{max}} \quad \text{Equation 2-82}$$

Here u_{eq} is the radial displacement of the tunnel boundary at the equilibrium point where the ground and the support interact (m), u_{sh} is the radial wall displacement before placing of the shotcrete (m), f_{cp} is the uniaxial compressive strength, and t_{sh} is the thickness of shotcrete (MPa). Other researchers (e.g. Aldrian, 1991, and Gschwandtner and Galler, 2012) also considered the time-dependent properties of shotcrete in their analyses using the CCM however the change in the post-peak response of shotcrete was not the focus

of their analyses. This is an aspect that will be discussed and investigated in more detail in this thesis.

In the pages to come, the focus is on the design of initial shotcrete lining sprayed close to the excavation face. Therefore, the mechanical properties of early-age shotcrete are required for stability analyses. Several researchers have investigated the mechanical properties of shotcrete and its evolution with time. The following sections provide a summary of these investigations and empirical equations developed for estimating the Young's modulus, the compressive strength, the tensile strength and the Poisson's ratio of shotcrete as a function of its age.

2.7.1. Young's Modulus

Weber (1979) proposed the following equation for estimating the change in the stiffness of shotcrete with time, $E(t)$:

$$E(t) = a_{sh} E_{28} \exp\left(\frac{c_{sh}}{T_{sh}^{0.6}}\right) \quad \text{Equation 2-83}$$

In this equation, E_{28} is the Young's modulus for a 28-day shotcrete, T_{sh} is the shotcrete age in days, and a_{sh} and c_{sh} are material constants which can be estimated according to the type of cement (Weber, 1979). The following equations were also suggested by Schubert (1988), CEB-FIP Model Code (1990), and Chang (1994) to calculate the Young's modulus of shotcrete as a function of shotcrete age.

$$E(t) = E_{28} \sqrt{\frac{T_{sh}}{4.2 + 0.85T_{sh}}} \quad \text{Equation 2-84}$$

$$E(t) = 1.062 E_{28} \exp\left(\frac{-0.446}{T_{sh}^{0.7}}\right) \quad \text{Equation 2-85}$$

$$E(t) = E_{28} \exp \left[s_{sh} \left(1 - \sqrt{\frac{28}{T_{sh}}} \right) \right]^{0.5}$$

Equation 2-86

Here, s_{sh} is a constant that depends on the cement type. This parameter indicates the change in stiffness with time and its value can be chosen according to the following guidelines (Schütz, 2010):

- $s_{sh} = 0.2$ for rapid hardening cements
- $s_{sh} = 0.25$ for normal hardening cements
- $s_{sh} = 0.38$ for slowly hardening cements

A comparison between the above methods for obtaining the elastic modulus of shotcrete as a function time is provided in Figure 2-29. It should be noted that E_{28} was assumed to be 30 GPa in this analysis. Figure 2-29 shows that the methods by Weber (1979) and CEB-FIP Model Code (1990) predict a higher hardening rate for shotcrete than those by Schubert (1988) and Chang (1994).

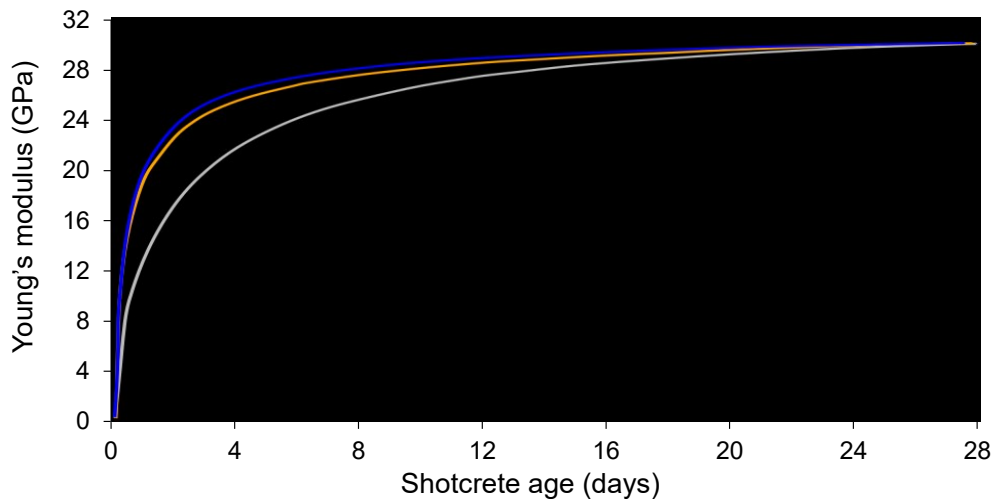


Figure 2-29 Comparison between empirical equations for estimating Young's modulus of shotcrete with time with $s_{sh} = 0.2$, $a_{sh} = 1.132$, and $c_{sh} = -0.915$ (after Schütz, 2010)

2.7.2. Compressive Strength

Several methods have been developed for estimating the compressive strength of shotcrete as a function of shotcrete age. These methods may result in a wide range of values for a specific shotcrete age due to different test conditions, hence the equations must be used with care. The following equations were proposed by Weber (1979), CEB-FIP Model Code (1990), Chang (1994) and Meschke et al. (1996). Note that Meschke et al. (1996) used two different equations for shotcrete age: one for shotcrete age less than 24 hours (Equation 2-90) and one for shotcrete age more than 24 hours (Equation 2-91). Equation 2-92 to Equation 2-94 are used to obtain the cement constants required for Equation 2-91.

$$f_{cp}(t) = af_{cp,28} \exp\left(\frac{c}{t^{0.55}}\right) \quad \text{Equation 2-87}$$

$$f_{cp}(t) = f_{cp,28} \exp\left[s_{sh} \left(1 - \sqrt{\frac{28}{T_{sh}}}\right)\right] \quad \text{Equation 2-88}$$

$$f_{cp}(t) = 1.105f_{cp,28} \exp\left(\frac{-0.743}{T_{sh}^{0.7}}\right) \quad \text{Equation 2-89}$$

$$f_{cp}(t) = f_{cp,1} \left(\frac{T_{sh}+0.12}{24}\right)^{0.72453} \quad \text{Equation 2-90}$$

$$f_{cp}(t) = a_c \exp\left(-\frac{b_c}{T_{sh}}\right) \quad \text{Equation 2-91}$$

$$a_c = \frac{f_{cp,28}}{\exp(\ln(k_{sh})/27)} \quad \text{Equation 2-92}$$

$$b_c = \frac{-672}{27} \ln(k_{sh}) \quad \text{Equation 2-93}$$

$$k_{sh} = \frac{f_{cp,1}}{f_{cp,28}}$$

Equation 2-94

In the above equations, $f_{cp,28}$ is the uniaxial compressive strength after 28 days, $f_{cp,1}$ is the uniaxial compressive strength after 24 hours, and T_{sh} is the shotcrete age in days. Note that T_{sh} in Equation 2-90 and Equation 2-91 are based on hours. The values of a_c and b_c depend on the type of cement, and s_{sh} is the cement parameter which defines how fast its stiffness changes with time.

Figure 2-30 shows the change in the compressive strength of shotcrete with time obtained from equations proposed by Meschke et al. (1996), Chang (1994), and CEB-FIP Model Code (1990). Note that the compressive strength of the 28-day shotcrete is assumed to be 40 MPa.

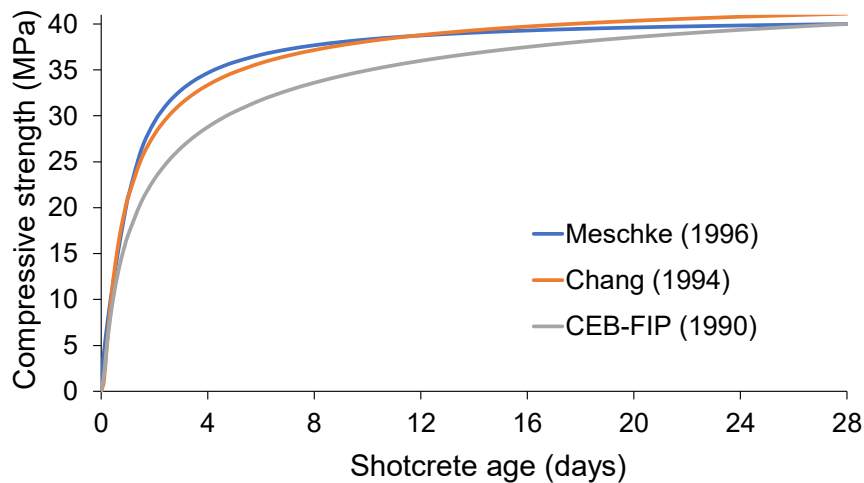


Figure 2-30 Comparison between different empirical equations for estimating the compressive strength of shotcrete as a function of age

2.7.3. Poisson's Ratio

Although there are several empirical equations for estimating the Young's modulus and compressive strength of shotcrete, limited information on the Poisson's ratio of shotcrete

and its change with shotcrete age is available. Aydan et al. (1992) proposed the following equation for estimating the Poisson's ratio of shotcrete as a function of age (T_{sh}):

$$v_{sh}(t) = 0.18 + 0.32 \exp^{-5.6T_{sh}} \quad \text{Equation 2-95}$$

Figure 2-31, based on Equation 2-95, shows that an early-age shotcrete has a Poisson's ratio of about 0.45 and its value reduces to 0.18 after 5 days. However, Carranza-Torres and Fairhurst (2000) suggested to use 0.25 for shotcrete regardless of its age.

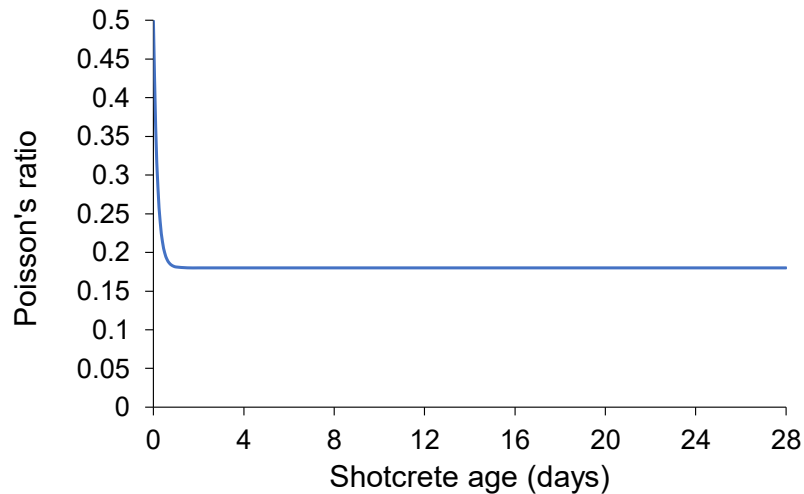


Figure 2-31 Poisson's ratio of shotcrete as a function of age (Aydan et al., 1992)

2.7.4. Tensile Strength

There are limited sources of data and equations regarding the tensile strength of early-age shotcrete. Byfors (1980) discussed how factors that increase the compressive strength of shotcrete with time also have an impact on its tensile strength. Furthermore, while Weigler (1974) found that the relationship between the compressive and tensile strengths of shotcrete is linear, Kasai et al. (1971) suggested a non-linear relationship between the two parameters. Byfors (1980) proposed the following equation for calculating the shotcrete tensile strength as a function of its compressive strength:

$$f_{tp}(T_{sh}) = 0.082f_{cp}(T_{sh})^{1.09}$$

Equation 2-96

where $f_{cp}(T_{sh})$ is the compressive strength of shotcrete at the age of T_{sh} and $f_{tp}(T_{sh})$ is the tensile strength of shotcrete at the age of T_{sh} . Figure 2-32 illustrates the change in the tensile strength of shotcrete with time. In this figure, the evolution of tensile strength with time is obtained using Equation 2-96 and by considering the compressive strength of different aged shotcrete estimated using the equations proposed by Meschke et al. (1996) (i.e. Equation 2-90 and Equation 2-91).

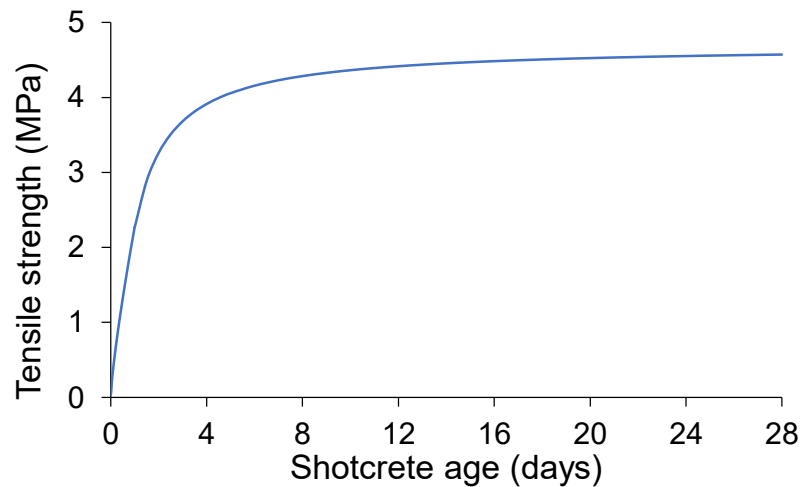


Figure 2-32 Change in the tensile strength of shotcrete with time (Byfors, 1980)

2.8. Summary

In this chapter, the *CCM* – which is a practical method for designing ground support in circular excavations – was discussed in detail and several approaches to construct the *CCM* components including the *GRC*, the *LDP* and the *SCC* were reviewed. Moreover, different methods for assessing the stability of support elements (i.e. shotcrete liner) including the load and displacement/strain factors of safety and the support capacity diagrams were examined.

The central objective of this thesis is to develop a methodology for the design of initial shotcrete linings in circular excavations by considering the excavation advance rate using 2D numerical modeling approaches. Therefore, the properties of shotcrete including the tensile and compressive strengths, the Young's modulus and the Poisson's ratio as a function of shotcrete age are required. For this purpose, the following will be taken into considerations for the simulation of the shaft and stability analysis of shotcrete/concrete lining in the future chapters.

- The excavation advance is simulated using the *IPR* approach in RS2.
- The excavation advance is simulated using the built-in *CS* approach in Irazu.
- Equation 2-64 and Equation 2-65 are used to obtain the *LDP*.
- Equation 2-89 is used to obtain the compressive strength of early-age shotcrete.
- Equation 2-96 is used to obtain the tensile strength of early-age shotcrete.
- Equation 2-84 and Equation 2-86 are used to obtain the elastic modulus of early-age shotcrete.
- The recommendation by Carranza-Torres and Fairhurst (2000) is used to obtain the Poisson's ratio of early-age shotcrete.

In the next chapter, a case study of a mine shaft supported using shotcrete and concrete liners will be reviewed. The stability of the initial shotcrete liner in this shaft will be evaluated by calculating the load factor of safety in the *CCM* and by analyzing the support capacity diagrams using 2D continuum models.

Chapter 3 Stability Assessment of Initial Shotcrete Lining Simulated as a Structural Element Using 2D Finite Element Method

3.1. Introduction

In this chapter, a 2D continuum numerical program (i.e. RS2) is used to simulate the 3D advance of a 10 m diameter mine shaft in an average quality rock mass. The rock mass properties used in the numerical model were obtained from a previously calibrated finite element model of an instrumented section of the shaft at a depth of 1.2 km. The calibrated model is first used to obtain the *GRC* and assess the stability of shotcrete linings of various thicknesses using the *CCM* by calculating their load factors of safety. Next, shotcrete linings of various thicknesses are simulated using the structural (beam) elements and their responses to the shaft advance are investigated using the support capacity diagrams.

3.2. Case History

The shotcrete lining design methodology presented in this chapter is based on a case history reported by Rafiei Renani et al. (2016), who back-analysed rock mass properties at an instrumented section of a 10 m diameter shaft at a depth of 1.2 km. Rafiei Renani et al. (2016) used both 2D and 3D continuum models to simulate the progressive shaft advance and assess the ground convergence. The instrumentation consisted of four multipoint extensometers installed radially at four locations around the shaft boundary at 1 m behind the shaft face. The magnitudes and orientations of the in-situ stress components for this site obtained from overcoring and hydraulic fracturing techniques are provided in Table 3-1.

Table 3-1 The in-situ stress field at the formation (after Rafiei Renani et al., 2016)

In-situ stress components	Magnitude (MPa)	Orientation
Major principal stress	32	Vertical
Intermediate principal stress	26	North-South
Minor principal stress	16	East-West

According to Rafiei Renani et al. (2016), the rock formation is composed of Cretaceous volcanic sediments. The mechanical properties of the intact rock determined from lab tests (i.e. uniaxial and triaxial compressive and Brazilian tensile tests) are summarized in Table 3-2. The value of *GSI* obtained for this formation was 62. Rafiei Renani et al. (2016) used the *GSI* system and the Hoek-Brown failure criterion to estimate the peak strength of the rock mass. Then, a reduced *GSI* value was used to determine the residual rock mass properties following the approach proposed by Cai et al. (2007).

Table 3-2 Mechanical properties of the intact rock determined from lab tests (after Rafiei Renani et al., 2016)

Parameters	σ_c (MPa)	E (GPa)	ν	m_i	σ_t (MPa)
Values	104	42	0.21	30	5.9

Figure 3-1 shows an overview of the shaft advance and the locations of extensometers, shotcrete and concrete liners relative to the shaft bottom. The shaft was excavated using the full-face drill and blast method through a sequence consisting of drilling, blasting, ventilation, mucking and support installation, with an advance rate of 3 m per 24 hours. The initial shotcrete lining was sprayed at 3 m behind the face, and the final concrete lining was installed at 12 m behind the face after four rounds of excavation (Figure 3-1).

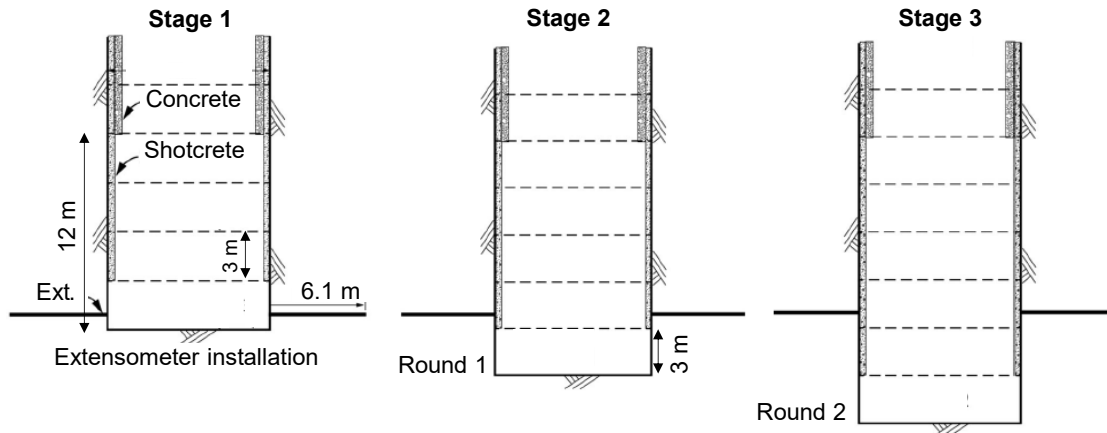


Figure 3-1 Extensometers and support installation during shaft advance (after Rafiei Renani et al., 2016)

The radial displacements measured from the extensometers after the first and second rounds of excavations are plotted in Figure 3-2. Rafiei Renani et al. (2016) excluded extensometer (Ext.) 1 from their analysis, as it shows significant scatter when compared to other extensometers (Figure 3-2a). They back analysed the measured displacements by using the 2D finite element program Phase2 (Rocscience, 2011; v.8) and the 3D finite difference program FLAC3D (Itasca, 2009). They found that the 3D model that used strain-softening material behaviour did not provide reasonable results whereas the 2D model using elastic-brittle material behaviour had an overall better match to the extensometer data. The calibrated rock mass properties employed by Rafiei Renani et al. (2016) to capture the extensometer measurements using Phase2 are summarized in Table 3-3.

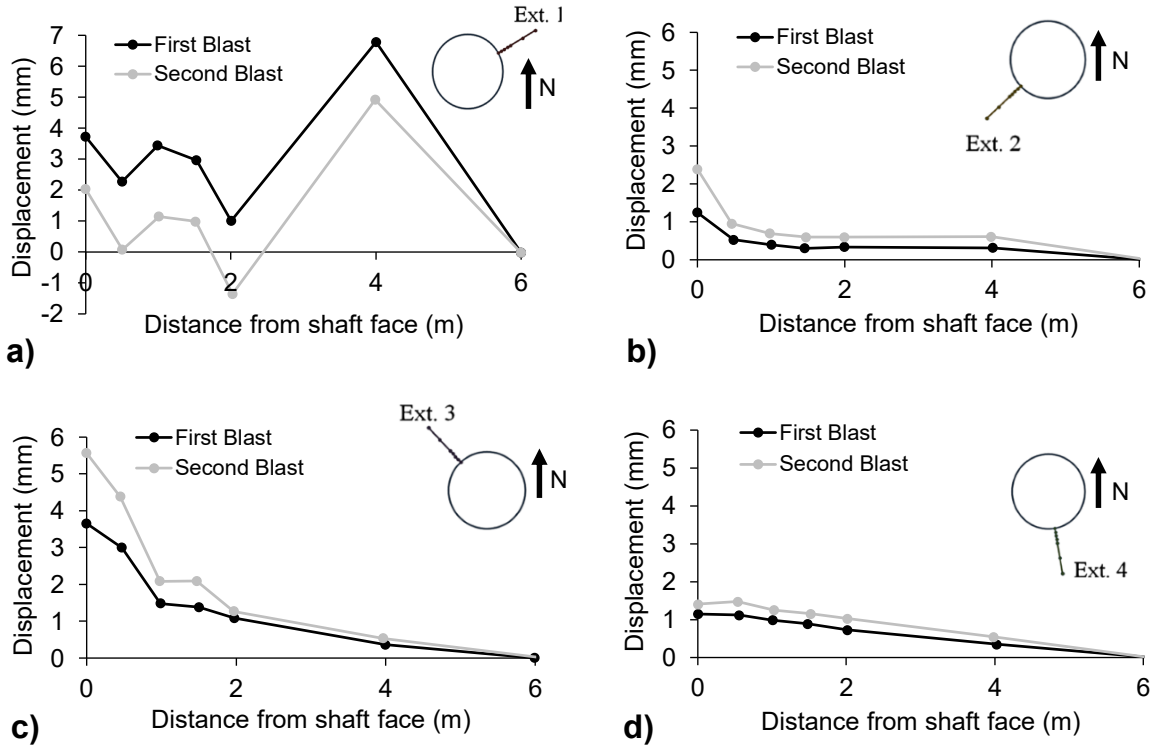


Figure 3-2 Measured displacements along: a) Ext. 1; b) Ext. 2; c) Ext. 3; and d) Ext. 4 (after Rafiei Renani et al. 2016)

Table 3-3 Calibrated rock mass properties by Rafiei Renani et al. (2016)

Parameters	Values	Parameters	Values
Peak cohesion	6 MPa	Young's modulus	27 GPa
Peak friction angle	43°	Poisson's ratio	0.25
Tensile strength	2 MPa	Dilation angle	17°
Residual cohesion	0.8 MPa		
Residual friction angle	41°		

In the next section, the results of extensometer measurements in Figure 3-2 along with the rock mass properties back calculated by Rafiei Renani et al. (2016) are adopted to simulate the 3D shaft advance using a 2D continuum model. The stability of the initial

shotcrete lining will be evaluated with the aid of the load factor of safety following the principles of the *CCM* and the support capacity diagrams.

3.3. Numerical Analysis

A 2D plane strain model using the finite element program RS2 (Rocscience, 2014; v. 9) was used to first simulate the 3D advance of the shaft described above, and then assess the stability of the initial shotcrete lining. The model specifications suggested by Rafiei Renani et al. (2016) including the geometry, mesh type and element size were adopted for this purpose. Figure 3-3 shows the RS2 model of the 10 m diameter shaft constructed using a circular external boundary with a diameter of 130 m (Figure 3-3a) and four-noded quadrilateral radial mesh elements with a minimum element size of 13 cm at the excavation boundary (Figure 3-3b).

In this chapter, the *IPR* approach is used to simulate the 3D shaft advance as opposed to the *CS* approach used by Rafiei Renani et al. (2016). As mentioned in the previous chapter, Vlachopoulos and Diederichs (2014) found that the results of the *IPR* approach is less dependent on the size and type of mesh elements and the number of stages than the *CS* approach. Moreover, it is possible to make a direct comparison between the *GRC* obtained from the *IPR* approach and that of analytical solutions (e.g. Carranza-Torres and Fairhurst, 2000; Carranza-Torres, 2004). As indicated in the previous chapter, in the *IPR* approach, an internal pressure with magnitudes and orientations respectively equal and opposite to the in-situ stresses is applied to the excavation boundary in the first modelling stage. The magnitude of internal pressure is gradually reduced in the subsequent stages until it reaches zero in the last stage, at which the maximum radial displacement corresponding to a distance far from the shaft face occurs. The *GRC* is then obtained by plotting the internal pressure as a function of radial displacement of a point on the excavation boundary.

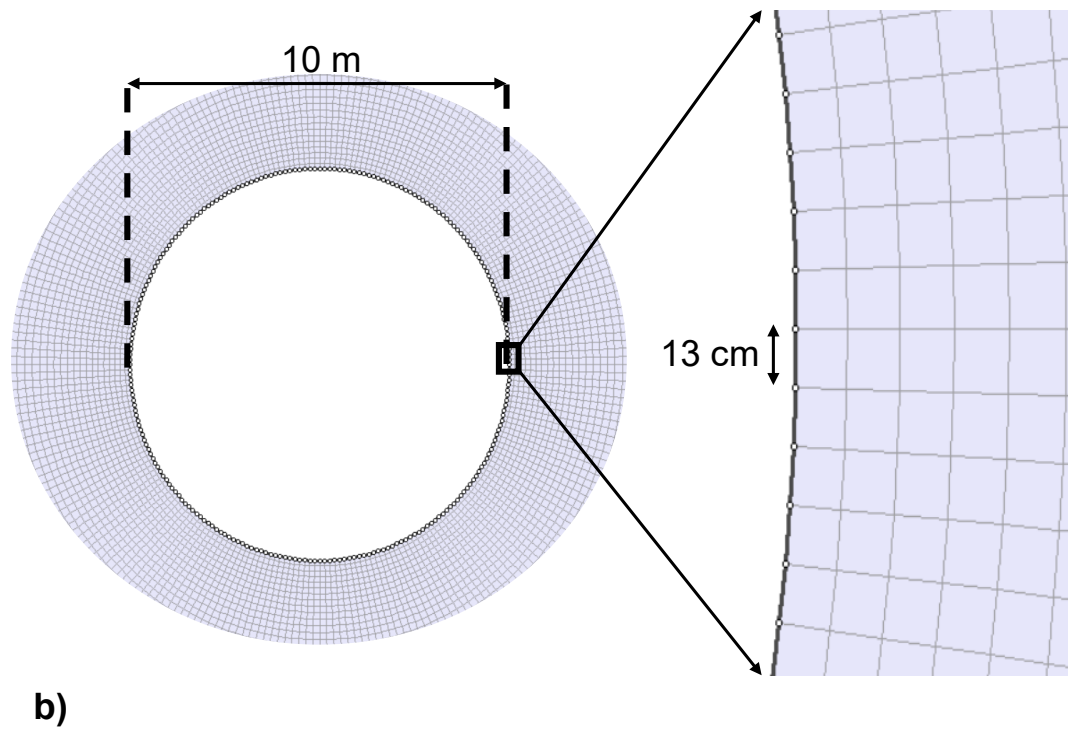
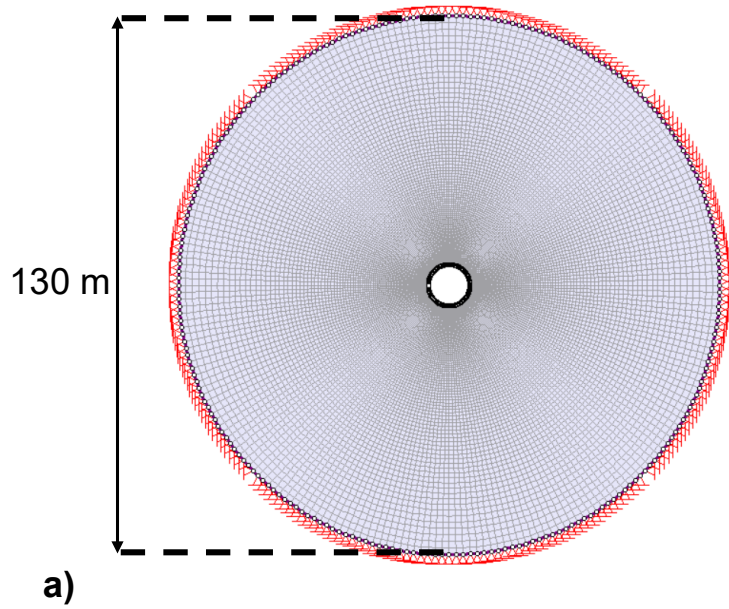
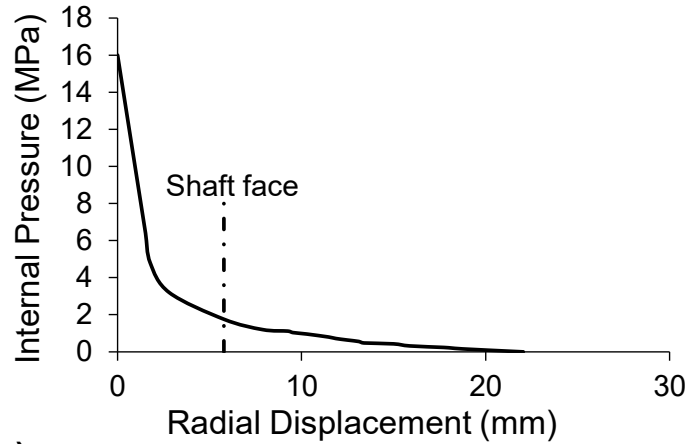


Figure 3-3 a) RS2 model geometry; and b) mesh type and geometry near the simulated shaft

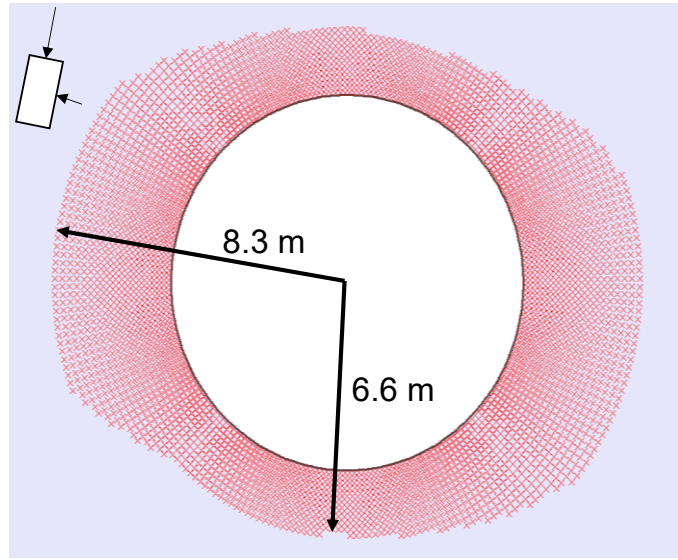
3.4. Model Calibration

Initial numerical simulations were conducted using the rock mass properties back calculated by Rafiei Renani et al. (2016). However, the results in terms of the depth of yielding and the displacements along the extensometers were slightly different from those reported by Rafiei Renani et al. (2016). Therefore, a series of sensitivity analyses were conducted on the residual rock mass strength parameters (i.e. residual cohesion and residual friction angle) and the dilation angle. It was found that by using a dilation angle of 13° instead of 17° and the peak and residual rock mass strength properties used by Rafiei Renani et al. (2016) (listed in Table 3-3), it is possible to capture the extensometer measurements. The reason for the difference between the results of the two models is not known. This minor difference might be related to the use of different versions of the finite element program (i.e., Phase2 version 8 by Rafiei Renani et al., 2016, versus RS2 version 9 in this study) and the different shaft advance simulation methods (i.e. *CS* approach by Rafiei Renani et al., 2016, versus *IPR* approach in this study).

Figure 3-4 shows the *GRC* and the shape and extent of the yielded zone around the shaft obtained from the calibrated model. As can be seen in this figure, the maximum and minimum plastic radii are 8.3 m and 6.6 m, respectively. Note that the *GRC* in Figure 3-4a is plotted for a point on the excavation boundary with a maximum radial displacement of 22 mm. By using the *LDP* equations developed by Vlachopoulos and Diederichs (2009), the radial displacement corresponding to the shaft face was determined to be 5.7 mm, as indicated on the *GRC* plot in Figure 3-4a.



a)



b)

Figure 3-4 a) GRC obtained from RS2 model; and b) yielded zone predicted using calibrated RS2 model

The radial displacements measured along the extensometers and those obtained from the calibrated model are compared in Figure 3-5. This figure shows a good agreement between the results of field measurements and numerical simulations for extensometers 3 and 4. However, the calibrated model in this study overestimates the displacements for extensometer 2 by a factor of about 2 at the excavation boundary. The simulated displacements along extensometers presented in Figure 3-5 are similar to those obtained by Rafiei Renani et al. (2016).

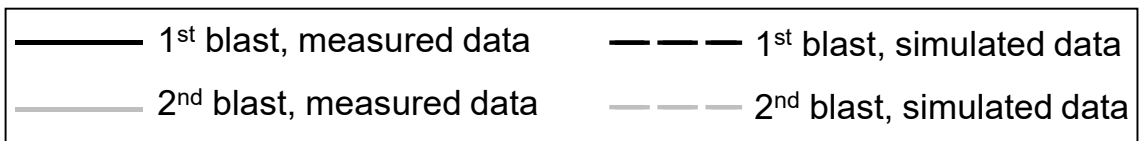
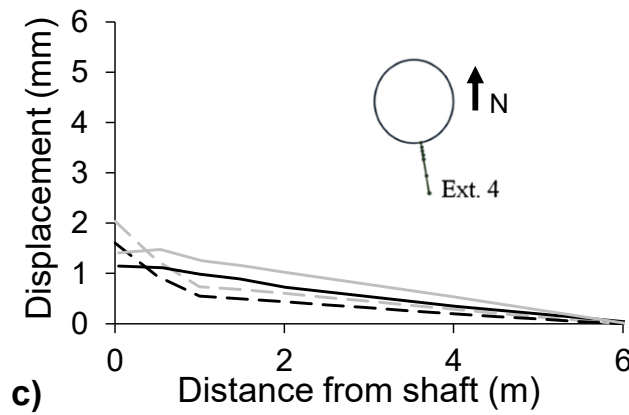
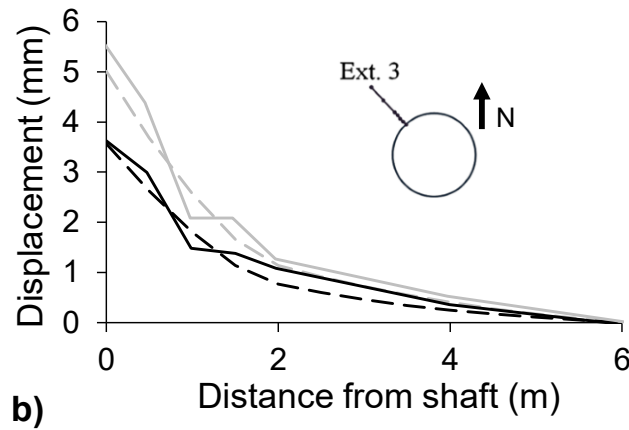
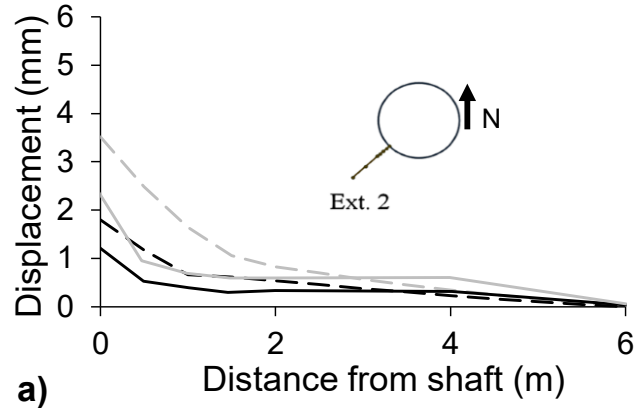


Figure 3-5 Comparison of measured and simulated displacements along: a) Ext. 2; b) Ext. 3; and c) Ext. 4

3.5. Shotcrete Properties

Once the numerical model was calibrated, it was used to simulate the ground support and analyze its stability. As mentioned earlier, the support system for the shaft consisted of an initial shotcrete lining sprayed at 3 m behind the face and a final concrete lining installed at 12 m behind the face after four rounds of excavations. No information on the specifications and properties of the shotcrete and concrete linings is available. Therefore, existing empirical equations reviewed in Section 2.7 were used to estimate its mechanical properties as a function of age.

The initial shotcrete lining was sprayed in the last step of the excavation sequence (i.e. drilling, blasting, ventilation, mucking and shotcrete). According to Rafiei Renani et al. (2016), the shaft advance length was 3 m and every round took 24 hours. The exact time between the installation of the initial shotcrete lining and the next round of the blast is not known. It was assumed that blasting took place 12 hours after the initial shotcrete was sprayed, which includes re-entry time, drilling and explosive charge loading. This means that the shotcrete hardened over a period of 12 hours before it was loaded due to the next 3 m shaft advance. As such, the properties of 12-hour shotcrete were used to account for the shaft advance rate of 3 m per excavation round. Note that no attempt was made to simulate changes in the properties of the shotcrete with time.

Several empirical relationships have been proposed for the mechanical properties of shotcrete as a function of age, as reviewed in Section 2.7 (e.g. CEB-FIP, 1990; Chang, 1994; Meschke et al., 1996; Carranza-Torres and Fairhurst, 2000). The relationships for the Young's modulus and compressive strength by Schubert (1988), and Chang (1994), along with those for Poisson's ratio and tensile strength by Carranza-Torres and Fairhurst (2000) and Meschke et al. (1996), were used to estimate the properties of the 12-hour shotcrete lining. Table 3-4 summarizes the mechanical properties of the initial shotcrete lining used in the numerical simulations.

Table 3-4 Properties of 12-hour shotcrete lining used in the numerical model

Properties	12-hour shotcrete
Young's modulus	12 GPa
Compressive strength	13.2 MPa
Tensile strength	1.36 MPa
Poisson's ratio	0.25

3.6. Stability Analysis of Initial Shotcrete Lining

In this section, two methods are used to assess the stability of the initial shotcrete lining. In the first method which is based on the *CCM*, the load factor of safety for the shotcrete lining is calculated from the analysis of the *GRC* and the *SCC*. In the second method, the shotcrete lining is simulated as a structural element with elastic properties and its stability is evaluated using the support capacity diagrams.

3.6.1 Load Factor of Safety

The load factor of safety (FS_{load}) for ground support has been traditionally determined using the *CCM* from the analysis of the *GRC* and the *SCC*. As discussed in Chapter 2, the *LDP* is used to determine the wall displacement corresponding to the shotcrete installation distance from the shaft face. Figure 2-22a shows the definitions of $FS_{load} > 1$ and $FS_{load} < 1$. In this figure, the FS_{load} is the ratio between the maximum support pressure P_s^{max} and the equilibrium pressure P_{eq} , which is the pressure at the intersection point of the *GRC* and the *SCC*. By plotting the *GRC* from the calibrated RS2 model of the mine shaft and the *SCC* for the initial 50 mm shotcrete lining, the FS_{load} was calculated for the point experiencing the maximum radial displacement as presented in Figure 3-6. This figure shows that the load factor of safety for this point is 0.55.

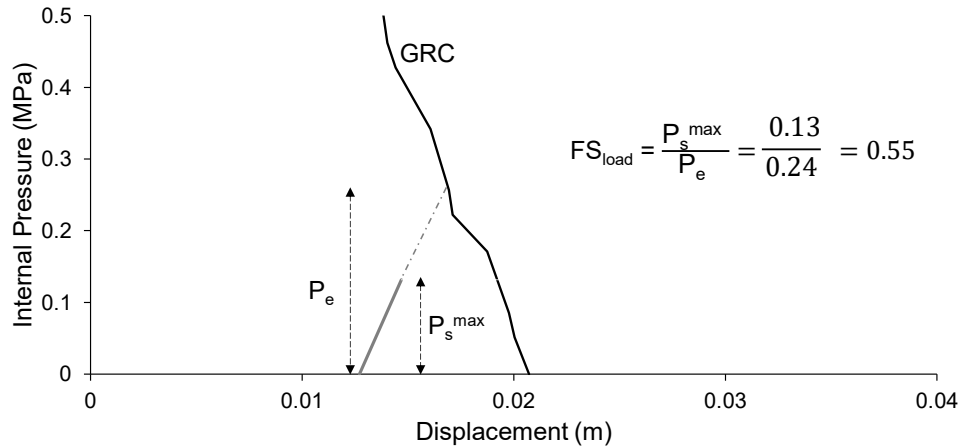


Figure 3-6 Load factor of safety (FS_{load}) calculated for 50 mm initial shotcrete lining

The FS_{load} from the analysis of the GRC and the SCC was also calculated for 36 points at every 10° around the shaft boundary for shotcrete thicknesses of 50 mm, 75 mm and 100 mm, and the results are presented in Figure 3-7. As depicted in this figure, the load factors of safety for all the points around the shaft boundary for all shotcrete thicknesses are less than unity.

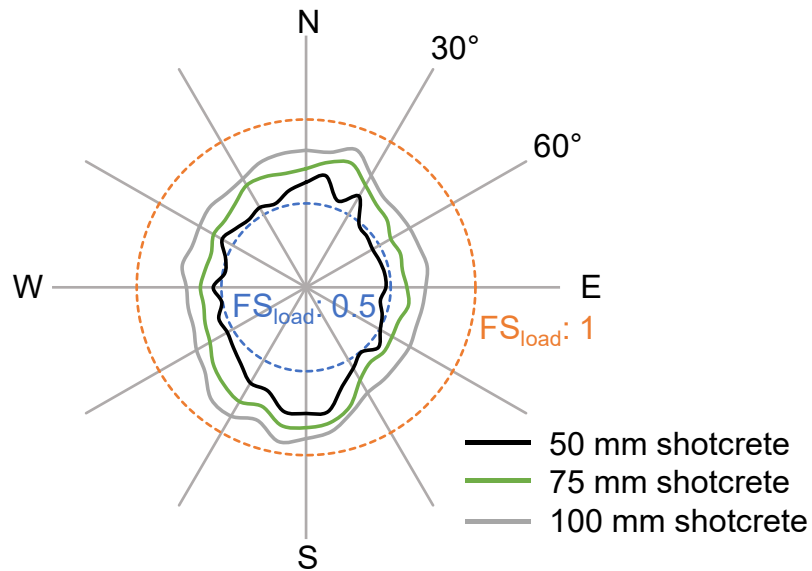


Figure 3-7 FS_{load} distribution around the shaft boundary for shotcrete thicknesses of 50 mm, 75 mm, and 100 mm

3.6.2 Support Capacity Diagram

The initial lining was simulated using the built-in structural (beam) element in RS2 with the properties listed in Table 3-4. In this analysis, it is assumed that the shotcrete behaves as an elastic material. Combining the *GRC* (Figure 3-4a) and the *LDP* (Vlachopoulos and Diederichs, 2009) allowed for the determination of the wall radial displacement corresponding to the distance of shotcrete lining from the shaft face. A series of sensitivity analyses were conducted to evaluate the influence of lining thickness on its stability in response to the shaft advance using the support capacity diagrams. Similar to the previous section, the analyses were conducted for initial shotcrete lining thicknesses of 50 mm, 75 mm and 100 mm.

As explained in the previous chapter, the support capacity diagram provides a method for determining the factor of safety for a liner. For a given factor of safety, capacity envelopes are plotted in axial force (thrust) versus moment. Values of thrust and moment are then calculated for all the segments along the structural element representing the liner and compared with the capacity envelopes. If the calculated thrust-moment values fall inside the relevant envelope, they have a factor of safety greater than the envelope's value. The calculation of thrust and moment values for the liner elements in RS2 is based on the methodology proposed by Carranza-Torres and Diederichs (2009).

Figure 3-8 shows thrust-moment diagrams calculated for factors of safety of 1 (black envelope) and 1.4 (grey envelope) for initial shotcrete lining thicknesses of 50 mm (Figure 3-8a), 75 mm (Figure 3-8b) and 100 mm (Figure 3-8c). The segments of structural elements with factors of safety of less than 1 (i.e. points outside the black envelopes) are highlighted in red in Figure 3-8b, d and f. As shown in these figures, the induced axial forces exceed the capacity of the shotcrete lining for several segments along the structural element on the right and left sides of the shaft wall. This is interpreted to be

due to high tangential stresses on the east and west sides of the shaft, resulting in extensive rock mass yielding, as shown in Figure 3-4b.

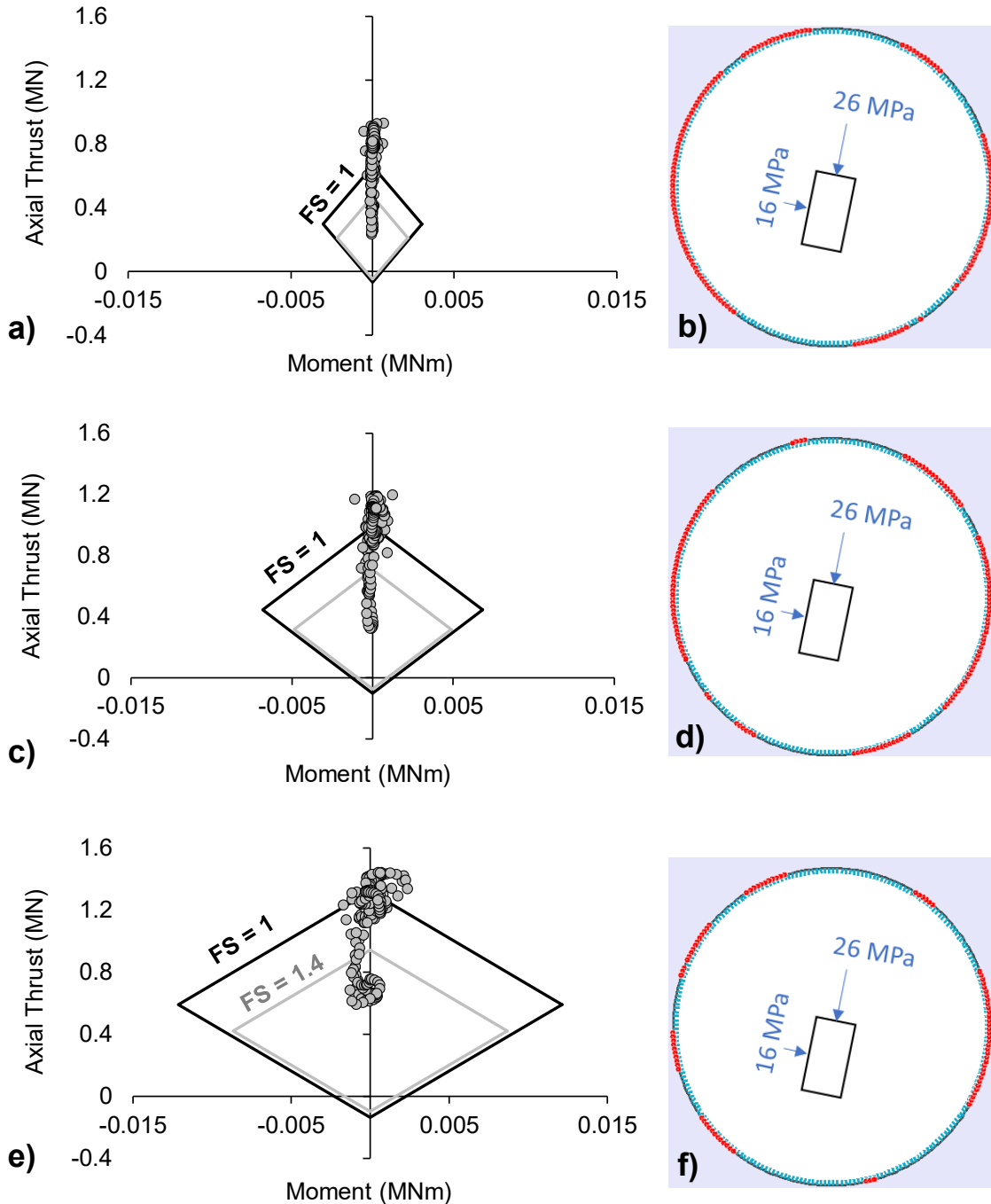


Figure 3-8 Thrust-moment diagrams and overloaded sections of initial shotcrete lining (red segments) with thicknesses of: a and b) 50 mm; c and d) 75 mm; e and f) 100 mm

The results of sensitivity analyses presented in Figure 3-8 demonstrate how an increase in the lining thickness increases the factor of safety and reduces overloaded lengths of the liner. This was further investigated by calculating the percentage of the liner segments having a factor of safety of less than unity for various lining thicknesses. It was found that 60% of the segments are overloaded (i.e. $FS < 1$) for the initial shotcrete lining thickness of 50 mm. The percentages of segments with factors of safety of less than unity decrease to about 51% and 37% for shotcrete lining thicknesses of 75 mm and 100 mm, respectively.

The results of initial shotcrete lining stability analyses presented in Figure 3-7 and Figure 3-8 suggest that overloading of initial shotcrete lining is inevitable. However, overloading does not necessarily imply complete failure. It is known that early-age shotcrete behaves in an elasto-plastic manner (John and Mattle, 2003). The early-age shotcrete can maintain the load and experience large plastic deformation before rupture occurs. Therefore, the stability of initial shotcrete may not be of great concern if its overloading results in minor cracking, by the time the permanent support (rock bolts and/or concrete liner) is installed. In the next section, a methodology for stability analysis of initial shotcrete lining based on its plastic deformation/strain during the excavation advance is proposed.

3.4. Summary

In this chapter, the 2D finite element program RS2 was used to simulate the 3D excavation advance of an instrumented section of a shaft at a depth of 1.2 km. The initial shotcrete liner was simulated using the built-in structural (beam) element in RS2. The information about the shaft advance rate allowed for determining the appropriate mechanical properties of the initial shotcrete lining. The stability of the initial lining was assessed using two methods:

- The first method was based the calculation of the load factor of safety for the initial shotcrete lining based on the analysis of the *GRC* and the *SCC* within the framework of the conventional *CCM*.
- In the second method, the thrust-moment diagrams were plotted for initial shotcrete lining thicknesses of 50 mm, 75 mm and 100 mm. This method allowed for the identification of overloaded sections of the liner around the shaft boundary.

It was found that the load factors of safety for the initial shotcrete liners of various thicknesses obtained from these two methods are less than 1. This suggests that the shotcrete liner is overloaded and deforms in a plastic manner. However, it is not possible to comment whether the initial shotcrete will remain stable by the time the final support element (i.e. concrete lining) is installed.

In the next chapter, the initial shotcrete liner will be simulated using a material model with elasto-plastic properties instead of the structural element. This will allow for capturing the progressive yielding of the shotcrete during the excavation advance as well as calculating its strain factor of safety to suggest the minimum allowable shotcrete thickness. In addition, a methodology for simulating the full support system consisting of the initial shotcrete and the final concrete liners installed at different distances from the shaft face in a single RS2 model will be proposed.

Chapter 4 Stability Assessment of Initial Shotcrete Lining Simulated as a Material Model Using 2D Finite Element Method

4.1. Introduction

Shotcrete and concrete liners are amongst the most widely used support elements in underground excavations. They are usually simulated as structural elements in numerical models, as was the case in the previous chapter. Although the simulation process using the structural element is straight forward and support capacity diagrams can be readily developed in RS2, this method cannot capture the yielding and plastic deformation of the liners as they are assigned elastic properties. To compensate for this, this chapter introduces an alternative method for simulating shotcrete liners using a material model. For this purpose, the behavior of the shotcrete liner simulated using this approach will then be investigated and compared to that of structural elements. The modifications to the RS2 model required for using this approach will be discussed in detail in the following pages.

In this chapter, the finite element numerical program RS2 is used to evaluate the stability of the initial shotcrete liner simulated using a material model by considering both elastic and elasto-plastic behaviors for the liner. First, a new mesh type is assigned to the RS2 model and the simulation results in terms of the rock mass displacement and the extent of rock mass yielding are compared with those provided in the previous chapter. Then, the initial shotcrete lining is simulated using a material model with both elastic and elasto-plastic properties. The stability of the liner simulated as an elastic material is assessed in terms of its strength factor and compared with the results presented in the previous chapter, where the liner was simulated as a structural element. Next, the progressive yielding of the liner due to the excavation of the shaft is investigated and a methodology for assessing the stability of initial shotcrete liners based on the plastic (post-peak)

deformation will be introduced. In the last section of this chapter, the stability of the full support system, which consists of the final concrete liner simulated as a structural element attached to the initial shotcrete liner simulated as a material model, will be investigated.

4.2. RS2 Model Specifications

One of the initial steps for building a numerical model is to determine the appropriate type and size of mesh elements for different zones (e.g. excavation and rock mass). In the previous chapter, a radial mesh with four-noded quadrilateral elements were used in the RS2 models. A minimum element size of 13 cm was chosen at the excavation boundary to be consistent with that of the Phase2 model constructed by Rafiei Renani et al. (2016).

In order to explicitly simulate the shotcrete liner, a material model had to be added to the excavation boundary. This required a remeshing of the RS2 model. It was found that the radial mesh in RS2 can only be used for a single excavation with one material as the rock medium. Figure 4-1 shows the error message that appears when a second material model is added to the excavation. Therefore, it was decided to use uniform mesh in order to be able to simulate the shotcrete liner with a material model in RS2.

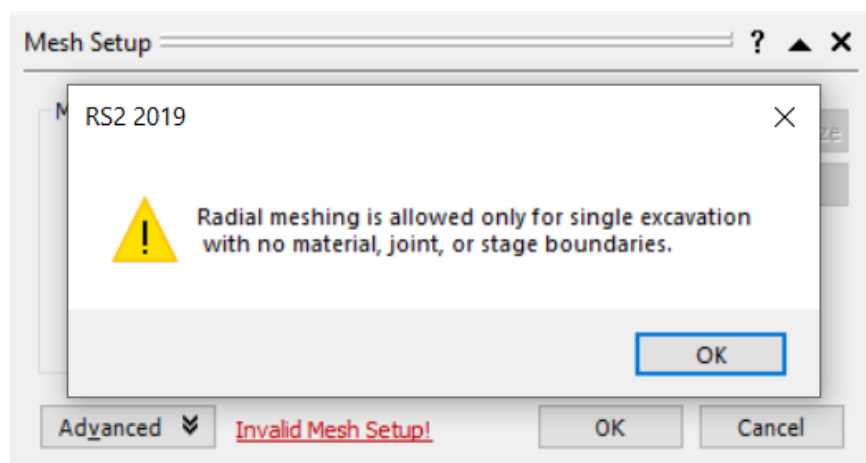


Figure 4-1 Error message in RS2 regarding the use of radial mesh with additional material model

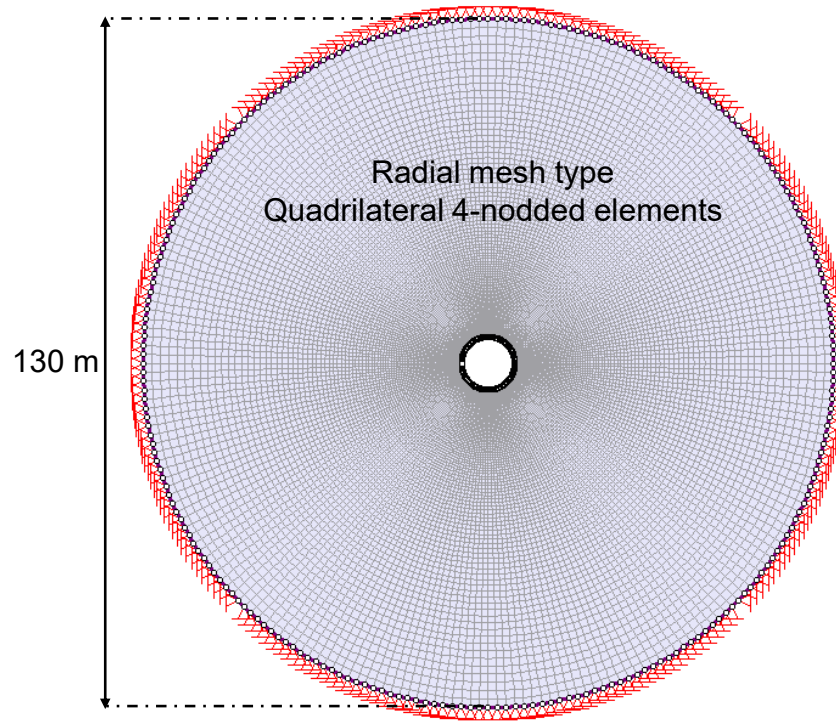
Due to the change in the mesh type, a full comparison between the new RS2 model and the one used in the previous chapter in terms of the mesh geometry, the radius of the plastic zone, the *GRC* and the anticipated rock mass deformation is provided in the following sections.

4.2.1. Model Geometry

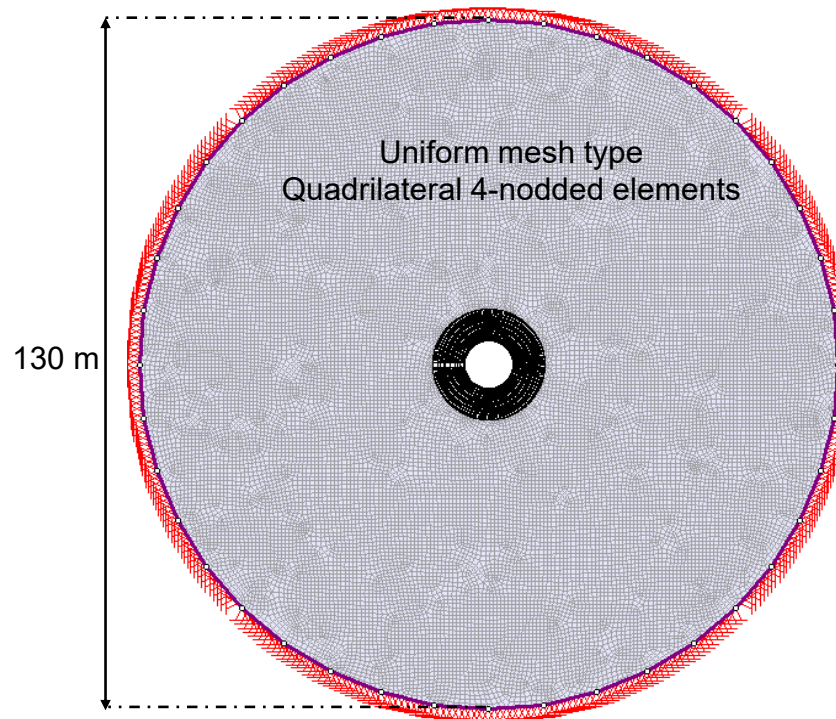
Figure 4-2 shows two plane strain RS2 models: one constructed using the radial mesh and the other one with the uniform mesh. The size of the external boundary in both models is 130 m. The shaft with a diameter of 10 m is located in the centre of both models. Figure 4-2a shows the model with the radial mesh in which the element size increases as the distance from the excavation increases. In the model with the uniform mesh (Figure 4-2b), the element size is constant throughout the model.

It was found that the size and shape of mesh elements have a significant impact on the model results in terms of the shape and extent of yielded zones near the excavation. Therefore, several circular material boundaries were added close to the excavation boundary in the model with the uniform mesh and discretized in such a way that shape and size of elements became comparable to those in the model with the radial mesh (Figure 4-2b and Figure 4-3). Figure 4-3 presents closer views of and provides a comparison between the mesh geometries in both models.

As illustrated in Figure 4-3a, the material boundaries near the shaft in the model with the uniform mesh is extended to a distance of 10 m from the model centre. Using these material boundaries, a constant element size of 13 cm was obtained at the excavation boundary, similar to that in the RS2 model with the radial mesh (Figure 4-3b).



a)



b)

Figure 4-2 Comparison between geometries of RS2 models constructed using: a) radial mesh; and b) uniform mesh

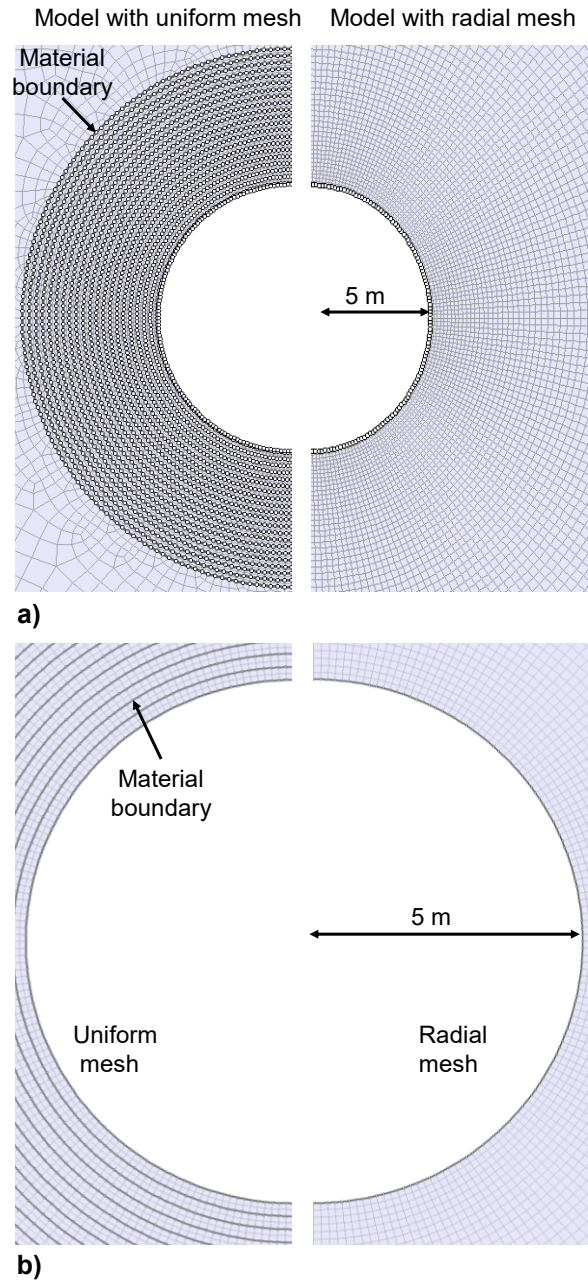


Figure 4-3 Comparison between RS2 models constructed using: a) uniform (left images) and radial (right images) mesh elements; b) zoomed-in view of the two models

4.2.2. Results of New Model

Since the mesh type in the new RS2 model was changed, the model results (with no support elements) in terms of the extent of the plastic zone and rock mass deformation

around the shaft had to be checked against those of the model with the radial mesh. This was required to ensure that the model with the revised mesh is calibrated and can therefore be used for the stability analysis of the initial shotcrete liner.

4.2.2.1. Plastic zone

The extent of plastic zones in the models constructed with radial and uniform mesh elements are compared in Figure 4-4. As illustrated in this figure, the shape of the plastic zone, and the maximum and minimum plastic radii in both models are comparable.

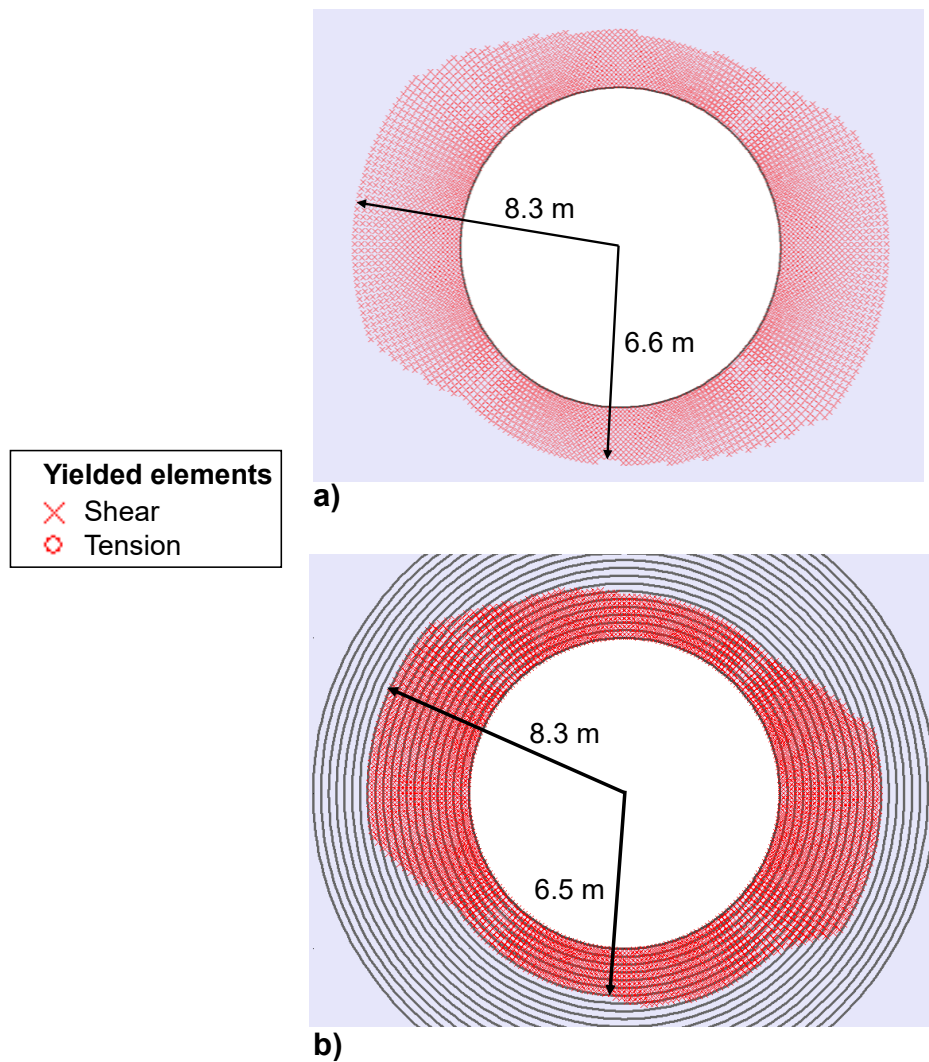


Figure 4-4 Comparison between the extent of plastic zone near the shaft using: a) radial mesh; and b) uniform mesh

4.2.2.2. Ground reaction curve

The *GRC* was constructed by selecting a point on the excavation boundary where the maximum radial displacement occurs. Then, the radial displacements and the internal pressure applied to this point were extracted for all the excavation stages and used to plot the *GRC*. The *GRCs* for the models with uniform and radial mesh elements are compared in Figure 4-5. The zoomed-in view of the *GRCs* (Figure 4-5b) indicates an excellent agreement between the two models in terms of the shape of the curve and the maximum radial displacement.

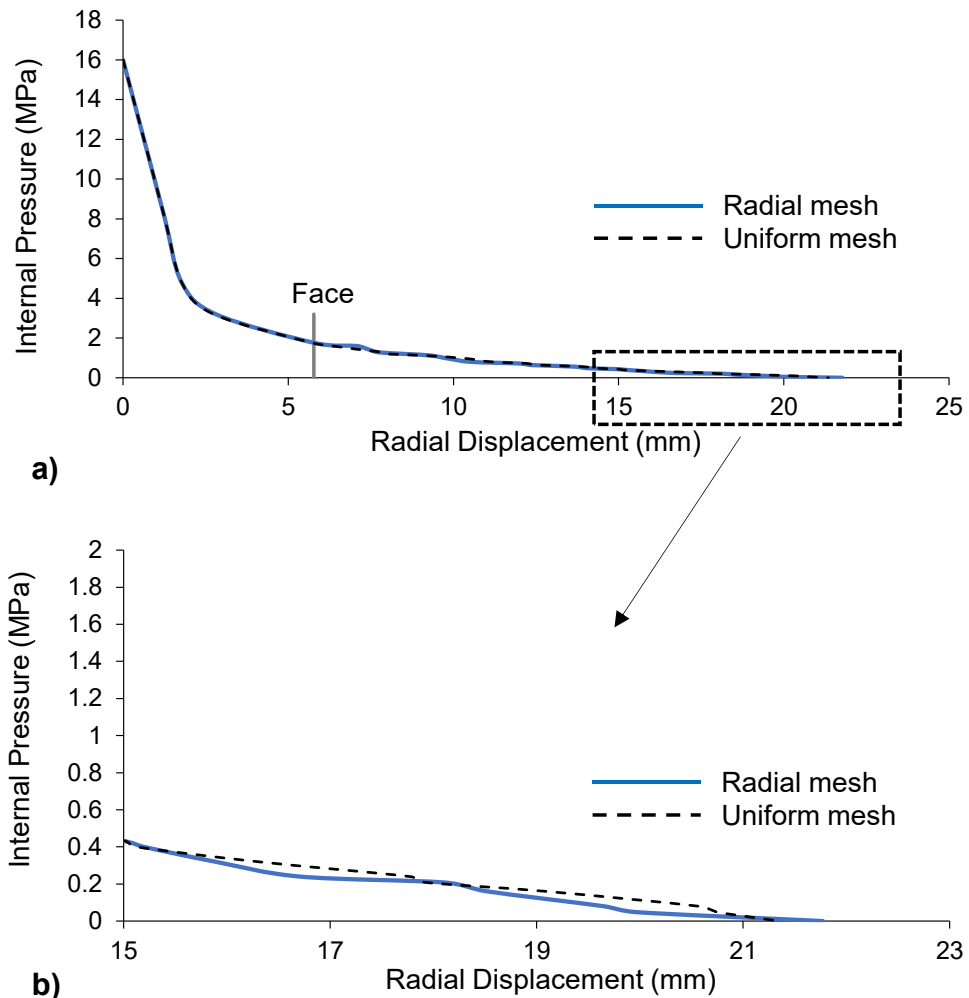


Figure 4-5 a) Comparison between the *GRCs* constructed for the unsupported shaft based on the models with radial and uniform mesh; and b) zoomed-in view of the boxed area in Figure 4-5a

4.2.2.3. Extensometer measurements

By considering the distance of the extensometers from the shaft face, the radial displacement along the extensometers in the model constructed with the uniform mesh were extracted and compared to those obtained from the model constructed with the radial mesh. Figure 4-6 demonstrates how comparable the radial displacements obtained from the two RS2 models are, especially for extensometer 3 (Figure 4-6b).

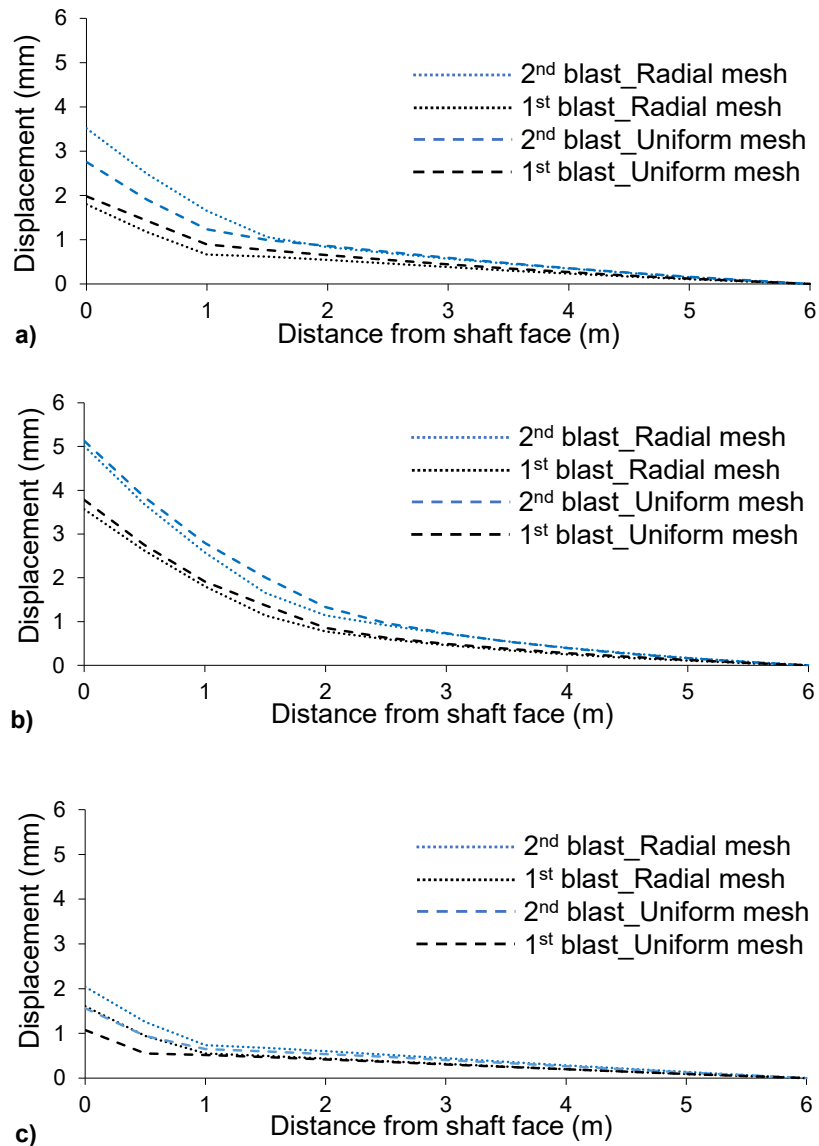


Figure 4-6 Comparison between simulated radial displacements in models constructed using radial and uniform mesh elements along: a) Ext. 2; b) Ext. 3; and c) Ext. 4

It was demonstrated in this section that the model with the uniform mesh provides comparable results to the one constructed with the radial mesh in terms of the extent and shape of the plastic zone, the *GRC* and the rock mass deformation (i.e. extensometer measurements). Therefore, it is reasonable to conclude that the RS2 model with the uniform mesh can be used as an alternative to assess the stability of the initial shotcrete liner simulated using a material model.

4.3. Simulation of Initial Shotcrete Lining Using Material Model

After confirming that the unsupported RS2 model with the uniform mesh behaves similar to that with the radial mesh, the initial shotcrete liner was simulated using a material model with elastic properties. In Figure 4-7, the RS2 models with shotcrete liners simulated as a material model (left image) and a structural element (right image) are compared. It should be noted that the mesh elements inside the liner simulated as a material model was made smaller than those at the excavation boundary in order to better capture the progressive yielding of shotcrete during shaft excavation.

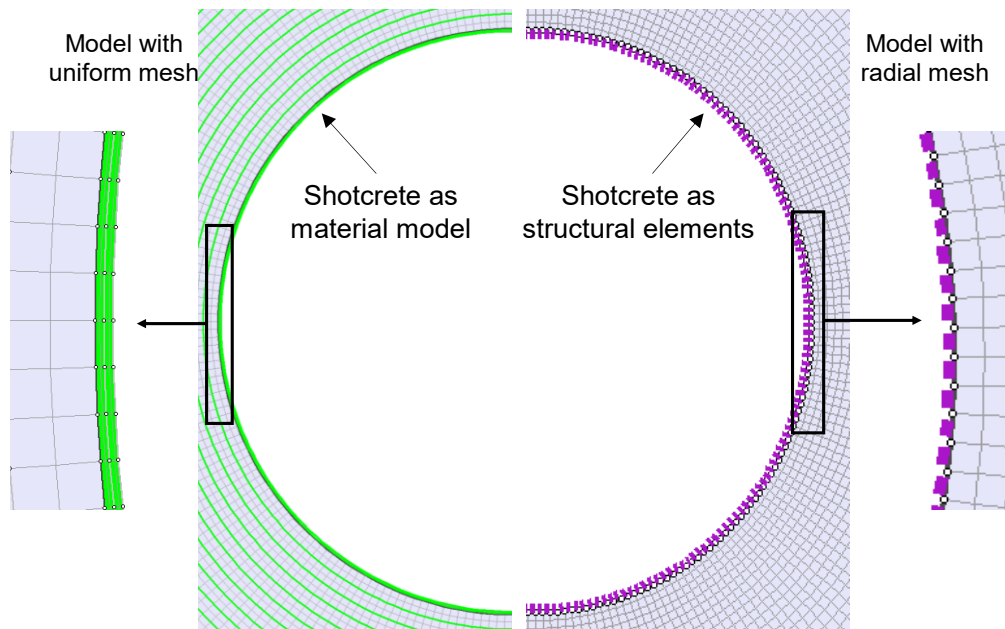


Figure 4-7 Comparison between RS2 models with shotcrete liner simulated as a material model (left) and a structural element (right)

Similar to the numerical analyses in Chapter 3, different thicknesses for the shotcrete liner were considered (i.e. 50 mm, 75 mm and 100 mm). Figure 4-8 shows the shotcrete liner simulated as a material model with thicknesses of 50 mm, 75 mm and 100 mm. As can be seen in this figure, there are four elements across the width of the shotcrete in all three models.

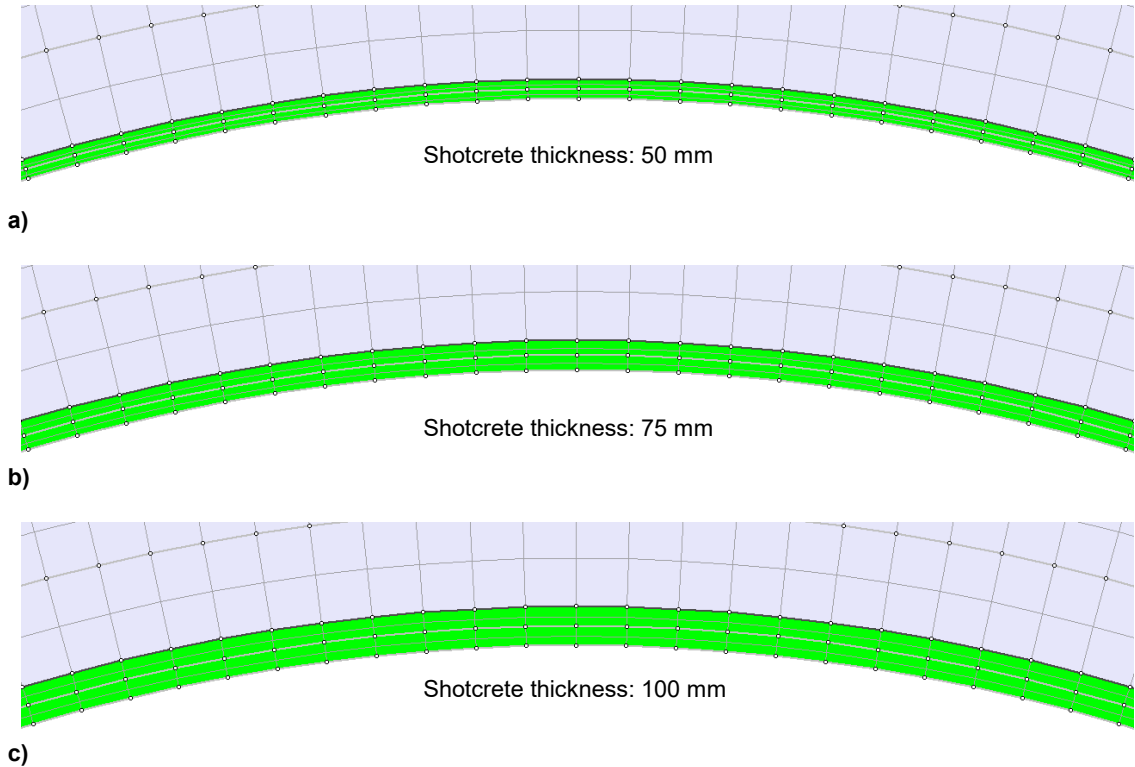


Figure 4-8 Shotcrete liner simulated as a material model with thicknesses of: a) 50 mm; b) 75 mm; and c) 100 mm

The process of installing the initial shotcrete liner simulated as a material model in RS2 using the *IPR* approach is demonstrated in Figure 4-9. Figure 4-9a shows the first stage, wherein the internal pressure applied to the shaft boundary is equal to the magnitude of in situ stress (i.e. $P_i/P_0 = 1$). The internal pressure is gradually reduced until it reaches a stage at which the shotcrete is activated, as illustrated in Figure 4-9b (i.e. $P_i/P_0 = 0.04$). Note that no initial loading is applied to the shotcrete. The internal pressure is then reduced to zero in the remaining stages, allowing the shotcrete to gradually get loaded

and deform during the excavation. Figure 4-9c shows the final excavation stage, at which the internal pressure is zero.

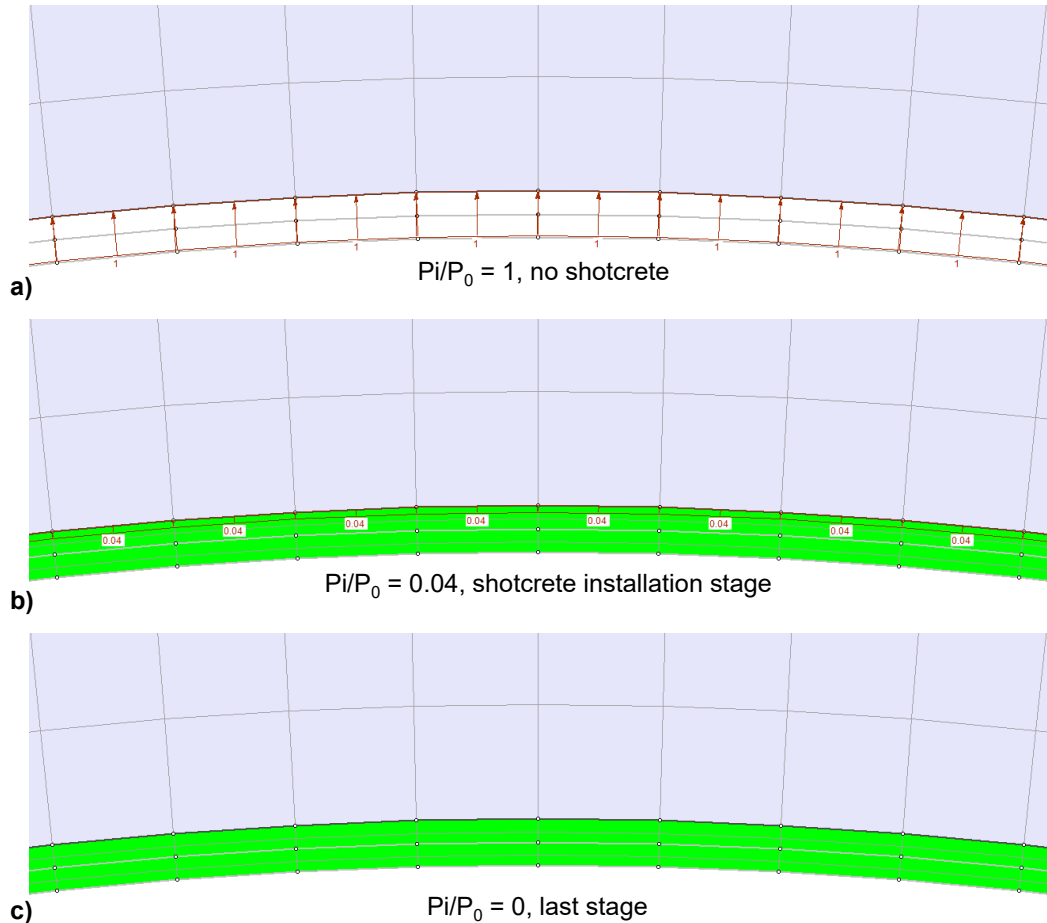


Figure 4-9 Installation of shotcrete simulated as a material model: a) initial stage; b) shotcrete installation stage; and c) final stage with zero internal pressure

Further comparison between the two RS2 models (i.e. those with uniform and radial mesh) were made by plotting their *GRCs* with and without the shotcrete liner. Figure 4-10a and Figure 4-10b show the *GRCs* of the unsupported and supported models with shotcrete liner simulated as a structural element and Figure 4-10c and Figure 4-10d show the *GRCs* of the unsupported and supported models with shotcrete liner simulated as a material model. By comparing the *GRCs* of the unsupported and supported models, it is concluded that the presence of the initial shotcrete liner results in the reduction of the maximum radial displacement by about 2 mm.

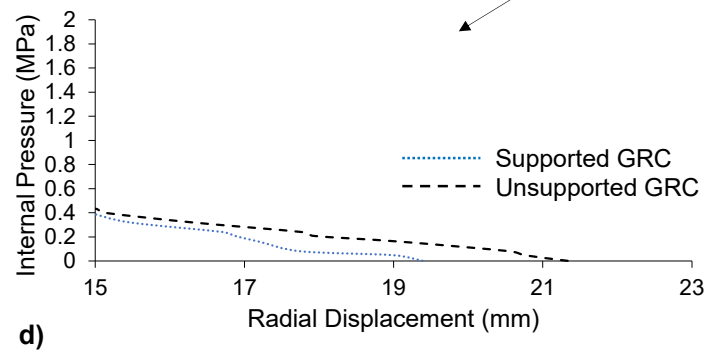
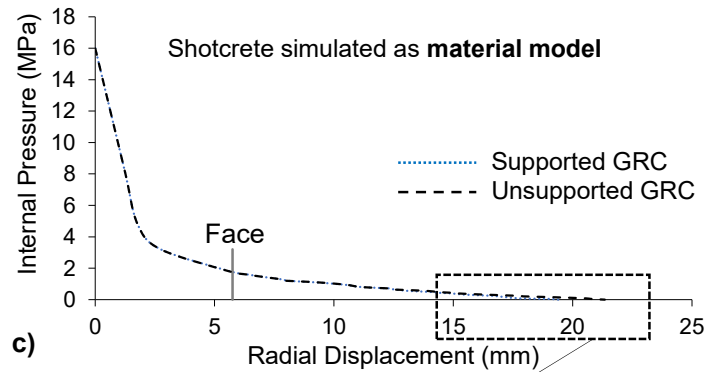
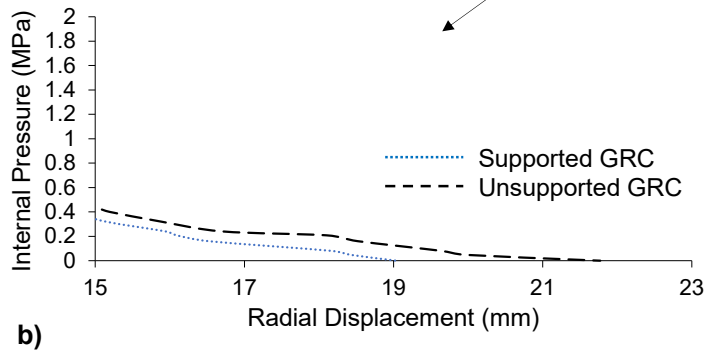
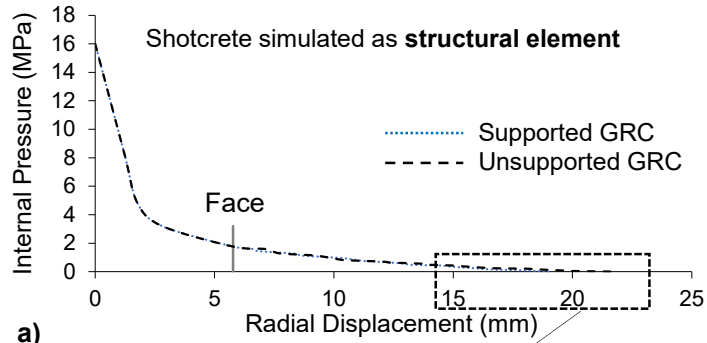


Figure 4-10 Comparison between GRCs in supported and unsupported models with: a) shotcrete liner simulated as a structural element in a model with the radial mesh; b) zoomed-in view of the boxed area in Figure 4-10a; and c) shotcrete liner simulated as a material model in a model with the uniform mesh; d) zoomed-in view of the boxed area in Figure 4-10c

4.4. Stability Analysis of Initial Shotcrete Lining

4.4.1. Shotcrete as an Elastic Material

Initial numerical analyses were conducted by considering the shotcrete liner as an elastic material with properties given in Chapter 3. This allowed for the calculation of the load factor of safety (i.e. strength factor contours) for the shotcrete liner and the comparison of the results with that of the model where the shotcrete liner was simulated as a structural element. Figure 4-11 shows the overloaded sections of the shotcrete liner (highlighted in red) simulated as structural elements (left images) and material models (right images) with thicknesses of 50 mm, 75 mm and 100 mm. By comparing the results of these two models – as presented in Figure 4-11 and summarized in Table 4-1 – the differences between the overloaded sections of shotcrete liners were found to be as small as 1% for the 50 mm shotcrete liner and increase to 3% and 6% for 75 mm and 100 mm shotcrete liners, respectively.

Table 4-1 Overloaded sections of shotcrete liner with FS < 1

Shotcrete thickness (mm)	FS < 1 (%)	
	Material model	Structural element
50 mm	61	60
75 mm	48	51
100 mm	30	36

In the following section, the shotcrete liner is simulated as a material model with elastoplastic properties. Then, a procedure for calculating the plastic strain factor of safety for the stability analysis of initial shotcrete linings is introduced.

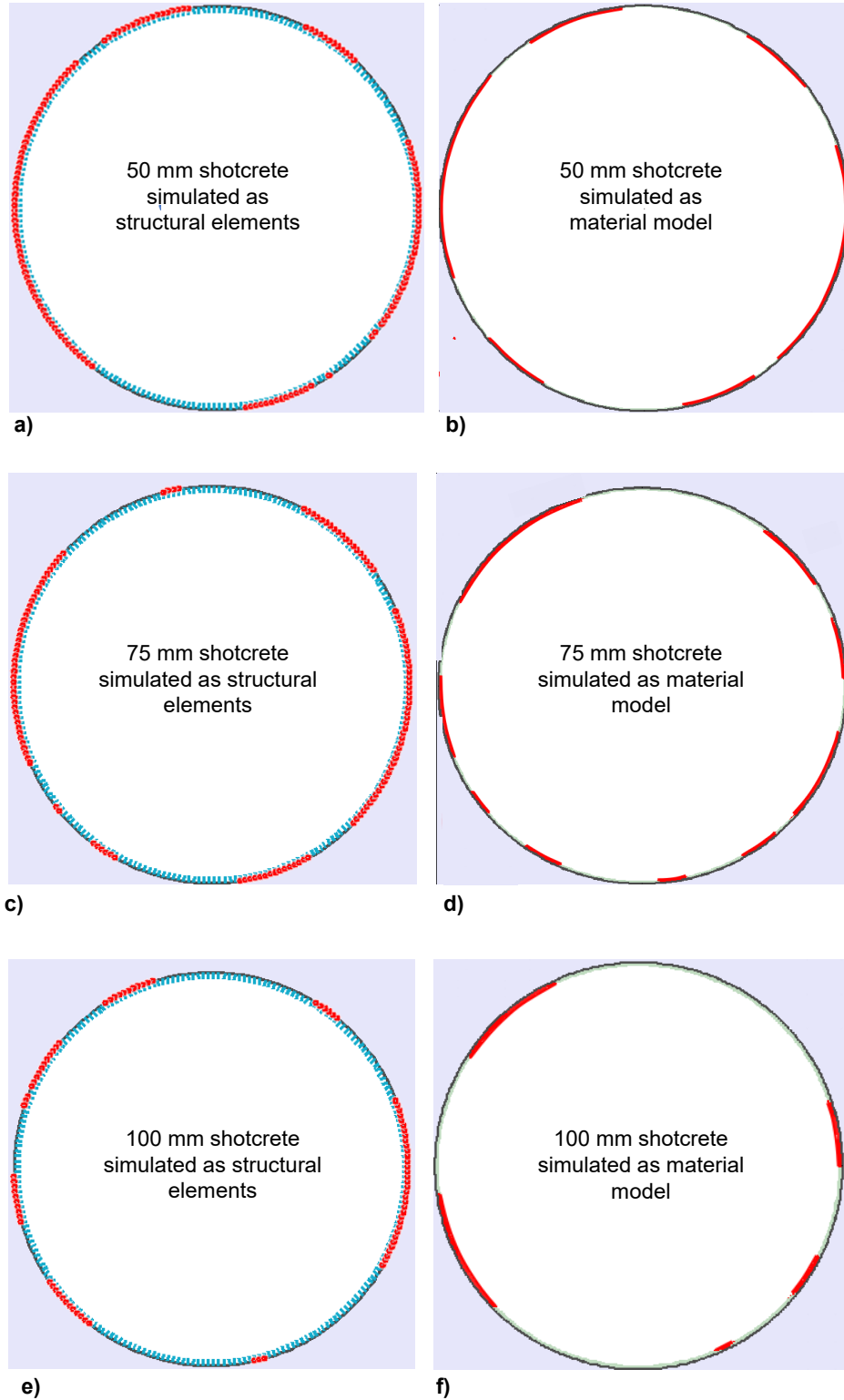


Figure 4-11 Comparison between overloaded sections of initial shotcrete lining (highlighted in red) simulated as structural elements (left images) and material models (right images) with thicknesses of: a and b) 50 mm; c and d) 75 mm; and e and f) 100 mm

4.4.2. Shotcrete as an Elasto-plastic Material

4.4.2.1. Progressive yielding of initial shotcrete liner

Explicit simulation of shotcrete liner as a material model with elasto-plastic properties allows for gaining deeper insights into the progressive yielding of the liner during the excavation advance. Figure 4-12 illustrates the shape and extent of rock mass yielding around the shaft supported with a 100 mm initial shotcrete liner. The local yielding of the shotcrete liner can be seen in this figure. Note that the legend in this figure shows the percentage of yielded elements, where blue and red indicate “no yielding” and “complete yielding”, respectively.

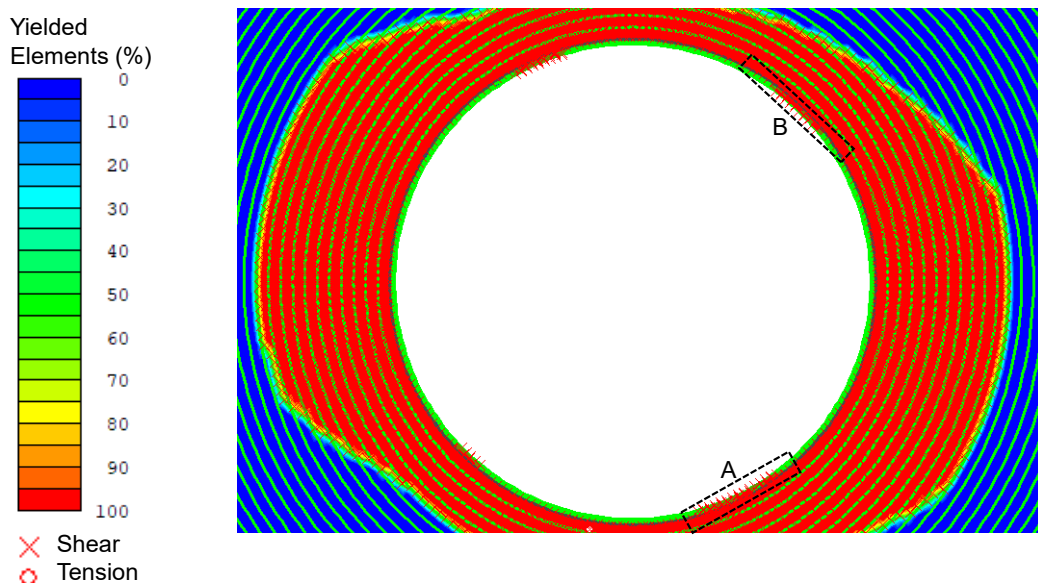


Figure 4-12 Yielding of the rock mass and 100 mm initial shotcrete liner

Figure 4-13 and Figure 4-14 provide closer views of the boxed areas A and B shown in Figure 4-12, which demonstrates the progressive yielding process of the shotcrete liner. Figure 4-13a and Figure 4-14a correspond to the stages where shotcrete is installed but yielding has not occurred. Yielding initiates from the outer surface of the shotcrete liner in the following stages (Figure 4-13b and Figure 4-14b) due to the reduction in internal pressure (i.e. excavation advance). In the last excavation stage where there is no internal pressure, yielding propagates across the liner width (Figure 4-13c and Figure 4-13f).

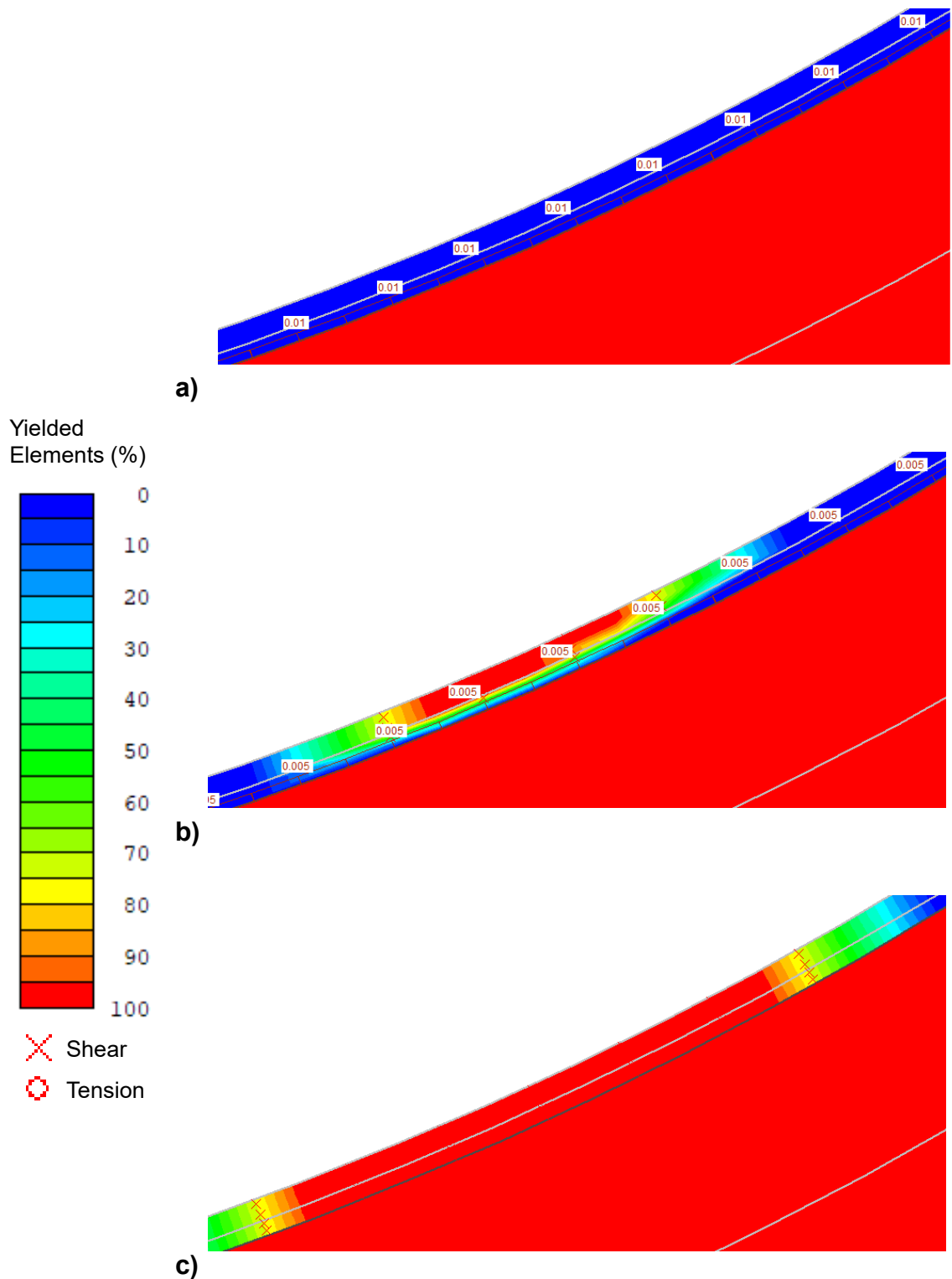


Figure 4-13 Closer views of the boxed area A in Figure 4-12 showing the progressive yielding of shotcrete liner: a) shotcrete installation stage; b) partial yielding of shotcrete; and c) complete yielding of shotcrete in the last excavation stage

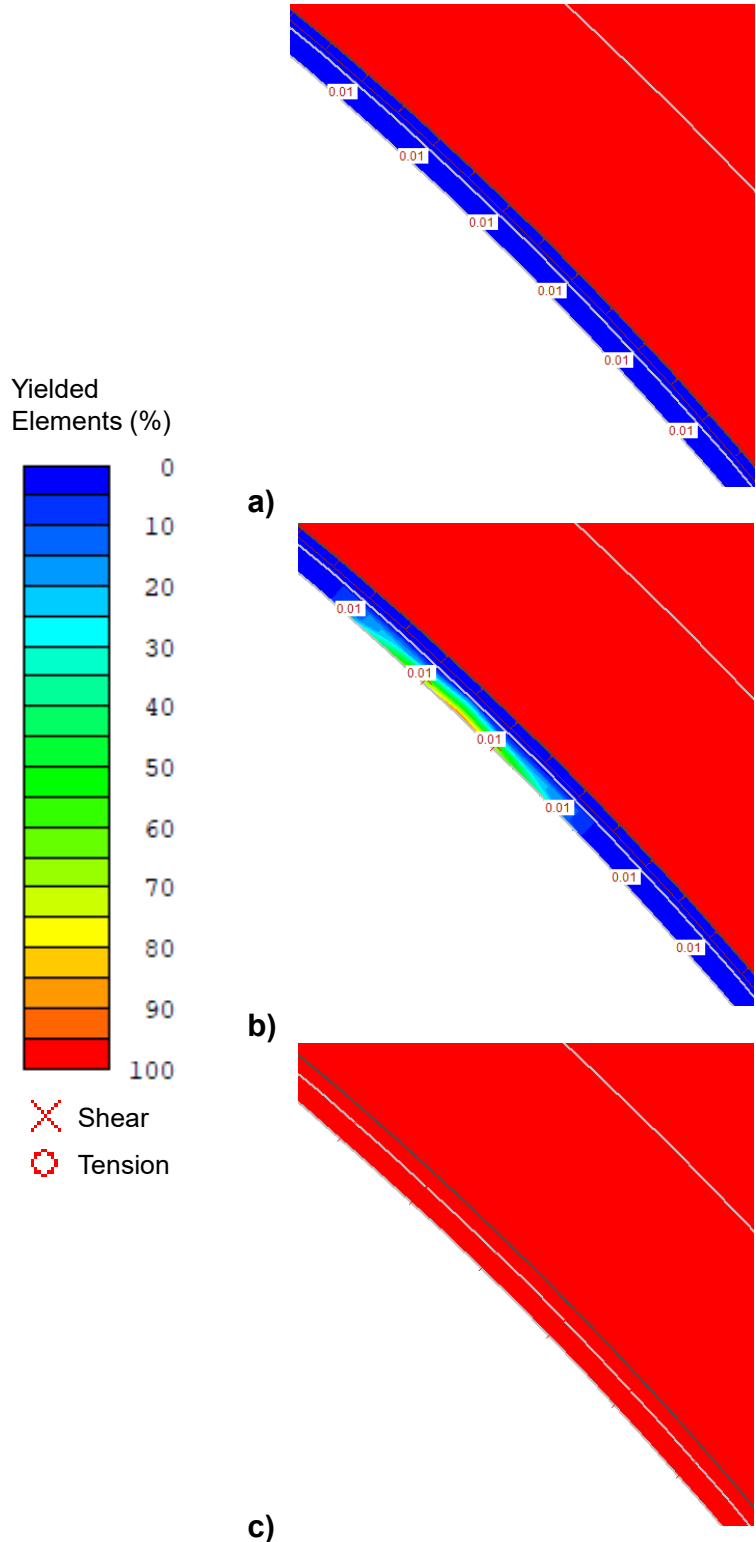


Figure 4-14 Closer views of the boxed area B in Figure 4-12 showing the progressive yielding of shotcrete: a) shotcrete installation stage; b) partial yielding of shotcrete; and c) complete yielding of shotcrete in the last excavation stage

A more realistic simulation of progressive fracturing processes leading to the failure of shotcrete linings can be carried out using a code based on the discrete element method. In the next chapter, a hybrid finite-discrete element method will be used to gain further insight into the fracturing process of shotcrete liner during the excavation advance and to assess its stability.

4.4.2.2. Strain factor of safety for initial shotcrete liner

In this section, the radial displacement of the shotcrete liner is obtained from the results of RS2 model and then used to calculate the strain factor of safety for the initial shotcrete liner. As demonstrated in Figure 4-15, when the shotcrete liner is under internal axial stresses due to the shaft advance and wall convergence, the liner deforms in the radial direction towards the centre of the shaft. Therefore, the lateral strain of shotcrete lining, as opposed to the axial strain should be used for the calculation of the strain factor of safety.

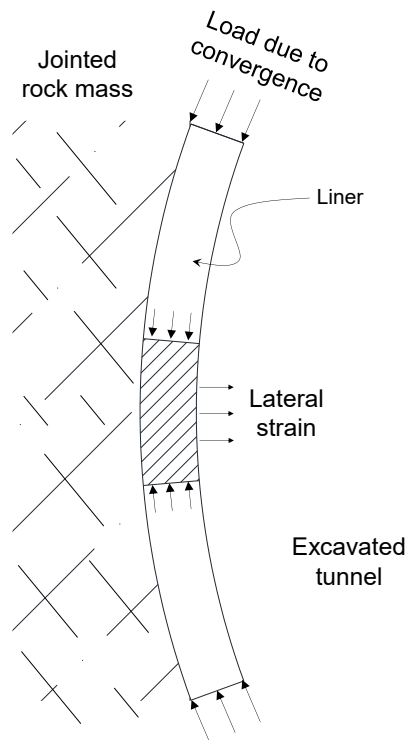


Figure 4-15 Schematic radial deformation of the shotcrete liner due to shaft wall convergence

In order to calculate the lateral strain factor of safety for the initial shotcrete lining, a relationship between the lateral strain of the shotcrete and its age must be developed. Unfortunately, laboratory test data on the lateral strain of shotcrete as a function of shotcrete age are scarce. The results of laboratory uniaxial compressive tests on steel fiber reinforced shotcrete reported by Saw et al. (2009) was used for this purpose.

Figure 4-16a presents the stress-strain curves for 50 mm thick shotcrete specimens with curing times of 1 day, 3 days, 7 days and 28 days. The test results show that the yield point and the peak stress increase with the curing time. After the yield point, non-linear strain hardening is observed until the peak strength is reached. Following the peak point, strain softening and/or sudden stress drop occurs, indicating brittle failure. The axial plastic strain seems to be less dependent of the shotcrete age. However, the lateral plastic strain increases along with the shotcrete age.

The stress-strain curves presented in Figure 4-16a were used to develop a relationship between the total (elastic and plastic) lateral strain and the shotcrete age (curing time). An example of the lateral strain determined for the 28-day shotcrete is presented in Figure 4-16a, and the plot of lateral strain versus the shotcrete age is provided in Figure 4-16b. The following function was used to fit to the data with an R^2 of 0.84.

$$\varepsilon_l = 0.59T_{sh}^{0.14} \quad \text{Equation 4-1}$$

In this equation, ε_l is the lateral strain (%) and T_{sh} represents the age of shotcrete (days). Using this equation, the lateral strain for the 12-hour shotcrete is estimated to be 0.54%.

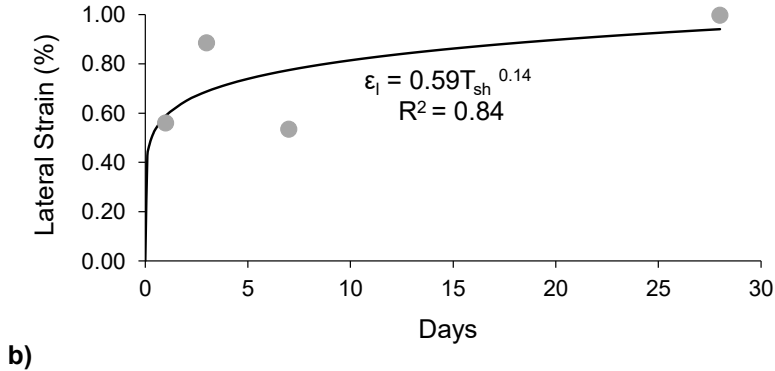
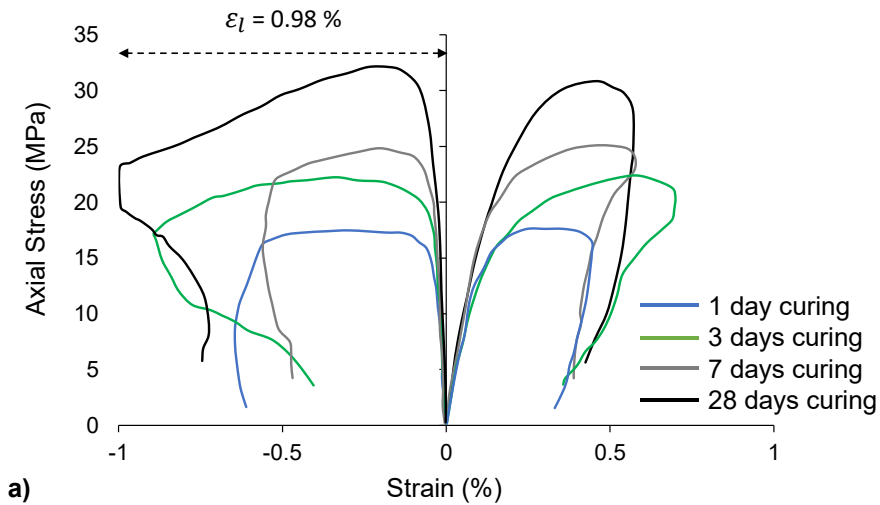


Figure 4-16 a) Stress-strain curves from UCS tests on 50 mm shotcrete specimens of different curing times (after Saw et al., 2009); and b) Best fit curve relating lateral strain to shotcrete age

The lateral strain for the shotcrete liner at a given stage in the RS2 model can be obtained by calculating the difference between the radial displacement at the surface of the liner and that of the excavation boundary and dividing it by the initial liner thickness. In Figure 4-17, the radial displacements of the shotcrete liner and the shaft boundary are depicted as d_l and d_b , respectively, and d represents the thickness of the shotcrete liner.

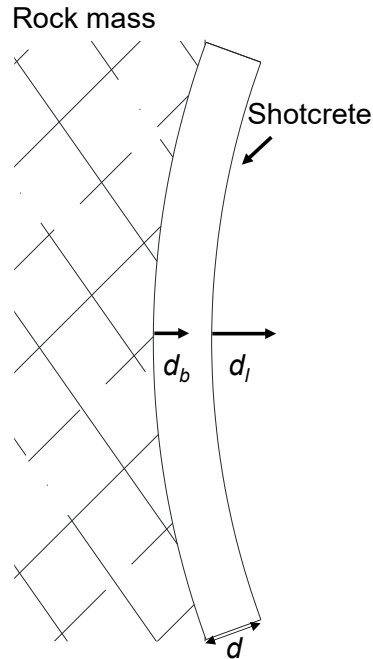


Figure 4-17 Radial displacements for shotcrete surface (d_b) and shaft wall (d_l)

Therefore, the total lateral strain (ε_l) for the initial shotcrete liner is calculated from the difference between the lateral strain of the shotcrete at a stage when the shotcrete liner is installed and that of the last excavation stage when the internal pressure is zero using the following equation:

$$\varepsilon_l = \left(\frac{(d_b - d_l)_i}{d} - \frac{(d_b - d_l)_f}{d} \right) \times 100 \quad \text{Equation 4-2}$$

where the subscripts i and f correspond to the stage when the shotcrete is installed and the final excavation stage when the internal pressure is zero, respectively. The strain factor of safety for the initial shotcrete lining (FS_{strain}) is defined as the ratio between the lateral strain capacity of the shotcrete obtained from the empirical equation derived based on the results of laboratory tests by Saw et al. (2009) (Equation 4-1), and the lateral strain of the shotcrete liner determined from the results of the RS2 model (Equation 4-2). Using this approach, the FS_{strain} was calculated for several points at every 10° along the shaft boundary, and the results for 50 mm shotcrete liner are shown in Figure 4-18.

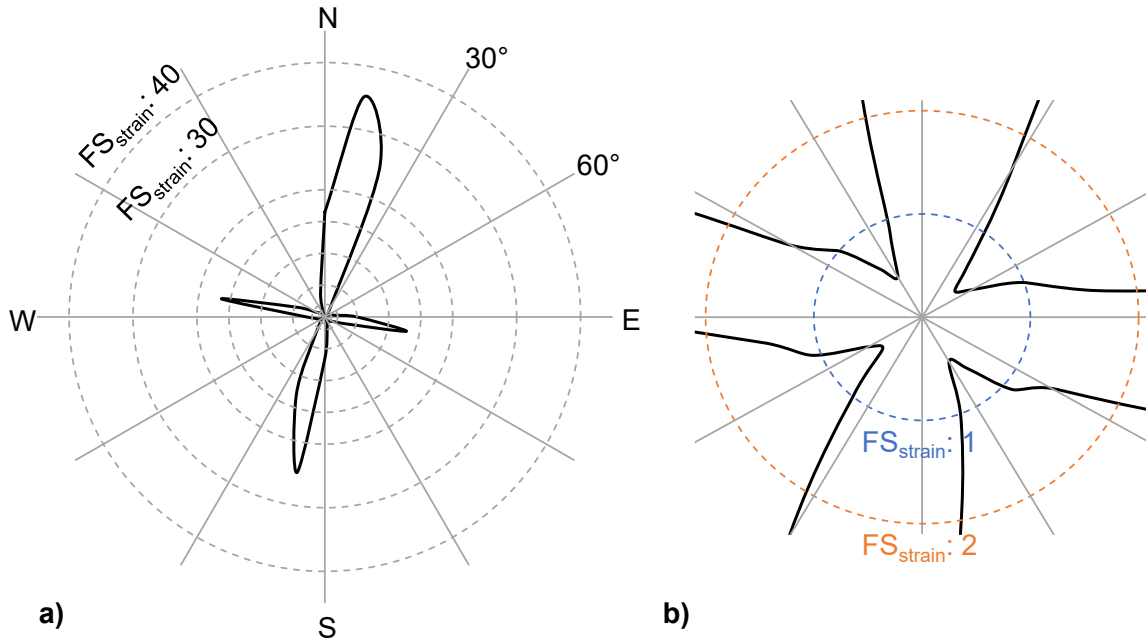


Figure 4-18 a) FS_{strain} distribution around the shaft boundary for 50 mm shotcrete liner; b) zoomed-in view of the centre of Figure 4-18a

It can be seen in Figure 4-18 that the FS_{strain} for 50 mm initial shotcrete liner ranges from less than unity to greater than 30. The sections of the liner with FS_{strain} less than one correspond to areas within the shotcrete liner where plastic yielding occurred (see Figure 4-12).

Assuming that Equation 4-1 can also be used to estimate the plastic strains of 75 mm and 100 mm shotcrete, the FS_{strain} was also calculated for these liner thicknesses. The distribution of strain factors of safety for 75 mm and 100 mm initial shotcrete liners around the shaft boundary are presented in Figure 4-19 (a-d). Using 75 mm shotcrete as the initial liner, some of the points along the boundary of the shaft have a FS_{strain} less than unity (Figure 4-19a & b). Note that a FS_{strain} less than 1 means rupture in the shotcrete. Therefore, the 75 mm thick shotcrete should not be used as an initial liner. As can be seen in Figure 4-19c and d, by increasing the thickness of the initial shotcrete to 100 mm, all the points around the shaft boundary have a FS_{strain} greater than unity with the lowest value being 1.07. Therefore, it is concluded based on the results of this analysis that the

100 mm shotcrete liner will remain stable and therefore can be used as a temporary support until the final concrete liner is installed.

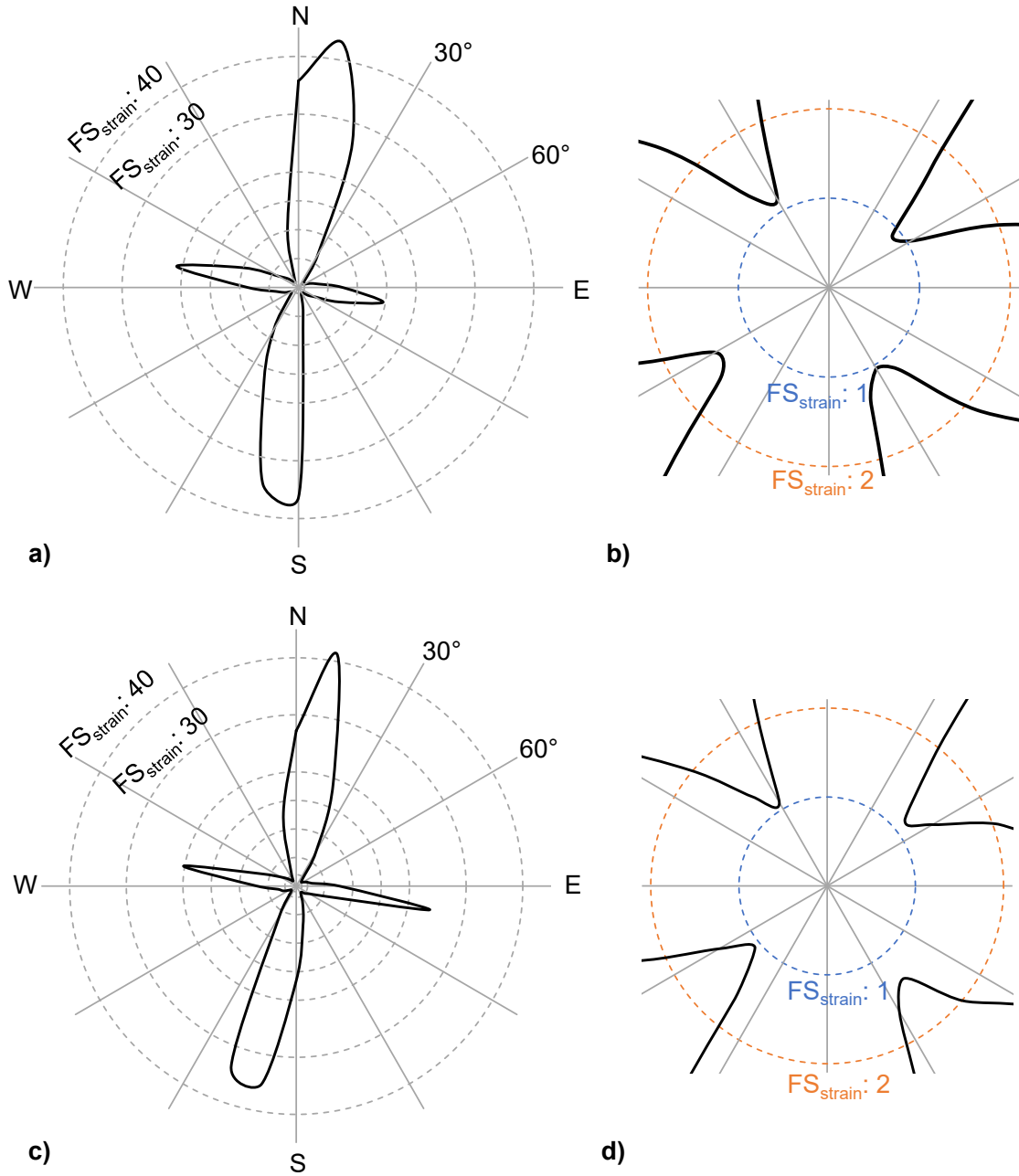


Figure 4-19 FS_{strain} distribution around the shaft boundary for: a) 75 mm shotcrete liner; b) zoomed-in view of the centre of Figure 4-19a; c) 100 mm shotcrete liner; and d) zoomed-in view of the centre of Figure 4-19c

4.5. Stability Analysis of Final Concrete Lining

As indicated in Chapter 3, the initial shotcrete liner and the final concrete liner were the two components of the support system used in the mine shaft. In this section, the stability analysis of the full support system consisting of both shotcrete and concrete liners is conducted in one model by simulating the initial shotcrete liner using a material model and the final concrete liner using the structural element. Note that the shotcrete and concrete liners were activated (installed) at different excavation stages by respecting their distances from the shaft face using the *GRC* and the *LDP*, following the procedure described in Chapter 2.

Figure 4-20 shows the *GRC* of the shaft showing the wall radial displacements corresponding to the location of the shaft face, the blasts, and the extensometer and the shotcrete and concrete lining installation stages. Further information about the internal pressures corresponding to these stages in the RS2 model is provided in Table 4-2.

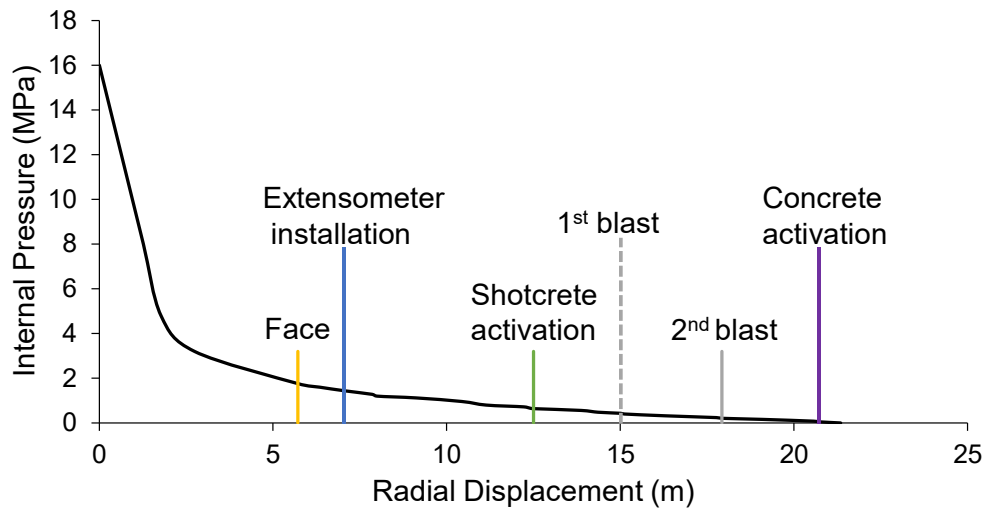


Figure 4-20 GRC showing the radial displacements corresponding to the excavation face, blasts, extensometer and liner installation stages

Table 4-2 RS2 stages and corresponding internal pressures

Stage #	P_i/P_0	Comment
1	1	
2	0.9	
3	0.7	
4	0.5	
5	0.3	
6	0.2	
7	0.11	Excavation Face
8	0.1	
9	0.09	
10	0.08	
11	0.075	Extensometer installation
12	0.07	
13	0.06	
14	0.05	
15	0.045	
16	0.041	
17	0.04	Shotcrete activation
18	0.035	
19	0.03	
20	0.027	1 st round of blast
21	0.025	
22	0.02	
23	0.015	
24	0.013	2 nd round of blast
25	0.01	
26	0.005	
27	0.003	
28	0.0029	Concrete activation
29	0	

The geometry of the RS2 model of the shaft with the full support system including the 100 mm initial shotcrete liner simulated using a material model and the 200 mm final concrete liner simulated using a structural element is shown in Figure 4-21. Note that the initial shotcrete liner is activated at stage 17, which corresponds to a distance of 3 m from the face, and the final concrete liner is activated at stage 28, which corresponds to a distance of 12 m from the face.

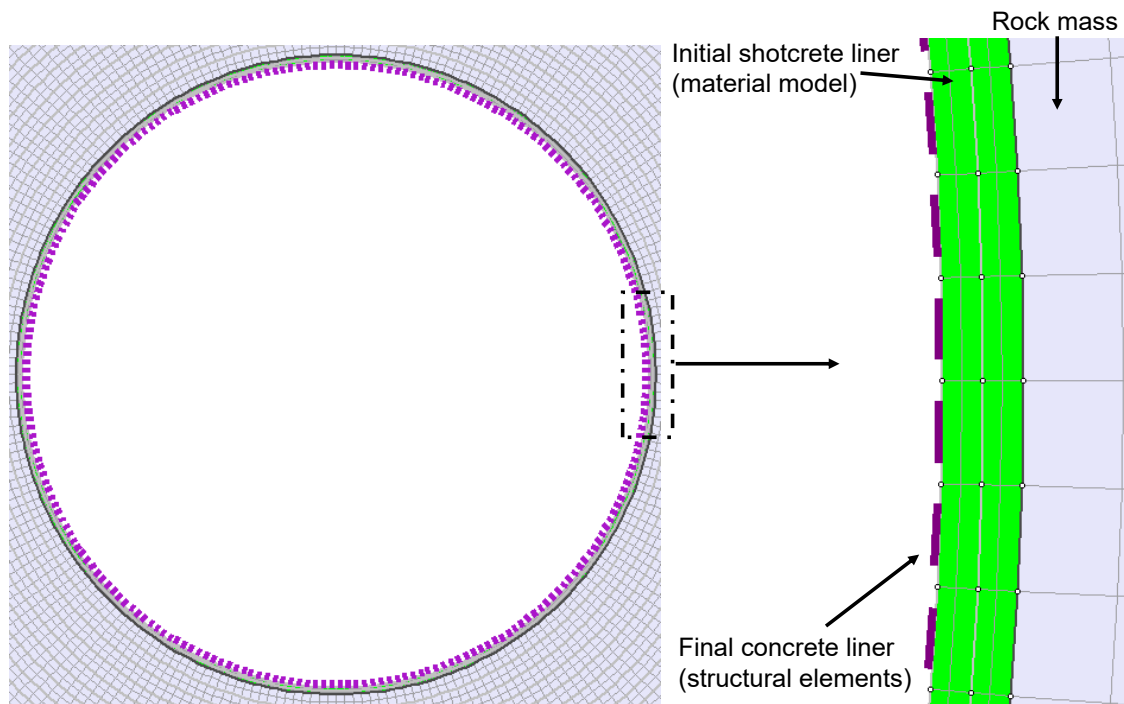


Figure 4-21 RS2 model showing the 100 mm initial shotcrete liner simulated using a material model and the final concrete liner simulated using a structural element

In the RS2 model shown in Figure 4-21, the shotcrete properties are the same as those used in Chapter 3, which corresponds to the properties of 12-hr shotcrete. Furthermore, the concrete properties are based on the Shütz (2010) for the 28-day concrete (Table 4-3). The thickness of the concrete liner is not known to the author. Therefore, a typical liner thickness of 200 mm was assumed in the numerical simulations. Note that the initial shotcrete liner was assumed to behave in an elasto-plastic manner while the final concrete liner was assigned elastic properties.

Table 4-3 Properties of final concrete liner used in the numerical model (Shütz, 2010)

Properties	Concrete liner
Young's modulus	30 GPa
Compressive strength	40 MPa
Tensile strength	3 MPa
Poisson's ratio	0.15
Thickness	200 mm

The support capacity diagram for the 200 mm final concrete lining attached to the initial shotcrete lining with a thickness of 100 mm is provided in Figure 4-22. The reason for using 100 mm shotcrete liner is due to its FS_{strain} . In the previous section, the FS_{strain} for 50 mm and 75 mm shotcrete liners were found to be less than unity for some points around the shaft boundary, whereas the FS_{strain} for 100 mm shotcrete liner were found to be greater than unity.

Figure 4-22 shows that the thrust-moment values for all the segments of the concrete liner fall well within the capacity envelopes, displaying factors of safety greater than 5. This is because the final concrete lining is installed after most of the ground convergence has taken place, which means that much less load is transferred to the final lining from the ground compared to that of initial lining.

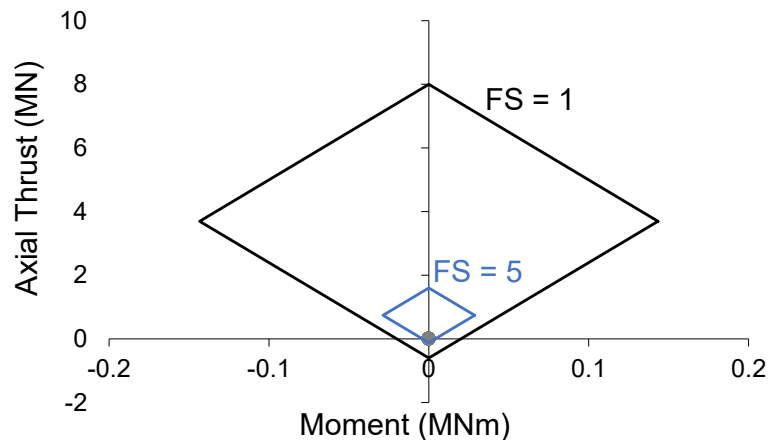


Figure 4-22 Thrust-moment diagram for the final 200 mm concrete liner attached to the initial shotcrete liner with a thickness of 100 mm

In chapters 3 and 4, the *IPR* method was used to simulate the shaft advance in RS2. In the next chapter, the *CS* method will be used to simulate the shaft advance and assess the stability of the initial shotcrete lining in Irazu (Geomechanica, 2018), which is a numerical program based on the hybrid finite-discrete element method.

4.6. Summary

In this chapter, a material model was used to explicitly simulate the shotcrete liner and to capture its progressive yielding process during the shaft excavation advance. Due to the limitation of using the radial mesh with an additional material model in RS2, a 4-noded quadrilateral uniform mesh was used and modified such that its mesh geometry near the excavation boundary became the same as that of the model constructed using the radial mesh. A full comparison between the results of the two models in terms of the shape and extent of the plastic zone, the *GRC* and the rock mass deformation demonstrated that the model with the modified uniform mesh is comparable to that constructed using the radial mesh.

The shotcrete liner was simulated with elastic and elasto-plastic material properties. In the model with elastic shotcrete, the location and extent of the sections of shotcrete liner with strength factors less than unity were found to be similar to those of the overloaded sections of the structural element representing the shotcrete liner. The model with elasto-plastic shotcrete properties provided further insight into the progressive yielding process of the shotcrete liner during the excavation advance. Next, the lateral strain of the shotcrete obtained from the results of the RS2 model was used to calculate the strain factor of safety for the initial liner. It was found that the strain factor of safety for shotcrete lining with a thickness of 100 mm was above unity.

In the last part of this chapter, the full support system consisting of the initial shotcrete lining and the final concrete lining was simulated in a single RS2 model. For this purpose, the 100 mm initial shotcrete liner and the final concrete liner were simulated using a

material model and the structural element, respectively. The analysis of the support capacity diagram for the 200 mm final concrete liner indicated that this support element can be used along with the 100 mm initial shotcrete lining for the shaft.

In the next chapter, the initial shotcrete and final concrete liners will be simulated as a material model in Irazu (Geomechanica, 2019), which is a numerical program based on the hybrid finite-discrete element method. The primary objective of this chapter is to explicitly simulate fracture initiation and propagation in shotcrete linings of various thicknesses and to investigate whether they can be used as a temporary support element until the final, permanent support element (concrete liner) is installed. The simulation of the rock mass and the liners using this numerical method requires excessive model calibration, which will be discussed in detail in the following pages.

Chapter 5 Stability Assessment of Initial Shotcrete Lining Using Hybrid Finite-Discrete Element Method

5.1. Introduction

The progressive failure of rock-like materials under different loading conditions, including crack/fracture initiation and propagation is a complex process. One of the main reasons for this complexity is the heterogeneous nature of rocks at different scales. Different numerical methods can be used to simulate the failure process of rock-like materials. These methods help better understand the mechanisms involved in and factors influencing the pre-peak fracturing stages of rock-like materials under different loading conditions at different scales (e.g. laboratory-specimen and field).

In Chapter 4, the yielding processes of the shotcrete liner during shaft excavation advance was captured using a continuum numerical method. In this method, the initiation of the cracks and their propagations cannot be explicitly captured. The discrete element method is a tool that can be used to simulate such processes explicitly. For this purpose, the hybrid finite-discrete element method (*FDEM*) is used in this chapter to gain better insights into the fracturing processes leading to the failure of initial shotcrete lining during the excavation advance and to determine the minimum shotcrete lining thickness required to support the shaft wall until the final concrete liner is installed.

In this chapter, the theory behind the *FDEM* is first introduced. Then, the shotcrete liner model is calibrated through simulating the *UCS* and Brazilian tensile tests and comparing the simulation results with those of laboratory tests. A series of sensitivity analyses are conducted to better understand the influence of different *FDEM* input parameters on the simulation results. Next, the model of the rock mass around the shaft is calibrated against the extensometer measurement data. In this process, the 3D excavation advance is simulated using the *CS* approach, and the stability of the initial shotcrete and the final

concrete liners are investigated. It is demonstrated in this chapter that the *FDEM* provides a much better insight into the fracturing processes of the shotcrete liner in response to the excavation advance compared to the finite element method (*FEM*).

5.2. Finite-Discrete Element Method (FDEM)

The failure process of brittle rocks under compression is characterized by complex micro-mechanical fracturing processes, including micro-crack initiation, propagation, and coalescence, which could lead to strain localization in the form of macroscopic fractures (Lockner et al. 1991; Martin and Chandler, 1994). Such a complex failure process is a result of different forms of grain-scale heterogeneities in rocks, including grain geometric heterogeneities (i.e. different shapes and sizes of grains) and grain property heterogeneities (e.g. different mineral grains of various stiffnesses and strengths) (Lan et al., 2010). The evolution of micro-cracks results in a non-linear stress-strain behavior. The post-peak response is often brittle (i.e. sudden stress drop following the peak stress) under an unconfined condition, then becomes strain-softening at low confinement, and exhibits an elasto-plastic behavior at high confining pressures.

The failure process of brittle rocks, as briefly described above, can be realistically simulated using discontinuum numerical methods, such as the discrete element method and the hybrid finite-discrete element method (Lisjak and Grasselli, 2014). In the discrete element method (*DEM*), a rock medium is simulated as an assembly of separate blocks. According to Cundall and Hart (1992), in these methods, finite displacements, detachment, and rotations of blocks are captured, and the detached bodies recognize new contacts throughout the simulation. By combining the continuum and discontinuum methods in a single model, a hybrid method is created. In this method, the simulation initiates with a continuum representation of the medium. New discrete bodies are formed throughout the medium as a result of fracturing, once the fracture criterion is satisfied. Therefore, the *FDEM* is a combination of the *FEM* and the *DEM* (Barla and Beer, 2012).

ELFEN (by Rockfield) and Irazu (by Geomechanica) are the programs utilizing the *FDEM* for simulating the failure processes of brittle rocks. In this chapter, Irazu (by Geomechanica) is used to simulate the shaft excavation advance and analyse the stability of the support system, including the initial shotcrete and final concrete linings.

The *FDEM* allows for the dynamic simulation of multiple interacting bodies. The simulation initiates with a single intact domain or an assembly of discrete intact bodies (Munjiza et al., 1995). The interacting bodies deform elastically while the simulation is in progress. The bodies translate, rotate, interact with each other, and form cracks if the fracture criterion is satisfied. New discrete bodies are formed following the formation of cracks. The new bodies can then undergo further movement, interaction, deformation, and fracture. Therefore, the *FDEM* employs the principles of both the *FEM* and the *DEM*. The *FEM* is used to assess the deformation and evaluate the failure criterion for fracturing, and the *DEM* is used to detect contacts and deal with translation, rotation, and interaction of discrete bodies (Irazu 2D theory manual, 2019). The medium in the *FDEM* approach is discretized into a mesh comprised of three-noded triangular elements, which are elastic elements bonded to each other through four-noded quadrilateral elements which are used to explicitly simulate cracks (called crack elements) (Figure 5-1).

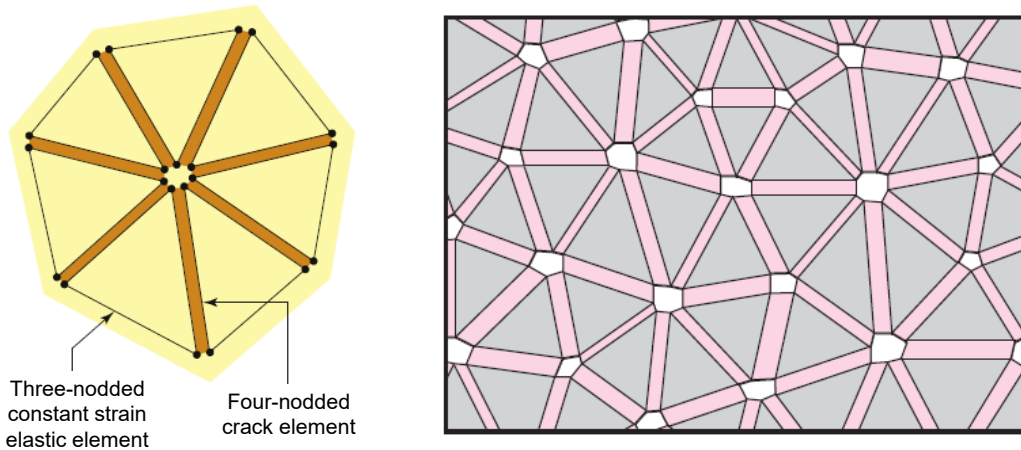


Figure 5-1 View of four-noded crack elements located along edges of all adjoining triangular finite elements (after Lisjak and Grasselli, 2014; Lisjak, 2013)

Figure 5-2a shows a conceptual model of tensile fracturing in a heterogeneous medium consisting of an intact part with micro-scale heterogeneities, the Fracture Process Zone (*FPZ*), and a tension crack. The *FPZ* is a zone in which the material behavior is non-linear and appears at the tip of a crack due to high stress concentration (Labuz et al., 1985; Lisjak, 2013). Figure 5-2b is the representation of this conceptual model in *FDEM*, demonstrating how the three-noded triangular and the four-noded crack elements interact to capture the tension crack and the *FPZ*.

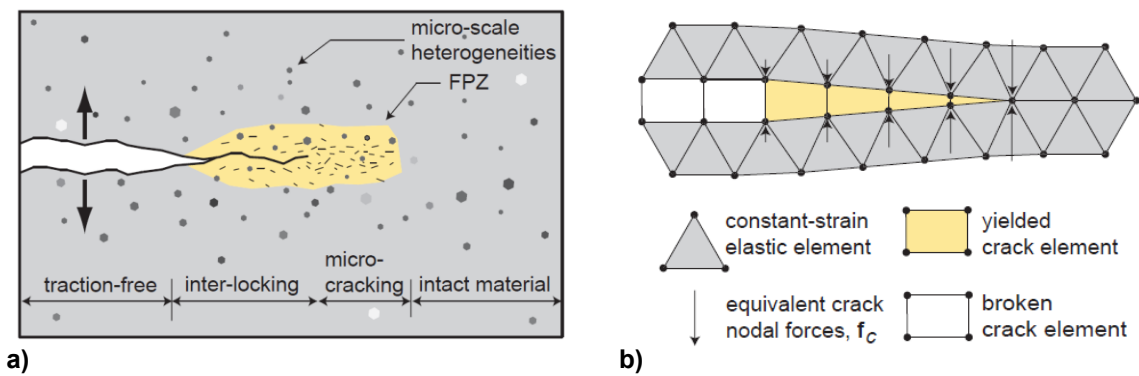


Figure 5-2 a) Conceptual model of a tensile crack in a heterogeneous brittle rock and the fracture process zone (*FPZ*); and b) theoretical *FPZ* model in *FDEM* (after Lisjak, 2013)

As described earlier and shown in Figure 5-1 and Figure 5-2b, the medium in the *FDEM* consists of four-noded crack elements embedded between the edges of the triangular elements. As the simulation progresses, the remeshing would not be allowed. Arbitrary fractures can be propagated through the constraints of the initial mesh topology (Lisjak, 2013). Fractures appear once the crack elements are broken. Figure 5-3 illustrates the simulation process in Irazu. As shown in this flowchart, first, the contact between three-noded elements are recognized, then the forces in response to the deformation and fracture propagation are determined. Following this step, new nodal coordinates are set.

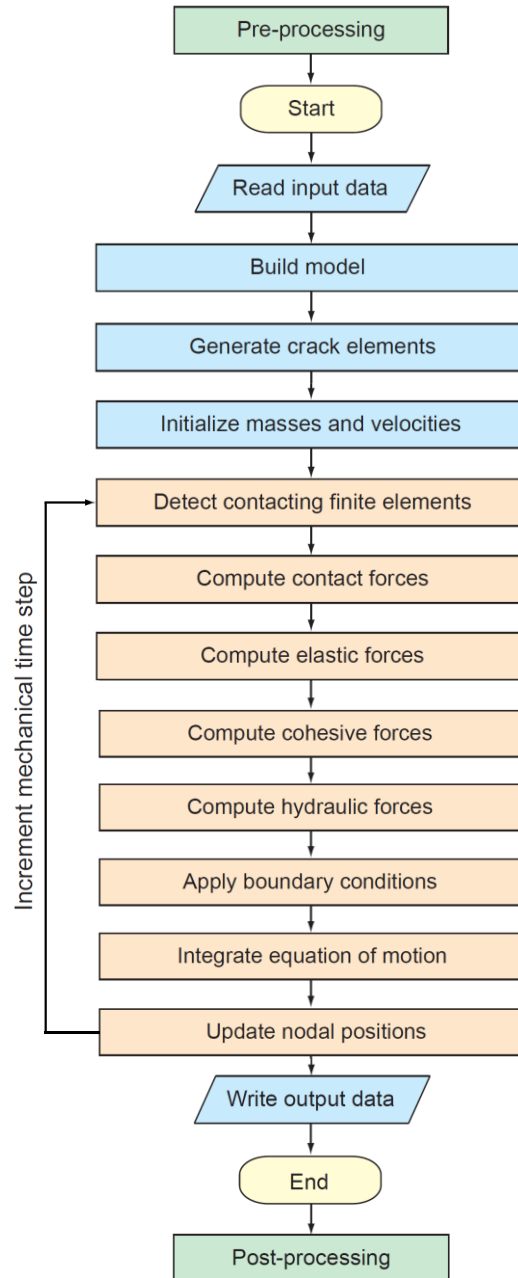


Figure 5-3 FDEM simulation process in Irazu (after Irazu 2D theory manual, 2019)

Figure 5-4 illustrates the constitutive behavior of the crack elements. In this figure, the normal and tangential bonding stresses, σ and τ , between the triangular elements are shown as a function of the fracture relative displacement in normal and tangential directions. Note that o represents the crack opening, and s is a short form of the crack sliding.

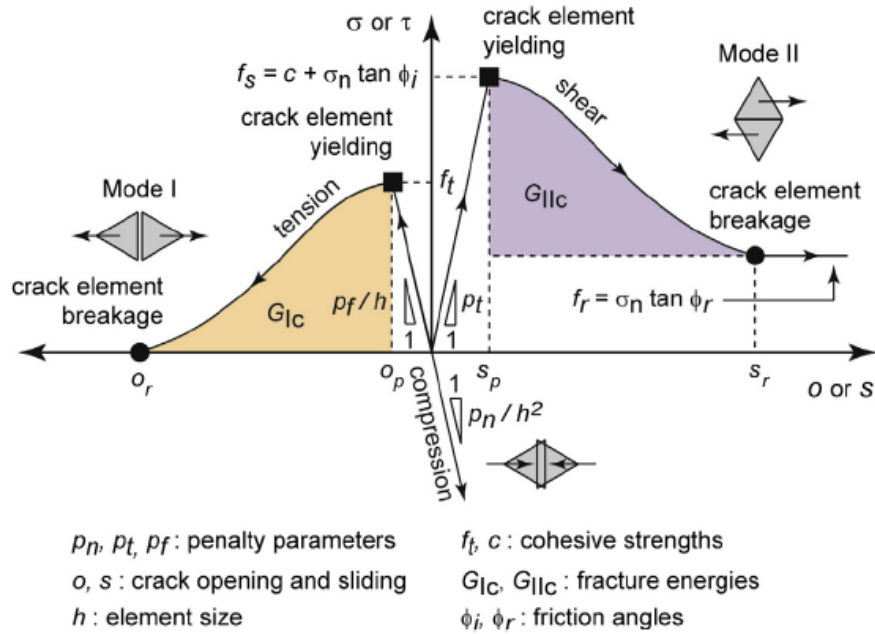


Figure 5-4 Constitutive behaviour for crack elements in Irazu described in terms of normal and tangential bonding stresses, σ and τ , versus relative displacements, opening (o) and sliding (s) (after Lisjak et al., 2014)

According to Figure 5-4, the simulated rock medium can be loaded elastically, under shear or tensile stresses. Considering the tensile stress as the effective load (i.e. mode I) on the crack elements, the crack element begins to yield when the opening displacement reaches a critical value, O_p , corresponding to the intrinsic tensile strength, f_t . The post-peak behavior is a function of the fracture energy discharge rate. The fracture energy is the consumed energy per unit crack length within the crack edges when fracturing occurs under tension (G_{Ic}) or shear (G_{IIc}) throughout the medium. With increasing displacement, the normal bonding stress gradually decreases until the ultimate detachment results at the point exceeding a residual opening value, O_r .

In a similar manner to mode I, the response of the crack elements in shear mode (i.e. mode II) is controlled by the peak shear strength and the fracture energy. The intrinsic shear strength (f_s) can be determined using the *MC* failure criterion.

$$f_s = c + \sigma_n \tan \varphi \quad \text{Equation 5-1}$$

Following the breakage of the crack element due to shear stress, the three-noded triangular elements are free to interact. The only governing rule on their interaction is a frictional resistance based on the fracture friction angle, φ . This residual frictional resistance can be determined using the following equation:

$$f_r = \sigma_n \tan \varphi \quad \text{Equation 5-2}$$

As shown in Figure 5-4, three penalty parameters, including the normal, tangential, and fracture penalty parameters (ρ_n , ρ_t , and ρ_f) control the deformation of crack elements under compressive, shear, and tensile loading conditions (Lisjak et al., 2014). To summarize, three broad classes of material parameters assigned to an *FDEM* model required for calibration are:

- Bulk parameters for the elastic triangular elements: Young's Modulus (E), Poisson's ratio (ν), and bulk density (ρ);
- Penalty parameters governing the elastic deformation of contacting elements: normal penalty (ρ_n), tangential penalty (ρ_t), and fracture penalty (ρ_f); and
- Strength parameters determining the fracture initiation and propagation: crack element tensile strength (f_t), cohesion (c), friction angle (φ), and fracture energy parameters (i.e. G_{Ic} for Mode I, and G_{IIc} for Mode II).

5.3. Laboratory Tests on Fiber Reinforced Shotcrete by Saw et al. (2009)

The calibration of the shotcrete model in Irazu, which will be described in the next section, is based on the results of laboratory tests reported by Saw et al. (2009), who conducted

unconfined compression and Brazilian tensile tests on steel fiber reinforced shotcrete. The following section provides a summary of the laboratory tests by Saw et al. (2009).

5.3.1. Mix Design and Curing Time for Shotcrete Specimens

The fiber reinforced shotcrete mixture used by Saw et al. (2009) was similar to that used at an underground gold mine in the Eastern Gold Fields region in Kalgoorlie, Western Australia. The mix design for the shotcrete is provided in Table 5-1. The shotcrete samples (cores) were obtained from shotcrete panels sprayed at the mine site and then stored in a curing chamber with a temperature of 30° and a humidity of 90%. Saw et al. (2009) chose four different curing periods, including 1, 3, 7, and 28 days for the laboratory tests.

Table 5-1 Mix design of the fiber reinforced shotcrete sample used in laboratory tests by Saw et al. (2009)

Material	Quantity for 1 m³ shotcrete mixture
Cement	400 kg
Coarse aggregate (7-10 mm)	220 kg
Crusher dust	1300 kg
Sand	1640 kg
Water	150 L
Steel fibres	30 kg
Liquid Meyco (MS 685)	11 L
Delvo Stabiliser	5 L
Rheobuild 1000	8 L
Pozzolith 322Ni	1.3 L
Accelerator	4% of cement

5.3.2. Methods of Axial Strain Measurements

Saw et al. (2009) used two different methods to measure the axial strain in the unconfined and confined tests. A comparison between the stress-strain curves measured using the strain gauges attached to the specimen (dashed lines) and those measured using the

relative axial displacement of the top and bottom platens (solid lines) under different confining pressures is presented in Figure 5-5.

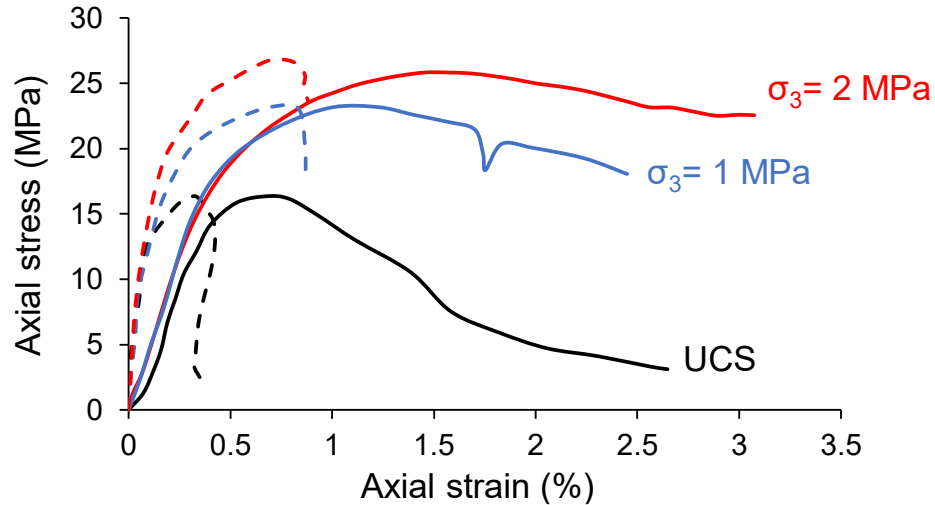


Figure 5-5 Stress-strain curves of shotcrete specimens under different confining pressures. Dashed lines represent the results obtained from the strain gauges and solid lines are those obtained from the displacement of the top and bottom platens (after Saw et al., 2009)

It can be seen in Figure 5-5 that the strains measured based on the relative displacement of the two platens results in a more ductile response than those obtained using the strain gauges. It is known that young shotcrete behaves in a ductile manner. Therefore, the stress-strain curves with the strains measured using the relative displacement of the top and bottom platens are believed to be more realistic. However, since the lateral strains for the shotcrete specimens were measured using the strain gauges, the stress-strain curves obtained from the strain gauges (in both axial and lateral directions) were used for the calibration of the Irazu models.

5.3.3. Uniaxial Compressive Test

Saw et al. (2009) used an Instron servo-controlled hydraulic testing machine with a loading rate of 0.12 mm/min for the UCS tests. They used two 10 mm long biaxial foil strain gauges to measure the axial and lateral strains. The strain gauges were installed diametrically at the mid-height of the shotcrete specimens, as shown in Figure 5-6. Based

on the length of the strain gauges in Figure 5-6, the width of the shotcrete specimens is estimated to be between 30 and 50 mm.

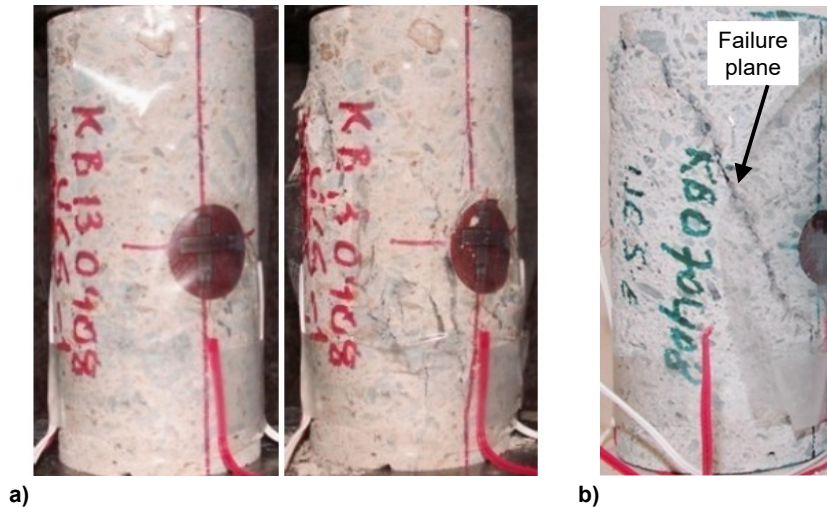
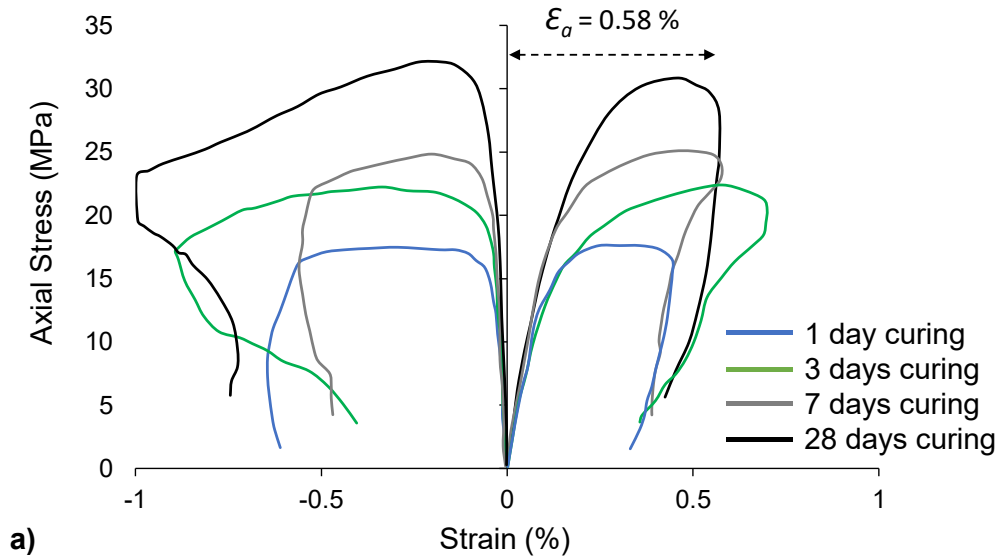


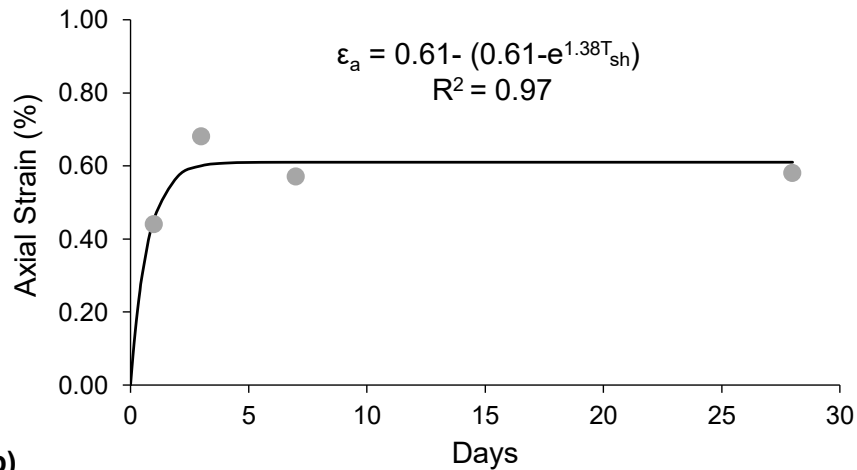
Figure 5-6 a) Shotcrete specimen before (left) and after (right) the UCS test (after Saw et al., 2009); b) failure mode of another shotcrete specimen under unconfined compression (after Saw et al., 2009)

As illustrated by Figure 5-6a, the shotcrete specimens failed in shear under an unconfined condition. Figure 5-6b shows another example of a failed specimen, suggesting that shearing is the primary mode of failure for the fiber reinforced shotcrete specimen under an unconfined condition.

As indicated earlier in this section, the results of laboratory tests on shotcrete reported by Saw et al. (2009), in terms of the mechanical properties and the failure mode will be used for model calibration. The shotcrete liner studied in this research is assumed to have an age of 12 hours. However, Saw et al. (2009) did not conduct any tests on 12-hr shotcrete. Therefore, based on the stress-strain curves of shotcrete with longer curing periods (i.e. 1, 3, 7, and 28 days) presented in Figure 5-7a, two empirical equations were derived to extrapolate the axial and lateral strains for the 12-hr shotcrete. The equation for estimating the lateral strain of 12-hr shotcrete was developed in Chapter 4 (Figure 4-16b and Equation 4-1). In this section, the equation for estimating the axial strain of 12-hr shotcrete is developed.



a)



b)

Figure 5-7 a) Stress-strain curves for shotcrete specimens with curing periods of 1, 3, 7, and 28 days (after Saw et al., 2009); b) empirical equation derived from the relationship between the axial strain and shotcrete age

In order to develop a relationship between the axial strain and shotcrete age, the axial strains were determined from the stress-strain curves for different shotcrete ages. The axial strain is measured from the beginning of the test until a point where the stress drop is observed. For example, the axial strain for 28-day shotcrete is determined to be 0.58%, as illustrated in Figure 5-7a. Figure 5-7b shows the relationship between the axial strain and the shotcrete age obtained from the stress-strain curves presented in Figure 5-7a. The following exponential function was used to fit to the data points in Figure 5-7b:

$$\varepsilon_a = 0.61 - (0.61 - e^{1.38T_{sh}})$$

Equation 5-3

Here, ε_a is the axial strain for the shotcrete specimen based on its age T_{sh} (in days). Equation 5-3 will be used in Section 5.4 to estimate the axial strain of the 12-hr shotcrete required for the calibration of the Irazu model.

5.3.4. Brazilian Tensile Test

Saw et al. (2009) also conducted the Brazilian tensile test on shotcrete samples. The Avery universal testing machine was used to apply and monitor load and the corresponding displacement. Figure 5-8 presents the failure mode of a shotcrete specimen following the Brazilian tensile test.



Figure 5-8 Shotcrete specimen after Brazilian test (after Saw et al., 2009)

5.4. Calibration of Laboratory-scale Model of Shotcrete

In Chapter 3 and Chapter 4, the shaft advance was simulated, and the stability of the shotcrete liner was assessed in RS2, which is a numerical program based on the finite element method (*FEM*). In this method, the rock mass was assumed to be homogeneous and its properties were calibrated against the extensometer measurement data. The shotcrete properties such as the *UCS* and the Young's modulus were estimated using the

empirical equations reviewed in Chapter 2 and directly assigned to the liner simulated using a structural element in Chapter 3 and a material model in Chapter 4. In the numerical simulations of rock-like materials using the continuum methods, where the materials are assumed to be homogeneous (e.g. rock mass and shotcrete liner in this research), the macro-properties including the *UCS* and Young's modulus are the model input parameters. However, in the *FDEM*, where the material is assumed to be heterogeneous, the micro-properties including those of the triangular elements (e.g. Poisson's ratio, Young's modulus, etc.) and the crack elements (e.g. penalty parameters, fracture energies, friction coefficient, etc.) are the model input parameters. In this method, the micro-properties are adjusted until the target macro-properties (e.g. *UCS* and Young's modulus) are obtained. This process is called model 'calibration'.

In this chapter, the rock mass model is calibrated against the extensometer measurement data obtained from Rafiei Renani et al. (2016), and the shotcrete model is calibrated by simulating the *UCS* and Brazilian tensile tests. In the *UCS* test simulation, the calibration of the Irazu model of shotcrete is based on the macro-properties of the 12-hr shotcrete obtained from empirical equations reviewed in Chapter 2 (e.g. *UCS* and Young's modulus) as well as the axial and lateral strains estimated from Equation 4-1 and Equation 5-3. In the Brazilian tensile test simulation, the Irazu model is calibrated against the Brazilian tensile strength of the 12-hr shotcrete estimated from the empirical equations reviewed in Chapter 2. In the following sections, the procedure for calibrating the Irazu models to the laboratory properties of 12-hr shotcrete is described.

5.4.1. Calibration Procedure

First, a *UCS* sample is created in Irazu and calibrated to the properties of 12-hr shotcrete, including the *UCS*, the Poisson's ratio, the Young's modulus as well as the axial and lateral strains. Then, the Brazilian tensile test is simulated, and the model is calibrated to the Brazilian tensile strength of the 12-hr shotcrete. The calibrated models are used to better

understand the progressive fracturing processes of the shotcrete in both tests. The simulated failure modes are also compared with those observed in the laboratory tests by Saw et al. (2009).

It is worth noting that since the results of *FDEM* simulations are sensitive to the size of mesh elements, a two-step calibration process is adopted for the shotcrete model. In the first step, model calibration is carried out using a specimen meshed with small elements. In the next step, the shotcrete model is re-built with coarse mesh elements and re-calibrated to the properties of 12-hr shotcrete by adjusting the micro-properties obtained from the first calibration step. The reason for this second calibration step is to improve the computation efficiency of the shaft model supported with the shotcrete liner by reducing the number of mesh elements in the shotcrete liner. This will be explained in detail in Section 5.6. Table 5-2 provides a summary of the laboratory properties of the 12-hr shotcrete obtained from various sources and used to calibrate the shotcrete model. It is worth noting that the lateral and axial strains shown in Table 5-2 are the total strain (i.e. elastic and plastic) of the shotcrete before the specimen fails.

Table 5-2 Properties of 12-hr shotcrete used to calibrate the shotcrete model in Irazu

Parameters	Values	Reference
UCS (MPa)	13.2	Chang (1994)
Young's modulus (GPa)	12	Chang (1994)/ Schubert (1988)
Poisson's ratio	0.25	Carranza-Torres and Fairhurst (2000)
Tensile strength (MPa)	1.36	Byfors (1980)
Total* axial strain (%)	0.3	Saw et al. (2009)
Total* lateral strain (%)	0.54	Saw et al. (2009)

* Total axial/lateral strain is the strain of the shotcrete specimen under uniaxial loading measured from the beginning of the test until the failure occurs.

5.4.2. Simulation of UCS Test Using FDEM Model with Fine Mesh

Figure 5-9 shows the numerical specimen constructed in Irazu to simulate the *UCS* test on 12-hr shotcrete. As shown in this figure, the length and width of the simulated shotcrete specimen is 104 mm and 52 mm, respectively. The two platens have a length and thickness of 56 mm and 4 mm, respectively. This model was meshed with triangular elements with an edge length of 2 mm, which resulted in a total of 3899 elements in the model. Note that the contact between the platens and the shotcrete specimen was assumed to be frictionless.

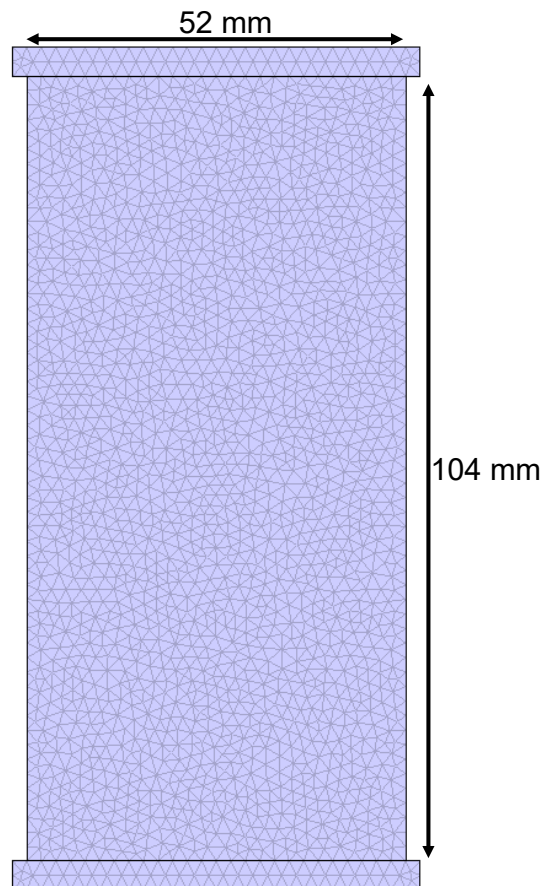


Figure 5-9 Irazu model constructed with fine mesh elements (i.e. edge length of 2 mm) and used to simulate *UCS* test on 12-hr shotcrete

The *UCS* test was simulated by applying a vertical velocity of 0.15 m/s to the elastic platens to maintain pseudo-static conditions during the test. The axial stress in

the *UCS* test was calculated by averaging the stresses of all the elements in the numerical specimen. The lateral strain was calculated from the relative horizontal displacements of two points on the two sides of the specimen at its mid-height. The axial strain was computed from the relative vertical displacements of the two platens. Once the stress-strain curves were obtained from the simulations, the macro-properties were determined and compared to the target shotcrete properties given in Table 5-2. If a match with one or more of the macro-properties could not be achieved, the shotcrete model would be re-calibrated by changing the micro-properties.

The results of the *UCS* test simulated on the calibrated shotcrete model, including the stress-strain curve and the failure mode are presented in Figure 5-10. Included in this figure is the target stress-strain curve constructed using the empirical equations derived for estimating the axial and lateral strains of 12-hr shotcrete (i.e. Equation 5-3 and Equation 4-1). The lower images in Figure 5-10 show the progressive failure of the calibrated shotcrete model at three stress levels: peak stress (A) and two other stress levels in the post-peak region (B and C). No visible crack can be identified at stress level A, whereas a few visible cracks initiate from the top right part of the specimen at stress level B. At stress level C, which is about 50% of the peak stress, two shear planes from the top right and top left parts of the specimen are developed.

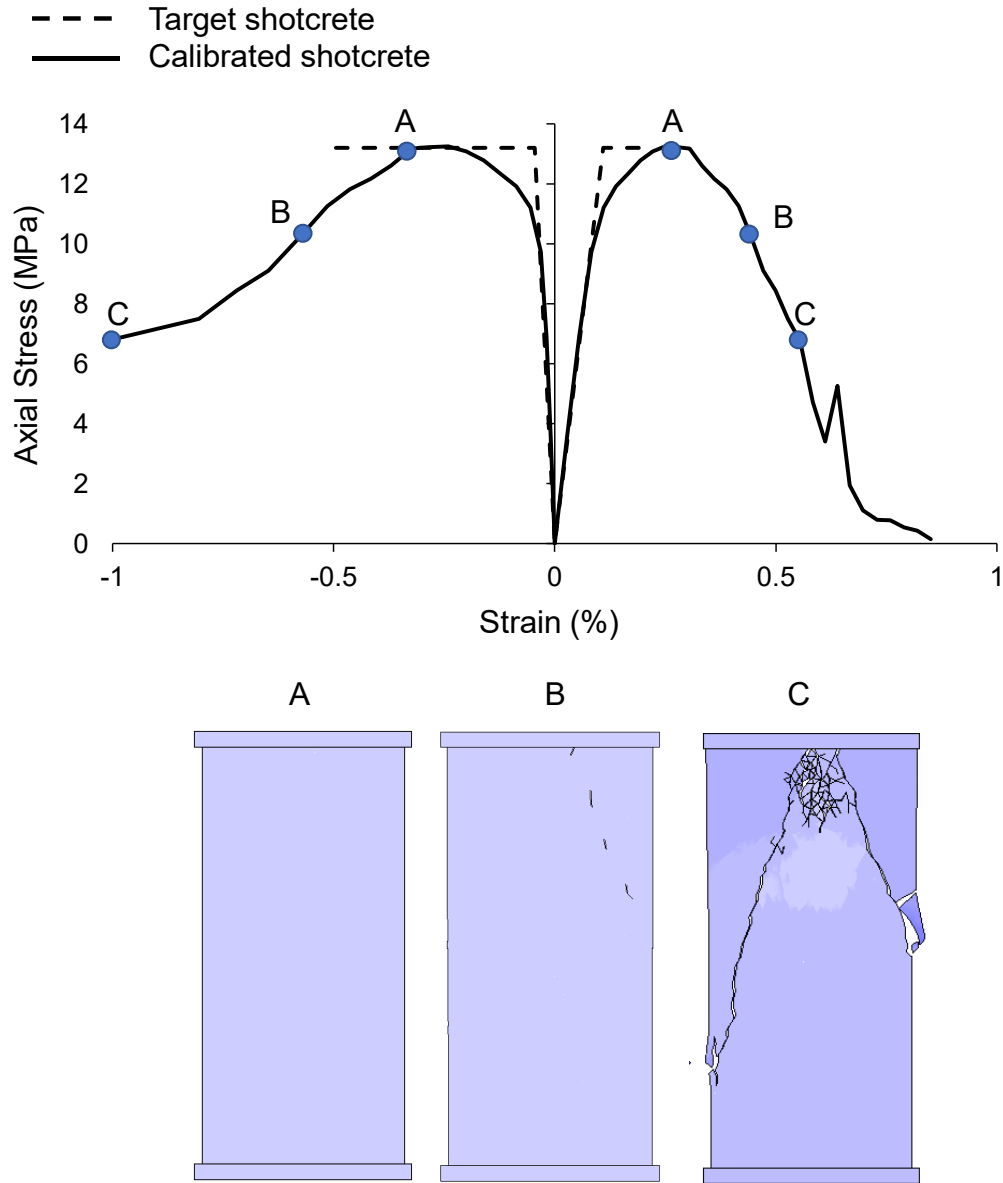


Figure 5-10 Stress-strain curve of the shotcrete model and its comparison with the target stress-strain curve. The lower images correspond to three stages of loading and show the progressive fracturing of shotcrete at peak and two stages in the post-peak region

Table 5-3 summarizes the micro-properties obtained from this calibration process, and Table 5-4 provides a comparison between the strength and deformation properties of the calibrated shotcrete model and the target values. Based on this comparison, it is concluded that the shotcrete model is reasonably calibrated to the strength and deformation properties of the 12-hr shotcrete.

Table 5-3 Micro-properties of the shotcrete model meshed with fine elements and calibrated to the laboratory properties of 12-hr shotcrete

Element Type	Parameter	Values
Crack element	Cohesion (MPa)	1.6
	Friction angle (°)	40
	Tensile strength (MPa)	0.7
	Mode I fracture energy ($\mu\text{N}/\text{mm}$)	50,000
	Mode II fracture energy ($\mu\text{N}/\text{mm}$)	400,000
	Fracture penalty (Pa)	1.2e+11 or (10 E)
	Normal penalty (Pa.mm)	1.2e+11 or (10 E)
	Tangential penalty (Pa/mm)	1.2e+11 or (10 E)
Triangular element	Young's modulus (GPa)	12
	Poisson's ratio	0.25
	Density (Kg/m^3)	2,500

Table 5-4 Comparison between macro-properties of calibrated shotcrete model meshed with fine elements and target values

Macro-parameters	Values	
	Target shotcrete	Calibrated shotcrete model
UCS (MPa)	13.2	13.2
Young's modulus (GPa)	12	12
Poisson's ratio	0.25	0.27

5.4.3. Influence of Platen-Specimen Contact Friction and Gravity

As can be seen in Figure 5-10, the post-peak response of the calibrated shotcrete model is strain-softening and does not follow the behavior expected for the 12-hr shotcrete shown by the dashed lines (i.e. sudden stress drop after some amount of plastic deformation in both axial and lateral directions). It was found during the calibration

process that obtaining a realistic post-peak response is challenging, especially the strain in the lateral direction due to the excessive lateral displacement of the model during uniaxial loading. Similar issues have been reported by other researchers who used Irazu and other distinct element programs such as PFC (by Itasca). For example, Figure 5-11 shows the stress-strain curve of an Irazu model calibrated to the strength and deformation properties of Lac du Bonnet granite under an unconfined condition by Vazaios et al. (2019). It can be seen in this figure that a realistic stress drop could not be captured in the lateral direction. Vazaios et al. (2019) noted that the lateral displacement in the numerical simulations was the result of excessive fracturing and deformation.

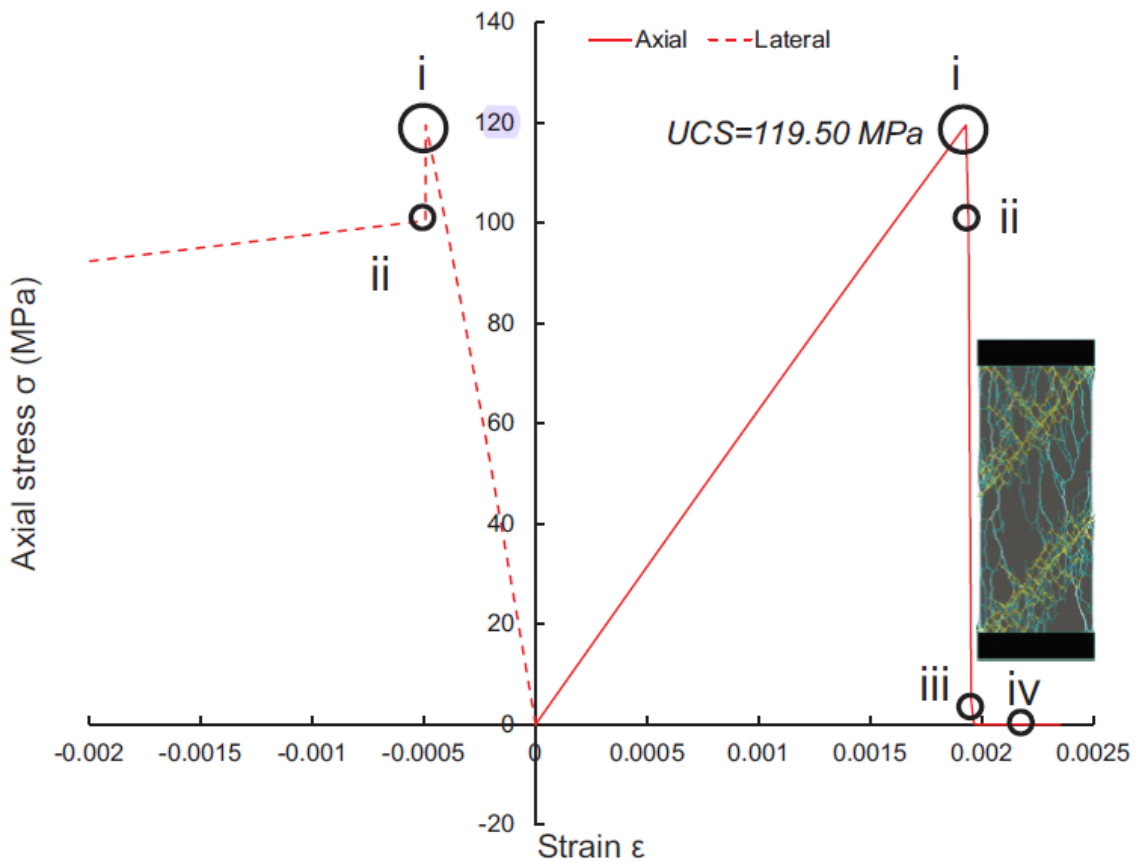


Figure 5-11 Stress-strain curve of an Irazu model calibrated to the strength and elastic modulus of Lac du Bonnet granite under unconfined condition (after Vazaios et al., 2019)

Another example is presented in Figure 5-12, which shows the stress-strain response of a PFC model calibrated to the strength and elastic modulus of Lac du Bonnet granite by Cho

et al. (2007). In this figure, the calibrated PFC model exhibits a strain softening behavior in the axial direction and plastic behavior in the lateral direction. The post-peak response of Lac du Bonnet granite is brittle in the axial direction. In the lateral direction, the stress drop occurs only after a small amount of lateral strain (i.e. < 1% lateral strain).

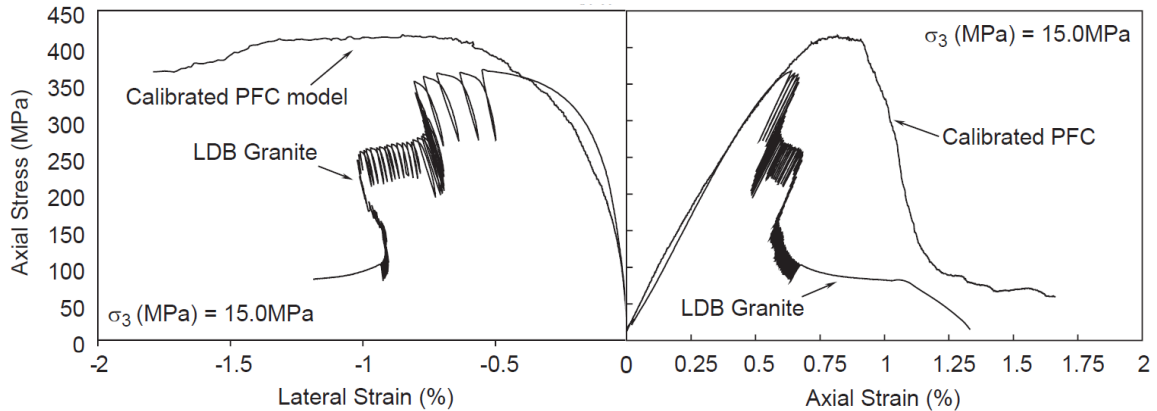
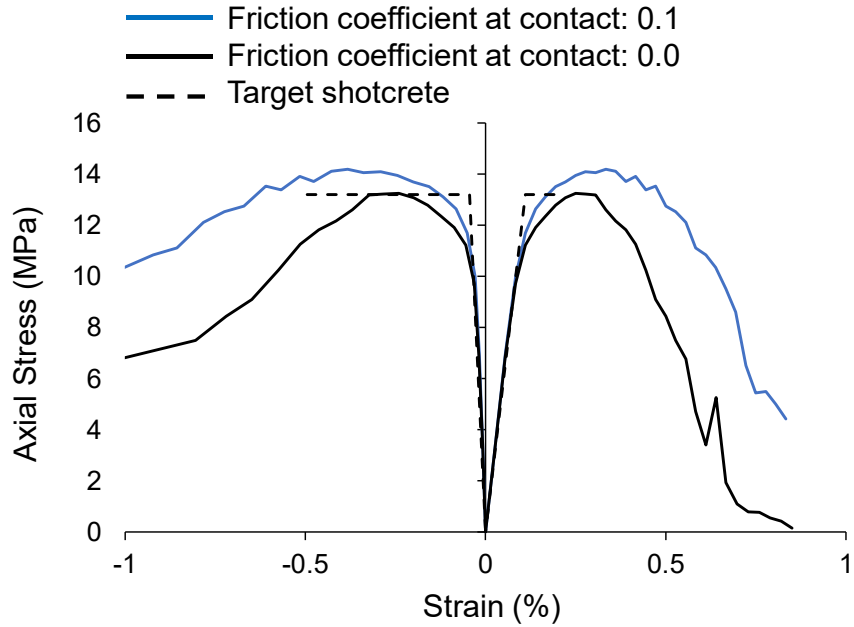


Figure 5-12 Stress-strain curve of a PFC model calibrated to the strength and elastic modulus of Lac du Bonnet granite under unconfined condition (after Cho et al., 2007)

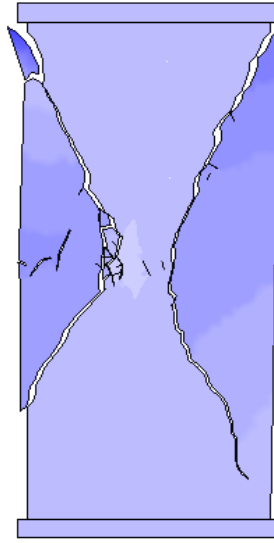
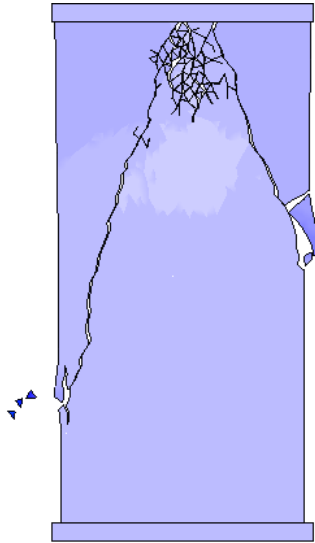
Further numerical simulations were conducted to investigate the influence of contact friction between the platens and the shotcrete specimen as well as gravity on the results of UCS test including the post-peak response. In the previous simulations, the contact between the platens and the shotcrete specimen was assumed to be frictionless. This is the norm in the numerical simulations. However, there still exists some small amount of friction between the platens and the rock in the laboratory tests even after careful preparation of the specimen. Therefore, another simulation was conducted on the calibrated model of the 12-hr shotcrete by using a platen-shotcrete contact friction coefficient of 0.1 (equivalent to a friction angle of 6°). A comparison between the stress-strain curves and the failure modes of the two simulations are presented in Figure 5-13.



a)

Platen-specimen contact
friction coefficient: 0.0

Platen-specimen contact
friction coefficient: 0.1



b)

c)

Figure 5-13 a) Stress-strain curves of the simulated shotcrete specimen with and without friction at the contact between the platens and the specimen and their comparisons with the target stress-strain curve. Failure modes of shotcrete models with platen-shotcrete friction coefficients of: b) 0.0; and c) 0.1

The results presented in Figure 5-13a indicate that the contact friction between the platens and the shotcrete specimen does not influence the elastic portion of the stress-strain curve. However, it slightly increases the peak strength and makes the post-peak response more ductile. It can be seen in this figure that the platen-shotcrete contact friction also affects the failure mode of the simulated shotcrete specimen (compare Figure 5-13b and Figure 5-13c). This is interpreted to be due to the confinement generated in the shotcrete specimen near the platens during uniaxial loading resulting in hour-glass or cone failure (Figure 5-13c).

The next simulation was conducted to investigate the influence of gravity on the results of the *UCS* test, including the stress-strain curve and the failure mode. In this model, the contact between the platens and the shotcrete specimen was assumed to be frictionless. Figure 5-14 shows that the post-peak response of the shotcrete model becomes ductile when gravity is considered in the simulations. In this model, a sudden stress drop in both axial and lateral directions is observed after some amount of plastic deformation in the post-peak region.

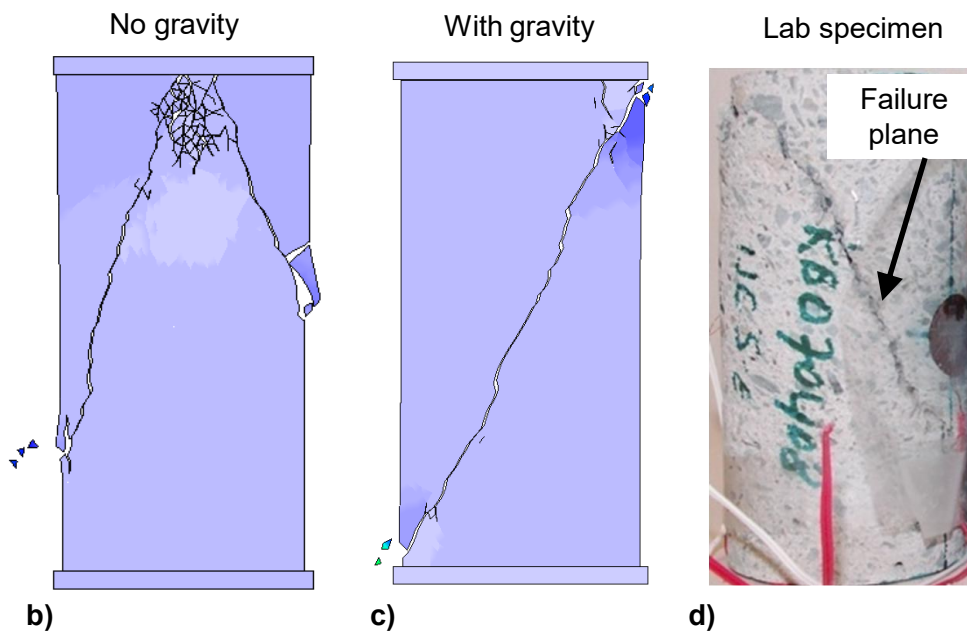
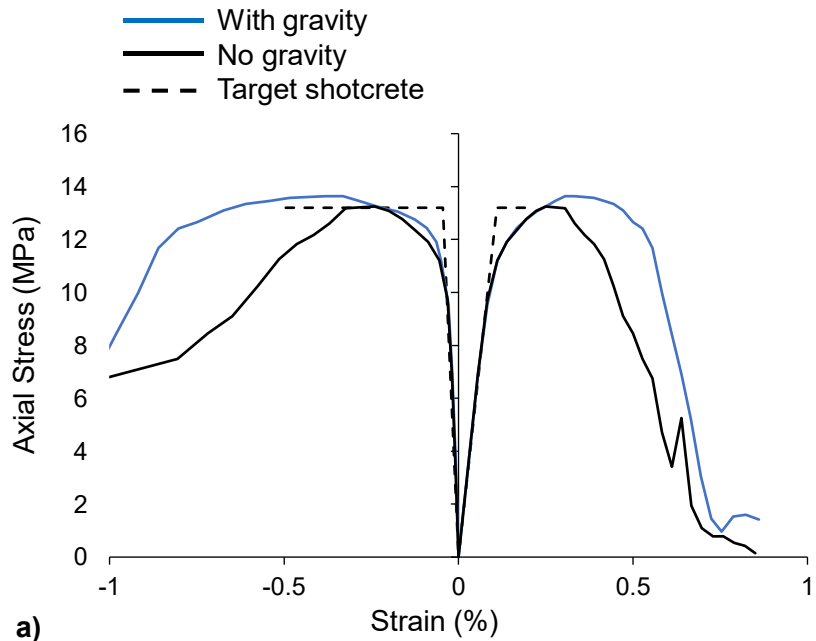


Figure 5-14 a) Stress-strain curves of the shotcrete model with and without the effect of gravity and their comparisons with the target stress-strain curve. The lower images show the failure modes of: b) numerical specimen without the effect of gravity; c) numerical specimen with the effect of gravity; and d) laboratory specimen (after Saw et al., 2009)

By comparing Figure 5-14b and Figure 5-14c, it is concluded that gravity has an influence on the failure mode of the simulated shotcrete specimen. It can be seen in Figure 5-14c that when gravity is considered in the simulations, the failure of the shotcrete model

occurs along a single shear plane. This mode of failure is similar to that observed in the laboratory by Saw et al. (2009) (compare Figure 5-14c and Figure 5-14d).

5.4.4. Simulation of Brazilian Test Using FDEM Model with Fine Mesh

This section presents the results of the Brazilian test simulated on the 12-hr shotcrete. Figure 5-15 shows the Brazilian disk with a diameter of 52 mm constructed in Irazu. The model was meshed with a minimum element size of 2 mm, which resulted in a total of 698 elements. A frictionless contact was used between the platens and the Brazilian disk. The calibration of the model was conducted with respect to the tensile strength of early age shotcrete suggested by Byfors (1980) (Table 5-2).

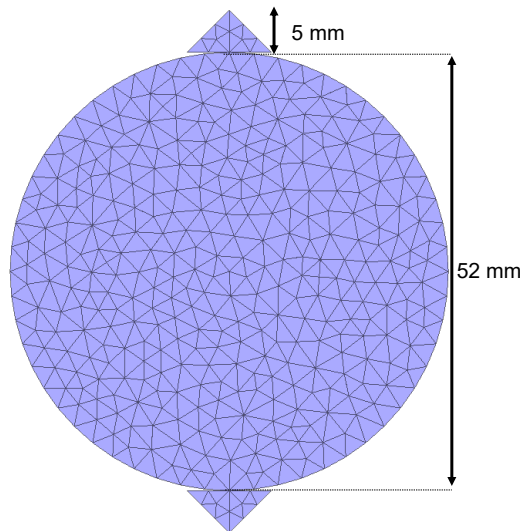


Figure 5-15 Brazilian disk and the elastic platens built in Irazu

The results of the Brazilian test simulated on the shotcrete model with micro-properties given in Table 5-3 including the force-displacement curve and the failure mode are provided in Figure 5-16. The tensile strength is calculated to be 1.4 MPa using the following equation:

$$\sigma_t = \frac{P_{max}}{\pi R_d t}$$

Equation 5-4

Here, P_{max} is the maximum force on the Brazilian disk, R_d is the disk radius, and t is the disk thickness, which is assumed to be 1.0 in 2D analyses.

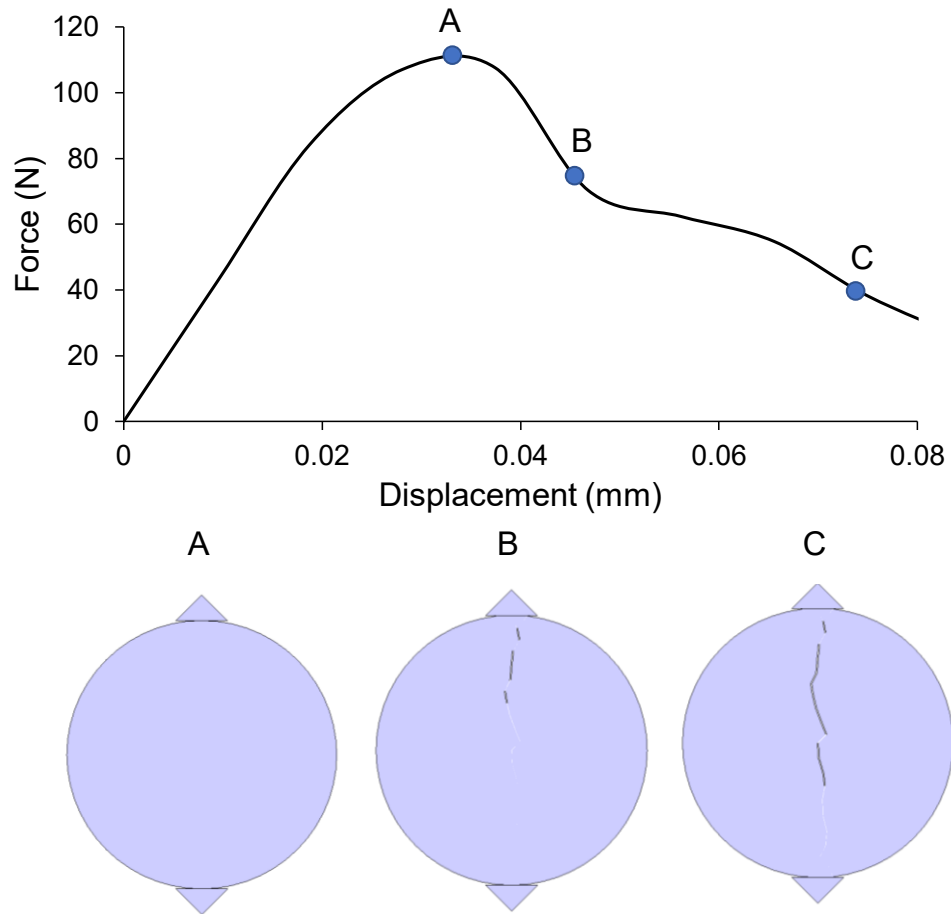


Figure 5-16 Force-displacement curve of the Brazilian test simulated on shotcrete in Irazu. The lower images correspond to three stages of loading showing progressive fracturing of shotcrete at peak (A) and two stages in the post-peak region (B and C)

The lower images in Figure 5-16 illustrate the progressive fracturing leading to the failure of the simulated Brazilian disk. No visible crack can be seen at stage A (i.e. peak force). As mentioned earlier, the force at this stage was used to calculate the tensile strength. A crack initiated from the upper part of the disk can be seen at stage B. At stage C, the crack has propagated through the disk. The final failure mode of the simulated Brazilian disk is similar to that observed by Saw et al. (2009), as compared in Figure 5-17.

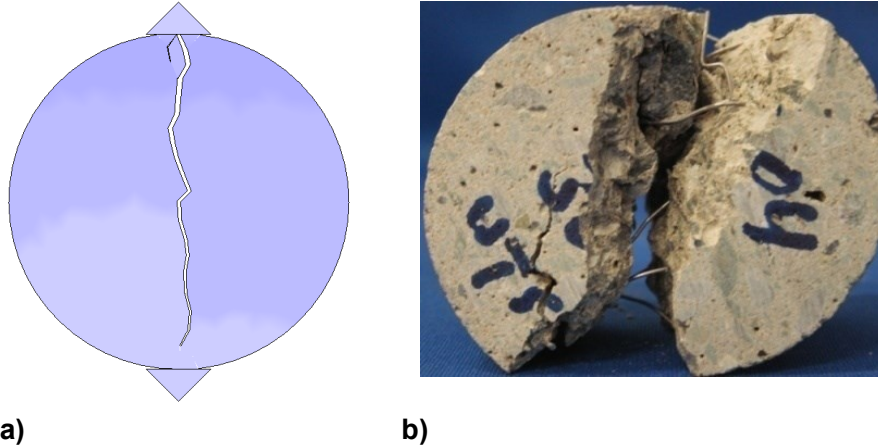


Figure 5-17 Comparison between the failure mode of Brazilian test on shotcrete: a) numerical simulation in Irazu; b) laboratory test by Saw et al. (2009)

5.5. Sensitivity Analysis

Prior to simulating the shaft, a series of sensitivity analyses on the micro-properties of the *FDEM* model were carried out. The objective of the sensitivity analysis was to better understand the influence of micro-properties on the macro-properties and the stress-strain response of the shotcrete model. For this purpose, the magnitudes of input parameters (i.e. micro-properties) were changed independently, and the changes on the peak strength and the stress-strain response of the model were investigated. This parametric study was conducted by simulating the *UCS* test on the calibrated shotcrete model meshed with fine elements shown Figure 5-9.

5.5.1. Model Sensitivity to Cohesion and Tensile Strength of Crack Elements

Given that the crack elements in an *FDEM* model are assigned finite cohesion and tensile strength values, the overall strength of the model is expected to be influenced by the magnitudes of these parameters. In this section, the influence of cohesion and tensile strength of the crack elements on the peak strength and post-peak response of the shotcrete model under an unconfined compression is investigated. Figure 5-18 presents

the stress-strain curves of the shotcrete models with the crack element cohesion values of 1.3 MPa, 1.6 MPa (i.e. crack element cohesion of the calibrated shotcrete model), and 1.9 MPa. The results show that the cohesion of the crack elements controls the peak strength of the shotcrete model; the higher the cohesion, the higher the peak strength. Moreover, a higher cohesion results in a smaller plastic strain and a more sudden stress drop following the peak stress (i.e. more brittle response).

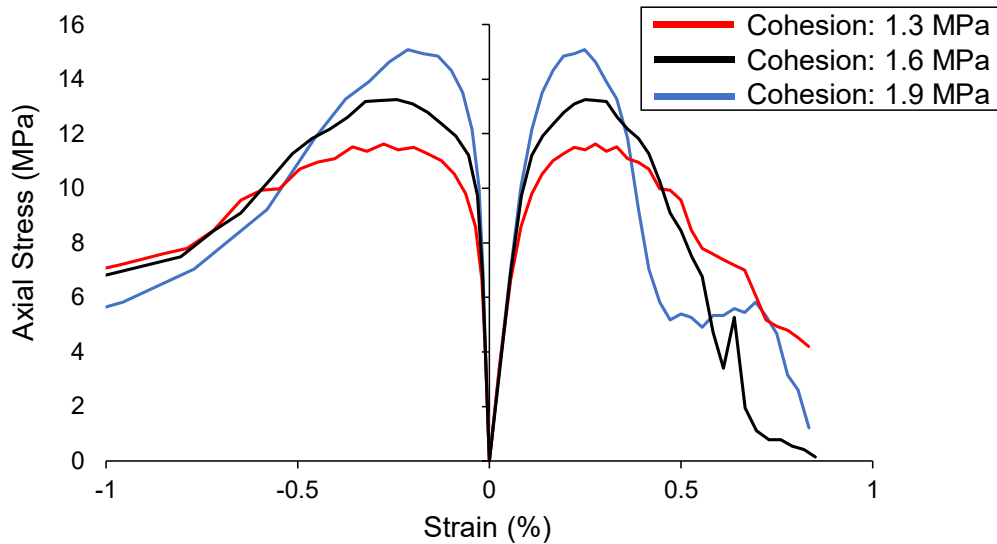


Figure 5-18 Influence of crack element cohesion on the stress-strain response of shotcrete model under unconfined compression

The results of the sensitivity analysis on the tensile strength of the crack elements are presented in Figure 5-19. The tensile strengths used in this sensitivity analysis are 0.4 MPa, 0.7 MPa (i.e. crack element tensile strength of the calibrated shotcrete model), and 1 MPa. This figure shows that similar to the previous analysis, the tensile strength of the crack elements directly influences the peak strength of the shotcrete model. However, the post-peak behavior of the model seems to be less dependent on this parameter.

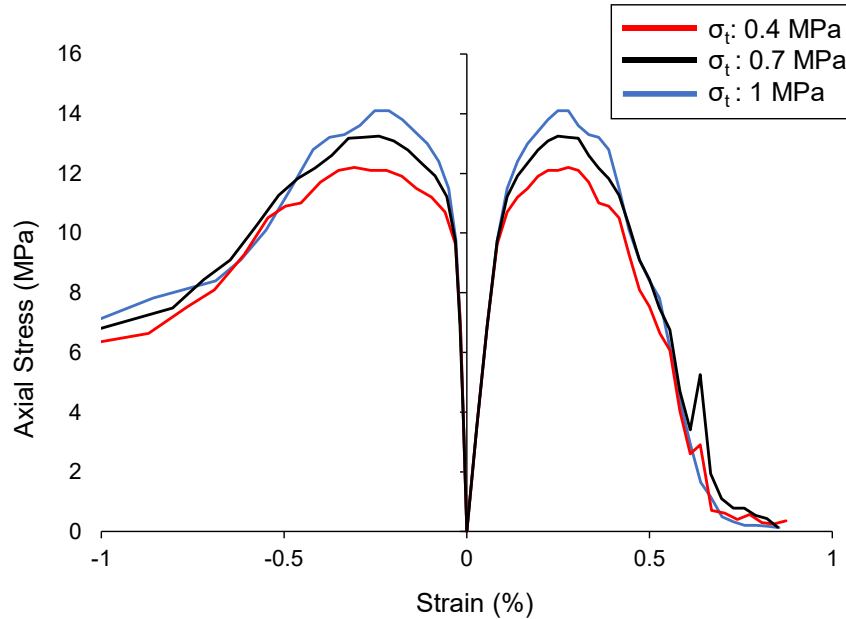


Figure 5-19 Influence of crack element tensile strength on the stress-strain response of shotcrete model under unconfined compression

A comparison between the results of sensitivity analyses presented in Figure 5-18 and Figure 5-19 indicates that the crack element cohesion has a more significant impact on the peak strength than the crack element tensile strength. For example, a 300 kPa increase in the crack element cohesion increased the model *UCS* by about 1 MPa, whereas the same amount of increase in the crack element tensile strength, increased the model *UCS* by 0.5 MPa.

5.5.2. Model Sensitivity to Friction Angle of Crack Elements

The crack element friction angle is one of the strength parameters in the *FDEM* model. Therefore, it is expected that the crack element friction angle has a direct impact on the *UCS* of the shotcrete model. To better understand the influence of this parameter on the macroscopic behavior of the shotcrete model, *UCS* tests were simulated on the models with crack element friction angles of 30°, 40° (i.e. crack element friction angle of the calibrated shotcrete model), and 50°. The results of this sensitivity analysis are provided in Figure 5-20.

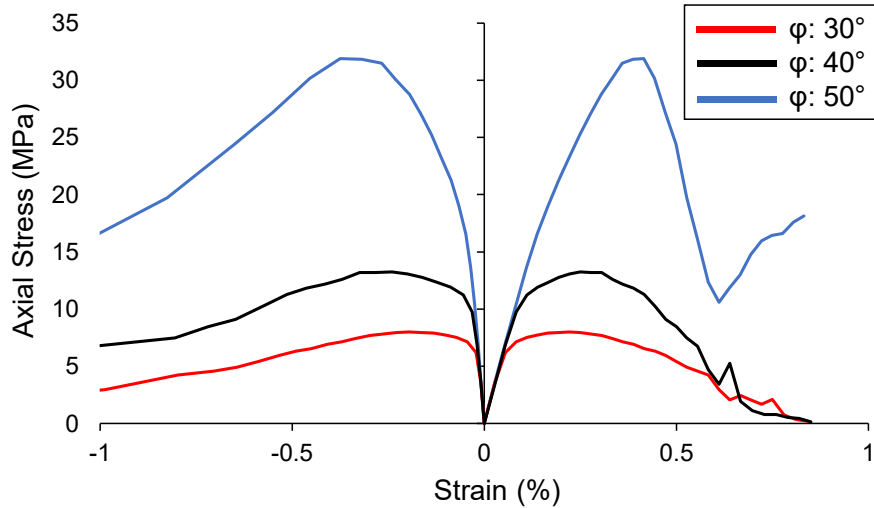


Figure 5-20 Influence of crack element friction angle on the stress-strain curve of shotcrete model under unconfined compression

As illustrated in Figure 5-20, both peak strength and post-peak responses are sensitive to the magnitude of the crack element friction angle. This figure demonstrates how the peak strength of the shotcrete model increases with increasing the crack element friction angle. Moreover, the post-peak response of the shotcrete model with a crack element friction angle of 50° is more brittle than those of the models with crack element friction angles of 40° and 30°.

5.5.3. Model Sensitivity to Fracture Energy Parameters of Crack Elements

Fracture energy parameters in an *FDEM* model (i.e. Mode I fracture energy G_{Ic} and Mode II fracture energy G_{IIc}) control the post-peak response of the crack element (i.e. the slope of the post-peak region). Fracture energy is the energy that should be absorbed by the crack element before its breakage. In this section, sensitivity analysis is conducted to gain insight into the influence of fracture energy parameters on the stress-strain response of the shotcrete model under an unconfined compression. For this purpose, G_{Ic} values of 25,000 $\mu\text{N}/\text{mm}$, 50,000 $\mu\text{N}/\text{mm}$ (i.e. input of the calibrated shotcrete model) and 75,000 $\mu\text{N}/\text{mm}$, and G_{IIc} values of 200,000 $\mu\text{N}/\text{mm}$, 400,000 $\mu\text{N}/\text{mm}$ (i.e. input of the calibrated

shotcrete model) and 600,000 $\mu\text{N}/\text{mm}$ were used in the sensitivity analyses. Figure 5-21 shows the influence of G_{Ic} and G_{IIc} on the stress-strain behavior of the shotcrete model.

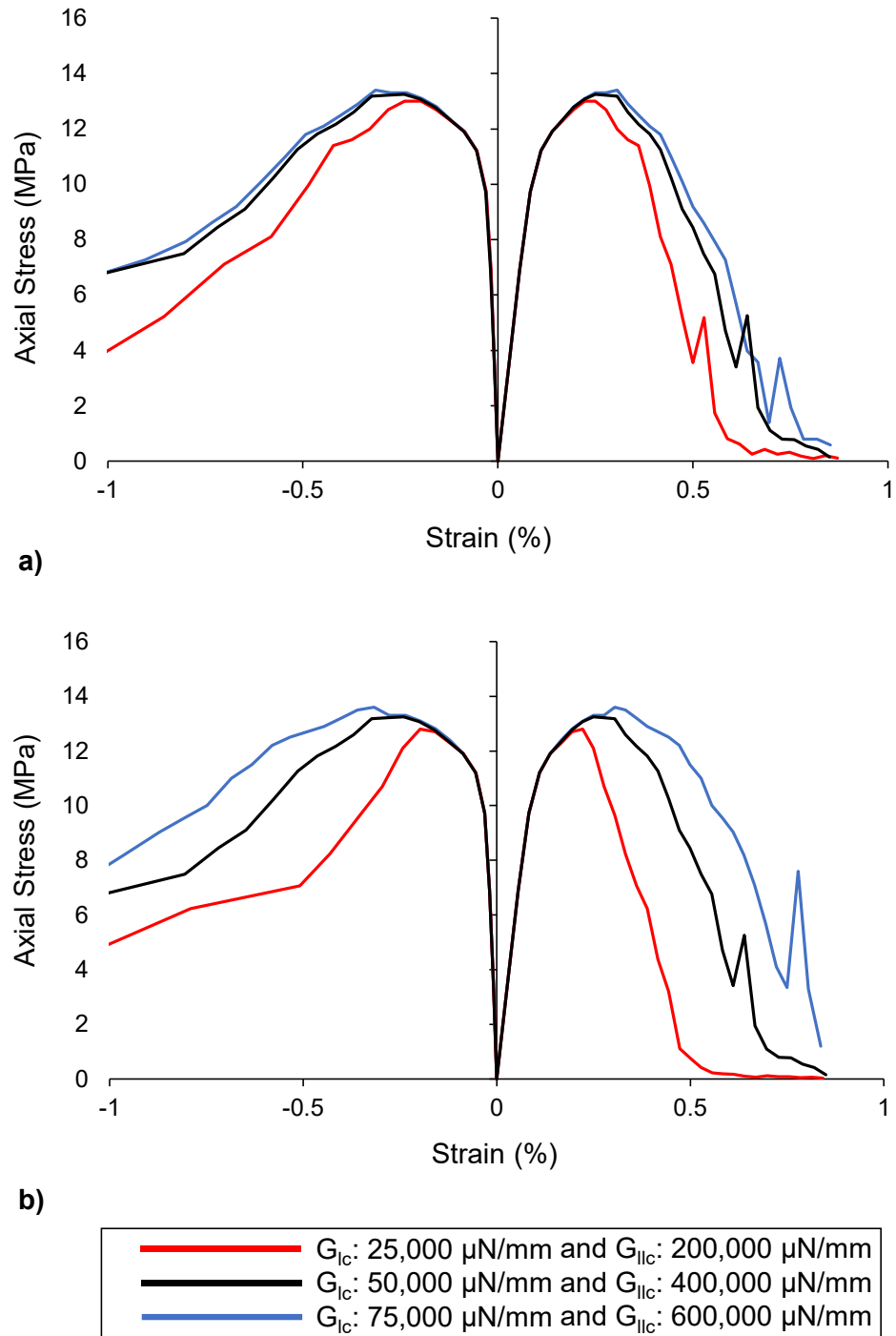


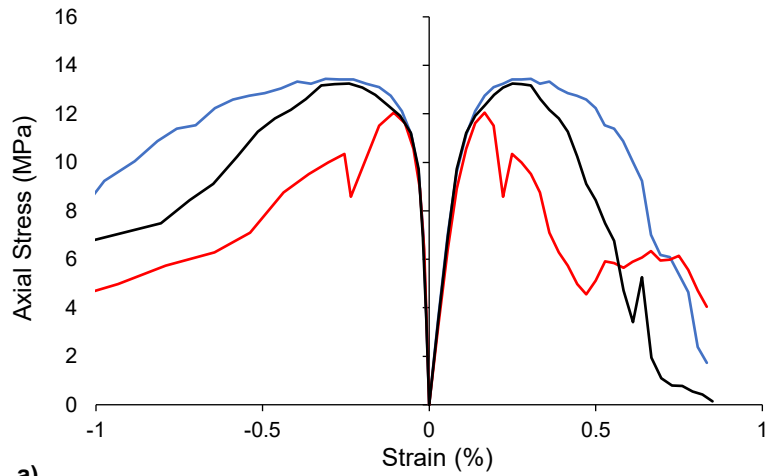
Figure 5-21 Influence of: a) Mode I fracture energy (G_{Ic}); and b) Mode II fracture energy (G_{IIc}) on the stress-strain response of the shotcrete model

As can be seen in Figure 5-21a, G_{lc} has a minor influence on the peak strength of the shotcrete model. This parameter also shows little influence on the post-peak behavior of the shotcrete model. Figure 5-21b shows that an increase in the value of G_{llc} has a more considerable impact on the peak strength and the post-peak ductility of the shotcrete model than G_{lc} .

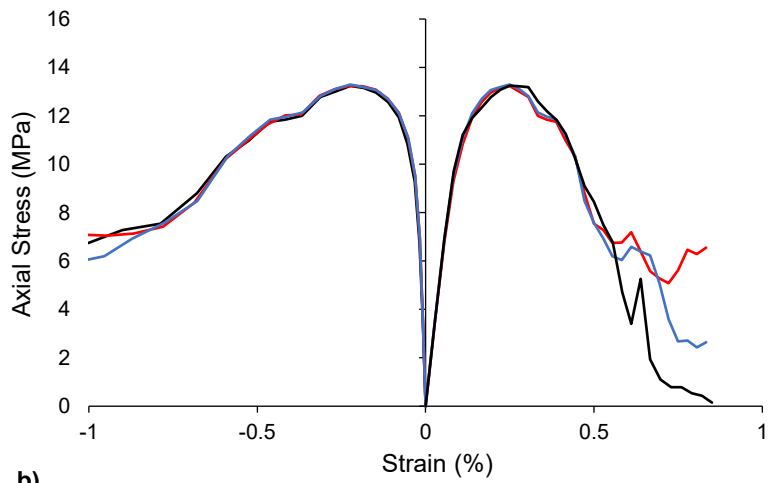
5.5.4. Model Sensitivity to Penalty Parameters of Crack Elements

In an *FDEM* model, the cohesive elements are assumed to have a finite stiffness, which is defined by the penalty parameters. In order to gain further insight into the role of penalty parameters on the simulation results, a series of sensitivity analyses were carried out on the three penalty parameters (i.e. normal penalty, tangential penalty, and fracture penalty). It is worth noting that the penalty parameters have been used in the *FDEM* simulation as a factor of the Young's modulus E (Li et al., 2019). In this regard, the penalty parameters are varied by an order of magnitude from those determined from the calibration process. In Figure 5-22, the influence of penalty parameters on the results of the *UCS* test is investigated.

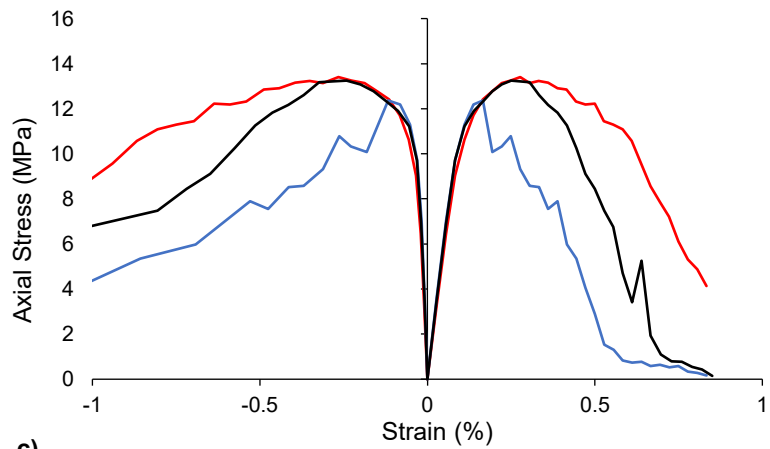
Based on the stress-strain curves illustrated in Figure 5-22a and c, it is concluded that the normal and the fracture penalty parameters control the peak strength and the post-peak response of the shotcrete model. However, the tangential penalty parameter has a negligible effect on the simulation results. It can be seen in Figure 5-22a that an increase in the value of the normal penalty parameter increases the peak strength and the post-peak ductility of the shotcrete model, whereas increasing the fracture penalty parameter (Figure 5-22c) has an exactly opposite influence. An increase in the fracture penalty parameter decreases the peak strength and results in a more brittle response in the shotcrete model.



a)



b)



c)

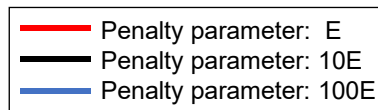


Figure 5-22 Influence of: a) normal penalty; b) tangential penalty; and c) fracture penalty on the stress-strain response of shotcrete model

The results of sensitivity analyses conducted in this section provided a better understanding of the influence of different input parameters (i.e. micro-properties) of the *FDEM* on the model results (i.e. macro-properties). The knowledge gained from this exercise has helped calibrate the shaft model more effectively and efficiently.

5.6. Simulation of UCS Test Using FDEM Model with Coarse Mesh

As mentioned earlier, the element size in the *UCS* and Brazilian specimens is 2 mm. The Irazu model constructed to simulate the shaft with initial shotcrete and final concrete liners has a boundary length of 130 m. In such a large model, simulating the shotcrete and concrete liners with a minimum element size of 2 mm is not practical. Therefore, in order to be able to reduce the computation time in the shaft model, the shotcrete and concrete specimens for both *UCS* and Brazilian tests were re-constructed and meshed with coarser elements. In the *UCS* model, the number of elements is reduced from 3899 to 166, and in the Brazilian model, the number of elements reduced from 698 to 88.

5.6.1. Shotcrete Model Calibration

In order to construct a 50 mm thick shotcrete specimen with coarse elements while being able to capture fracture initiation and propagation throughout the specimen realistically, the model was meshed with an element size of 6 mm. This resulted in approximately 8 elements across the width of the *UCS* and Brazilian specimens, as depicted in Figure 5-23a. Note that the contacts between the elastic platens and the specimens were assumed to be frictionless and gravity was not considered in these simulations.

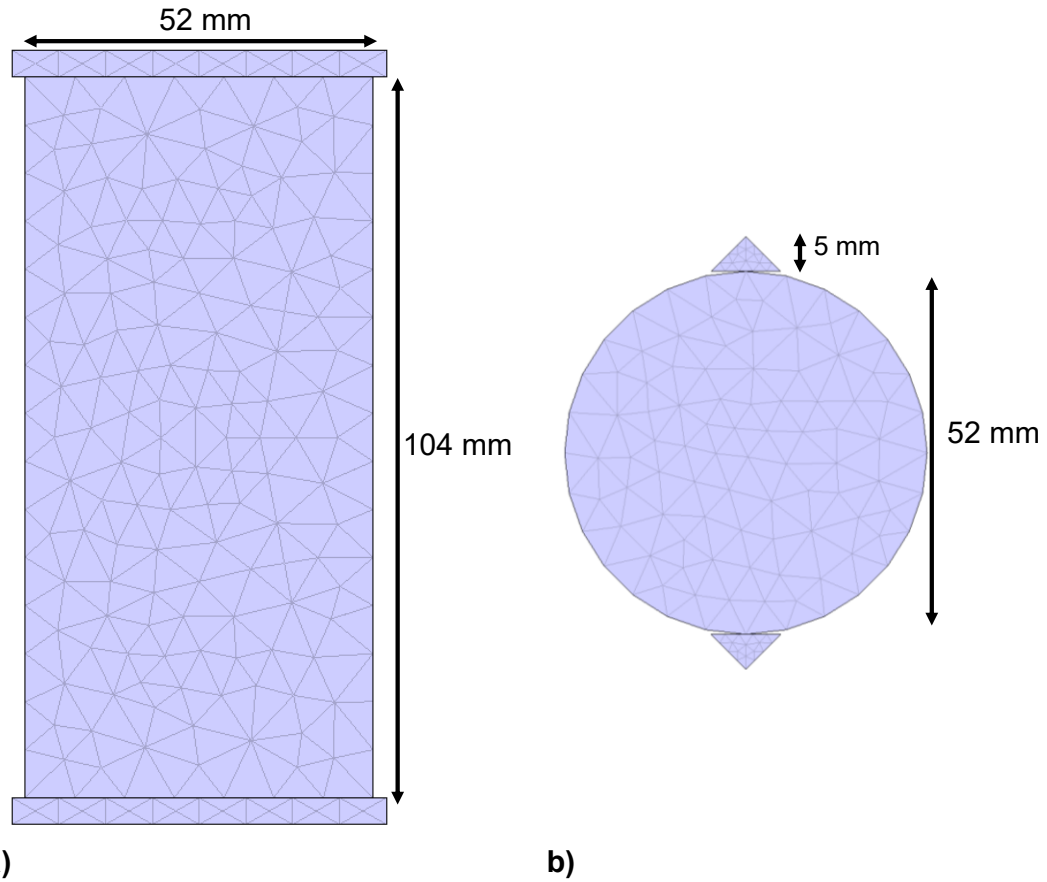


Figure 5-23 Irazu model constructed using coarse mesh elements for the simulation of: a) UCS test; and b) Brazilian test

Since the results of *FDEM* simulations are dependent on the size of mesh elements, the shotcrete model constructed with coarse elements had to be re-calibrated. Initial model runs were carried out using the micro-properties of the calibrated shotcrete model constructed with fine elements. The micro-properties were then adjusted until the macro-properties of the model were matched with those of 12-hr shotcrete. Based on the comparison between the macro-properties of the shotcrete model meshed with coarse elements and those of 12-hr shotcrete, a new set of micro-properties was determined as summarized in Table 5-5.

Table 5-5 Micro-properties of the shotcrete model meshed with coarse elements and calibrated to the properties of 12-hr shotcrete

Element Type	Parameter	Values
Crack elements	Cohesion (MPa)	1.2
	Friction angle (°)	44
	Tensile strength (MPa)	0.7
	Mode I fracture energy ($\mu\text{N}/\text{mm}$)	50,000
	Mode II fracture energy ($\mu\text{N}/\text{mm}$)	1,000,000
	Fracture penalty (Pa)	1.2e+11 (or 10 E)
	Normal penalty (Pa.mm)	1.2e+11 (or 10 E)
	Tangential penalty (Pa/mm)	1.2e+11 (or 10 E)
Triangular elements	Young's modulus (GPa)	12
	Poisson's ratio	0.25
	Density (Kg/m^3)	2,500

The stress-strain and force-displacement curves, along with the progressive fracturing of the calibrated shotcrete model meshed with coarse elements, are presented in Figure 5-24a and c. For comparison purposes, the stress-strain and force-displacement curves of the calibrated shotcrete model meshed with fine elements are also shown in this figure. The comparison between the two models reveals that the model meshed with coarse elements results in a better agreement with the target response (dashed line) in both axial and lateral directions. The force-displacement responses of the Brazilian models (i.e. coarse meshed and fine meshed) are similar up to the peak point, as shown in Figure 5-24c. This figure shows that the model meshed with coarse elements exhibits a more brittle post-peak response compared to that meshed with fine elements.

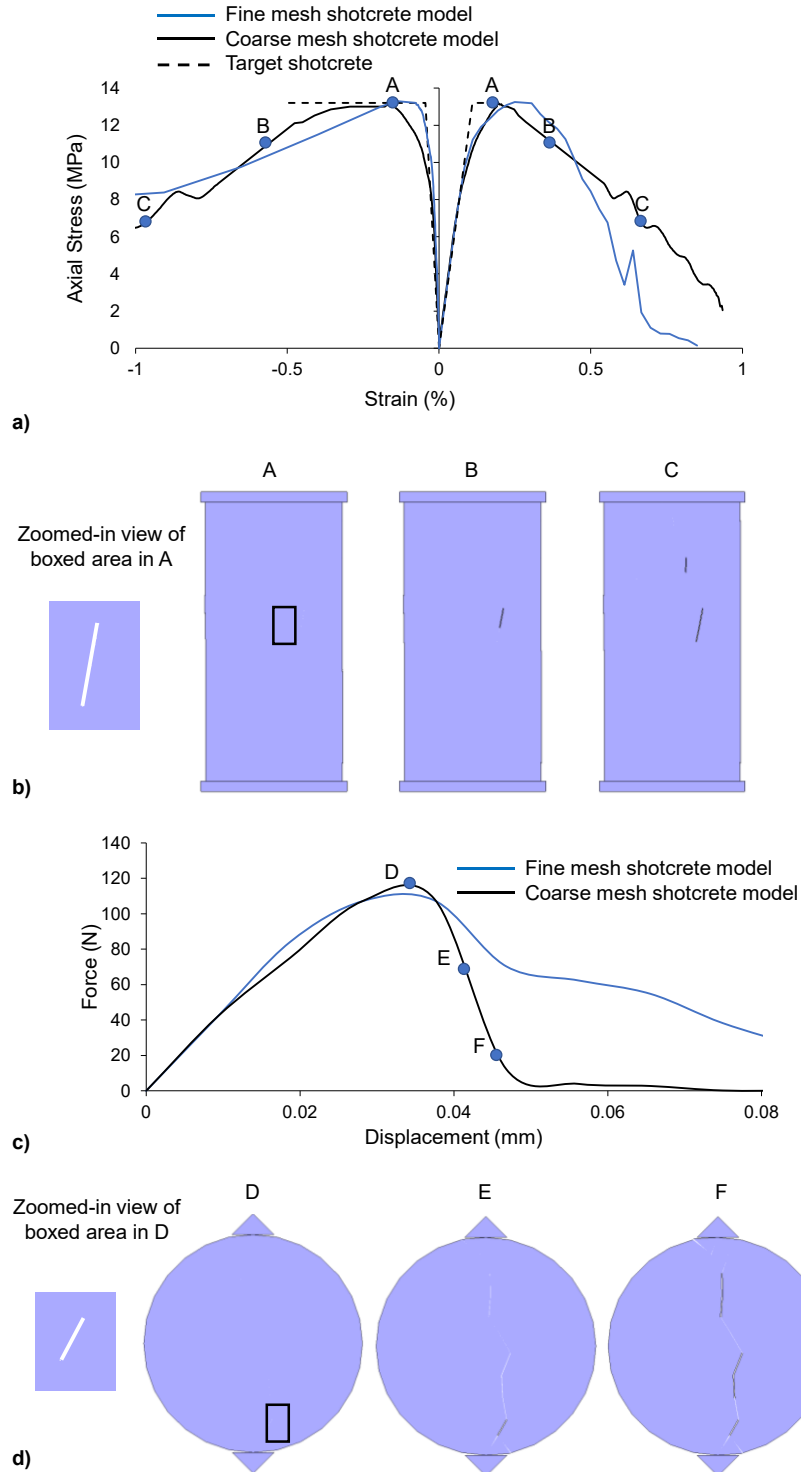


Figure 5-24 a) Stress-strain and c) force-displacement curves of shotcrete models meshed with fine and coarse elements. The lower images correspond to three stages of shotcrete loading during: b) UCS; and d) Brazilian test and show the progressive fracturing of shotcrete at peak (A and D) and two stages in the post-peak region (B, C, E, and F). Zoomed-in views of the boxed areas show cracks initiated at stages A and D

The failure mode of the simulated shotcrete specimen under an unconfined condition is presented in Figure 5-25a. It can be seen in this figure that the failure mode of the shotcrete model meshed with coarse elements is similar to that of laboratory tests. This figure shows that the shotcrete model fails in shear.

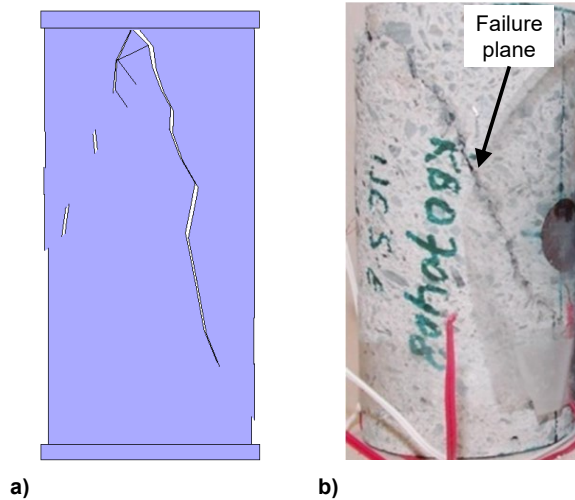


Figure 5-25 Comparison between the failure modes of shotcrete specimens: a) numerical simulation in Irazu; b) laboratory test by Saw et al. (2009)

A comparison between the macro-properties of calibrated shotcrete models constructed using coarse and fine mesh elements and the target properties (i.e. 12-hr shotcrete) is provided in Table 5-6.

Table 5-6 Comparison between properties of shotcrete models constructed with coarse and fine mesh elements and target 12-hr shotcrete

Parameters	Values		
	target shotcrete	shotcrete model with fine mesh	shotcrete model with coarse mesh
UCS (MPa)	13.2	13.2	13.6
Young's modulus (GPa)	12	12	12.5
Poisson's ratio	0.25	0.27	0.27
Tensile Strength (MPa)	1.36	1.43	1.33

As indicated earlier in this chapter, capturing a realistic post-peak response (especially in the lateral direction) using discontinuum models is challenging. Therefore, considering the elastic portion of the stress-strain curve, the peak strength and the failure mode of the shotcrete model constructed with coarse mesh elements and their comparisons with those of 12-hr shotcrete obtained from laboratory tests and empirical equations, it is concluded that this model is reasonably calibrated, and therefore can be used for the simulation of 12-hr shotcrete liner in the shaft model.

5.6.2. Concrete Model Calibration

This section presents the results of numerical simulations of the *UCS* and Brazilian tensile tests on 28-day concrete. The properties of the 28-day concrete were obtained from the empirical equations reviewed in Chapter 2 and are listed in Table 5-7.

Table 5-7 Properties of 28-day concrete

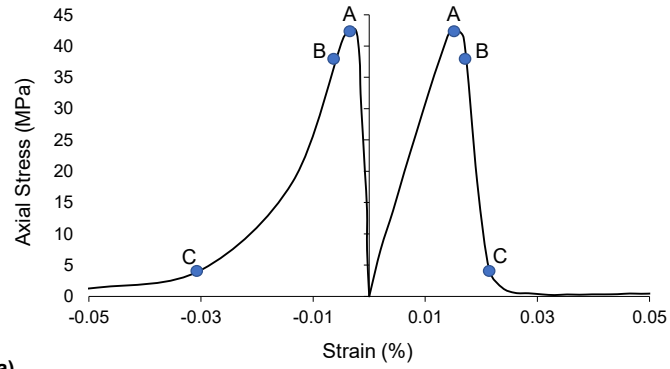
Parameters	Values	Reference
UCS (MPa)	40	Meschke et al. (1996)
Young's modulus (GPa)	30	Schubert (1988)
Poisson's ratio	0.15	Carranza-Torres & Fairhurst (2000)/ Schütz (2010)

The *UCS* and the Brazilian tensile tests were simulated and calibrated to the macro-properties of the 28-day concrete, including the *UCS*, the Young's modulus, the Poisson's ratio, and the tensile strength given in Table 5-7. Note that the model geometry and the mesh size are the same as those of the shotcrete model constructed with coarse mesh. The contact between the specimen and the platens is frictionless, and gravity was not considered in the simulations. The micro-properties of the calibrated model are summarized in Table 5-8.

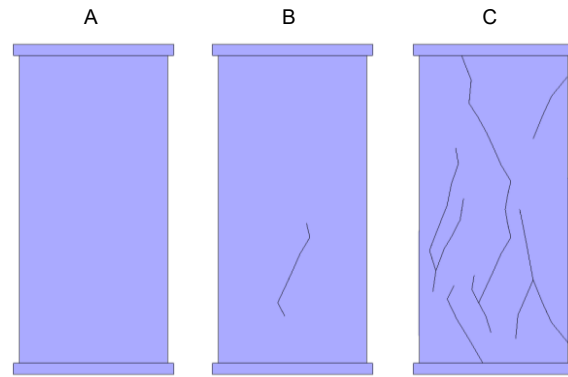
Table 5-8 Micro-properties of the concrete model calibrated to the laboratory properties of 28-day concrete under unconfined condition

Element Type	Parameter	Values
Crack element	Cohesion (MPa)	6
	Friction angle (°)	43.5
	Tensile strength (MPa)	3
	Mode I fracture energy ($\mu\text{N}/\text{mm}$)	1,100
	Mode II fracture energy ($\mu\text{N}/\text{mm}$)	11,000
	Fracture penalty (Pa)	1.5e+11
	Normal penalty (Pa.mm)	1.5e+11
Triangular element	Tangential penalty (Pa/mm)	1.5e+11
	Young's modulus (GPa)	30
	Poisson's ratio	0.15
	Density (Kg/m^3)	2,500

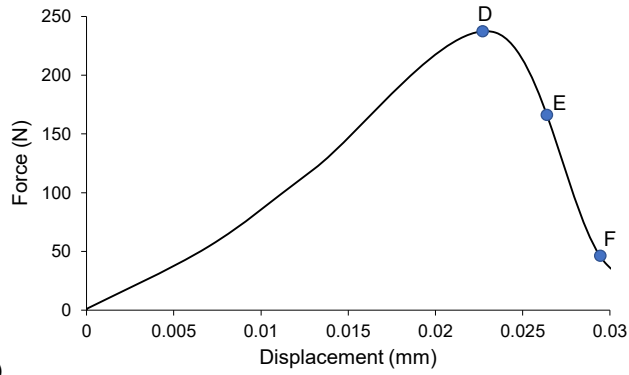
The stress-strain and force-displacement curves from the *UCS* and Brazilian tests conducted on the concrete model along with the fracturing processes and the final failure modes in both tests are presented in Figure 5-26. In both tests, the concrete model exhibits a brittle response once the peak stress is reached. No visible crack can be seen at the peak stress (stages A and D). Subvertical cracks appear in the post-peak region at stages B and E. Based on the fracture pattern at stages C and F, the failure mode of the concrete model is defined to be axial splitting in both tests.



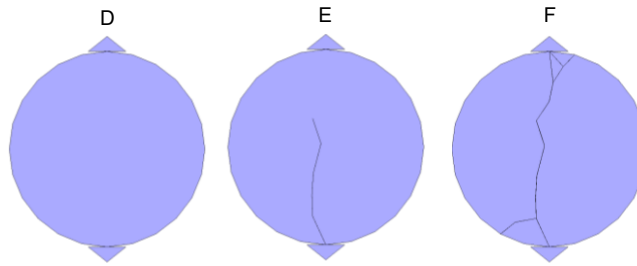
a)



b)



c)



d)

Figure 5-26 a) Stress-strain and b) force-displacement curves of the concrete model with coarse mesh. The lower images correspond to three stages of loading of concrete sample during: b) UCS; and d) Brazilian test and show progressive fracturing of concrete model at peak (A and D) and two stages in the post-peak region (B, C, E, and F)

Table 5-9 provides a comparison between the macro-properties of the simulated concrete specimen and those of 28-day concrete obtained from empirical equations. Based on the results of this comparison, it is concluded that the concrete model is reasonably calibrated, and therefore its micro-properties can be used as input for the concrete liner in the shaft model.

Table 5-9 Comparison between macro-properties of calibrated concrete model and laboratory properties of 28-day concrete

Parameters	Macro-properties	
	28-day concrete	Calibrated concrete model
UCS (MPa)	40	42.7
Young's modulus (GPa)	30	29.2
Poisson's ratio	0.15	0.15
Tensile Strength (MPa)	3	2.9

5.7. Simulation of 3D Shaft Advance Using 2D FDEM Model

The main objective of this chapter is to evaluate the stability of the full support system for the shaft, including the initial shotcrete liner and the final concrete liner, by capturing the crack initiation and propagation through the liners during the excavation advance. For this purpose, the initial shotcrete liner, the final concrete liner, and the rock mass in the Irazu model must be calibrated. For the shotcrete and concrete liners, the micro-properties of the shotcrete and concrete models meshed with coarse elements and calibrated to the properties of laboratory tests are used (see Table 5-5 and Table 5-8). The model calibration for the rock mass near the shaft is based on the extensometer measurement data.

5.7.1. Model Geometry

As indicated in Section 5.7, in order to be able to simulate fracture initiation and propagation in the shotcrete liner yet reduce the run time of the shaft model to a practical limit, the shotcrete liner must be meshed with coarse elements. For this purpose, a minimum element size of 6 mm was used in the shotcrete *UCS* specimen and the shotcrete liner in the shaft model, as shown in Figure 5-27. It can be seen in this figure that the same minimum element size in the *UCS* specimen and the liner resulted in a similar mesh geometry in both models.

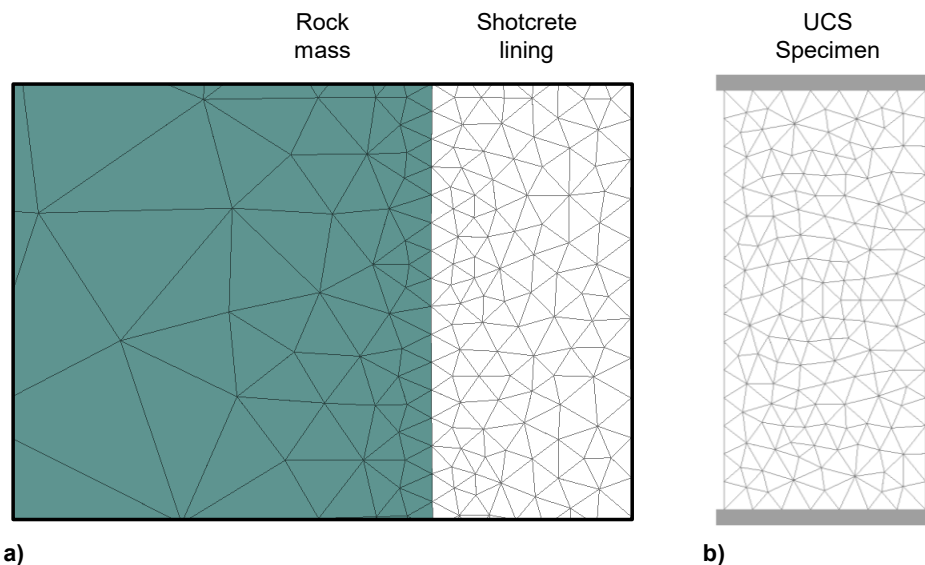


Figure 5-27 Comparison between the geometry and size of mesh elements in: a) shotcrete liner attached to the shaft wall; and b) shotcrete *UCS* specimen used for model calibration

Similar to the RS2 shaft model, a circular external boundary with a radius of 65 m was used to construct the shaft model in Irazu. The circular excavation with a radius of 5 m was added to the centre of the Irazu model, as illustrated in Figure 5-28a. This figure shows that the Irazu model is divided into three sub-domains, and each sub-domain is meshed with different element sizes. The element size ranges from 0.006 to 1 m in sub-domain A, from 0.006 to 3 m in sub-domain B, and from 3 to 10 m in sub-domain C. This was done to improve the computation efficiency, following the approach used by Vazaios

et al. (2019), who simulated the *URL* (i.e. Underground Research Laboratory) test tunnel, as shown Figure 5-28b.

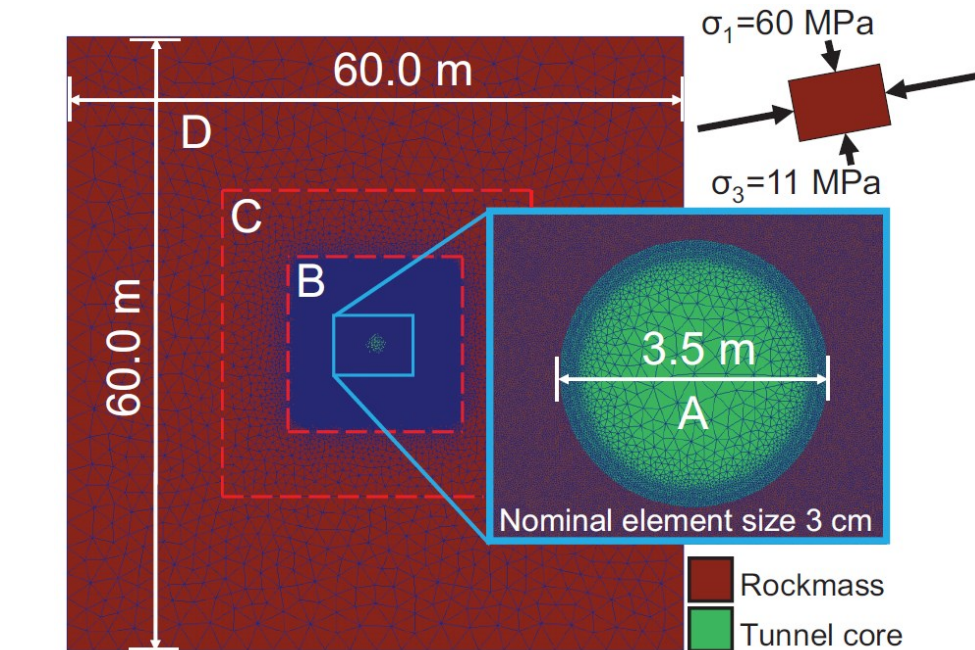
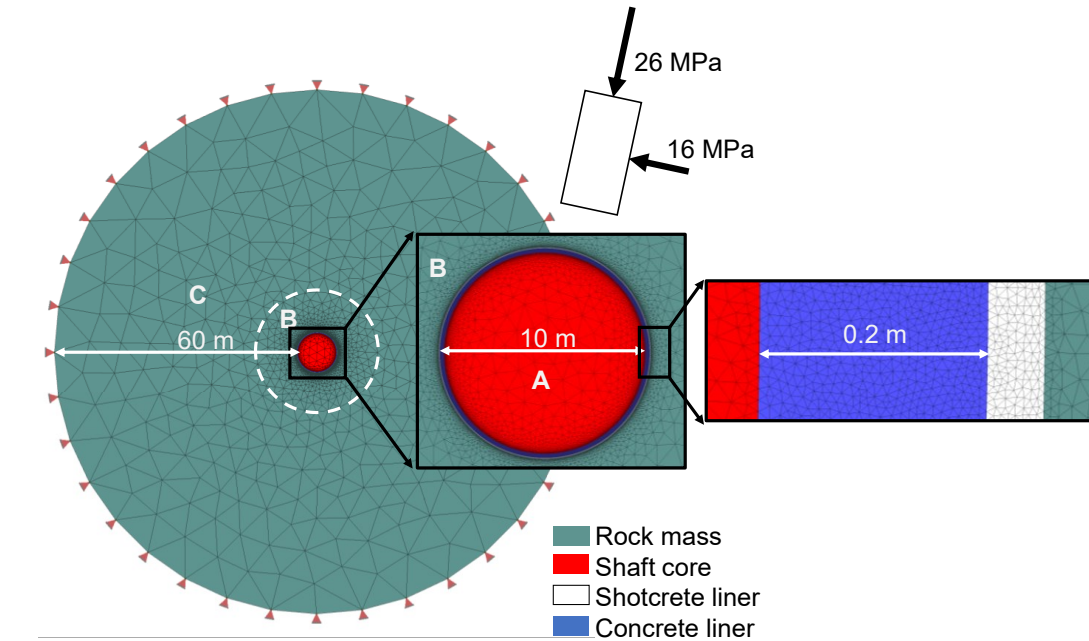


Figure 5-28 a) Geometry of the shaft model showing the mesh size in three sub-domains as well as the shotcrete and concrete liners; b) geometry of the model of the *URL* test tunnel showing the mesh size in four sub-domains (after Vazaios et al., 2019)

It should be noted that a minimum element size of 6 mm was used in both shotcrete and concrete liners in the shaft model. This element size is equal to the minimum element size used to mesh sub-domains A and B. The model of the mine shaft shown in Figure 5-28a consists of a total of about 310,000 triangular elements. The in situ stresses used in the Irazu model are consistent with those in the RS2 models in Chapter 3 and Chapter 4. The model boundary is fixed in both horizontal and vertical directions, as shown by the red triangles in Figure 5-28a.

The next step after constructing the shaft model is to calibrate it against extensometer measurements by adjusting the properties of the triangular and crack elements representing the rock mass. In Irazu, the 3D excavation advance is simulated using the built-in core softening (*CS*) approach. It is worth noting that although the concept of the *CCM* and its components including the *GRC* and the *LDP* were developed based on the assumption that the rock mass is continuum and homogeneous, it has also been used with success in discontinuum models (e.g. Vazaios et al., 2019).

In the following sections, the calibration procedure for the shaft model and the methodology to construct the *GRC* and obtain the radial displacements corresponding to the shaft face and liner installation distance to the shaft face based on the approach proposed by Vazaios et al. (2019) are described.

5.7.2. Model Calibration

The simulation of the 3D shaft advance in Irazu required an extensive iterative calibration process, in which multiple calibration steps were carried out to ensure that an agreement between the simulation results and the measured data was reached. The vital tool for model calibration was the *CCM* (i.e. *GRC* and *LDP*). As a reminder, the *GRC* relates the internal pressure applied to the inner boundary of the excavation to the radial displacement in response to the excavation advance (i.e. decrease of the internal pressure). The *LDP* provides a relationship between the radial wall displacement and the

distance from the excavation face. In order to use the *LDP* and the *GRC*, the radius of the plastic zone and the maximum displacement are required as explained in Chapter 2.

In the Irazu model, since the rock mass around the shaft becomes fractured as the simulation progresses, the deformation and stress redistribution near the excavation wall cannot be directly compared to those of the RS2 model. Therefore, it is not recommended to build a *GRC* from an unsupported excavation in Irazu and compare the results with those of the RS2 model. Instead, the *GRCs* obtained from the supported excavations in Irazu and RS2 models should be compared. If an elastic shotcrete is used as a liner in the Irazu model, the failed rock pieces do not fall into the excavation. In this case, the damaged zone will be limited, and the deformation around the shaft becomes comparable to that of the RS2 model. Then, by combining the *GRC* and the *LDP*, the time steps corresponding to the excavation face and liner installation distances from the face can be determined in the Irazu model.

Before showing the model results, the calibration procedure for the *URL* test tunnel employed by Vazaios et al. (2019) is briefly reviewed. The process to determine the micro-properties of the rock mass in Irazu is illustrated in the flowchart in Figure 5-29. As can be seen in this figure, the calibration begins by simulating a *UCS* test. Then, the deformation and strength properties obtained from this simulation are compared with those of laboratory tests. If the results of numerical simulations and laboratory tests are comparable, the calibrated model properties are used as input in the tunnel model, and the extent of damaged/failure zones are compared with field measurements and observations. Further adjustment of the strength micro-properties may be required at this stage to match the simulated damage zone with field observations. Once the model is calibrated, the *GRCs* for different points around the excavation are plotted. These *GRCs* are then compared with those of the RS2 model. This comparison is provided in Figure 5-30.

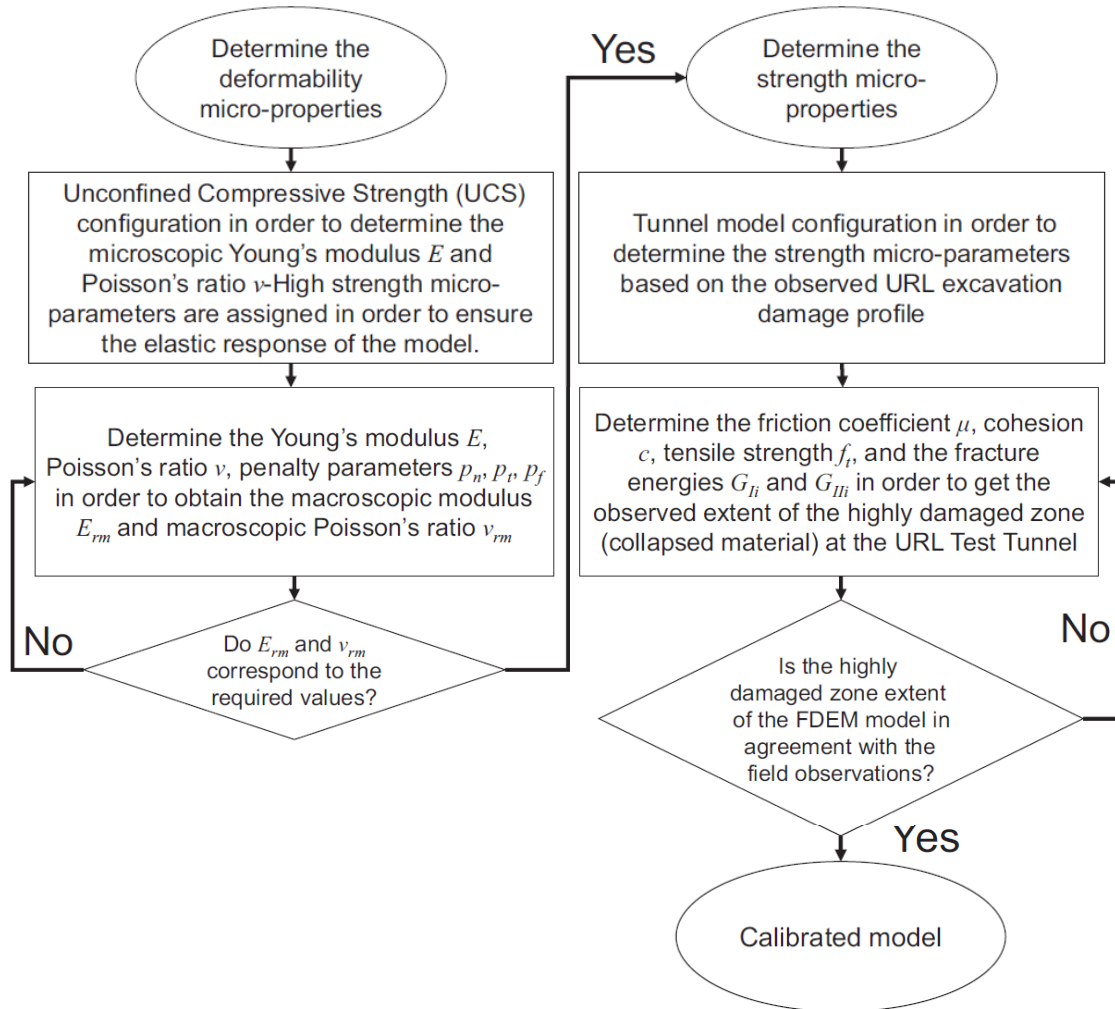


Figure 5-29 Calibration procedure to determine the input parameters for the Irazu model of URL test tunnel (after Vazaios et al., 2019)

Figure 5-30 shows that the *GRCs* obtained from the Irazu model are comparable with that of the RS2 model of the *URL* test tunnel (Vazaios et al., 2019). As can be seen in this figure, the *GRCs* of different points in the Irazu model show a rapid stress drop up to a radial displacement of about 1 mm. This sudden stress drop in the *FDEM* analysis is an indication of the transition in the rock mass from continuum to discontinuum due to fracture initiation at the crown and bottom notches of the tunnel, as shown in Figure 5-30. In the *URL* test tunnel, rock failure processes involved spalling at the tunnel wall, which then lead to the v-shaped notch failure with a depth of about 0.5 m. In Figure 5-30, the *GRC* obtained from the RS2 model is smoother than those of the Irazu model.

Moreover, since rock mass fracturing and failure are not explicitly captured in the RS2 model, the maximum radial displacement in this model has a finite value of 25 mm.

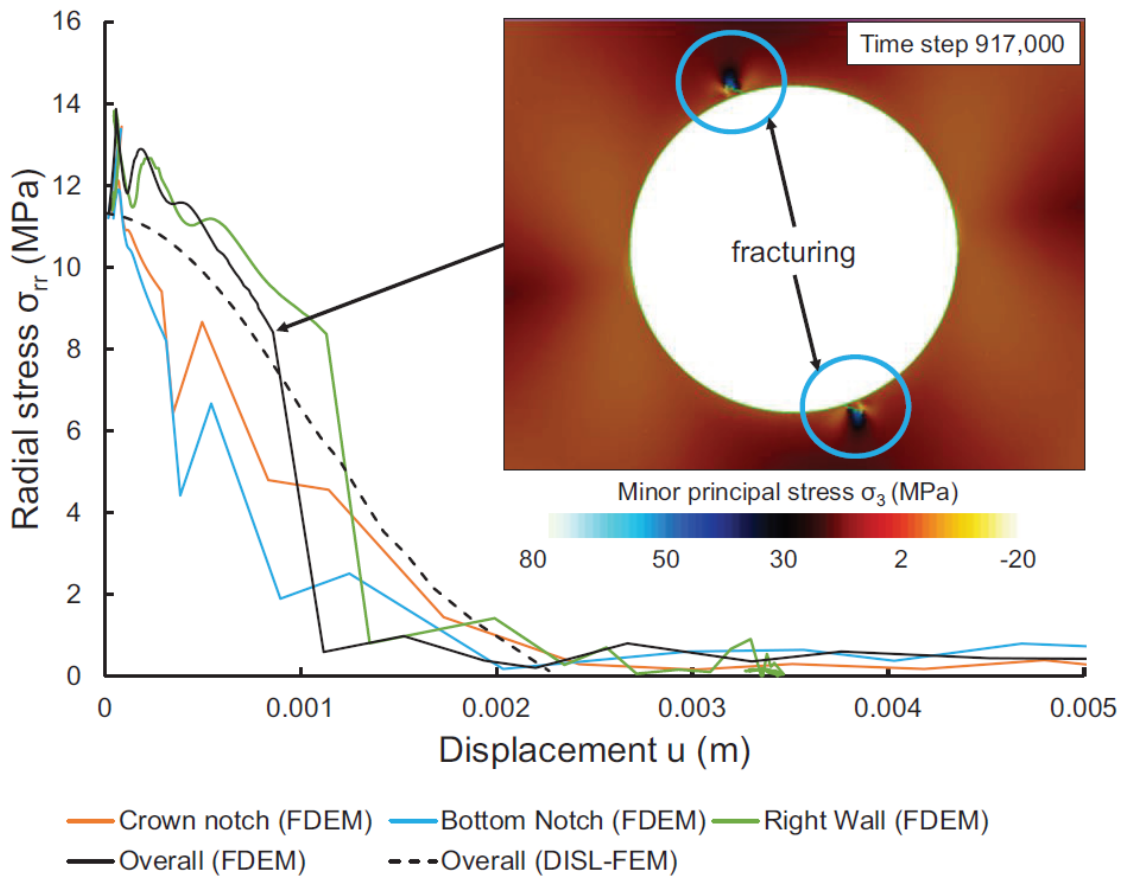


Figure 5-30 Comparison between GRCs obtained from right wall, crown notch, and bottom notch of the URL test tunnel in the FDEM model and the GRC obtained from the FEM model (after Vazaios et al., 2019)

The procedure to calibrate the shaft model using Irazu in this study was similar to that proposed by Vazaios et al. (2019) and shown in Figure 5-29. The main difference is that the full support system consisting of shotcrete and concrete liners were included in the shaft model. As discussed earlier, this would stop the failed rock pieces from falling into the excavation and would make the comparison between the results of Irazu and RS2 models possible. Table 5-10 provides a summary of the micro-properties of the shaft model calibrated against the extensometer data.

Table 5-10 Micro-properties of the rock mass in the shaft model calibrated to extensometer data

	Parameter	Values
Crack element	Cohesion (MPa)	14
	Friction angle (°)	43
	Tensile strength (MPa)	3
	Mode I fracture energy (μN/mm)	12,000
	Mode II fracture energy (μN/mm)	190,000
	Fracture penalty (Pa)	1.5e+11
	Normal penalty (Pa.mm)	1.5e+11
	Tangential penalty (Pa/mm)	1.5e+11
Triangular element	Young's modulus (GPa)	15
	Poisson's ratio	0.25
	Density (Kg/m ³)	2,700

In the following sections, the results of the calibrated Irazu model, including the extent of the damaged zone, the *GRC*, and the deformation along the extensometers and their comparison with field measurements, are discussed.

5.7.2.1. Convergence confinement method

The built-in core softening method was used to construct the *GRCs* from the calibrated Irazu model simulating the mine shaft with both shotcrete and concrete liners with the input properties given in Table 5-10. As shown in Figure 5-31a, two points on the excavation boundary, marked with A and B, are selected to monitor the radial deformation and to construct the *GRCs*. The *GRCs* obtained from the RS2 model are also plotted for the same points. Figure 5-31b and Figure 5-31c present the internal pressure normalized by the in situ stress as a function of the radial displacement of the mine shaft for points A and B, respectively.

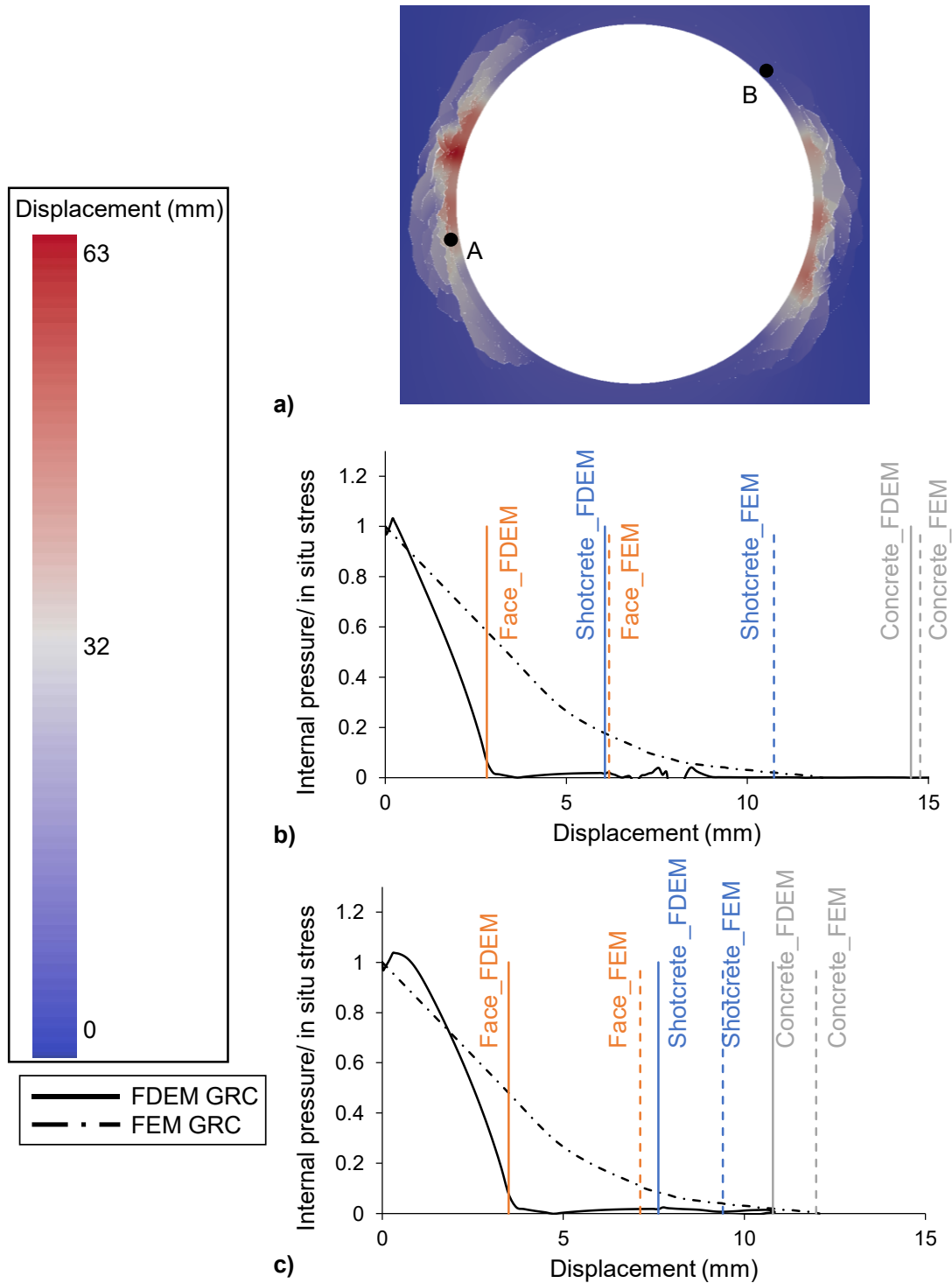


Figure 5-31 a) Irazu model of the mine shaft showing the extent of fractured zone. Comparison between the GRCs obtained from calibrated Irazu and RS2 models for two points on the shaft boundary: b) GRCs for point A; c) GRCs for point B

Figure 5-31b shows the comparison between the *GRCs* obtained from the calibrated RS2 and Irazu models for point A, where the rock mass is fractured. The *GRCs* obtained from both models are comparable, showing an initial linear behavior with increasing the radial displacement. The *GRC* from the Irazu model shows a more rapid stress drop compared to that of the RS2 model. A similar behavior was captured by Vazaios et al. (2019), as shown in Figure 5-30. A further analysis of the *GRCs* of the two models indicate that the maximum radial displacements predicted by the two models are comparable.

In Figure 5-31c, the *GRCs* are plotted for point B located on the excavation boundary where the rock mass is not fractured. Similar to point A, the *GRC* for point B from the Irazu model exhibits a more rapid stress drop compared to that of the RS2 model, while the maximum radial displacement for the two models are comparable. Table 5-11 provides a comparison between the results of calibrated Irazu and RS2 models in terms of the radius of the plastic/fractured zone and the maximum radial displacement for points A and B.

Table 5-11 Comparison between the results of calibrated RS2 and Irazu models

Program	Radius of plastic/fractured zone (m)	Maximum radial displacement (mm)	
		Point A	Point B
Irazu	1.1	16.1	11
RS2	3	14.9	12

The radial displacements corresponding to the shaft face and liner installation distances from the shaft face were obtained from the *LDP* and are indicated in Figure 5-31b and Figure 5-31c. For the *LDP*, the maximum radial displacement and the radius of the fractured zone were first obtained from the Irazu model. Then the radial displacements corresponding to the excavation face and liner installation distances from the shaft face were determined. Figure 5-32 is a flowchart showing the step-by-step procedure to determine the wall radial displacement corresponding to any given distance from the face for the mine shaft in Irazu based on the approach proposed by Vazaios et al. (2019).

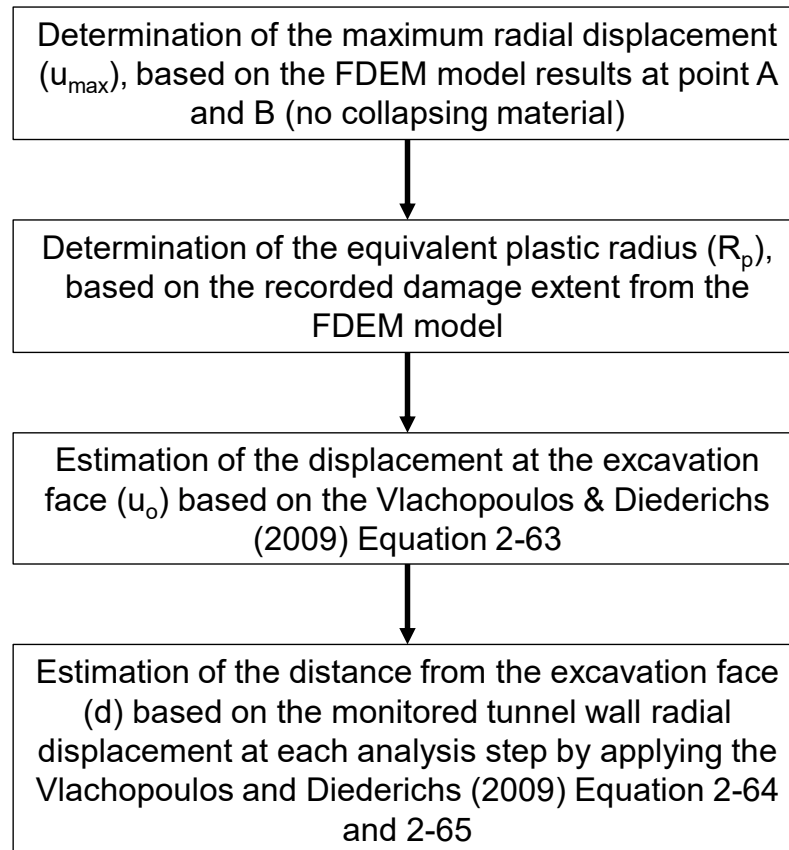


Figure 5-32 Procedure to use the *FDEM* model results (e.g. radius of plastic zone and the radial displacement) to determine displacements corresponding to any given distance from the shaft face (modified from Vazaios et al., 2019)

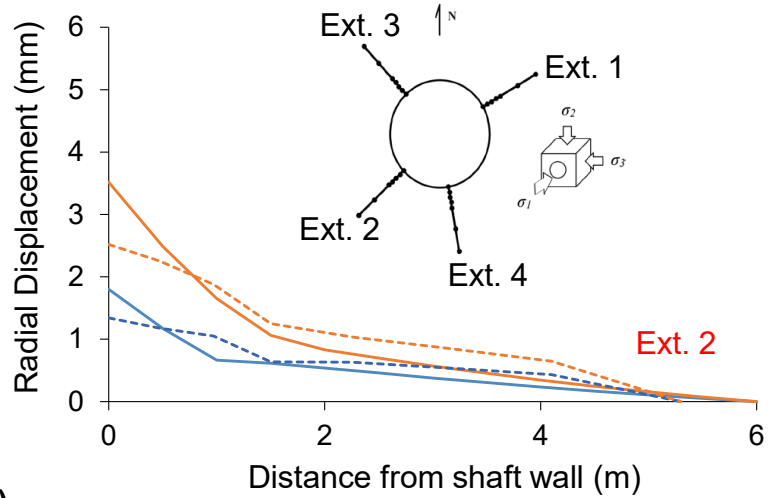
It can be seen in Figure 5-31b and Figure 5-31c that the radial displacements corresponding to the shaft face and liner installation distances from the shaft face are not comparable in the Irazu and RS2 models. This is due to the difference between the extent of the plastic and fractured zones in the two models. The radius of the plastic zone in the RS2 model is two times the radius of the fractured zone in the Irazu model (see Table 5-11).

In the next section, the rock mass radial displacements near the mine shaft obtained from the calibrated Irazu model are compared with the extensometer measurements. Then, the calibrated model will be used to investigate the stability of the shotcrete liner and the full support system consisting of the initial shotcrete liner and the final concrete liner.

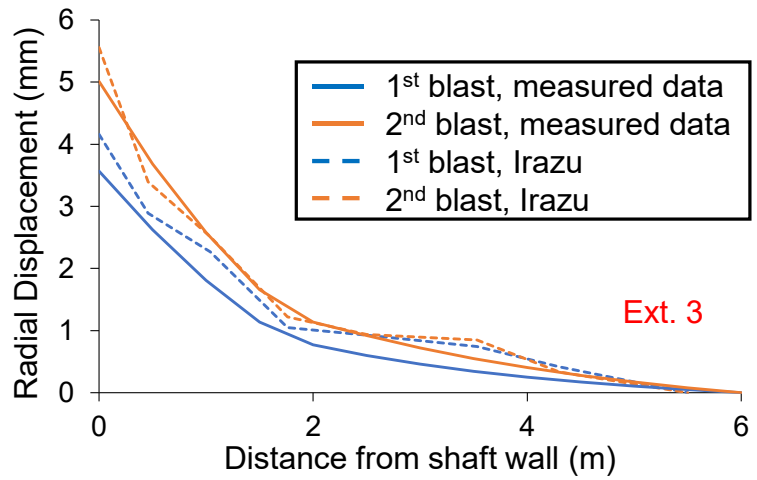
5.7.2.2. Extensometer measurements

The flowchart presented in Figure 5-32 was followed to determine the wall radial displacements corresponding to the distance from the face at which the extensometer readings were made. As mentioned in Chapter 3, four extensometers were installed near the shaft face to record the radial displacements following the first and the second rounds of the blast. Three of these extensometers were used for model calibration. These extensometers were installed 1 m behind the face, and the advance rate was 3 m per day. Therefore, by using Figure 5-32, the time steps and the radial displacements corresponding to 1 m, 4 m, and 7 m behind the face were determined. Figure 5-33 shows the radial displacements along the extensometers as a function of the distance from the shaft boundary.

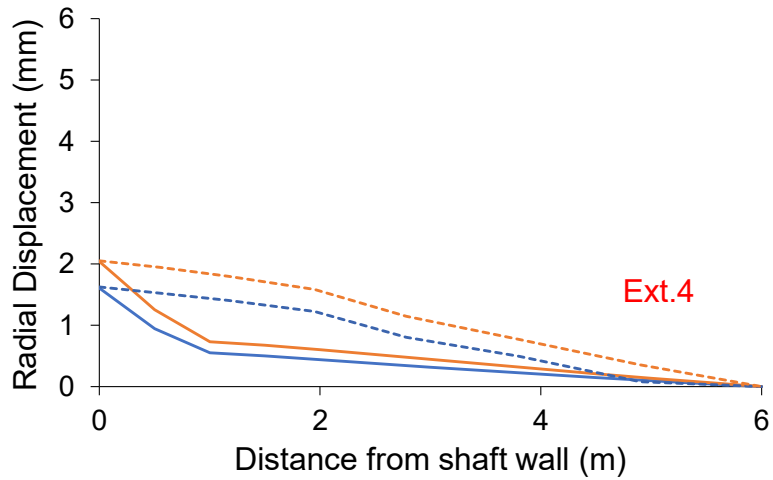
The radial displacements measured along the extensometers and those obtained from the calibrated Irazu model are compared in Figure 5-33. The extensometer measurements are presented by the solid lines, and the results of the Irazu model are shown by the dashed lines for two measurements made after each round of blasting. Figure 5-33a and Figure 5-33b show an acceptable agreement between field measurements and the results of numerical simulations for extensometers 2 and 3, respectively. For extensometer 4, although the Irazu model predicts a similar maximum radial displacement at the shaft boundary (i.e. Figure 5-33c), it overestimates the radial displacement away from the shaft boundary measured by the extensometer.



a)



b)



c)

Figure 5-33 Comparison of measured and simulated displacements along: a) Ext. 2; b) Ext. 3; and c) Ext. 4

Considering the results of the Irazu model presented in the last two sections including the *GRCs* and their comparison with the RS2 model (Figure 5-31), as well as the radial deformations near the shaft boundary and their comparison with the extensometer measurements (Figure 5-33), it is concluded that the Irazu model is reasonably calibrated. Therefore, in the next step, the calibrated model will be used to analyze the stability of the shotcrete liner as a sole support element and in combination with the concrete liner.

5.8. Stability Analysis of Initial Shotcrete Liner

Now that the shaft model is calibrated and the input parameters of the rock mass, the initial shotcrete and the final concrete liners are known, the next step is to assess the stability of the shotcrete liner and better understand its fracturing processes during the shaft advance. For this purpose, two scenarios are considered as described below:

Scenario A: In this scenario, it is assumed that the shotcrete liner is the only support element used for the stability of the mine shaft. The 12-hr shotcrete liner has a thickness of 50 mm, and its installation timing (i.e. wall radial displacement at which the liner is installed) is shown in Figure 5-31. The model geometry for this scenario is presented in Figure 5-34. As can be seen in this figure, the model consists of three sub-domains with similar element sizes used in Figure 5-28a.

Scenario B: In this scenario, both the initial shotcrete and the final concrete liners are used to support the mine shaft. The 12-hr shotcrete and 28-day concrete liners have thicknesses of 50 mm and 200 mm, respectively. The installation timings (i.e. wall radial displacements at which the liners are installed) for both liners are shown in Figure 5-31. The model geometry including the sizes for mesh elements in different sub-domains are shown in Figure 5-28a.

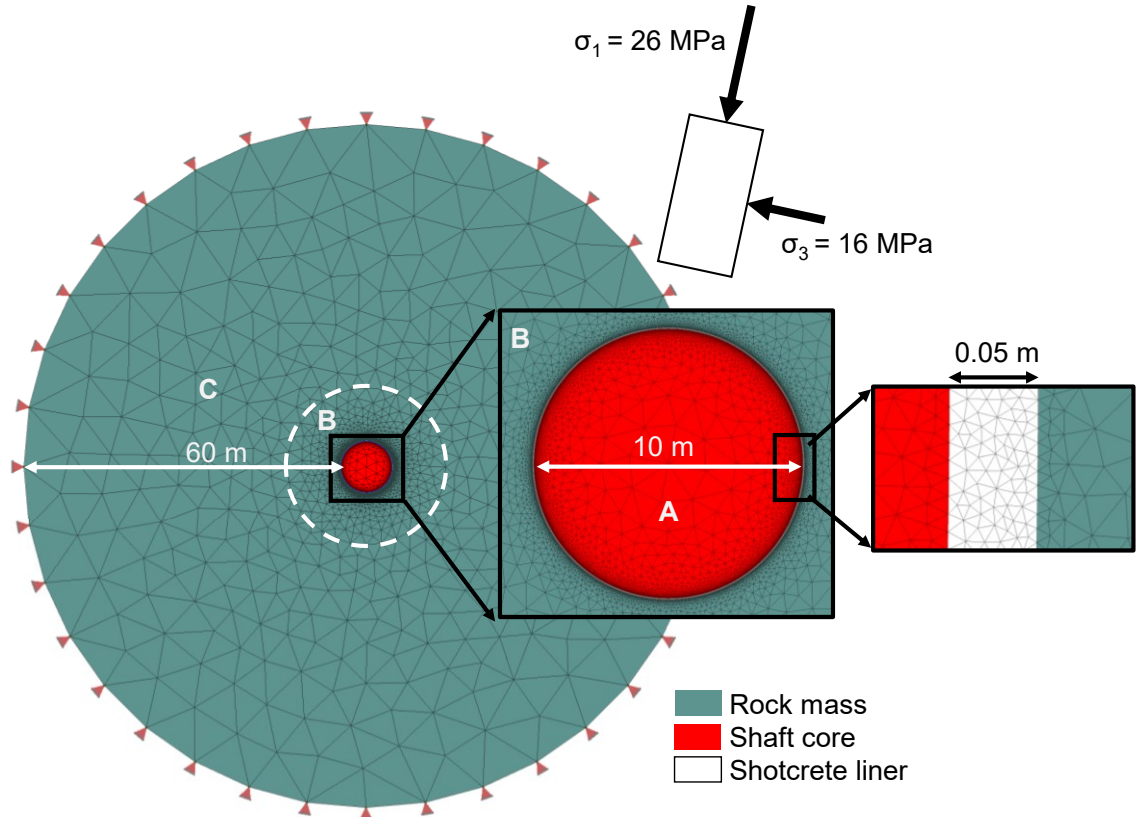


Figure 5-34 Geometry of the mine shaft supported with the initial shotcrete liner simulated in Irazu using different sub-domains with different mesh element sizes for the rock mass, the core and the liner

5.8.1. Analysis of Scenario A

In Chapter 2, the results of the stability analysis of the initial shotcrete liner, where the liner was simulated as a structural element with elastic properties in RS2, suggest that the liner is overloaded, meaning that its load capacity is exceeded during the excavation advance. However, it was not possible to conclude whether overloading results in the complete failure of the shotcrete liner. In Chapter 4, the shotcrete liner was simulated as a material model with elasto-plastic properties. The results of this analysis indicated that some sections of the shotcrete liner yield. The calculation of the strain factor of safety revealed that the yielded sections of the 50 mm shotcrete fail as their strain factors of

safety were calculated to be less than unity. In these simulations, the shotcrete was assumed to be the only support element in the shaft model.

A similar analysis was conducted in Irazu by considering the 50 mm shotcrete liner as the only support element in the mine shaft. The results of this analysis are presented in Figure 5-35. Figure 5-35a shows the extent of the fractured zone around the shaft. The boxed area in Figure 5-35a is zoomed-in and shown in Figure 5-35b. This figure illustrates the bulking of the fractured rock mass behind the shotcrete towards the center of the shaft. The shotcrete liner is buckled at this location. Figure 5-35c clearly shows the failure mode of the shotcrete liner, which includes tensile fracturing near the outer surface of the liner and fracturing of the inner surface of the liner at the shotcrete-rock contact due to compressive stresses generated as a result of buckling of the liner. As a reminder, the thrust-moment diagram of the shotcrete liner analyzed in Chapter 3 shows an excessive thrust generated in the shotcrete liner due to the shaft convergence. In the Irazu model, both the axial thrust due to shaft convergence and the lateral pressure caused by rock mass bulking have resulted in buckling of the shotcrete liner towards the center of the shaft and its failure, as illustrated in Figure 5-35c.

Therefore, based on the results of finite and hybrid finite-discrete element models, it is concluded that the 50 mm shotcrete liner should not be used as the only support element for this mine shaft. Further simulations with the use of the 50 mm shotcrete liner and the 200 mm concrete liner were conducted and the results are presented next.

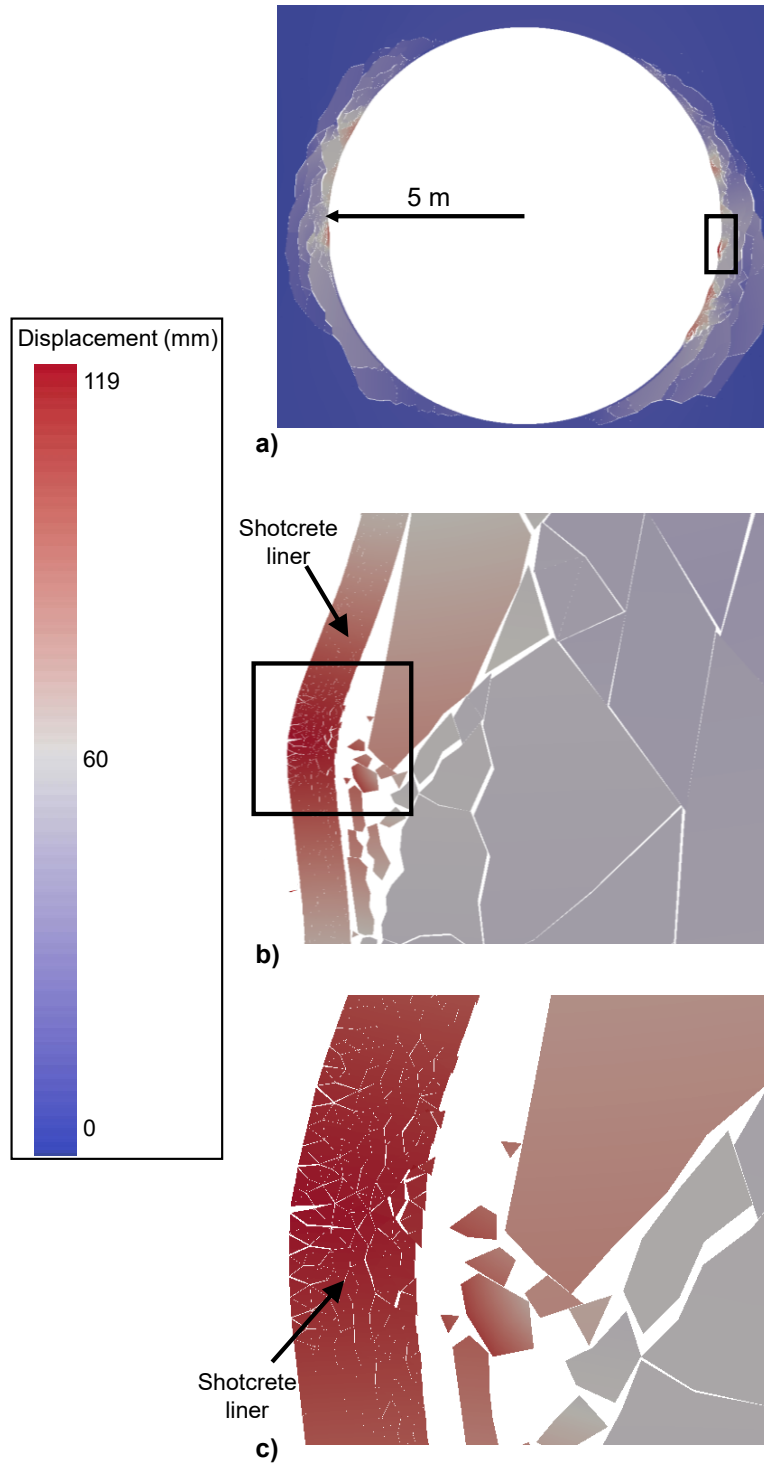


Figure 5-35 a) Extent of rock mass fracturing near the mine shaft supported with initial 12-hr shotcrete liner as the only support element; b) zoomed-in view of the boxed area in Figure 5-35a, showing bending of the shotcrete liner due to axial thrust and rock mass bulking; c) zoomed-in view of the boxed area in Figure 5-35b, indicating the failure of shotcrete liner

5.8.2. Analysis of Scenario B

It was found in Chapter 4 that the strain factor of safety for the shotcrete liner simulated as a material model with elasto-plastic properties increases to above unity if the thickness of the liner increases to 100 mm from 50 mm. This suggests that the minimum shotcrete thickness required for the stability of the liner is 100 mm. It was also found that the factor of safety of the 28-day concrete liner simulated using the structural element with elastic properties is well above 1.4 if it is used along with the 100 mm initial shotcrete liner.

In scenario B, both the initial and final liners are simulated as a material model in Irazu. The initial shotcrete liner with a thickness of 50 mm was assigned the micro-properties of the calibrated 12-hr shotcrete model (Table 5-5). The final concrete liner with a thickness of 200 mm was assigned micro-properties of the calibrated 28-day concrete model (Table 5-8). The results of this simulation are presented in Figure 5-36.

Figure 5-36a shows that the extent of the fractured zone around the shaft is less than that in Figure 5-35a. This is due to the addition of the final concrete liner to the support system. Figure 5-36b presents a closer view of the boxed area in Figure 5-36a. This figure indicates that although the rock mass near the shaft wall is fractured, the shotcrete seems to remain intact. A closer view of the shotcrete liner in Figure 5-36c shows that the shotcrete is slightly damaged. By comparing the geometry of the cracks in this figure with those observed in the *UCS* test (stage A in Figure 5-24), it is concluded that the load capacity of the shotcrete liner is reached when the final concrete liner is installed.

The results presented in Figure 5-35 suggests that although the shotcrete liner is damaged, the concrete liner remains intact during the shaft advance. Therefore, it can be concluded that the 50 mm shotcrete liner can be used as a temporary support for the mine shaft until the 200 mm concrete liner is installed.

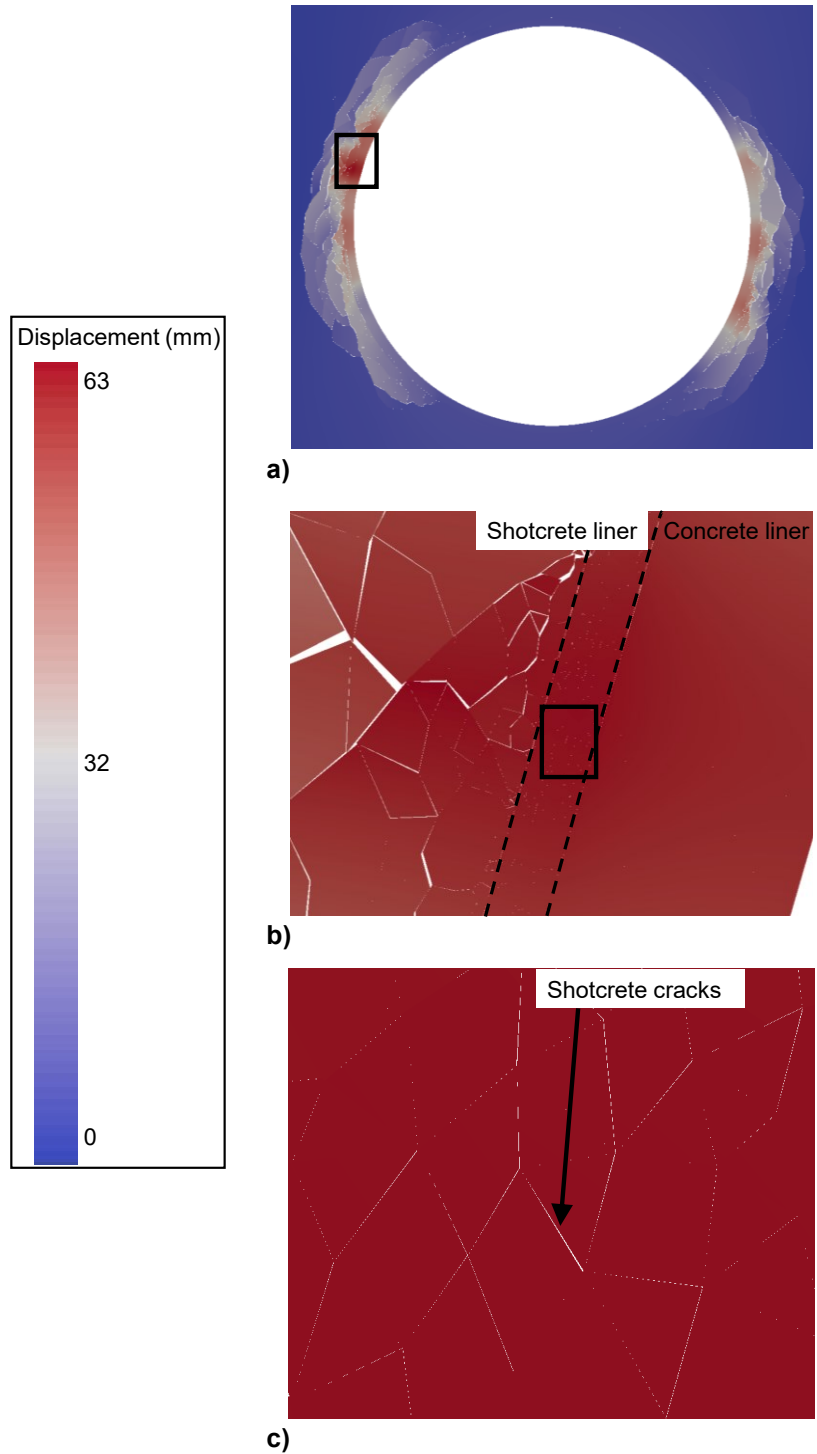


Figure 5-36 a) Extent of rock mass fracturing near the mine shaft supported with 12-hr shotcrete liner and 28-day concrete liner; b) zoomed-in view of the boxed area in Figure 5-36a, showing the fractured zone in the rock mass near the liner (dashed lines show concrete-shotcrete and shotcrete-rock mass contacts); and c) zoomed-in view of the boxed area in Figure 5-36b, indicating minor cracking of the shotcrete liner

5.9. Summary

In this chapter, Irazu, which is a two-dimensional numerical program based on the hybrid finite-discrete element method (*FDEM*) was used to simulate the shaft excavation advance and assess the stability of the shotcrete liner used as a temporary support. In this numerical method, the input parameters of the model are adjusted until the macro-properties become comparable to the laboratory test or field measurement results, through an iterative process called 'model calibration'. For the stability analysis of the mine shaft with all the support components in Irazu, model calibration was conducted for the shotcrete, the concrete and the rock mass near the shaft.

The calibration of the shotcrete and concrete models were based on the *UCS*, the Brazilian indirect tensile strength, and the Young's modulus of the 12-hr shotcrete and the 28-day concrete obtained from various sources. For the mine shaft, the model calibration was conducted by comparing the simulated radial deformation and the extensometer measurements after two rounds of blasting. Two scenarios were considered to analyze the stability of the initial shotcrete liner. In the first scenario, the shotcrete liner with a thickness of 50 mm was assumed to be the only support element. In the second scenario, the 50 mm shotcrete liner and the concrete liner with a thickness of 200 mm were the two elements of the support system for the mine shaft.

In the first scenario, the shotcrete liner failed due to bending caused by the shaft convergence resulting in excessive thrust in the liner as well as rock mass bulking behind the liner. In the second model, the shotcrete liner was found to be stable, although a few small cracks could be identified inside the liner. The results of numerical simulations suggest that the 50 mm shotcrete liner would not be used as the only support element for the mine shaft. Instead, it would sustain the shaft convergence even after reaching its peak strength until the 200 mm final concrete liner is installed. It is therefore concluded that the support system consisting of the 50 mm initial shotcrete liner sprayed to the shaft

wall 3 m behind the face and the 200 mm final concrete liner installed 12 m behind the face would ensure the stability of the mine shaft.

Chapter 6 Influence of Excavation Advance Rate on Stability of Initial Shotcrete Lining

6.1. Introduction

The aim of mining companies is to access deep mineral deposits by enhancing the excavation advance rates while maintaining safe workplaces. The application of mechanized excavation machinery in the development of shafts and tunnels leads to an increase in the overall performance and thus the net present value of the mining projects. Underground spaces are excavated using two main methods: drill and blast (D&B) and mechanized (Mech) excavations. While the Mech excavation is an ideal approach in moderately strong to weak rocks, the D&B method has been used in a wide range of rock conditions (i.e. hard to weak) in the mining industry. However, with technological advances, the mining industry has been looking into the Mech excavation method as an alternative in hard rocks (Stewart et al., 2006).

In this chapter, the influence of excavation advance rate on the stability of initial shotcrete lining will be investigated. For this purpose, typical shaft sinking advance rates for Mech and D&B excavation methods will be used to obtain the corresponding shotcrete ages and therefore their mechanical properties. The initial shotcrete liner will be simulated using both the structural element and the material model in RS2, and its stability will be evaluated in terms of load and strain factors of safety.

6.2. Advance Rates in Drill and Blast and Mechanized Tunnels

6.2.1. Drill and Blast (D&B) Excavation

The cycle in D&B excavations includes drilling, charging, blasting, ventilation, mucking, and ground support installation. According to Stewart et al. (2006), improvements to the

advance rate of D&B excavations in mine development headings have been achieved by using:

- faster drills,
- long round drilling (e.g. rounds longer than 5 m),
- emulsion explosives, which results in reduced number of holes, loading time, undesirable back and wall conditions, scaling, and therefore cycle time (Neumann, 2001),
- innovative scaling and ground support (e.g. use of hydro scaling), and by
- improving the operation and processes (i.e. dedicated development teams and equipment).

Stewart et al. (2006) compiled typical advance rates for different mine development headings in Canada and found that the average advance rate in D&B excavations is 6.5 m/day. They conducted a series of investigations to assess the limits of the advance rates in D&B excavations. The first sets of investigations were based on single-parameter analysis. They found that eliminating ground support time has the largest potential to improve the advance rate, and the use of shielding increases the advance rate by 29%. In the multi-parameter analysis, they found that the advance rate can be increased by 92% if the following conditions are implemented:

- using shield instead of ground support,
- reducing set-up times to 50%,
- using three-boom jumbo,
- reducing preparation time for drilling, and
- reducing the explosive charging time by 30%.

Stewart et al. (2006) further elaborated that by using a container truck and long rounds of drilling the advance rate can be increased by 178%. Therefore, based on the average advance rate in Canada (i.e. 6.5 m/day) and following the conditions mentioned above,

the advance rate can be increased to 18.6 m/day. Note that this advance rate was determined based on the assumption that it is theoretically possible to achieve the above technical developments and advances.

6.2.2. Mechanized (Mech) Excavation

As mentioned earlier, the Mech excavation method is more practical in soft rocks and has not been widely used in underground hard rock mining. However, there are a few case examples where the Tunnel Boring Machine (*TBM*) has been used successfully in mines (e.g. Stillwater platinum/palladium mine, Montana, USA). According to the benchmark study by Stewart et al. (2006), the average advance rate of *TBM* tunnels is 23.8 m/day. A more comprehensive compilation of advance rates in *TBM* tunnels in different rock masses of different qualities have been reported by Bruland (1998). Table 6-1 demonstrates how the advance rate of *TBM* tunnels changes as a function of *RMR*.

Table 6-1 Advance rates of *TBM* in different rock qualities (Bruland, 1998)

Rock Type		Advance rate (m/day)
Very hard	RMR = 90	10
Good	RMR = 70	23.7
Fair	RMR = 50	17
Poor	RMR = 30	18

6.3. Advance Rates in Drill and Blast and Mechanized Shafts

Conventional D&B is the typical excavation method in modern-day shaft sinking (Gleeson, 2018). The average advance rate in shafts (vertical developments) is much lower than that in tunnels (horizontal developments). Today, the average advance rate in shafts has reduced to 40-50 m/month (i.e. 1.5 m/day) from 100 m/month (i.e. 3.3 m/day). This is

mainly due to safety considerations and increasing challenging underground conditions associated with mining deeper orebodies (Gleeson, 2018).

In recent years, due to technological advances, there has been a tendency towards mechanical excavation methods for shaft sinking. The Shaft Boring Enlarger (*SBE*) is a shaft sinking technology that acts like a vertically oriented hard-rock *TBM*. This technology reduces shaft sinking time by 20-30% compared to conventional shaft sinking methods (Gleeson, 2018). The *SBE* operates in three stages: 1. Pilot hole, 2. enlargement to pilot borehole diameter with a reamer, and 3. enlargement to final diameter (i.e. 7.5 – 9.5 m). The average advance rate for this technology is 7-7.5 m/day but can reach to up to 10 m/day at its peak in soft rocks (e.g. Primsmulde shaft at Endsdorf colliery coal mine in southern Germany).

The Shaft Boring Roadheader (*SBR*) is another mechanized shaft sinking technology which was developed as part of Rio Tinto's 'Mine of the Future' program for shaft sinking in soft to medium-hard rock with diameters from 8-12 m (Gleeson, 2018). The main innovation in the *SBR* is the pneumatic mucking system that sucks up the loosened rock from the shaft bottom and transfers it to 20 m above the working level. Furthermore, it installs shotcrete from an upper working deck while cutting is going on at the shaft face. An example of shaft sinking using this method is two 1,000 m shafts with 8-11 m diameters through soft-medium strength rock in Jansen potash mine, Saskatchewan, Canada. It is suggested that an advance rate of 3 m/day can be achieved with improvements in the pneumatic mucking system (Gleeson, 2018).

Two other shaft sinking technologies designed for hard rock applications (UCS > 120 MPa) as part of the Rio Tinto's 'Mine of the Future' program include the Shaft Boring Machine (*SBM*) and Shaft Boring Cutterhead (*SBC*). These technologies can create shafts with diameters of up to 12 m, down to depths of 2000 m in the case of the *SBM* and 1000 m in the case of the *SBC*. In these technologies, shotcrete is also introduced via remote control directly behind the cutting wheel. It is expected that the *SBC* can deliver an advance rate

of 6 m/day (Gleeson, 2018). Note that it is still early days for these technologies and neither the *SBM* nor *SBC* are in use.

One of the methods used for increasing the advance rate in both D&B and Mech shafts is the application of fibre reinforced shotcrete as a temporary support element instead of rock bolts. This method was successfully used at Shaft 10 at the Resolution copper project in Arizona, US (Gleeson, 2018). In this approach, shotcrete is sprayed to the wall as a temporary support element until the final concrete lining is installed far from the face. This results in increasing safety while speeding up the development process.

In the following, two shaft sinking advance rates (i.e. 1.5 m/day and 6 m/day) corresponding to those of D&B and Mech excavation methods will be considered in the numerical simulations. The objective of this chapter is to investigate the influence of advance rate on the stability of initial (temporary) shotcrete lining simulated using both the structural element and the material model in RS2.

6.4. Stability Analysis of Shotcrete Lining in D&B and Mech Excavations

In the previous chapters, the numerical simulations were conducted for a shaft excavated using the D&B method with an advance rate of 3 m/day (referred to as the 'base case' here). In this chapter, excavation advance rates of 1.5 m/day and 6 m/day corresponding to a slow D&B excavation and a fast Mech excavation (i.e. *SBC* technology) are considered in the numerical simulations. In the case of Mech excavation, the shotcrete liner has less time to gain strength and stiffness for a given excavation advance compared to the base case, where the advance rate is 3 m/day. In the case of slow D&B excavation, shotcrete has more time to gain strength and stiffness until the next round compared to the base case. For these two cases, numerical simulations are conducted for the shotcrete lining age reached at 3 m behind the face, which is assumed to take 6 hours in the case of Mech excavation and 18 hours in the case of D&B excavation.

Therefore, in order to evaluate the stability of initial shotcrete linings in slow D&B and fast Mech excavations, the properties of shotcrete were obtained from empirical relationships reviewed in Section 2.7. Table 6-2 summarizes the properties of 6-hour and 18-hour shotcrete used for stability analysis of initial linings in slow D&B (1.5 m/day advance) and fast Mech (6 m/day advance) excavations along with the properties of 12-hour shotcrete used for the analysis of the base case with an advance rate of 3 m/day.

Table 6-2 Properties of shotcrete used for numerical simulations of shaft advance with different advance rates

Properties	Shotcrete age (hours)			References
	6	12	18	
Young's modulus (GPa)	9	12	16	Weber (1979); CEB-FIP Model Code (1990)
Compressive strength (MPa)	6.2	13.2	18	Chang (1994)
Tensile strength (MPa)	0.6	1.36	1.9	Byfors (1980)
Poisson's ratio	0.25	0.25	0.25	Carranza-Torres and Fairhurst (2000)

In Chapter 3 and Chapter 4, structural element and material model were used to simulate the initial shotcrete liner in RS2 and obtain its load and strain factors of safety. In this chapter, the same methods are used to simulate the shotcrete liners with thicknesses of 50 mm and 100 mm and analyze their stability in the two excavation methods with different advance rates (i.e. shotcrete properties given in Table 6-2).

6.4.1. Load Factor of Safety in CCM

As described in Chapter 3, the load factor of safety (FS_{load}) for the shotcrete liner can be determined by analyzing the *GRC* and the *SCC* in the *CCM*. FS_{load} is calculated from the ratio between the load capacity of the shotcrete and the load at the intersection point of the *SCC* and the *GRC*. For this purpose, the FS_{load} was calculated along the boundary of the shaft for different shotcrete thicknesses (e.g. 50 mm and 100 mm). The analyses were

conducted for advance rates of 6 m/day and 1.5 m/day representing Mech and slow D&B excavation methods. The following figure illustrates the FS_{load} variation along the boundary of the shaft.

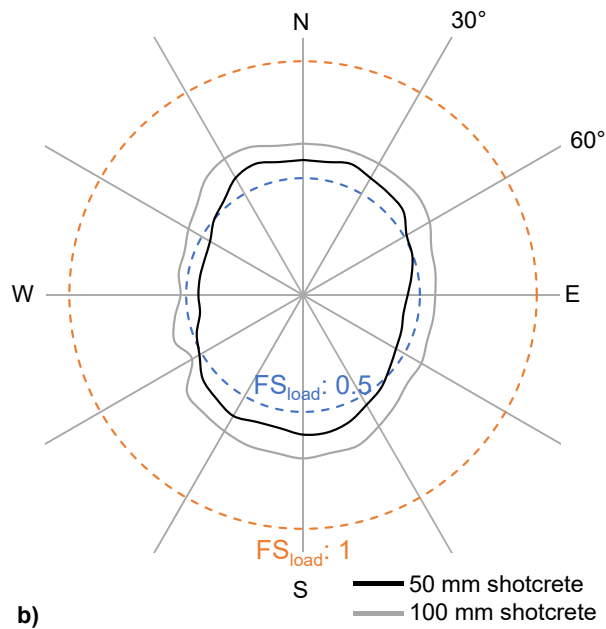
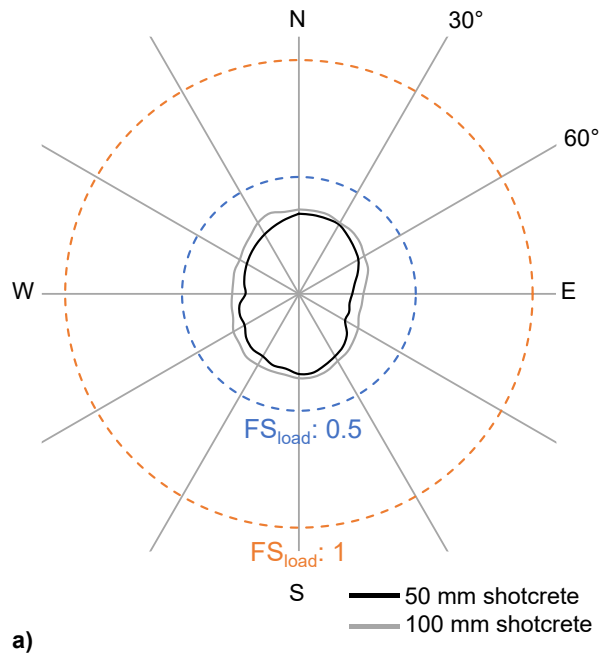


Figure 6-1 FS_{load} distribution around the shaft boundary for shotcrete thicknesses of 50 mm and 100 mm using: a) Mech method with an excavation advance rate of 6 m/day; and b) D&B method with an excavation advance rate of 1.5 m/day

In Figure 6-1a, the FS_{load} distributions are compared for two shotcrete thicknesses in the Mech excavation method, whereas, in Figure 6-1b, the comparison is shown for different shotcrete thicknesses in a slow D&B excavation method. It can be seen in these figures that by increasing the thickness of the shotcrete liner from 50 mm to 100 mm, the FS_{load} increases in both excavation methods. The results presented in Figure 6-1 indicate that the shotcrete liner is overloaded ($FS_{load} < 1$) independent of the excavation method and the liner thickness. As discussed in previous chapters, overloading does not necessarily mean complete shotcrete failure, as shotcrete especially at its early age behaves in an elasto-plastic manner. Therefore, the strain factor of safety based on the methodology introduced in Chapter 4 should be used to more reliably assess the stability of the shotcrete liner in both excavation methods.

6.4.2. Thrust-Moment Diagram

Further analyses were conducted by simulating the shotcrete liner using the structural element in RS2 with properties of 1.5-hour and 6-hour shotcrete representative for Mech and D&B excavations, as provided in Table 6-2. Note that in these analyses, the shotcrete liner is assumed to behave as an elastic material.

Figure 6-2 shows the support capacity diagrams for 50 mm (Figure 6-2a) and 100 mm (Figure 6-2b) shotcrete liners in Mech excavation (i.e. advance rate of 6 m/day). The overloaded segments of the liners are shown in red in the right images of Figure 6-2. It can be seen in this figure that 80% and 78% of the liner segments have factors of safety of less than unity in the models with 50 mm and 100 mm shotcrete liners, respectively. In the Mech excavation, the advance rate is higher than that in the D&B excavation, and therefore the shotcrete liner has less time to gain strength and stiffness. This would result in a lower factor of safety for the liner in Mech excavation than those of D&B excavations with lower advance rates (i.e. 3 m/day or 1.5 m/day).

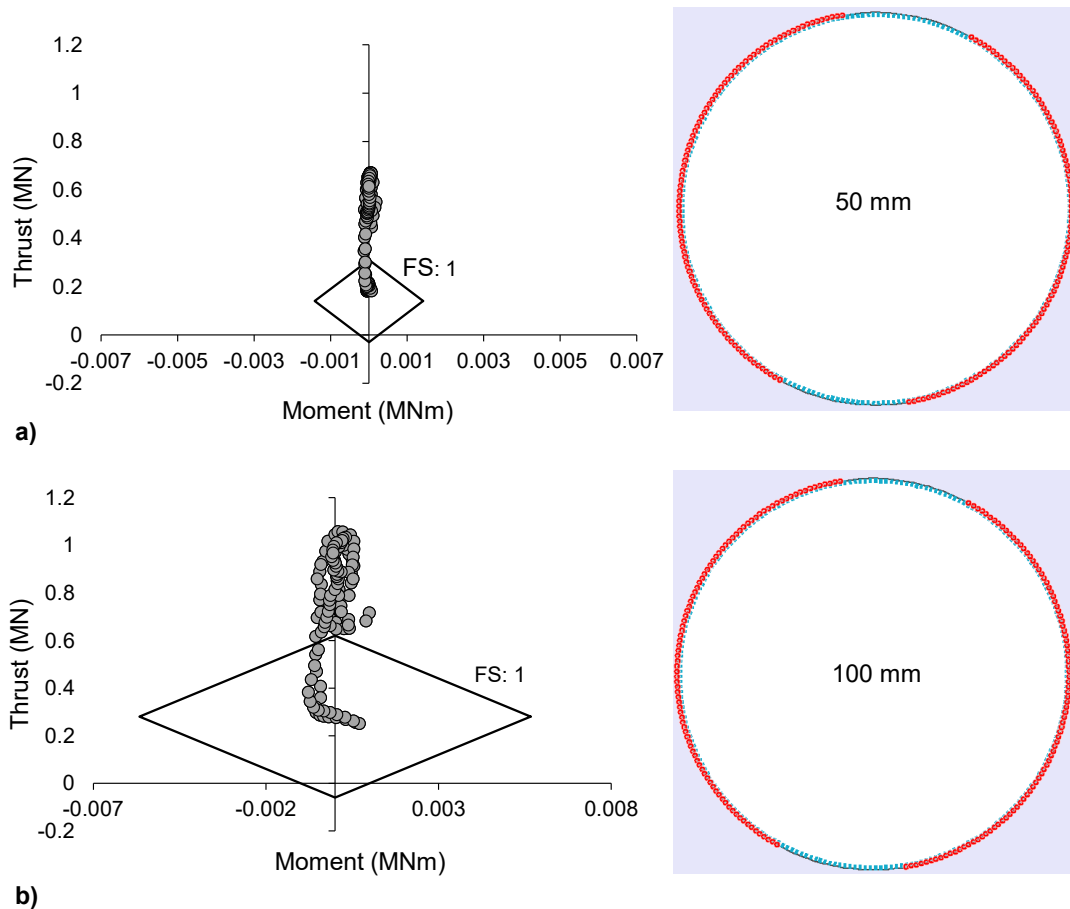


Figure 6-2 Thrust-moment diagrams and overloaded sections of 6-hr shotcrete lining (red segments) with thicknesses of: a) 50 mm and b) 100 mm for Mech excavation with an advance rate of 6 m/day

As illustrated in Figure 6-3, the liner factor of safety in the D&B excavation with an advance rate of 1.5 m/day (i.e. 18-hour shotcrete) is higher than those of Mech excavation (Figure 6-2) and D&B excavation with an advance rate of 3 m/day (Figure 3-8). The right image in Figure 6-2a indicates that in the case of 50 mm shotcrete, 42% of the liner segments have a factor of safety of less than unity. However, in the case of 100 mm shotcrete, all the liner segments have factors of safety of greater than unity.

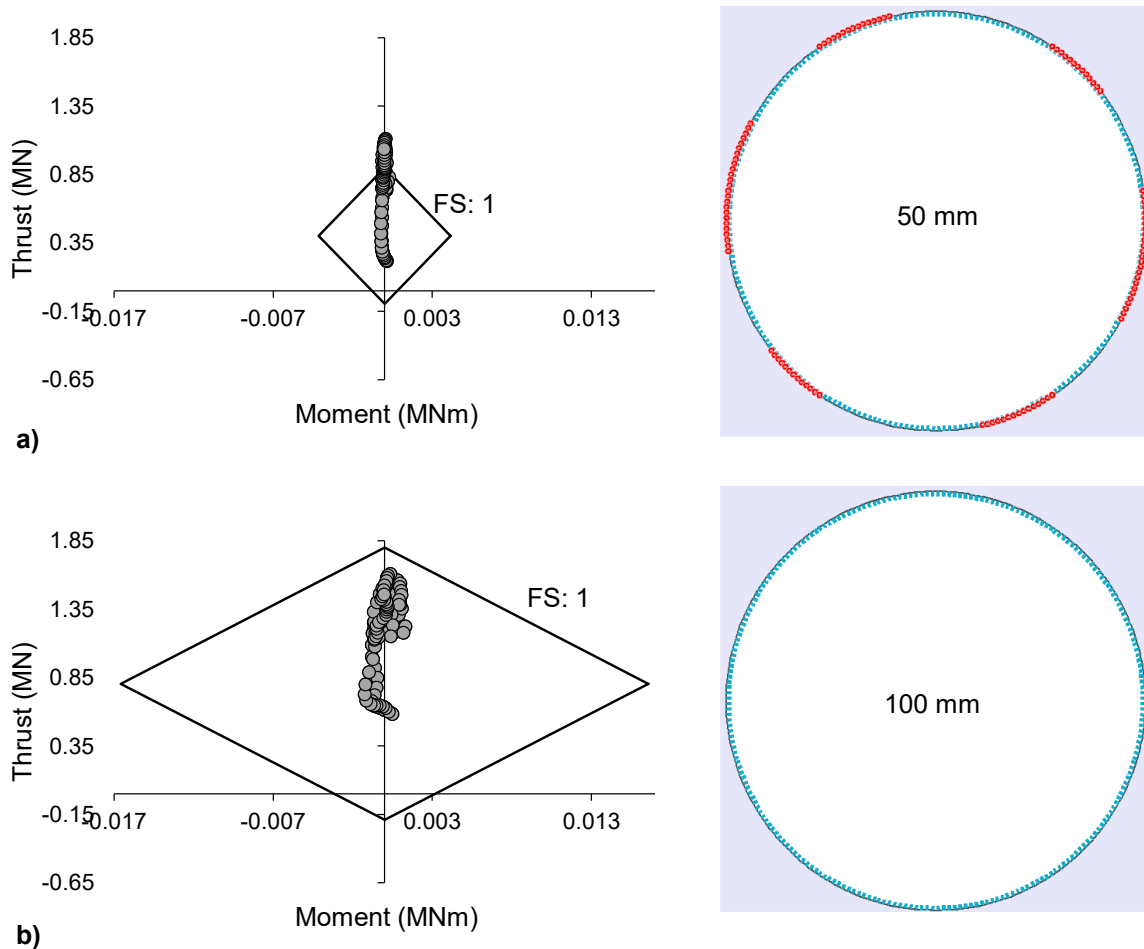


Figure 6-3 Thrust-moment diagrams and overloaded sections of 18-hr shotcrete lining (red segments) with thicknesses of: a) 50 mm and b) 100 mm for D&B excavation with an advance rate of 1.5 m/day

6.4.3. Strength Factor

In the next step, the material model with elastic properties was used to simulate the initial shotcrete liner and calculate the overloaded sections of the liner (i.e. strength factor less than 1) for 50 mm and 100 mm shotcrete in Mech and D&B excavation methods. The results presented in Figure 6-4 are comparable with those of models where the shotcrete liner was simulated using the structural element (Figure 6-2 and Figure 6-3).

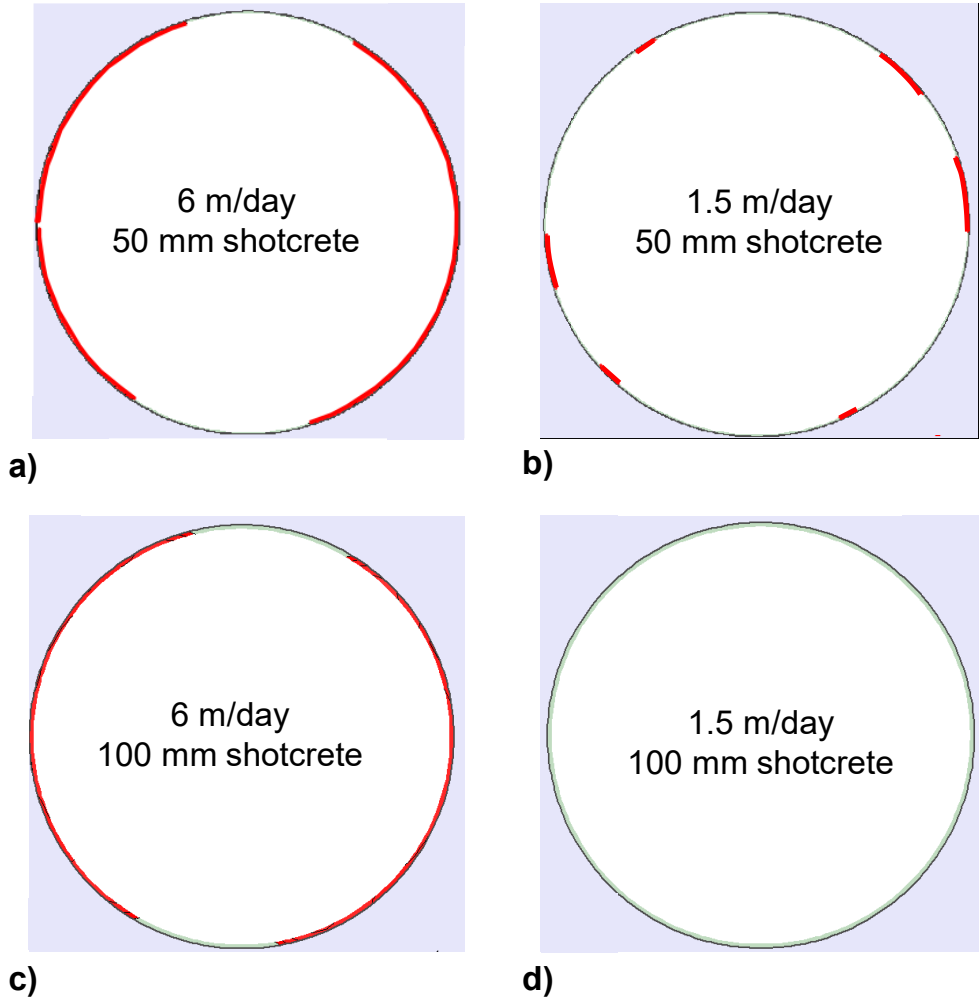


Figure 6-4 Comparison between overloaded sections of initial shotcrete lining (strength factor < 1 highlighted in red) simulated as material model: a) 50 mm shotcrete with advance rate of 6 m/day (i.e. fast Mech excavation); b) 50 mm shotcrete with advance rate of 1.5 m/day (i.e. slow D&B excavation); c) 100 mm shotcrete with advance rate of 6 m/day; and d) 100 mm shotcrete with advance rate of 1.5 m/day

The results of shotcrete liner simulations using the structural element and material model are summarized in Table 6-3. Note that in the case of shaft excavated with an advance rate of 1.5 m/day (i.e. slow D&B excavation) and supported with 100 mm initial shotcrete lining, all the structural elements have a strength factor of greater than unity.

Table 6-3 Comparison between percentage of overloaded sections of shotcrete liner simulated using material model and structural element in different excavation methods

Shotcrete thickness (mm)	Advance rate (m/day)	Shotcrete age (h)	Factor of safety < 1 (%)	
			Material model	Structural element
50 mm	6	6	74	80
	3	12	61	60
	1.5	18	26	36
100 mm	6	6	77	78
	3	12	30	36
	1.5	18	0	0

6.4.4. Strain Factor of Safety

Using the material model to simulate the shotcrete liner with elasto-plastic properties allowed for the calculation of FS_{strain} for the liner. In this section, the method introduced in Chapter 4 to calculate the strain factor of safety for the liner is used to investigate its variation along the boundary of the shaft for different shotcrete thicknesses and excavation methods (i.e. advance rates). In this method, the relative radial displacement of the shotcrete liner (calculated from the modeling stage it is installed up to the last stage where the internal pressure is zero) is used to determine the lateral strain of the shotcrete liner using Equation 4-2. Then, by comparing the shotcrete lateral strain determined from the numerical simulation (i.e. demand) and the lateral strain capacity of shotcrete estimated using Equation 4-1, the FS_{strain} for the liner can be calculated.

Using Equation 4-1, the lateral strains for 6-hr (i.e. 6 m/day advance rate) and 18-hr (i.e. 1.5 m/day advance rate) shotcrete were found to be 0.49% and 0.57%, respectively. The results of the strain factor of safety calculated for 50 mm shotcrete liner in Mech and D&B excavations (i.e. 6 m/day and 1.5 m/day advance rates) are presented in Figure 6-5.

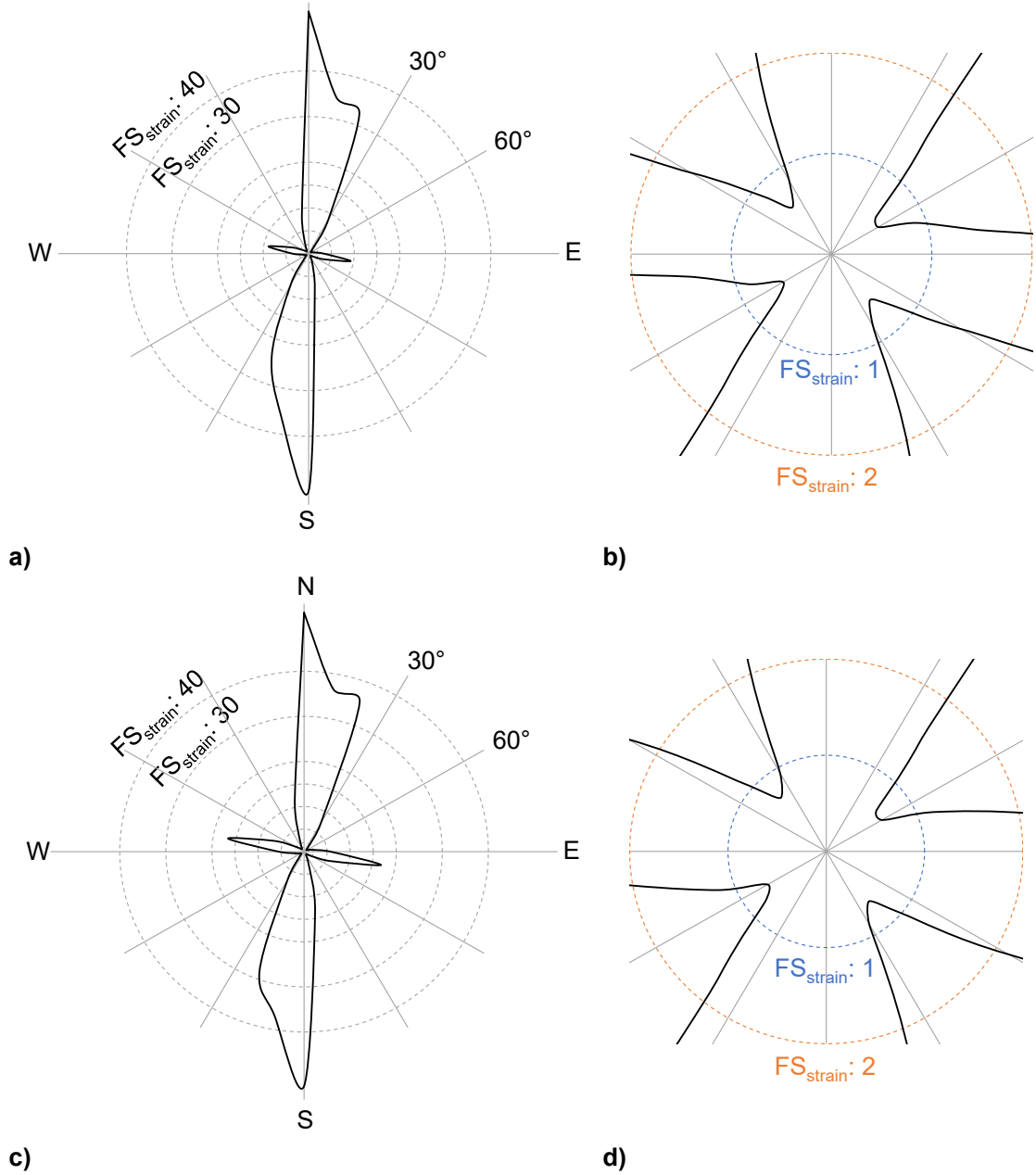
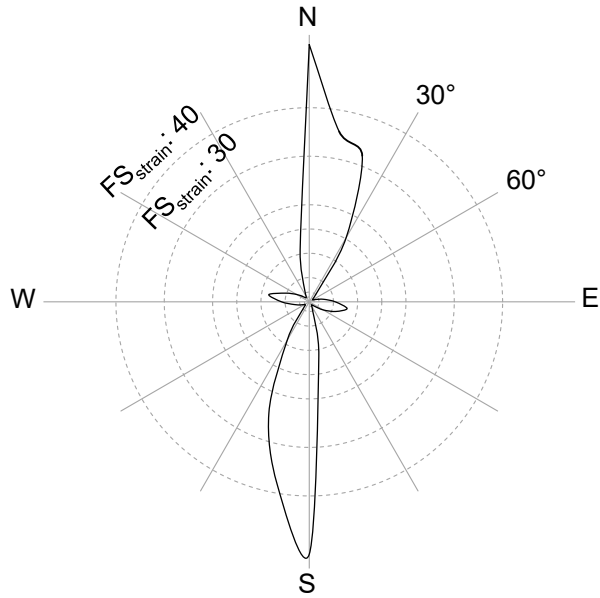


Figure 6-5 a) FS_{strain} distribution around the shaft boundary for 50 mm shotcrete liner with advance rate of 6 m/day; b) zoomed-in view of the centre of Figure 6-5a; c) FS_{strain} distribution around the shaft boundary for 50 mm shotcrete liner with advance rate of 1.5 m/day; and d) zoomed-in view of the centre of Figure 6-5c

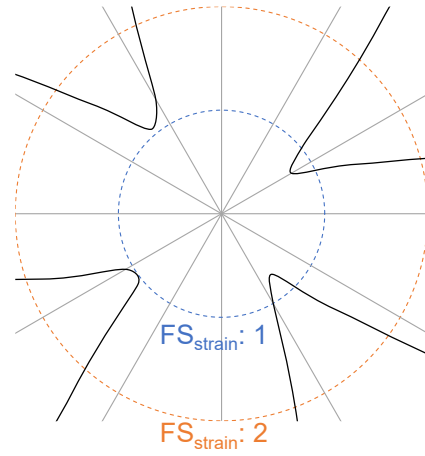
As illustrated in Figure 6-5a-b and Figure 6-5c-d, the strain factors of safety for 50 mm shotcrete is less than unity for some points along the shaft boundary. Note that even by reducing the excavation advance rate (from 6 m/day to 1.5 m/day) or in other words, increasing the shotcrete age (from 6 hours to 18 hours), the strain factor of safety is still

less than unity for some points along the shaft boundary. As a reminder, it was found in Chapter 4 that the 50 mm shotcrete liner is susceptible to failure in the mine shaft excavated using the D&B method with an advance rate of 3 m/day. Therefore, based on the calculated FS_{strain} , it is suggested that the 50 mm shotcrete liner should not be used as the temporary support element for the mine shaft excavated using the D&B nor Mech excavation methods.

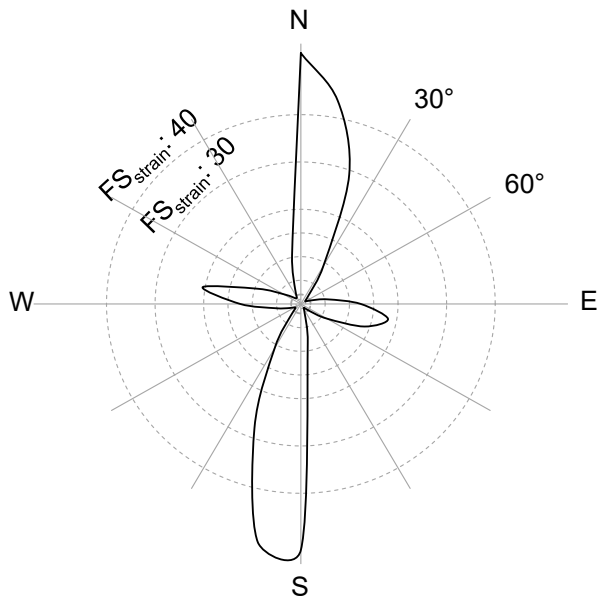
Further analysis was carried out by calculating the FS_{strain} for 100 mm shotcrete liner for Mech and slow D&B excavations having advance rates of 6 m/day and 1.5 m/day, respectively. As a reminder, it was found in Chapter 4 that the FS_{strain} of 100 mm shotcrete liner is greater than unity in the shaft excavated using the D&B method with an advance rate of 3 m/day. Figure 6-6a and Figure 6-6c show the variation of FS_{strain} along the shaft boundary for Mech and slow D&B excavations, respectively. It can be seen in Figure 6-6b that FS_{strain} for 100 mm shotcrete liner is less than unity for a few points around the shaft boundary in the Mech excavation with an advance rate of 6 m/day. Note that $FS_{strain} < 1$ is an indication of shotcrete failure. By adopting the D&B excavation method with an advance rate of 1.5 m/day, the FS_{strain} becomes greater than unity for all the points around the shaft boundary (Figure 6-6d). Therefore, it is concluded that 100 mm shotcrete liner can be used as a temporary support in the shaft using the D&B excavation method until the permanent concrete lining is installed.



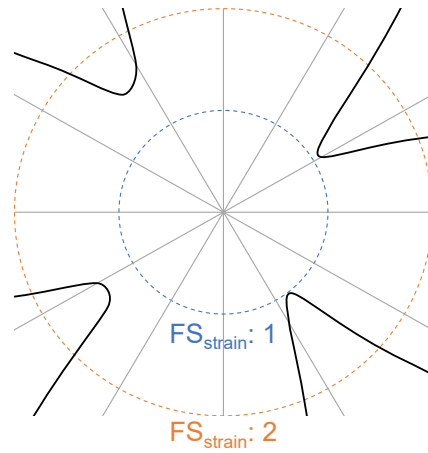
a)



b)



c)



d)

Figure 6-6 a) FS_{strain} distribution around the shaft boundary for 100 mm shotcrete liner with advance rate of 6 m/day; b) zoomed-in view of the centre of Figure 6-6a; c) FS_{strain} distribution around the shaft boundary for 100 mm shotcrete liner with advance rate of 1.5 m/day; and d) zoomed-in view of the centre of Figure 6-6c

6.5. Summary

In this chapter, typical advance rates for different excavation methods in horizontal and vertical developments were first reviewed. Next, RS2 was used to investigate the influence of the excavation method and the corresponding advance rate on the stability of initial shotcrete liners of various thicknesses (i.e. 50 mm and 100 mm). For this purpose, a slow D&B and a fast Mech excavation methods with advance rates of 1.5 m/day and 6 m/day were considered in the numerical analyses. The shotcrete liner was simulated as the structural (beam) element with elastic properties and the material model with both elastic and elasto-plastic properties. Both FS_{load} and FS_{strain} were used for the stability analysis of the initial shotcrete liner.

Table 6-4 provides a summary of the results of all the analyses conducted in Chapter 3, 4, and 6, in terms of the load and strain factors of safety calculated for initial shotcrete liner of different thicknesses in Mech and D&B excavations considering their advance rates. As can be seen in this table, the excavation advance rate plays an important role on the stability of initial shotcrete lining. Based on the analyses conducted for this mine shaft, it is concluded that the FS_{load} for the initial shotcrete liner is less than 1 independent of the excavation method and the liner thickness. The FS_{strain} is also less than unity except for the case when 100 mm shotcrete liner is used in the D&B excavation with an advance rate of 3 m/day or less.

Table 6-4 Calculated factors of safety for initial shotcrete lining in D&B and Mech excavations

Shotcrete thickness (mm)	Excavation method	Advance rate (m/day)	Shotcrete age (h)	FS _{load}	FS _{strain}
50	Mech	6	6	< 1 (overloaded)	< 1 (unstable)
	D&B	3	12	< 1 (overloaded)	< 1 (unstable)
	D&B	1.5	18	< 1 (overloaded)	< 1 (unstable)
100	Mech	6	6	< 1 (overloaded)	< 1 (unstable)
	D&B	3	12	< 1 (overloaded)	> 1 (stable)
	D&B	1.5	18	< 1 (overloaded)	> 1 (stable)

Note that the results presented in Table 6-4 are based on the assumption that shotcrete liner is the only support element for the shaft. When combined with other (permanent) support measures such as rock reinforcement and concrete liner, it might be possible to use 100 mm shotcrete in Mech excavation or 50 mm and 75 mm shotcrete liners in both D&B and Mech excavation methods.

Chapter 7 Summary, Conclusions, and Recommendations

7.1. Summary

In this research, RS2 which is a 2D numerical program based on the *FEM* and Irazu which is a 2D numerical program based on the *FDEM* were used to simulate the 3D excavation advance of a mine shaft and to assess the stability of the shotcrete liner used as a temporary support by considering the excavation advance rate. In this shaft, four extensometers were installed to monitor the radial deformation of the rock mass near the excavation boundary. The monitoring data were used to calibrate the 2D models. The shotcrete liner was simulated using a structural element in RS2 (Chapter 3), and a material model in RS2 (Chapter 4 and Chapter 6) and Irazu (Chapter 5). The concrete liner was simulated using structural elements in RS2 (Chapter 4) and material model in Irazu (Chapter 5).

The load (Chapter 3) and strain factors of safety (Chapter 4) were determined to assess the stability of the initial shotcrete liner based on the results of RS2 models. The numerical simulation of the shaft in Irazu required extensive calibration for the shotcrete, the concrete, and the rock mass near the shaft. The calibration of the shotcrete and the concrete models was based on the strength and deformation properties of 12-hr shotcrete and 28-day concrete obtained from the results of laboratory tests and empirical equations. The calibration of the rock mass in the shaft model was based on the extensometer measurements. The calibrated Irazu model was used to explicitly simulate progressive fracturing of the rock mass and the shotcrete liner during the excavation advance and to investigate the stability of the shotcrete liner as a sole support element and in combination with the concrete liner (Chapter 5). The influence of the excavation advance rate on the stability of the initial shotcrete liner for two excavation methods (i.e. fast mechanized and slow drill-and-blast excavations) was investigated using the *FEM* model (Chapter 6).

It should be emphasized that the details of the support design for this shaft, such as the type, thickness, and properties of the shotcrete and concrete liners, were not available. Therefore, the analyses presented in this thesis were based on engineering judgment, assumptions, and information obtained from various sources in the literature. Thus, the conclusions drawn from the results of this investigation should remain within the bounds and limitations outlined in this thesis.

7.2. Conclusions

The following conclusions were drawn from the results of numerical simulations conducted through this research:

- Conventional load factor of safety

The *CCM* and its components (*GRC*, *LDP* and *SCC*) were used to calculate the load factor of safety, FS_{load} . The FS_{load} is the ratio between the maximum capacity of the support element to the maximum pressure applied to it. The *GRC* was obtained for several points around the shaft boundary and used to calculate the FS_{load} . It was found that the load factor of safety for the initial shotcrete is less than unity independent of its thickness (i.e. 50 mm, 75 mm and 100 mm). This suggests that the shotcrete liner is overloaded and experiences plastic deformation.

- Support capacity diagram

The initial shotcrete liner was simulated using a structural element with elastic properties in RS2. The support capacity diagrams (i.e. thrust-moment diagram) for shotcrete and concrete liners of various thicknesses were developed. Based on the results of this analysis, it was found that the initial shotcrete liner, independent of its thicknesses (50 mm, 75 mm, and 100 mm), is overloaded (i.e. some sections along the liner exhibit a factor of safety less than unity). The factor of safety for the 200 mm final (28-day) concrete liner was found to be well above 1.4.

- Strain factor of safety

To consider the plastic deformation of early-age shotcrete for the stability analysis of the shotcrete liner, the liner was simulated using a material model with elastic-perfectly plastic material behavior in RS2. The lateral strain capacity of the shotcrete estimated from the results of laboratory tests was compared with the radial strain of the liner obtained from the RS2 shaft model to calculate the strain factor of safety FS_{strain} for the shotcrete liner. The variation of the FS_{strain} along the boundary of the shaft was obtained for different liner thicknesses (i.e. 50 mm, 75 mm, and 100 mm). It was found that the strain factors of safety for 50 mm and 75 mm shotcrete liners are less than unity. The minimum shotcrete thickness to reach a strain factor of safety above unity was found to be 100 mm. By considering the results of previous analyses, it is concluded that the 100 mm shotcrete liner is overloaded (i.e. $FS_{load} < 1$) and therefore deforms plastically during the excavation advance but remains stable until the final concrete is installed.

- Progressive yielding and fracturing processes of shotcrete liner

Some sections of the shotcrete liner simulated in RS2 using the material model with elastic-perfectly-plastic properties were found to yield and deform plastically by the time the final concrete liner was installed. Analyses of the results of RS2 models showed that yielding starts from the outer boundary of the shotcrete and propagates towards the boundary of the shaft. In Irazu, both the shotcrete and concrete liners were simulated using material models. Two scenarios were considered for the stability analysis: First, the 50 mm shotcrete liner was assumed to be the only support element for the shaft. In this scenario, it was observed that the shotcrete liner is progressively fractured during the excavation and eventually fails. In the second scenario, the 50 mm initial shotcrete and the 200 mm final concrete liners were the two elements of the support system for the shaft. In this scenario, it was found that the shotcrete would crack, but not failed, by the time the final concrete liner is installed. In other words, the shotcrete cracks and deforms plastically but remains stable until the final, permanent concrete liner is installed. From

this analysis, it is concluded that the minimum shotcrete thickness required to provide a temporary support for the shaft until the final concrete liner is installed is 50 mm.

- Effect of excavation advance rate on the stability of initial shotcrete liner

The mechanical properties of shotcrete are a function of shotcrete age (i.e. curing time). In this research, the shotcrete age after the first round of blast (or excavation advance) was estimated based on the excavation advance rate. Different excavation advance rates corresponding to different excavation methods were considered for the stability analyses of shotcrete liners of various thicknesses. The excavation methods considered for this investigation included a mechanized excavation with an advance rate of 6 m/day and a slow drill-and-blast excavation with an advance rate of 1.5 m/day. The stability of the initial shotcrete liner for these excavations was investigated by assigning different properties to the shotcrete liner corresponding to different shotcrete ages (i.e. curing time) estimated based on the excavation advance rates. In the model simulating the mechanized excavation (i.e. advance rate of 6 m/day), the load and strain factors of safety for the shotcrete liner were calculated to be less than unity, independent of the thickness of the liner (i.e. 50 – 100 mm). The stability analysis of the shotcrete liner simulated using the structural element in the model simulating a slow drill-and-blast excavation (i.e. advance rate of 1.5 m/day) suggested that the load factor of safety for 100 mm shotcrete liner is above unity. Moreover, the strain factor of safety for the 100 mm shotcrete liner in this excavation method was calculated to be greater than unity.

7.3. Recommendations for Future Work

Considering the results presented in this thesis and the numerical methods used, the following recommendations for future research directions are provided:

- Excavation surface irregularities

In this research, the shaft boundary was assumed to be smooth with no irregularities. An underground opening excavated using the drill-and-blast method is unlikely to have a smooth surface. Excavation surface irregularities may result in stress concentration increasing the potential for local failure of the rock mass near the excavation. Surface irregularities can be simulated in 2D models to investigate its effect on the stability of shotcrete liners. It is known that surface irregularities increase the bending moment on the liner which may result in local failure of the shotcrete.

- Blast damage

Underground excavations are subjected to blast damage, which includes cracking of the rock mass near the excavation boundary. Blast damage results in the reduction in the strength and deformation modulus of the rock mass around the excavation. In the future, blast damage can be considered in the simulations by assigning different properties (i.e. lower strength and deformation properties) to the rock mass near the excavation.

- Time-dependent shotcrete properties

As pointed out in this document, shotcrete properties change with time. In this research, the shotcrete properties were estimated based on the advance rate and the age of shotcrete. The age of shotcrete was assumed to be the period from the liner installation to the next round of blasting. However, the change in the shotcrete age and therefore its properties were not considered in the numerical simulations. Therefore, the results of this research in terms of shotcrete stability analysis are conservative, as the shotcrete becomes harder and stiffer with the excavation advance. The progressive evolution of shotcrete strength and deformation properties can be considered in the future research, especially in 3D models.

- Laboratory tests on early-age shotcrete (< 12 hrs)

In this research, shotcrete models were calibrated based on properties extrapolated from the results of laboratory tests on shotcrete reported by Saw et al. (2009). Further laboratory experiments on young shotcrete (< 12 hrs) to obtain its mechanical properties including the full stress-strain curves in both axial and lateral directions are suggested.

- 3D numerical modeling

2D numerical modeling is the norm for preliminary design of underground excavations and ground support. A more detailed excavation design can be conducted using 3D numerical models. In this study, the 3D shaft advance was simulated in 2D models using the internal pressure reduction approach in RS2 and the core softening approach in Irazu. The goal was to develop a design methodology for initial (temporary) shotcrete lining in circular excavations. In the next step, it is recommended to simulate the mine shaft with liners using an axisymmetric model. However, in this modeling approach the stress field should be hydrostatic, and the rock mass is assumed to be homogenous. A more detailed excavation design can be carried out using full 3D numerical models. In such models, the change in the properties of the shotcrete lining during the excavation advance can also be considered.

References

- AFTES-groupe de travail numero 7 (1983) Recommendation sur l'emploi de la methode convergence-confinement. Dans Tunnels et ouvrages souterrains, vol. 59, pp 218-238
- Aldrian W (1991) Beitrag zum Materialverhalten von fruh belastetem Spritzbeton; Dissertation; Institut fur Geomechanik, Tunnelbau und Konstruktiven Tiefbau, Montanuniversitat Leoben.
- Alejano L.R, Rodriguez-Dono A, Alonso E, & Fdez-Manin G (2009) Ground reaction curves for tunnels excavated in different quality rock masses showing several types of post-failure behavior. Tunnelling and Underground Space Technology, vol. 24, no. 6, pp. 689-705
- Alonso E, Alejano L.R, Varas F, Fdez-Manin G, & Carranza-Torres C (2003) Ground reaction curves for rock masses exhibiting strain-softening behaviour. International Journal of Numerical and Analytical Methods in Geomechanics, vol. 27, pp. 1153-1185.
- ASCCT - Austrian Society for Concrete- and Construction Technology (2004), Guideline sprayed concrete, Csöngei GmbH.
- Aydan O, Sezaki M, & Kawamoto T (1992) Mechanical and numerical modelling of shotcrete, in Pande & Pietruszczak, eds, Numerical Models in Geomechanics, pp. 757-764.
- Barla M & Beer G (2012) Issue on advances in modeling rock engineering problems. International Journal of Geomechanics, vol. 12, no. 6, p. 617
- Barton N.R, Lien R, & Lunde J (1974) Engineering classification of rock masses for the design of tunnel support. Rock Mechanics, vol. 6, no. 4, pp. 189-239.
- Bernaud D & Rousset G (1996) The 'New Implicit Method' for tunnel analysis. International Journal of Numerical and Analytical Methods in Geomechanics, vol. 20, no. 9, pp. 673-690.
- Bieniawski Z.T (1974) Geomechanics classification of rock masses and its application in tunneling. In Proceeding of the Third Congress ISRM, Denver, 2, Part A, pp.27-32.
- Brown E.T, Bray J.W, Ladanyi B, & Hoek E (1983) Ground response curves for rock tunnels.
- Bruland A (1998) Future Demands and Development Trends, Norwegian Tunneling Society.
- Byfors J (1980) Plain concrete at early ages, Technical report, Swedish Cement and Concrete Research Institute.
- Cai M, Kaiser P.K, Tasaka Y, & Minami M (2007) Determination of residual strength parameters of jointed rock masses using the GSI system. International Journal of Rock Mechanics and Mining Sciences, vol. 44, pp. 247-265.
- Cantieni L & Anagnostou G (2009) The effect of the stress path on squeezing behaviour in tunnelling. Rock Mechanics and Rock Engineering, vol. 42, no. 2, pp. 289-318.

- Carranza-Torres C & Fairhurst C (2000) Application of the convergence–confinement method of tunnel design to rock masses that satisfy the Hoek-Brown failure criterion. *Tunnelling and Underground Space Technology*, vol. 15, no. 2, pp. 187-213.
- Carranza-Torres C (1998) Self similarity analysis of the elastoplastic response of underground openings in rock and effects of practical variables. Ph.D. Thesis, University of Minnesota.
- Carranza-Torres C (2004) Elasto-plastic solution of tunnel problems using the generalized form of the Hoek–Brown failure criterion. *International Journal of Rock Mechanics and Mining Sciences*, vol. 13, no. 3, pp. 629-639.
- Carranza-Torres C, Diederichs M.S (2009) Mechanical analysis of circular liners with particular reference to composite supports. For example, liners consisting of shotcrete and steel sets. *Tunnelling and Underground Space Technology*, vol. 24, pp. 506-532.
- CEB-FIP Model Code (1990) Design Code - Comite Euro-International du Beton, Thomas Telford, London.
- Chang Y (1994) Tunnel support with shotcrete in weak rock - A rock mechanics study, PhD thesis, Royal Institute of Technology, Stockholm, Sweden.
- Chern J.C, Shiao F.Y, & Yu C.W (1998) An empirical safety criterion for tunnel construction, *Proceedings of Regional Symposium on Sedimentary Rock Engineering*, Public Construction Commission, Taipei, Taiwan, pp. 222-227.
- Cho N, Martin C.D, & Sego D.C (2007) A clumped particle model for rock. *International Journal of Rock Mechanics and Mining Sciences*, vol. 44, no. 7, pp. 997-1010.
- Constrado (1983) *Steel Designers' Manual*. Granada: Constructional and Steel Research and Development Organisation.
- Corbetta F, Bernaud D, & Nguyen-Minh D (1991) Contribution a'la method convergence–confinement par le principe de la similitude. *Rev Fr Geotech*, vol. 54, pp. 5-11
- Coulomb C.A (1776) *Essai sur une application des regles des maximis et minimis a quelques problemes de statique relatifs, a la architecture*. *Mem. Acad. Roy. Div. Sav.*, vol. 7, pp. 343-387.
- Cundall P.A & Hart R.D (1992) Numerical modelling of discontinua. *Engineering Computations*, vol. 9, pp. 101-113.
- Den Hartog J.P (1961) *Strength of Materials*. Dover Publications, Inc., New York.
- Dimmock R, Rispin M, & Knight B (2003) Early re-entry into working faces in mines through modern shotcrete technology, Canadian Institute of Mining, Metallurgy and Petroleum Annual General Meeting, Canadian Institute of Mining, Metallurgy and Petroleum, Westmount.
- Duncan Fama M.E (1993) Numerical Modeling of Yield Zones in Weak Rock, In J.A. (ed) *Hudson Comprehensive Rock Engineering*, Pergamon, Oxford, vol. 2. pp. 49-75.
- Fowler D.W (2009) Failure, Distress and Repair of Concrete Structures. *Woodhead Publishing Series in Civil and Structural Engineering*, Chapter 7, pp. 194-207.
- Geomechanica (2019) 'Irazu', version 4, Toronto, Canada.

- Geomechanica (2019) Irazu 2D Geomechanical Simulation Software. Verification Manual.
- Gercek H (2007) Poisson's ratio values for rocks, *International Journal of Rock Mechanics and Mining Sciences*, vol. 44, pp. 1–13.
- Gieck K (1977) *Technische Formelsammlung*. Berlin: Verlag.
- Gleeson D (2018) *International Mining*, vol. Sep, pp. 28-34.
- González-Nicieza C, Álvarez-Vigil A.E, Menéndez-Díaz A, & González-Palacio C (2008) Influence of the depth and shape of a tunnel in the application of the convergence–confinement method. *Tunnelling and Underground Space Technology*, vol. 23, pp. 25-37.
- Graziani A, Boldini D, & Ribacchi R (2005) Practical Estimate of Deformations and Stress Relief Factors for Deep Tunnels Supported by Shotcrete. *Journal Rock Mechanics and Rock Engineering*, vol. 38, no. 5, pp. 345-372.
- Gschwandtner G.G & Galler R (2012) Input to the application of the convergence confinement method with time-dependent material behaviour of the support, *Tunneling and Underground Space Technology*, vol. 27, no. 1, pp. 13-22.
- Guilloux A, Bretelle S, & Bienvenue F (1996) Prise en compte des presoutenements dans le dimensionnement des tunnels. *Géotechnique*, vol. 76, pp. 3–16.
- Hoek E & Brown E.T (1980) Empirical strength criterion for rock masses. *Journal of Geotechnical and Environmental Engineering*, vol. 106, pp. 1013-1035.
- Hoek E & Brown E.T. (1997) Practical estimates of rock mass strength. *International Journal of Rock Mechanics and Mining Sciences and Geomechanics Abstracts*; vol. 34, no. 8, pp. 1165-1186.
- Hoek E & Brown E.T. (2019) The Hoek-Brown failure criterion and GSI - 2018 edition. *Journal of Rock Mechanics and Geotechnical Engineering*; vol. 11, no. 3, pp. 445-463.
- Hoek E & Guevara R (2009) Overcoming squeezing in the Yacambú-Quibor tunnel. *Venezuela Rock Mechanics and Rock Engineering*, vol. 42, pp. 389-418.
- Hoek E (1994) Strength of rock and rock masses. *ISRM News Journal*, vol.2, no. 2, pp. 4-16.
- Hoek E (2007) Tunnels in weak rocks. *Practical rock engineering*; Rocscience website.
- Hoek E, Carranza-Torres C, & Corkum B (2002) Hoek-Brown criterion edition. In: Hammah R, Bawden W, Curran J, Telesnicki M, editors. *Mining and tunnelling innovation and opportunity, proceedings of the 5th North American rock mechanics symposium and 17th tunnelling association of Canada conference*. Toronto, Canada. Toronto: University of Toronto, pp. 267-273.
- Hoek E, Carranza-Torres C, Diederichs M.S, & Corkum B (2008) Kersten Lecture: Integration of geotechnical and structural design in tunnelling. *Proceedings University of Minnesota 56th Annual Geotechnical Engineering Conference*. Minneapolis, pp 1–53.
- Hoek E, Kaiser P.K, & Bawden W.F (1995) *Support of Underground Excavation in Hard Rock*. Balkema, Rotterdam.
- Itasca (1997) 'FLAC3D', version 2, Minneapolis, United States.

- Itasca (2004) 'FLAC3D', version 2.1, Minneapolis, United States.
- Itasca (2004) 'PFC2D', version 3.1. Minneapolis, United States.
- Itasca (2005) 'FLAC3D', version 3.3, Minneapolis, United States.
- Itasca (2009) 'FLAC3D', version 4, Minneapolis, United States.
- Iwaki K, Hirama A, Mitani K, Kaise S, & Nakagawa K (2001) A quality control method for shotcrete strength by pneumatic pin penetration test. *NDT and E International*, vol. 34, pp. 395-402.
- John M & Mattle B (2003) Shotcrete lining design: factors of influence, *Proceedings of Rapid Excavation and Tunnelling Conference (RETC)*, Society for Mining Metallurgy and Exploration, New Orleans, pp. 726-734.
- Kaiser P.K & Barlow J.P (1986) Rational assessment of tunnel liner capacity. *Canadian Tunneling Canadien*, p. 14.
- Kaiser P.K (2014) Deformation-based support selection for tunnels in strainburst-prone ground. In *Proceedings of the Seventh International Conference on Deep and High Stress Mining*, Australian Centre for Geomechanics, Perth, pp. 227-240.
- Kaiser P.K (2019) From common to best practices in underground rock engineering. In: *Proceeding of 14th ISRM congress*, Iguasu falls, Brazil.
- Kasai Y, Yokoyama K, & Matsui I (1971) Tensile properties of early-age concrete. In *Proceedings of the International Conference on Mechanical Behaviour of Materials*, pp. 288-299.
- Kirsch (1898) Die Theorie der Elastizität und die Bedürfnisse der Festigkeitslehre. *Zeitschrift des Vereines deutscher Ingenieure*, vol. 42, pp. 797-807.
- Labuz J.F & Zang A (2012) Mohr–Coulomb Failure Criterion. *Journal Rock Mechanics and Rock Engineering*, vol. 38, no. 45, pp. 975-979.
- Labuz J.F, Shah S.P, & Dowding C.H (1985) Experimental analysis of crack propagation in granite. *International Journal of Rock Mechanics and Mining Sciences & Geomechanics Abstracts*, vol. 22, pp. 85-98.
- Lan H, Martin C.D, & Hu B (2010) Effect of heterogeneity of brittle rock on micromechanical extensile behavior during compression loading. *Journal of Geophysical Research*, vol. 115, no. B1.
- Li C.C (2017) Principles of rockbolting design. *Journal of Rock Mechanics and Geotechnical Engineering*, vol. 9, pp. 396-414.
- Li X, Kim E, & Walton G (2019) A study of rock pillar behaviors in laboratory and in-situ scales using combined finite-discrete element method models. *International Journal of Rock Mechanics and Mining Sciences*, vol. 118, pp. 21-32.
- Lisjak A & Grasselli G (2014) A review of discrete modeling techniques for fracturing processes in discontinuous rock masses. *Journal of Rock Mechanics and Geotechnical Engineering* vol. 6, no. 4, pp. 301-314
- Lisjak A (2013) Investigating the influence of mechanical anisotropy on the fracturing behaviour of brittle clay shales with application to deep geological repositories. Ph.D. thesis, University of Toronto, Toronto, Canada.

- Lisjak A, Figi D, & Grasselli G (2014) Fracture development around deep underground excavations: Insights from FDEM modelling. *Journal of Rock Mechanics and Geotechnical Engineering*, vol. 6, pp. 493-505.
- Lockner D.A, Byerlee J.D.B, Kusenko V, Ponomarev A, & Sidorin A (1991) Quasi-static fault growth and shear fracture energy in granite. *Nature*, vol. 350, pp. 39-42.
- Londe P (1988) Discussion on the determination of the shear stress failure in rock masses. *ASCEJ Journal of the Geotechnical Engineering Division*, vol. 4, no. 3, pp. 374-376.
- Lunardi P (2000) The design and construction of tunnels: analysis of controlled deformation in rocks and soils. *Tunnels & Tunnelling International special supplement, (ADECO-RS approach)*
- Martin C.D & Chandler N.A (1994) The progressive fracture of Lac du Bonnet granite. *International Journal of Rock Mechanics and Mining Sciences & Geomechanics Abstracts*, vol. 31, no. 16, pp. 643-659.
- Meschke G, Kropik C, & Mang H (1996) Numerical analysis of tunnel linings by means of a viscoplastic material model for shotcrete, *International Journal for Numerical Methods in Engineering*, vol. 39, no. 18, pp. 3145-3162.
- Mohajerani A, Rodrigues D, Ricciuti C, & Wilson C (2015) Early-age strength measurement of shotcrete. *Journal of Materials*. Article ID 470160, p. 10.
- Munjiza A, Owen D.R.J, & Bicanic N (1995) A combined finite-discrete element method in transient dynamics of fracturing solids. *Engineering with Computers*, vol. 12, pp. 145-174.
- Neumann M (2001) CAMIRO Safe and Rapid Development Project – Benchmarking of 12 Canadian Mine, Neumann Engineering and Mining Services.
- Nguyen-Minh D & Guo C (1996) Recent progress in convergence confinement method. In: Barla G (ed) *Prediction and performance in rock mechanics and rock engineering: EUROCK' 96*, Balkema, Rotterdam, pp. 855-860
- Oke J, Vlachopoulos N, & Diederichs M.S (2013) Modification of the supported longitudinal displacement profile for tunnel face convergence in weak rock. In 47th US rock mechanics/geomechanics symposium. American Rock Mechanics Association, San Francisco.
- Oke J, Vlachopoulos N, & Diederichs M.S (2018) Improvement to the Convergence-Confinement Method: Inclusion of Support Installation Proximity and Stiffness, *Rock mechanics and rock engineering*, vol. 51, no. 5, pp. 1495-1519.
- Oreste P.P & Pelia D (1997) Modelling progressive hardening of shotcrete in convergence-confinement approach to tunnel design. *Tunneling and Underground Space Technology*, vol. 12, no. 3, pp. 425-431.
- Oreste P.P (1995) Nuovi modelli di calcolo delle strutture di rinforzo e precontenimento in galleria. Ph.D. Thesis, Politecnico di Torino.
- Oreste P.P (a) (2003) A procedure for determining the reaction curve of shotcrete lining considering transient conditions. *Rock Mechanics and Rock Engineering*, vol. 36, no. 3, pp. 209-236.

- Oreste P.P (b) (2003) Analysis of structural interaction in tunnels using the convergence-confinement approach. *Tunnelling and Underground Space Technology*, vol. 18, pp. 347-363.
- Panet M & Guenot A (1982) Analysis of convergence behind the face of a tunnel. *Proceedings of International Symposium Tunnelling*, Institution of Mining and Metallurgy, London, pp. 197-204.
- Panet M (1993) Understanding deformations in tunnels. In Hudson JA, Brown ET, Fairhurst C, Hoek E (eds) *Comprehensive Rock Engineering*, vol. 1. Pergamon, London, pp. 663-690.
- Panet M (1995) *Calcul des Tunnels par la Méthode de Convergence–Confinement*. Presses de l’Ecole Nationale des Ponts et Chaussées, Paris, p. 178.
- Rafiei Renani H, Martin C, & Hudson R (2016) Back analysis of rock mass displacements around a deep shaft using two- and three-dimensional continuum modeling. *Rock Mechanics and rock Engineering*, vol. 49, no. 4, pp. 1313-1327.
- Rispin M, Kleven O.B, Dimmock R, & Myrdal R (2017) Shotcrete: early strength and re-entry revisited—practices and technology. In *Proceedings of Underground Mining Technology*, in M Hudyma & Y Potvin (eds), Australian Centre for Geomechanics, Sudbury, pp. 55-70.
- Rocscience (2004) ‘Phase2’, version 5, Toronto, Canada.
- Rocscience (2011) ‘Phase2’, version 8, Toronto, Canada.
- Rocscience (2014) ‘RS²’, version 9, Toronto, Canada.
- Rocscience (2019) ‘RS²’, version 10, Toronto, Canada.
- Salencon J (1969) Contraction Quasi-Statique D’une Cavite a Symetrie Spherique Ou Cylindrique Dans Un Milieu Elastoplastique. *Annales Des Ponts Et Chaussees*, pp. 231-236.
- Saw H.A, Villaescusa E, Windsor C.R, & Thompson A.G (2009) Non-linear elastic-plastic response of steel fibre reinforced shotcrete to uniaxial and triaxial compression testing, In *Proceedings of Shotcrete for Underground Support XI*, Engineering Conferences International, Davos, Switzerland.
- Shütz R (2010) Numerical Modelling of Shotcrete for Tunnelling. PhD thesis, Imperial College London, London, England.
- Schubert P (1988) Beitrag zum rheologischen Verhalten von Spritzbeton, vol. 6, no. 3, pp. 150-153.
- Stewart P, Ramezanzadeh A, & Knights P (2006) Benchmark Drill and Blast and Mechanical Excavation Advance Rates for Underground Hard-Rock Mine Development. In *Proceedings of Australian Mining Technology Conference*, Hunter Valley, Australia.
- Timoshenko S.P (1976) *Strength of Materials*. third ed. Krieger Publishing Company, Florida.
- Unlu T & Gercek H (2003) Effect of Poisson’s ratio on the normalized radial displacements occurring around the face of a circular tunnel. *Tunneling and Underground Space Technology*, vol. 18, no. 5, pp. 547-553.

- Vazaios I, Vlachopoulos N, & Diederichs M.S (2019) Mechanical analysis and interpretation of excavation damage zone formation around deep tunnels within massive rock masses using hybrid finite–discrete element approach: case of Atomic Energy of Canada Limited (AECL) Underground Research Laboratory (URL) test tunnel. *Canadian Geotechnical Journal*, vol. 56, no. 1, pp. 35-59.
- Vlachopoulos N & Diederichs M.S (2009) Improved longitudinal displacement profiles for convergence confinement analysis of deep tunnels. *Rock Mechanics and Rock Engineering*, vol. 42, no. 2, pp. 131-146.
- Vlachopoulos N & Diederichs M.S (2014) Appropriate uses and practical limitations of 2D numerical analysis of tunnels and tunnel support response. *Geotechnical and Geological Engineering*, vol. 32, no. 2, pp. 469-488.
- Weber J (1979) Empirische Formeln zur Beschreibung der Festigkeitsentwicklung und des E-Moduls von Beton. *Betonwerk- und Fertigerteiltechnik*, vol. 12, pp. 753-756.
- Weigler K (1974) Junger Beton - Beanspruchung - Festigkeit – Verformung. Technical Report 20, Institut für Massivbau, University Darmstadt, Germany.